QUANTITATIVE DATA INTEGRATION FOR FRACTURE CHARACTERIZATION
USING STATISTICAL ROCK PHYSICS

A DISSERTATION

SUBMITTED TO THE DEPARTMENT OF GEOPHYSICS

AND THE COMMITTEE ON GRADUATE STUDIES

OF STANFORD UNIVERSITY

IN PARTIAL FULFILLMENT OF THE REQUIREMENTS

FOR THE DEGREE OF

DOCTOR OF PHILOSOPHY

Diana Sava

August 2004

I certify that I have read this dissertation and that, in my opinion, it is fully adequate in scope of and quality as a dissertation for the degree of Doctor of Philosophy.

_____

Gary Mavko (Principal Adviser)

I certify that I have read this dissertation and that, in my opinion, it is fully adequate in scope of and quality as a dissertation for the degree of Doctor of Philosophy.

_____

Biondo Biondi

I certify that I have read this dissertation and that, in my opinion, it is fully adequate in scope of and quality as a dissertation for the degree of Doctor of Philosophy.

_____

Tapan Mukerji

Approved for the University Committee on Graduate Studies:

_____

iii

Abstract

The goal of this dissertation is to design a methodology for quantitative integration of geological information with seismic data using rock physics theories, formulated in the framework of an inverse problem. I illustrate this method with fracture characterization of hydrocarbon reservoirs.

There are different types of information that can be used to study fractures, such as geologic, seismic, and well-log, and each one of them contributes in a different way to fracture characterization. Thus, by using these different sources of information, we can better constrain the predictions on the fracture parameters, such as fracture density and orientation. The various types of data from geology and seismic can be combined quantitatively if we translate them into the common language of probability theory. This probabilistic approach allows us to integrate quantitatively the various types of information and to estimate the uncertainty in our predictions.

A general way of expressing mathematically the prior geological knowledge about the fracture parameters is through *a priori* probability density functions (PDFs). I present a method to estimate the prior PDF for fracture parameters from geological constraints, using the Maximum Entropy Principle. At the same time, seismic data is affected by measurement errors. Therefore, I express the seismic information using PDFs, representing the measurement uncertainties. Furthermore, the theoretical relations between the fracture parameters and the seismic data, given by rock physics theories, are also uncertain. This uncertainty is due to approximations in the rock physics models and to natural variability of the rock properties. I present a method to estimate the uncertainty

in the theoretical relation between the fracture parameters and the seismic data, caused by the natural variability of the rock properties. This uncertainty can also be expressed mathematically using PDFs. The final result for the integration is represented by the *a posteriori* PDF for the fracture parameters. This posterior PDF represents an updated measure of uncertainty, obtained after combining quantitatively the prior geological information, the seismic measurements and the information from the rock physics theories. From the posterior PDFs I derive the expected values for the fracture parameters, and also probability maps, as a general way to express the uncertainty in the estimates.

I demonstrate this methodology with a fractured carbonate reservoir in eastern Texas. The fracture orientation is determined from seismic data, based on rock physics theories. I use a bootstrap method to estimate the uncertainty in the fractures' strike, due to seismic measurement errors. The fracture density is determined using rock physics theories, by integrating quantitatively the prior information, obtained from the geological interpretation of a fault at the top of the reservoir, with reflectivity attributes derived from a 3D seismic data set. I emphasize the uncertainty in the fracture density, and the relative impact of the prior geologic information in comparison with the seismic information on the final results for fracture density distribution.

This methodology provides a framework for integrating diverse data into one consistent result for subsurface rock properties, with an estimate of uncertainty associated with it. Therefore, this method facilitates an informed decision-making process for reservoir management, based on the uncertainty estimates.

Acknowledgements

My time spent at Stanford is forever in the present tense. It cannot be otherwise. It is so alive, so fresh, so unique. I am very grateful to the many people who have made it so special.

First and foremost, I would like to extend my deepest gratitude to my advisor, Gary Mavko. Among his students there is a consensus: Gary is a wonderful advisor. He is not only a bright, innovative scientist and an excellent teacher, but also a very kind person, considerate, patient, understanding, and full of humor. I am deeply thankful for his professional and personal support, for his positive feedback and encouragements, which have helped me tremendously. Gary has been a great source of scientific inspiration and friendly advice throughout the years of my studies. I was honored to be one of his students.

I would also like to thank my defense and reading committee members, Biondo Biondi, Jerry Harris and Tapan Mukerji, for their constructive comments and excellent suggestions, during my qualification exam, annual reviews, and interesting discussions.

I am also thankful to Amos Nur for his trust in me. Amos sent me the letter of acceptance to the Ph.D. program in the Stanford Rock Physics and Borehole Geophysics (SRB) group, when I was about to accept the offer of the rival university across the bay. Now I am privileged to be part of the large SRB family, where Gary Mavko, Jack Dvorkin, Amos Nur, Francis Muir, Tapan Mukerji, Manika Prasad, Youngseuk Keehm, and the students provide an excellent and friendly working environment, scientifically

Even though he is not among us anymore, I would like to thank my father, Ioan Eros, for passing me his love for science, especially for physics and mathematics, early in my childhood. He would have been very happy to see me where I am today. There are not enough words to express my gratitude for my mother, Viorica Eros. With her selfless love, tremendous support, infinite devotion and generosity, coupled with an innate modesty, my mother is the model that guides me through my life.

Finally, I would like to thank my husband, Paul, for bringing me to Stanford in the first place. I am deeply thankful for his decision and, in general, for his great vision regarding our life together. I thank him a lot for his steady support, and for the inspiring discussions we had on our way to the office every morning. If it were not for his unique way of motivating me, I would have not completed this work. The most important reason, for which I am happy to have Paul as my husband, is our daughter, Iulia Victoria, who has given my life the deepest meaning. This dissertation is the book that I kept telling Iulica about when I left her every morning for the office. She wanted me so much to finish it sooner, so that I can spend more time with her. Thank you for being patient, my little one. Even though you will find it not nearly as fascinating as the children's fairy-tales, this book is dedicated to you, with my whole love.

Table of Contents

List of Tables

List of Figures

xvi

Chapter 1

Introduction

1.1   Motivation and objectives

Estimating subsurface properties in the geosciences is a challenging problem, always subject to uncertainty. The main contributing causes for this uncertainty are limited measurement resolution, insufficient measurements relative to the subsurface complexities, a limited understanding of the physical and geological phenomena, and natural variability of the target rock properties, among others. Each geoscience discipline brings different information -often complementary, but sometimes contradictory- about the subsurface heterogeneities. Therefore, integrating different types of geological and geophysical information can better constrain our predictions of the subsurface rock properties. The challenge is to combine quantitatively these various types of information into one consistent result, together with an estimate of the uncertainty associated with it.

The main objective of this thesis is to address this challenge by designing a methodology for quantitative integration of geological information with seismic data using rock physics theories (Mavko et al., 1998). The second objective is to apply this methodology to fracture characterization of hydrocarbon reservoirs.

Fracture characterization is of great practical importance not only in hydrocarbon recovery, but also in mine and well stability, earthquake studies, CO_2 sequestration,

nuclear waste isolation, etc.. In particular, fractures are of great importance for hydrocarbon exploration and production, because significant amounts of hydrocarbons are trapped in tight reservoirs. In such formations, natural fractures are the main factors controlling fluid flow. The key requirement for efficient management of such reservoirs is the ability to locate fractures and to describe their parameters, such as fracture density, orientation, and type of fluid saturating the fractures.

Many types of information can be used to study fractures, and each one of them contributes in a different way to fracture characterization. For example, geological outcrop studies give us direct observations of the fracture orientation, spatial density, and sometimes even their length. However, the challenge is to extrapolate this information at the reservoir depth. Seismic data, on the other hand, provide a good coverage at depth, but the measurements are indirectly related to fractures, and their resolution is lower than the scale of the features we are interested in. However, even though we cannot directly image the fractures from seismic measurements, we can use various seismic attributes, which give us information about fracture density, orientation, and sometimes the type of fluid saturating the fractures.

In this thesis, I integrate these various types of geological and seismic information using rock physics theories, in the framework of an inverse problem, as defined by Tarantola (1982, 1987). A typical inverse problem has three different elements: 1) the model parameters, represented by the subsurface rock properties that we are interested in, (e.g. fracture characteristics), 2) the data parameters (e.g. seismic measurements), and 3) the physical laws that relate the model parameters to the data parameters, which are given by rock physics theories. In addition to the seismic measurements, we often have prior information about the subsurface rock properties (model parameters) from geological interpretation. These various types of geological and seismic information can be combined quantitatively if we translate them into the common language of probability theory.

A general way of expressing mathematically the prior geological knowledge about the model parameters is through *a priori* probability density functions (PDFs). The seismic data, which is affected by measurement errors, can also be described through

PDFs, representing the measurement uncertainties. Furthermore, the theoretical relations between the model parameters (fracture characteristics) and the data parameters (seismic attributes), given by rock physics theories, are also uncertain. This uncertainty is due to approximations in the rock physics models and to natural variability of the rock properties. We can also use PDFs to express mathematically the uncertainty in the physical correlations between the model and data parameters.

The language of probability theory allows us to integrate quantitatively the various types of information and, at the same time, to estimate the uncertainty in our predictions. The solution to an inverse problem formulated in this framework is represented by the *a posteriori* PDF for the model parameters (fracture characteristics), obtained by combining quantitatively the prior geological information, the seismic measurements and the information from the rock physics theories. From this PDF we can obtain the posterior expected values for fracture parameters, but we can also derive probability maps, as a general way of expressing the uncertainty in our estimations. The language of probability also allows us to estimate the impact of each type of information in reducing the uncertainty in our predictions (Shannon, 1948; Takahashi et al., 1999). Therefore, this method can have a significant impact in risk and decision analysis.

1.2   Thesis outline

The structure of this dissertation follows closely the methodology introduced in the preceding section. The first part of the thesis focuses on the rock physics theories on fractures, which relate the model to data parameters, the second part focuses on the data parameters, represented by seismic attributes from a 3D seismic data set acquired over a fractured carbonate reservoir, and the last part presents the integration methodology, in the framework of an inverse problem.

The key link between the fracture characteristics (model parameters) and the seismic measurements (data parameters) is given by rock-physics models. In Chapter 2 of the thesis, I review some of the existing rock-physics theories on fractures, such as Hudson's (1980, 1981, 1997) and Schoenberg's (1980, 1983, 1989) models. The validity of these various theoretical models has hardly been tested experimentally. Therefore, one

objective of this chapter is to explore the validity of these models and of the relations between them, to choose the most appropriate one for field fracture characterization. To achieve this goal, I compare the theoretical predictions of the various fracture models with laboratory measurements on simulated fractured media, performed by Hsu and Schoenberg (1993). Another objective of this chapter is to calibrate the fracture density parameter, defined in Hudson's model, based on the comparison between the theoretical predictions and the laboratory results. I also analyze the collection of field data on shear-wave anisotropy acquired in various places around the globe by different authors and summarized by Crampin (1994). The goal of this analysis is to get prior constraints on the fracture parameters as a function of depth, assuming that the observed shear-wave anisotropy is caused by the alignment of fractures.

Chapter 3 presents the results of the rock physics fracture modeling, based on well-log data from a gas carbonate reservoir in eastern Texas. An important objective of this chapter is to determine which seismic attributes are optimal to differentiate the gas-filled fractured zones from the other heterogeneities in this reservoir. Another objective is to assess the uncertainty in the fracture characterization caused by the natural variability of the unfractured rock properties, through *Monte Carlo* simulations. The stochastic approach allows us to incorporate the natural geologic variability of rock properties into deterministic elastic models (Mavko and Mukerji, 1998; Mukerji et al., 2001).

Chapter 4 focuses primarily on the data parameters, represented by the reflectivity attributes from a 3D seismic data set acquired over the fractured carbonate reservoir in eastern Texas. In the geological hypothesis of a single set of aligned, vertical fractures, Amplitude Variation with Azimuth (AVAZ) at far offsets is a useful attribute to determine the fracture orientation and the relative intensity of fracturing, as previous field studies show (Mallick et al. , 1998; Teng, 1998; Perez et al., 1999; Shen et al., 2002) The main goal of this chapter is to determine the fracture orientations and the azimuthal anisotropy of the reflectivity at the top of the reservoir, together with a measure of uncertainty about these estimates, caused by the errors in the seismic reflectivity data.

Finally, Chapter 5 presents the methodology for quantitative integration of geological information with seismic data using rock physics theories discussed in Chapters 2 and 3.

The main objective is to constrain the prior information about fracture density, derived from the geologic interpretation of a fault at the top of the reservoir, with reflectivity attributes derived from the 3D seismic data set presented in Chapter 4. I also present a method for estimating prior uncertainties in the fracture density, using geological constraints. I emphasize the relative impact of the prior geological information, in comparison with the seismic measurements and associated errors, on the posterior fracture density distribution.

Chapter 6 summarizes the main findings and contributions of the thesis.

Chapter 2

Fracture Models and Bounds on Crack Density: Comparison with Laboratory and Field Measurements

2.1 Abstract

Fracture characterization from seismic data requires elasticity theories that relate the mechanical properties of fractured rocks to the physical parameters of fractures, such as fracture density, fracture orientation, type of fluids filling the fractures, etc. Hudson's penny-shaped crack model is one of the theories that predict the elastic properties of a fractured medium, assuming distributions of penny-shaped cracks. This model is valid for crack densities up to 0.1. I address several questions in this chapter: How far can we go beyond this limit before the rock loses its strength? How prevalent is fracturing at crack density of 0.1? Can we improve our physical understanding of this model parameter to better represent real fractures?

In this chapter I review in detail some of the existing fracture models, such as the penny-shaped crack model and the linear-slip model. These two models are equivalent to the first order. However, I show that, if we use the relationship between these two models

beyond the limit of validity of penny-shaped crack model, we can obtain unphysical results.

I also use the collection of field data by Crampin (1994) on shear-wave anisotropy to suggest practical bounds for crack density as a function of depth. This collection of data indicates that there is an upper bound on the shear-wave anisotropy, and implicitly on the crack density, that decreases with depth. For example, the upper bound on shear-wave anisotropy decreases from 14% at the surface to about 3% at 5 km depth. This observation can be used to constrain the crack density values as a function of depth.

In this chapter I also compare published laboratory measurements on simulated fractured media with the predictions of various theoretical models. I find good agreement of these theoretical fracture models with the lab measurements.

2.2   Introduction

Fracture models provide a quantitative link between the elastic properties of the fractured rocks, determined from seismic data (observable parameters), and the physical characteristics of fractures (model parameters). There are two widely used fracture models, both corresponding to effective medium theory. The first one is represented by Hudson's (1980, 1981) model, which approximates fractures as ellipsoidal cracks. The second one is the Schoenberg's (1980, 1983, 1989) linear-slip model, which represents fractures as infinitely extended planes of weakness. These two models, while very different in their description of fractures, are elastically equivalent to first order (Schoenberg and Douma, 1988; Li Teng, 1998). Therefore, we can use the relation between them to exploit their specific advantages. The linear-slip model, unlike to the penny-shaped crack model, does not contain porosity information. However, based on the equivalence between the two models, we can use the ratio between normal and tangential excess compliances due to fractures, as described in the linear-slip model, as an indicator of fluid content. I also show that if we use the relationship between these two models beyond the limit of validity of the Hudson's model, we obtain unphysical results.

In this chapter I also review the more recently developed fracture model by Hudson (1997), which is a combination of the penny-shaped crack model and the linear-slip model. In this work, the fracture is modeled as a planar distribution of open penny-shaped cracks, between which the faces of the fracture are held in contact by the ambient pressure and friction. This model has the advantages of both the penny-shaped crack model and the linear-slip model, while also providing a better physical representation for the fractures. Hudson also considers the case of a planar distribution of approximately circular welded regions, between which the faces are separated as a fracture. These new models can be applied to heavily fractured media.

There are many published papers regarding the theoretical effective medium models of fractures. However, little work has been done to test the validity of these various models and of the relationships among them. Hsu and Schoenberg (1993) perform physical measurements on a simulated fractured medium to test the assumption of the linear-slip model. I use their laboratory results to explore the validity of the relationship between the linear-slip model and the penny-shaped crack model with volumetric distributions of cracks (Hudson, 1981). I also compare the theoretical predictions of Hudson's model (1997) with a planar distribution of cracks, with the results from the laboratory measurements. I find good agreement between the theoretical predictions and the actual measurements on the simulated fractured medium. This comparison suggests that a crack density of 0.1 as expressed by Hudson's model represents a relatively high degree of fracturing at realistic reservoir pressures.

The collection of the shear-wave anisotropy data from around the globe, reported by different authors and summarized by Crampin (1994), can help put valuable constraints on the fracture density distribution as a function of depth. This collection suggests the presence of an upper bound for the shear-wave anisotropy, and implicitly for the crack density. The upper-bound decreases with increasing depth, due to higher pressures encountered deeper in the Earth's crust.

2.3 Fracture models

In this section I present a review of Hudson's penny-shaped crack models (1981, 1997) and the Schoenberg's linear-slip model (1980, 1983, 1989).

2.3.1 Hudson's penny-shaped crack model

Hudson's model (1980, 1981, 1990, 1994) is an effective medium theory that assumes an elastic solid with an internal distribution of thin, penny-shaped cracks (Figure 2.1). Hudson uses crack density (e) and the aspect ratio of the oblate sphereoidal cracks (α) to describe the structure of fracture systems. The aspect ratio is the ratio between the short and the long semi-axes of the penny-shaped crack. The crack density, or fracture density, is defined as follows:

$$e = \frac{N}{V} a^3 = \frac{3\phi}{4\pi\alpha} .$$

(2.1)

Here, a is the crack radius, N/V is the number of cracks per unit volume, ϕ is the crack-induced porosity, and α is the aspect ratio of the cracks. The effective moduli are given as follows:

$$C_{ij}^{eff} = C_{ij}^0 + C_{ij}^1 + C_{ij}^2 ,$$

(2.2)

where C_{ij}^0 are the components of the isotropic background elastic stiffness tensor, and C_{ij}^1, C_{ij}^2 are the first and second order corrections, respectively, which depend on the crack orientation, density, aspect ratio, and the bulk and shear moduli of the material filling the cracks. The second-order corrections have the flaw that for increasing crack density the rock does not fall apart. On the contrary, the second order correction predicts that the elastic stiffness of the rock increases with increasing crack density for values of crack density larger than 0.1. Therefore, in the analysis presented in this chapter, I use only the first order corrections. In this case, the elastic stiffness of the rock decreases monotonically as the crack density increases, until the rock loses completely its strength.
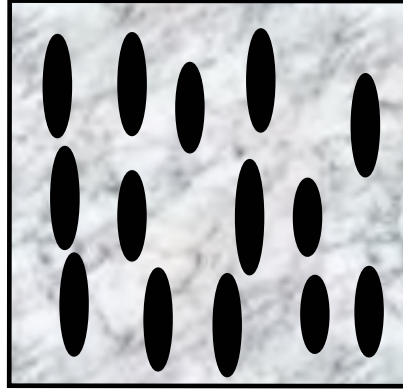
Figure 2.1: Graphical representation of vertical fractures using the penny-shaped crack model with volumetric distribution of cracks (Hudson, 1981).

Hudson's theory is well developed for diverse crack distributions, including one or more sets of parallel fractures, a conical distribution of the crack normals, and a random distribution of fracture orientations. The limitation is that it only works for crack densities smaller than 0.1 and for small aspect ratios, up to 0.3.

For a single set of parallel fractures with the crack normals aligned along the x_1-axis, the cracked medium shows a transversely isotropic elastic symmetry, and the first-order effective elastic stiffness matrix is given by

$$
\begin{pmatrix}
(\lambda+2\mu)\left(1-\dfrac{\lambda+2\mu}{\mu}eU_{33}\right) & \lambda\left(1-\dfrac{\lambda+2\mu}{\mu}eU_{33}\right) & \lambda\left(1-\dfrac{\lambda+2\mu}{\mu}eU_{33}\right) & 0 & 0 & 0 \\
\lambda\left(1-\dfrac{\lambda+2\mu}{\mu}eU_{33}\right) & (\lambda+2\mu)\left(1-\dfrac{\lambda^2}{\mu(\lambda+2\mu)}eU_{33}\right) & \lambda\left(1-\dfrac{\lambda}{\mu}eU_{33}\right) & 0 & 0 & 0 \\
\lambda\left(1-\dfrac{\lambda+2\mu}{\mu}eU_{33}\right) & \lambda\left(1-\dfrac{\lambda}{\mu}eU_{33}\right) & (\lambda+2\mu)\left(1-\dfrac{\lambda^2}{\mu(\lambda+2\mu)}eU_{33}\right) & 0 & 0 & 0 \\
0 & 0 & 0 & \mu & 0 & 0 \\
0 & 0 & 0 & 0 & \mu(1-eU_{11}) & 0 \\
0 & 0 & 0 & 0 & 0 & \mu(1-eU_{11})
\end{pmatrix}
\tag{2.3}
$$

U_{11} and U_{33} depend on the crack conditions:

$$
U_{11} = \frac{16(\lambda+2\mu)}{3(3\lambda+4\mu)}\frac{1}{1+M} \,,
\tag{2.4}
$$

$$U_{33} = \frac{4(\lambda + 2\mu)}{3(\lambda + \mu)} \frac{1}{1 + k},$$

(2.5)

with:

$$M = \frac{4\mu'(\lambda + 2\mu)}{\pi \alpha \mu (\lambda + \mu)},$$

(2.6)

$$k = \frac{\left[K' + (4/3)\mu'\right](\lambda + 2\mu)}{\pi \alpha \mu (\lambda + \mu)}.$$

(2.7)

K' and μ' are the bulk and shear moduli of the inclusion material, λ and μ are the Lame constants of the unfractured rock, and α is the aspect ratio of the penny-shaped crack.

2.3.2 Schoenberg's linear-slip model

Schoenberg's linear-slip model (1983, 1988, 1989) is based on the Backus (1962) average. This model treats fractures, regardless of their shape and microstructure, as either infinitely thin and highly compliant layers, or planes of weakness with linear-slip boundary conditions (Figure 2.2). These two representations are equivalent in the long-wavelength limit.

Figure 2.2: Graphical representation of fractures using the linear-slip model with infinitely long planes of weaknesses.

The exact Backus averaging procedure for parallel, thin layers embedded in an isotropic rock leads to the following simple form of the effective compliance matrix S:

$$S = So + S_f , \tag{2.8}$$

where *So* is the compliance matrix of the host rock and S_f is the excess compliance associated with the layers (Schoenberg, 1983). It may be proved, by means of reflectivity matrix method, that for vertical layers orthogonal to the x_1 axis, S_f is given by:

$$S_f = v \begin{pmatrix} S_{11f} & 0 & 0 & 0 & S_{15f} & S_{16f} \\ 0 & 0 & 0 & 0 & 0 & 0 \\ 0 & 0 & 0 & 0 & 0 & 0 \\ 0 & 0 & 0 & 0 & 0 & 0 \\ S_{15f} & 0 & 0 & 0 & S_{55f} & S_{56f} \\ S_{16f} & 0 & 0 & 0 & S_{56f} & S_{66f} \end{pmatrix}, \tag{2.9}$$

where v represents the fraction of the total volume occupied by the thin layers, while S_{ijf} are the excess compliances of the fracture layers' material. The above equation can also be used to describe a set of parallel fractures of infinite extent with the fracture normals parallel to the x_1 axis. Therefore, the matrix of excess fracture compliance can be written as follows:

$$S_f = \begin{pmatrix} K_N & 0 & 0 & 0 & K_{NV} & K_{NH} \\ 0 & 0 & 0 & 0 & 0 & 0 \\ 0 & 0 & 0 & 0 & 0 & 0 \\ 0 & 0 & 0 & 0 & 0 & 0 \\ K_{NV} & 0 & 0 & 0 & K_V & K_{VH} \\ K_{NH} & 0 & 0 & 0 & K_{VH} & K_H \end{pmatrix}. \tag{2.10}$$

The jumps in the stress tensor and displacement vector "*u*" across the planes of weakness satisfy the boundary conditions of linear slip (Schoenberg, 1980, Molotkov and Bakulin, 1997, Bakulin et al., 2000):

$$\left[\sigma_{11}\right] = \left[\sigma_{12}\right] = \left[\sigma_{13}\right] = 0$$
$$\left[u_1\right] = H\left(K_N\sigma_{11} + K_{NH}\sigma_{12} + K_{NV}\sigma_{13}\right)$$
$$\left[u_2\right] = H\left(K_{NH}\sigma_{11} + K_H\sigma_{12} + K_{VH}\sigma_{13}\right)$$
$$\left[u_3\right] = H\left(K_{NV}\sigma_{11} + K_{VH}\sigma_{12} + K_V\sigma_{13}\right)$$

(2.11)

Here, H is the average spacing between fractures, σ are the stresses, and u are the displacements. Square brackets indicate jumps across the interface. Based on the above relations, we can also interpret the physical meaning of the compliances K_N, K_V, K_H, K_{NV}, K_{NH}, K_{VH}. For example, K_N is the normal fracture compliance relating the jump per unit length of the normal displacement u_1 to the normal stress σ_{11}. In the same way, K_V and K_H are the two shear compliances along the vertical (x_3) and horizontal (x_2) directions. The compliance K_{NV} is the coupling factor between the jump of the normal displacement u_1 and the shear stress σ_{13}, or equivalently between u_3 and σ_{11}. Such a coupling may be caused by a slight roughness of the fracture surfaces, with peaks and troughs somewhat offset from one side to the other of the fracture (Schoenberg and Douma, 1988). If K_{NV} is nonzero, then the normal and shear slips with respect to the fracture plane (u_1 and u_3) are coupled. In this case the medium has a monoclinic symmetry.

The simplest form of the matrix of excess fracture compliance is obtained if we assume no coupling between the slips along the coordinate directions. This type of fracture set is called rotationally invariant by Schoenberg and Sayers (1995) and satisfies the following relationships (Hsu and Schoenberg, 1993):

$$K_{NV} = K_{NH} = K_{VH} = 0$$
$$K_V = K_H = K_T$$

(2.12)

As a result, the matrix of fracture excess compliance reduces to

$$S_f = \begin{pmatrix} K_N & 0 & 0 & 0 & 0 & 0 \\ 0 & 0 & 0 & 0 & 0 & 0 \\ 0 & 0 & 0 & 0 & 0 & 0 \\ 0 & 0 & 0 & 0 & 0 & 0 \\ 0 & 0 & 0 & 0 & K_T & 0 \\ 0 & 0 & 0 & 0 & 0 & K_T \end{pmatrix}.$$

(2.13a)

We can also write the matrix of fracture stiffness as follows:

$$C_f = \begin{pmatrix} (\lambda+2\mu)/(1+E_N) & 0 & 0 & 0 & 0 & 0 \\ 0 & 0 & 0 & 0 & 0 & 0 \\ 0 & 0 & 0 & 0 & 0 & 0 \\ 0 & 0 & 0 & 0 & 0 & 0 \\ 0 & 0 & 0 & 0 & \mu/E_T & 0 \\ 0 & 0 & 0 & 0 & 0 & \mu/E_T \end{pmatrix}. \tag{2.13b}$$

Here, E_N and E_T represent the non-negative, dimensionless fracture compliances, which express the ratios of the compliance in the fractures to the corresponding compliance in the fractured medium. These quantities are also called the specific compliances.

Hsu and Schoenberg (1993) introduce two dimensionless quantities:

$$\Delta_N = \frac{E_N}{1+E_N} = \frac{(\lambda+2\mu)K_N}{1+(\lambda+2\mu)K_N}, \tag{2.14}$$

$$\Delta_T = \frac{E_T}{1+E_T} = \frac{\mu K_T}{1+\mu K_T}. \tag{2.15}$$

These quantities represent the normal and tangential weaknesses, and they vary from 0 to 1.

In the case of an HTI medium generated by planes of slip with their normals orthogonal to the x_1-axis, the effective elastic stiffness matrix is as follows:

$$\begin{pmatrix} (\lambda+2\mu)(1-\Delta_N) & \lambda(1-\Delta_N) & \lambda(1-\Delta_N) & 0 & 0 & 0 \\ \lambda(1-\Delta_N) & (\lambda+2\mu)\left(1-\frac{\lambda^2}{(\lambda+2\mu)^2}\Delta_N\right) & \lambda\left(1-\frac{\lambda}{\lambda+2\mu}\Delta_N\right) & 0 & 0 & 0 \\ \lambda(1-\Delta_N) & \lambda\left(1-\frac{\lambda}{\lambda+2\mu}\Delta_N\right) & (\lambda+2\mu)\left(1-\frac{\lambda^2}{(\lambda+2\mu)^2}\Delta_N\right) & 0 & 0 & 0 \\ 0 & 0 & 0 & \mu & 0 & 0 \\ 0 & 0 & 0 & 0 & \mu(1-\Delta_T) & 0 \\ 0 & 0 & 0 & 0 & 0 & \mu(1-\Delta_T) \end{pmatrix}. \tag{2.16}$$

Although general HTI models are described by five independent parameters, the stiffness matrix from Equation 2.16 depends on just four quantities: λ, μ of the host rock, and the dimensionless fracture weaknesses, Δ_N and Δ_T. This medium is called TI (LSD),

where the initials TI correspond to transversely isotropic, while the initials LSD come from the "linear-slip deformation" assumption. Therefore, there is an additional constraint between the stiffness matrix components that can be written as follows (Schoenberg and Sayers, 1995):

$$C_{11}C_{33} - C_{13}^2 = 2C_{44}\left(C_{11} + C_{13}\right). \tag{2.17}$$

2.3.3   Relationship between the fracture models

In the linear-slip model, the descriptors of the fracture system - the specific compliances, E_N and E_T, and the spacing - are quite different from the description based on penny-shaped cracks. However, Schoenberg and Douma (1988) and Teng (1998) show that, to the first order, Hudson's model is equivalent to the linear-slip model, such that:

$$\Delta_N = \frac{\lambda + 2\mu}{\mu} U_{33} e, \tag{2.18}$$

$$\Delta_T = U_{11} e. \tag{2.19}$$

Here, Δ_N and Δ_T are the normal and tangential weaknesses as described through the linear-slip model, and U_{11}, U_{33}, and e are used in Hudson's model. These relationships are evident if we compare the stiffness matrices for an HTI medium from Equation 2.3 and Equation 2.16.

From Equations 2.18 and 2.19 we get these relations:

$$e = \frac{\mu}{\lambda + 2\mu} \frac{\Delta_N}{U_{33}}$$
$$e = \frac{\Delta_T}{U_{11}} \tag{2.20}$$

This means that, once we fix a value of fracture density, the normal and tangential weaknesses must satisfy the following relationship:

$$\Delta_N = \frac{\lambda + 2\mu}{\mu} \frac{U_{33}}{U_{11}} \Delta_T. \tag{2.21}$$

If we now introduce the relations for U_{11} and U_{33} from Equations 2.4 and 2.5 into Equation 2.20, we get new expressions for the weaknesses (Bakulin et al., 2000):

$$\Delta_N = \frac{4e}{3g(1-g)\left[1+\dfrac{1}{\pi(1-g)}\left(\dfrac{K'+4/3\mu'}{\mu\alpha}\right)\right]},$$ (2.22)

$$\Delta_T = \frac{16e}{3(3-2g)\left[1+\dfrac{4}{\pi(3-2g)}\dfrac{\mu'}{\mu\alpha}\right]}.$$ (2.23)

In the Equations 2.22 and 2.23, g is given as follows:

$$g = \left(\frac{V_s}{V_p}\right)^2.$$ (2.24)

V_P and V_S represent the P- and S-wave velocities of the unfractured, isotropic background rock.

2.3.3.1 Pitfall: Pushing the Hudson's model beyond its limit of validity

In this section I explore the consequences of the first-order equivalence between the linear-slip model and the penny-shaped crack model for dry cracks.

Making $K'= 0$ and $\mu' = 0$ in Equations 2.22 and 2.23 we obtain the following relations between the fracture weaknesses and the crack density for dry cracks:

$$\Delta_N = \frac{4e}{3g(1-g)}$$

$$\Delta_T = \frac{16e}{3(3-2g)}$$ (2.25)

We observe that, for the dry cracks case, the description of the fractures using Hudson's model is based only on the crack density, while the description of the fractures using the linear-slip model is based on two parameters, both the normal and the tangential weaknesses. Therefore, the first-order equivalence between the Hudson's model and the linear-slip model implies that, for a certain crack density, the ratio between the normal and tangential weaknesses is fixed for dry cracks. In other words, the weaknesses Δ_N and

Δ_T are not independent. The normal weakness is related to the tangential weakness in the following way:

$$\Delta_N = \frac{3 - 2g}{4g(1 - g)}\Delta_T = \frac{(2 - \upsilon)(1 - \upsilon)}{(1 - 2\upsilon)}\Delta_T. \tag{2.26}$$

In Equation 2.26, v represents the Poisson's ratio of the unfractured rock. Therefore, if the normal and tangential weaknesses do not respect the relation from Equation 2.26, then when we use the relations in Equation 2.25 to predict the equivalent fracture density, we obtain two different values for crack density evaluated using Δ_N and Δ_T, respectively.

The fracture weaknesses must satisfy these conditions:

$$\begin{aligned} 0 < \Delta_N < 1 \\ 0 < \Delta_T < 1 \end{aligned} \tag{2.27}$$

where $\Delta = 0$ corresponds to an unfractured rock, and $\Delta = 1$ corresponds to a rock that has lost coherence, and is falling appart.

Therefore, based on the relations from Equation 2.25, the crack density should satisfy these conditions:

$$\begin{aligned} 0 < e < \frac{3}{4}g(1 - g) \\ 0 < e < \frac{3}{16}(3 - 2g) \end{aligned} \tag{2.28}$$

Figure 2.3 shows the variation of the upper limits for crack density as a function of the V_P/V_S ratio of the host rock. These limit values are calculated for $\Delta_N = 1$ (red curve) and for $\Delta_T = 1$ (blue curve) respectively.
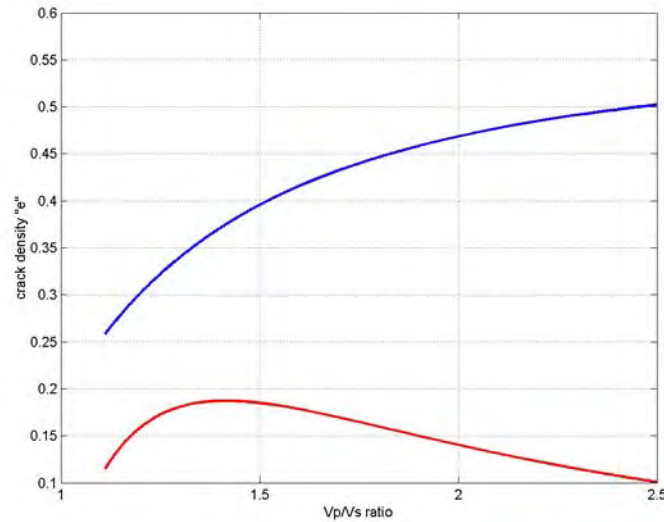
Figure 2.3: Variation of the upper limit for crack density as a function of the V_P/V_S ratio of the host rock such that $\Delta_N = 1$ (red curve) and $\Delta_T = 1$ (blue curve). The cracks are considered dry.

From Figure 2.3 we can see that when the normal and tangential weaknesses tend to 1, we are beyond the validity of the Hudson's model, and nonphysical behavior begins to appear. Firstly, the crack density exceeds the limit of 0.1 for all values of the V_P/V_S ratio of the unfractured host rock. Secondly, if we push its limits of validity, the Hudson model predicts for dry cracks that the rock will lose first its compressional strength, and then its shear strength, due to increasing fracture density. This result seems unrealistic. There is no physical reason described in Hudson's (1980, 1981) model why the rock should lose its compressional strength before its shear strength.

We can also observe in Figure 2.3 that for dry cracks embedded into carbonate rocks ($V_P/V_S = 2$), the crack density at which the rock loses it compressional strength is smaller than 0.15. Thus, a fracture density of 0.1 represents a relatively large degree of fracturing, especially for rocks with a high V_P/V_S ratio, such as carbonates.

Figure 2.4 shows the maximum values for the normal and tangential weaknesses as a function of the V_P/V_S ratio of the host rock, computed using the relations in Equation 2.25 for a crack density of 0.1. This crack density corresponds to the limit of validity for Hudson's model.
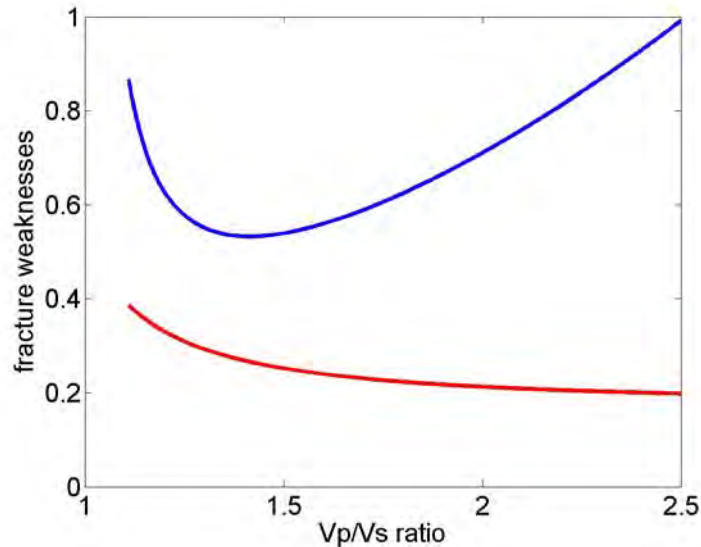
Figure 2.4: Variation of the upper limits for the normal (blue) and tangential (red) weaknesses as a function of the V_P/V_S ratio of the host rock, calculated using Equation 2.25 for a crack density equal to 0.1 (the limit of validity for Hudson's model). The cracks are considered dry.

Figure 2.4 gives the maximum values for the normal and tangential weaknesses that can be safely mapped into crack density for dry fractures. However, to insure the same solution whether the crack density is evaluated from the normal or tangential weakness, the weaknesses should satisfy the relation from Equation 2.26.

2.3.3.2 Fluid information in the linear-slip model

The linear-slip model does not contain porosity information. Therefore, we cannot conduct fluid substitution when using this model. However, we can use the equivalence of the linear-slip model with the penny-shaped crack model to gain insights about fluid effects in the fractures.

For example, the ratio between the normal and tangential excess compliances introduced by fractures (K_N/K_T) can be used as an indicator of fluid content (Schoenberg and Sayers, 1995). We begin with the Hudson's model, specifying the elastic bulk modulus of the fluid of interest, and then we find the equivalent K_N and K_T that give the same elastic tensor. Figures 2.5 and 2.6 show this ratio (K_N/K_T) for dry cracks and fluid-

filled cracks as a function of the V_P/V_S ratio of the host rock. Different curves correspond to different values of fracture density, from 0.01 to 0.1. For the fluid filled cracks, the aspect ratio is 0.001. For dry fractures, the results are independent of the aspect ratio, with the limitation given by the theory ($\alpha < 0.3$)
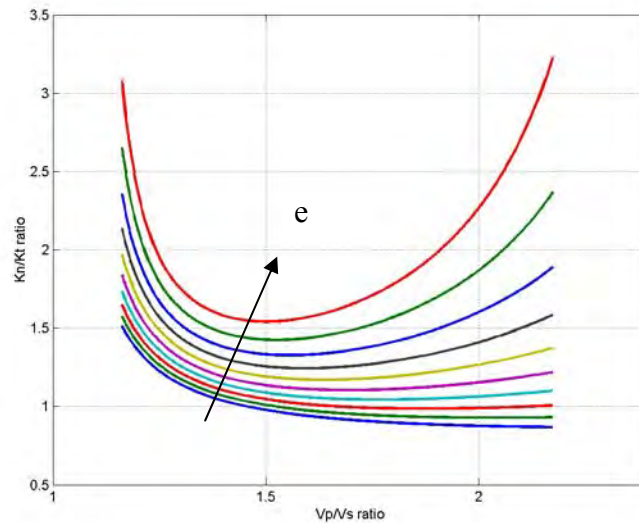
Figure 2.5: The ratio between normal and tangential compliances introduced by fractures as a function of the V_P/V_S ratio of the host rock. Different curves correspond to different values of fracture density. Fractures are considered dry.

As we can see from Figure 2.5, the values of K_N/K_T ratio are larger than 1. This means that for dry fractures, K_N is larger than K_T. In other words, Hudson's model predicts that the dry fractures are more compliant in compression than in shear. Also, the ratio increases with increasing fracture density.
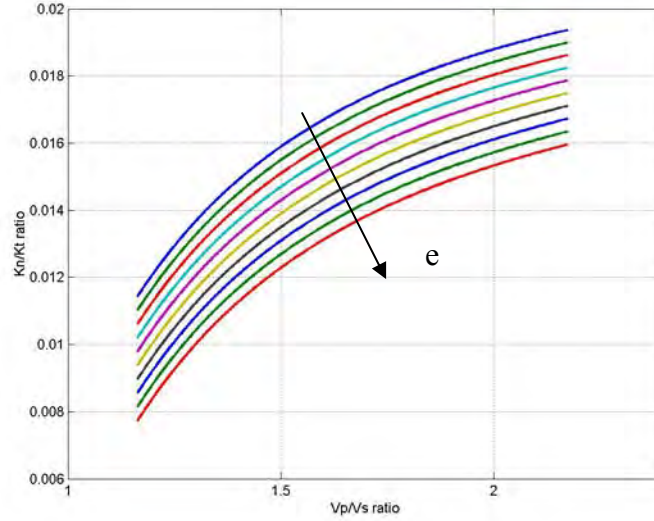
Figure 2.6: The ratio between normal and tangential compliances introduced by fractures as a function of V_P/V_S ratio of the host rock. Different curves correspond to different values of fracture density. Fractures are filled with a fluid whose bulk modulus is one order of magnitude lower than the shear modulus of the rock.

For fluid-filled cracks with small aspect ratio ($\alpha << 0.1$), we get the following inequality: $(K'+4/3\mu')/(\mu\alpha) >> 1$. Consequently, Δ_N goes to 0. Then, for fluid-filled cracks we have the following relations:

$$\Delta_N \rightarrow 0$$
$$\Delta_T = \frac{16e}{3(3-2g)}$$

(2.29)

Therefore, in contrast with the case for dry cracks, for fluid-filled fractures with small aspect ratios (0.001), the K_N/K_T ratio is much smaller than 1, and its values are very close to zero. In this case, Hudson's model predicts that the fractures are more compliant in shear than in compression. This ratio decreases as we increase the fracture density in the Hudson model.

Therefore, the ratio between the normal and tangential compliance introduced by fractures can be used as a fluid indicator for the linear-slip model.

2.3.4 Hudson's model for heavily fractured media

More recently, Hudson et al. (1997) have published fracture models that are a conceptual combination of the previous penny-shaped crack model and the linear-slip model. In this new model, the fracture is an infinite plane with two rough surfaces in contact. The fraction of the interface that is open is represented as a planar distribution of approximately penny-shaped cracks, while elsewhere the faces of the fracture are held together by the ambient pressure and friction (Figure 2.7). The interactions between cracks on the fracture planes are taken into account, while the interactions between cracks from different planes are ignored. Hudson also considers the case of a plane distribution of approximately circular welded regions within an area where otherwise the faces are separated as for a fracture (Figure 2.9).

Figure 2.7: Graphical representation of fractures using the penny-shaped crack model with planar distribution of cracks (Hudson, 1997).

For the first case of a planar distribution of cracks on a fracture plane, the normal and tangential weaknesses are given by

$$\Delta_N = \frac{E_N}{E_N + 1}, \tag{2.30}$$

$$\Delta_T = \frac{E_T}{E_T + 1}, \tag{2.31}$$

with

$$E_N = \frac{v^s a^3}{H} \frac{\lambda + 2\mu}{\mu} U_{33} \left\{ 1 + \left(v^s a^2\right)^{\frac{3}{2}} U_{33}\pi \left[1 - \left(\frac{V_S}{V_P}\right)^2 \right] \right\}$$

$$E_T = \frac{v^s a^3}{H} U_{11} \left\{ 1 + \left(v^s a^2\right)^{\frac{3}{2}} U_{11} \frac{\pi}{4} \left[3 - 2\left(\frac{V_S}{V_P}\right)^2 \right] \right\}$$

(2.32)

The variable are as follows:

v^s is the number density of cracks on the fracture surface,

a is the mean radius of the cracks,

H is the average spacing between fractures,

V_P and V_S are the P and S wave velocities of the unfractured rocks,

U_{11} and U_{33} are given in equations 2.4 and 2.5 and depend on crack conditions.

The overall crack density is as follows:

$$e = \frac{v^s a^3}{H} = \frac{r}{\pi} \frac{a}{H}.$$

(2.33)

Here, r represents the proportion of the fault surface occupied by cracks:

$$r = \pi v^s a^2.$$

(2.34)

We can see from Equation 2.32 that the fracture dimensionless compliances, E_N and E_T, depend on the number density of cracks in a nonlinear way. The dependence has a power law of 5/2.

In this model, the relative area of cracking, r, can vary from 0 to 0.2 ($0 < r < 0.2$) If we assume the relative area of cracking to be the maximum acceptable by the theory (0.2), we can compute the overall crack density depending on the ratio between the radius of the crack (a) and the spacing (H). Figure 2.8 presents the crack density as a function of the ratio of the average crack radius on the fracture plane to the fracture spacing, on a logarithmic scale.
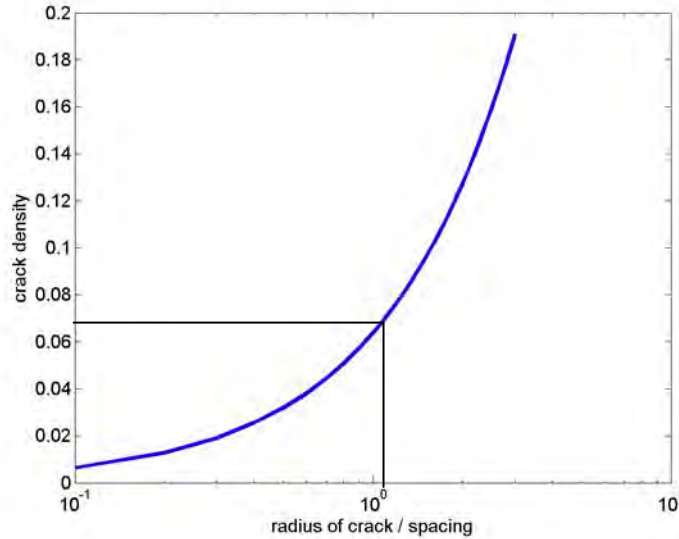
Figure 2.8: Crack density as a function of the ratio between the average radius of the cracks on the fracture planes and the fracture spacing. The values are computed using Equation 2.34, where the relative area of cracking is assumed to be 0.2. The corresponding crack density for a ratio of crack radius and spacing equal to 1 is schematically represented in this figure.

From Figure 2.8 we can see that for fracture spacing one order of magnitude higher than the mean radius of the crack, the overall crack density is very small. When the ratio between the radius of crack and the fracture spacing is 1, then the overall crack density is equal to 0.0637, for a relative area of cracking on the fracture planes equal to 0.2. In other words, when the height of the crack (two times its radius) is equal to the spacing between fractures, the overall crack density is 0.127. This fracture density estimated for a spacing equal to the crack height may be interpreted as the saturation level, as described by Bai (2000).

For fracture spacing one order of magnitude smaller than the radius of the crack, the overall crack density may increase significantly.

Hudson and Liu (1999) give an alternative approach to replace each fracture (or slip-interface) by an equivalent thin layer of material whose properties are given by

$$K_f = K' - \frac{\pi \Delta \mu}{4ar} \frac{\mu}{(\lambda + 2\mu)} \left\{ 1 - \frac{4}{3} \left(\frac{r^3}{\pi} \right)^{\frac{1}{2}} \right\}, \qquad (2.35)$$

$$\mu_f = \mu' + \frac{3\pi\Delta\mu}{16ar}\left(\frac{3\lambda + 4\mu}{\lambda + 2\mu}\right)\left\{1 - \frac{4}{3}\left(\frac{r^3}{\pi}\right)^{\frac{1}{2}}\right\}. \tag{2.36}$$

Here K' and μ' are the bulk and shear moduli of the inclusion material, Δ is the thickness of the equivalent layer for the fracture, a is the average radius of cracks, r is the relative area of cracking, and λ and μ are the Lame constants for the unfractured medium. The thickness of the layer is given by $\Delta = rd$. Here, d is the mean aperture of the cracks. Therefore, the aspect ratio of the cracks α, is given by $\alpha = \Delta/ar = d/a$.

For the second case, when the fracture is modeled as a planar distribution of welded regions (Figure 2.9) we have new expressions for E_N and E_T (Hudson and Liu, 1999):

$$E_N = \frac{(\lambda + 2\mu)^2}{4\mu(\lambda + \mu)}\frac{1}{v^w Hb}\left(1 + 2\sqrt{v^w b^2}\right)^{-1}$$
$$E_T = \frac{3\lambda + 4\mu}{8(\lambda + \mu)}\frac{1}{v^w Hb}\left(1 + 2\sqrt{v^w b^2}\right)^{-1} \tag{2.37}$$

Here v^w represents the number density of contacts, H is the average spacing of slip interfaces, and b is the average radius of the welded region.

The proportion of the fracture face that consists of open cracks is given by

$$r = 1 - \pi v^w b^2. \tag{2.38}$$

Figure 2.9: Graphical representation of the fractures modeled with a planar distribution of circular welded regions.

We can also represent the fracture as an equivalent thin layer of thickness Δ, whose elastic properties are given by Hudson and Liu (1999):

$$K_f = K' - \frac{4\Delta\mu(1-r)}{3\pi b} \frac{(\lambda+\mu)(4\mu-\lambda)}{(3\lambda+4\mu)(\lambda+2\mu)} \left\{ 1 + 2\left(\frac{1-r}{\pi}\right)^{\frac{1}{2}} \right\}, \qquad (2.39)$$

$$\mu_f = \mu' + \frac{8\Delta\mu(1-r)}{\pi b} \left(\frac{\lambda+\mu}{3\lambda+4\mu} \right) \left\{ 1 + 2\left(\frac{1-r}{\pi}\right)^{\frac{1}{2}} \right\}. \qquad (2.40)$$

Here, K' and μ' are the bulk and shear moduli of the inclusion material, Δ is the thickness of the equivalent layer for the fracture, b is the average radius of the welded region, and r is the proportion of the fracture face that consists of open cracks.

The thickness is related to the relative area of cracking by $\Delta = rd$, where d is the mean aperture of the cracks and r is the relative area of cracking. This model is valid for r between 0.8 and 1. When $r \rightarrow 1$, the two faces of the crack lose contact completely, and the fractured rock falls apart.

To calculate the effective elastic stiffnesses of the medium with such parallel fractured zones, we can use the Backus (1964) average method where the background properties are K and μ, while the fracture planes properties are K', and μ', and the thickness is Δ.

These models enable us to determine the elastic properties of heavily fractured structures, while they also give a more realistic physical representation of the fractures.

In the next section, I explore the validity of these reviewed theoretical models of fractures with published laboratory measurements on simulated fractured media.

2.4 Comparison of the models with laboratory measurements

The technical literature abounds in papers on the theoretical models of fractures. However, there are very few papers on testing the validity of these various models, and of the relationships among them. Hsu and Schoenberg (1993) perform measurements on

simulated fractured media to test the assumption of the linear-slip model. They find a good agreement between the linear-slip theory and the laboratory measurements.

In this section, I compare the results of their laboratory measurements with the theoretical predictions of the penny-shaped crack models of Hudson (1981, 1997). The main goal is to explore the validity of the relationship between the linear-slip model and the penny-shaped crack model.

Hsu and Schoenberg (1993) measure the ultrasonic velocities on a block of lucite plates with roughened surfaces, pressed together with a static normal stress, to simulate a fractured medium. In their experiment, the 3rd axis is orthogonal to the fracture planes, such that the effective medium model is VTI (transversely isotropic with vertical axis of symmetry).

The measurements, normal, parallel and oblique to the fractures, show that, for wavelengths much larger than the individual thickness of a plate, the block of lucite plates can be modeled as a particular type of TI medium that depends on four parameters: the two isotropic background moduli, and the normal and tangential fracture compliances. This TI medium behavior is the same as that of an isotropic solid in which are embedded a set of parallel linear-slip interfaces. In this assumption, the elastic stiffness matrix of the effective fractured medium can be derived based on only four measurements of P- and S-wave velocities, polarized parallel and perpendicular to the fracture planes. However, for the linear-slip assumption, there is an additional constraint that should be satisfied (Equation 2.17).

First, Hsu and Schoenberg fit a TI model to the five different measurements performed at different pressure states, and obtain all five elements of the stiffness matrix (C_{11}, C_{33}, C_{44}, C_{66}, C_{13}). Table 2.1 presents, in columns 2 to 6, the five TI moduli, normalized by the density of the bulk lucite, determined from the five ultrasonic measurements of velocities. The velocity measurements are performed at four different levels of normal stress, from 6 MPa to 24 MPa.

Then, to verify the linear-slip assumption, they use the equivalent of Equation 2.17 for a model with a vertical axis of symmetry to predict again the off-diagonal term of the stiffness matrix, C'_{13}, but this time based only on the measured C_{11}, C_{33} and C_{66}. The

values of the C'_{13} term, normalized by density, are given in the 7th column of Table 2.1. The maximum difference between the C_{13} values determined from the P-wave velocities propagating oblique to the stack of lucite plates, and C'_{13} values calculated from the P- and S-wave velocities polarized parallel and perpendicular to the fracture planes assuming a linear-slip model, is only 3.8%.

Table 2.1: Elastic moduli for the TI medium from ultrasonic velocity measurements. (Hsu and Schoenberg, 1993)

Stress (MPa)	C11/ρ (MPa m3/Kg)	C33/ρ (MPa m3/Kg)	C44/ρ (MPa m3/Kg)	C66/ρ (MPa m3/Kg)	C13/ρ (MPa m3/Kg)	C13'/ρ (MPam3/Kg)
6	6.656	4.494	1.513	1.858	2.209	2.224
12	6.970	5.476	1.664	1.858	2.656	2.754
18	7.076	5.954	1.742	1.860	2.868	2.982
24	7.129	6.150	1.769	1.863	3.024	3.077

Then, Hsu and Schoenberg derive the normal and tangential excess compliances introduced by fractures (E_N and E_T). As expected, these non-dimensional excess compliances due to fractures decrease with increasing static stress, implying that the asperities on either side of the plates get closer, increasing the contact area on the fracture surfaces.

Table 2.2 summarizes the fit of the laboratory measurements to a linear-slip model, for all of the normal static stress states, as derived by Hsu and Schoenberg. V_P and V_S are the inverted velocities for the unfractured bulk lucite, while E_N and E_T are the inverted normal and tangential excess dimensionless compliances, as defined in Equation 2.13b. In Table 2.3, the V_S of the unfractured lucite block and the tangential dimensionless compliance E_T are uniquely determined from the measurements of S-wave velocities polarized parallel and orthogonal to the fracture planes. V_P of the unfractured lucite block and the normal dimensionless compliance E_N are determined from the measurements of the P-wave velocity propagating perpendicular to the fractures, the S-wave velocity polarized parallel to the fractures, and the quasi-P-wave velocity propagating oblique to the fractures. The other set of estimates, V_P' and E_N', are determined from the measurements of the P-wave velocities propagating perpendicular and parallel to the fractures, and the S-wave velocity polarized parallel to the fractures. The numbers in

parentheses are the ratios of the fit parameters to the actual velocities, measured independently on a reference lucite block.

Table 2.2: Results for the linear slip model fitting for the P and S wave velocity of the bulk lucite and for the normal and tangential dimensionless compliances added by the fractures (Hsu and Schoenberg, 1993). The numbers in parentheses are the ratios of the fit parameters to the actual velocities measured independently on a reference lucite block.

Stress (MPa)	V_S (m/s) (Bulk lucite)	E_T	V_P (m/s) (Bulk lucite)	E_N	V_P' (m/s) (Bulk lucite)	E_N'
6	1363(0.996)	0.228	2703(0.992)	0.626	2.713(0.995)	0.637
12	1363(0.996)	0.117	2686(0.986)	0.318	2.734(1.003)	0.365
18	1364(0.997)	0.067	2679(0.983)	0.205	2.730(1.002)	0.252
24	1365(0.998)	0.053	2707(0.994)	0.192	2.730(1.002)	0.212

Using their experimental results, I first explore the theoretical relationship between the linear-slip model and the Hudson (1981) model with a volumetric distribution of penny-shaped cracks. Then, I also model the variation of the relative area of cracking on the surface of the fractures with increasing stress, using Hudson's model (1997) with planar distributions of cracks. Finally, I compare the theoretical predictions of velocities parallel and perpendicular to fractures with the ultrasonic measurements on the simulated fractured medium.

For calculating the equivalent crack densities from Hudson's (1981) penny-shaped crack model with a volumetric distribution of cracks, at each pressure step I use the relations from Equations 2.22 and 2.23. I assume the bulk modulus of the air that fills the simulated fractures to be 1 bar. The radius of the penny-shaped cracks is assumed to be 1/10 of the wavelength, to ensure the assumption of an effective medium, while the maximum aperture of the crack is equal to the dimension of the asperities on the fault plane (10 μm). Therefore, the average aspect ratio of the penny-shaped cracks is estimated at 0.01, given by the ratio between the half aperture (the small semiaxis of the ellipsoidal crack), and the radius of the crack.

Table 2.3 summarizes the results of the crack density calculations based on the normal and tangential excess compliances at each pressure step. The last column gives the average crack density.

Table 2.3: Crack density calculations based on the theoretical relationship between the linear-slip model and a volumetric distribution of penny-shaped cracks for an aspect ratio of 0.01.

Stress (MPa)	6	12	18	24
crack density (from E_N)	0.0545	0.0342	0.0241	0.0228
crack density (from E_T)	0.0869	0.0490	0.0294	0.0236
Average crack density	0.0707	0.0416	0.0267	0.0232

As we can observe from Table 2.3, the crack density calculated from the tangential excess compliance is larger than the crack density evaluated from the normal excess compliance. However, the differences between the two predictions decrease significantly with increasing stress. At 24 MPa normal stress, this difference is only about 3%.

If we allow for an additional degree of freedom through the aspect ratio of the cracks in Hudson's model, we can reduce the difference between the crack density values evaluated from E_N and E_T, at 6 MPa normal stress. Table 2.4 presents the values of crack density evaluated from E_N and E_T for an aspect ratio of 0.0001. As Equation 2.23 predicts, the tangential excess compliance does not change with aspect ratio for fluid-filled cracks. Therefore, the crack density derived from E_T does not change with aspect ratio, as we can see by comparing Tables 2.3 and 2.4. However, the crack density evaluated from the normal excess compliance at 6 MPa is closer to that derived from the tangential excess compliance at the same stress state of 6 MPa.

Table 2.4: Crack density calculations based on the theoretical relationship between the linear-slip model and a volumetric distribution of penny-shaped cracks, for an aspect ratio of 0.0001.

Stress (MPa)	6	12	18	24
crack density (from E_N)	0.0674	0.0443	0.0324	0.0293
crack density (from E_T)	0.0869	0.0490	0.0294	0.0236
average crack density	0.0771	0.467	0.309	0.0264

Based on the average crack density from Table 2.4, I compute the normal excess compliances, again using the relationship between the linear-slip model and the Hudson's penny-shaped crack model. Table 2.5 gives in the second column the Hudson's predictions for the normal excess compliances. For comparison, I added in the third and fourth columns of the same table the inverted normal compliances by Hsu and Schoenberg, using their two different approaches, as explained previously. The fifth

column gives the average values of the two inverted excess normal compliances. The sixth column shows the absolute values of differences between the two different inverted normal excess compliances, while the seventh column gives the absolute differences between Hudson's predictions and the average values for the inverted normal compliances. We observe that at 6 MPa static stress, Hudson's model predicts larger normal excess compliance than the ones inverted by Hsu and Schoenberg. This difference is about 19.4%, as we can observe from Table 2.5, column 7. However, we can also see from Table 2.5 in column 6, that the largest discrepancy between the two different fits for normal excess compliance by Hsu and Schoenberg is 18.6%. Therefore, the difference between Hudson's prediction and the average inverted normal excess compliance is of the same order of magnitude as the difference between the two inverted normal excess compliances by Hsu and Schoenberg. Therefore, based on this analysis, we can consider that either the linear slip model or the penny-shaped crack model can be used to describe equally well the effective properties of the fractured media.

Table 2.5: Comparison between the normal compliances inverted by Hsu and Schoenberg (1993) and the normal compliance predicted by Hudson's model with a volumetric distribution of cracks.

Stress (MPa)	E_N^{Hudson} *Hudson (1981)*	E_N	E_N'	$(E_N+E_N')/2$ $E_N^{Hsu\_average}$ *average*	$\dfrac{E_N - E_N'}{E_N'}$	$\dfrac{E_N^{Hudson} - E_N^{Hsu\_average}}{E_N^{Hudson}}$
6	0.7957	0.626	0.637	0.6315	0.0173	0.1939
12	0.3663	0.318	0.365	0.3415	0.1288	0.0572
18	0.2157	0.205	0.252	0.2285	0.1865	0.0690
24	0.1788	0.192	0.212	0.2020	0.0943	0.1389
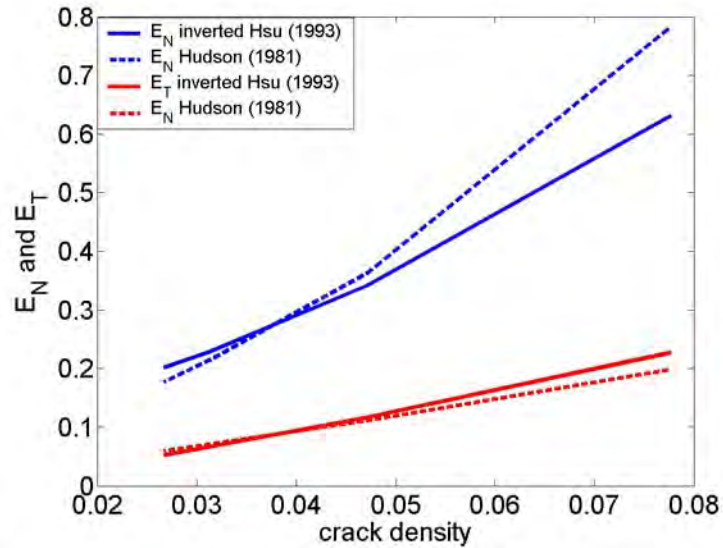
Figure 2.10: Normal (blue) and tangential (red) excess compliance obtained by Hsu and Schoenberg (solid lines) and predicted by Hudson's model with a volumetric distribution of cracks (dashed lines), as a function of the average crack density from Table 2.4, evaluated using the relation between the Schoenberg's (1983) linear-slip model and Hudson's model (1981).

Figure 2.10 presents the comparison between the inverted normal and tangential compliances derived by Hsu and Schoenberg, and the theoretical predictions using Hudson's model with volumetric distribution of cracks. In this figure, the normal excess compliances fitted by Hsu and Schoenberg represent the average of the two different estimations from Table 2.5. The x-axis represents the average crack density from Table 2.4. The aspect ratio of the cracks is assumed to be 0.0001. From Figure 2.10, we can observe a good agreement between the inverted and theoretically modeled tangential excess compliances (red curves). The differences between the average of the inverted normal excess compliances and Hudson's predictions are relatively small for small crack densities. The largest difference is obtained for a crack density of approximately 0.08, estimated at 6 MPa static stress, as we can see in Table 2.5.

One important observation is that all of the estimated crack density values are smaller than 0.1, the limit of validity for Hudson's model (1981). From Table 2.3 and 2.4 we see that fracture density decreases as the normal stress increases, as expected. In the absence of the normal stress, the block of lucite plates would fall apart, due to fractures. However,

as we increase the pressure, we get positive values for the elastic moduli of the corresponding TI medium, as we can see in Table 2.1. The highest estimated crack density value is 0.0869, obtained at 6 MPa using the tangential excess compliance.

For most fractured reservoirs, the normal effective stress on the fracture planes is larger than 6 MPa. This suggests that a value of 0.1 for fracture density represents a high degree of fracturing in most practical situations.

Even though the spacing between the slip-interfaces in the lucite block practically does not change as we increase the normal stress, the crack density decreases significantly. This happens because the excess compliances decrease with increasing stress, implying that asperities on either side of the plates get into closer contact, gradually increasing the contact area on the fracture surfaces. This suggests that the fracture index taken alone (defined as the ratio between the fracture spacing and the bed thickness) is not a complete description of the seismic degree of fracturing. We need to also take into account the degree of open space on the fracture plane. This parameter impacts significantly both the elastic and the transport properties of the fractured medium.

Next, I compare the laboratory results of Hsu and Schoenberg with Hudson's (1997) model with a planar distribution of cracks. In this model, the faces of the fracture are held together by the ambient pressure and friction. As we increase the confining stress, the area of contact on the fracture surfaces increases, while the crack density on the fracture surfaces decreases. I derive the equivalent crack densities using Hudson's (1997) model with planar distributions of cracks, by numerically solving Equation 2.32. The aspect ratio of the cracks is considered to be 0.01, while the spacing of the fracture planes is 7mm.

Table 2.6 summarizes the calculations for crack density and the corresponding relative area of cracking on the fracture surfaces, as defined in Equation 2.34 for a planar distribution of cracks. All of these values are smaller than 0.1, which is the theoretical limit of validity for Hudson's (1981) model with a volumetric distribution of cracks.

Table 2.6: Crack density and relative area of cracking, using Hudson's (1997) model
for planar distributions of cracks.

Stress (MPa)	6	12	18	24
crack density (from E_N)	0.0760	0.0420	0.0290	0.0260
crack density (from E_T)	0.0880	0.0500	0.0300	0.0240
Relative area of cracking (from E_N)	0.3673	0.2030	0.1402	0.1257
Relative area of cracking (from E_T)	0.4253	0.2417	0.1450	0.1160

From Table 2.6 we observe that the relative difference between the two predictions for crack density based on E_N and E_T is about 13% at 6 MPa, while at 18 MPa this difference decreases to only 3%.

Also, the values of crack density for a planar distribution of cracks calculated from E_T are very similar to the equivalent values calculated using Hudson's model (1981) for a volumetric distribution of ellipsoidal cracks (Table 2.3). The relative differences between them are smaller than 2% for all of the stress states. This suggests that, to first order, it does not matter if the parallel cracks are distributed volumetrically, or if they are confined in parallel planes.

As, expected, the crack density decreases as we increase the normal stress on the fracture planes, while the relative area of cracking on the fracture plane decreases.

Figure 2.11 shows the variation of the relative area of cracking on the fracture surfaces with the increasing normal stress, calculated using Hudson's model (1997) for planar distributions of ellipsoidal cracks. At 6 MPa normal stress, the relative area of cracking is approximately 0.43. This value is above the limit of validity of the model (0.2). Despite this, we can still see a relatively good agreement between the measured ultrasonic P-wave velocities orthogonal and parallel to fractures, and the corresponding P-wave velocities calculated using Hudson's model (1997) with planar distributions of ellipsoidal cracks (Figure 2.12).
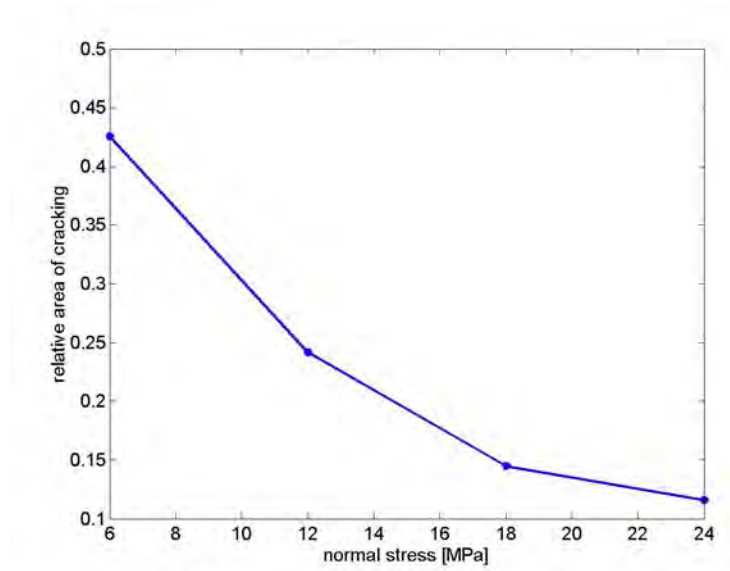
Figure 2.11: Relative area of cracking on the fracture planes as a function of the normal stress, evaluated from tangential excess compliance E_T, using Hudson's model with planar distribution of cracks.

Figure 2.12 presents a summary of the comparisons between the ultrasonic measurements of velocities on the simulated fractured medium with lucite plates (Hsu and Schoenberg, 1993), and the theoretical predictions of Hudson's models with both volumetric (blue curves), and planar (red curves) distributions of cracks. The theoretical velocities for distributions of parallel penny-shaped cracks are determined using the mean values of fracture density derived from E_N and E_T. The aspect ratio of the cracks is considered to be 0.01.

The P- and S-wave velocities polarized orthogonal to fractures increase with the normal stress, while the P- and S-wave velocities polarized parallel to fracture planes are less sensitive to stress, as expected.

We observe good agreement between the laboratory measurements on the simulated fractured medium (Hsu and Schoenberg, 1993) and the theoretical predictions of the penny-shaped crack models of Hudson (1981, 1997), especially for the velocities polarized parallel to the fracture planes. The larger discrepancy occurs for the P-wave velocity orthogonal to fractures at 6 MPa, estimated by Hudson's model with volumetric distribution of cracks. The theoretical prediction is 9% smaller than the actual measurement. However, as we increase the normal stress, the predictions improve

considerably. At 12 MPa normal stress, the error is 2%, while at 24 MPa it is only 0.4%. For normal stress larger than 6 MPa, both models of penny-shaped cracks give very good predictions for the P- and S-wave velocities orthogonal and parallel to fractures.
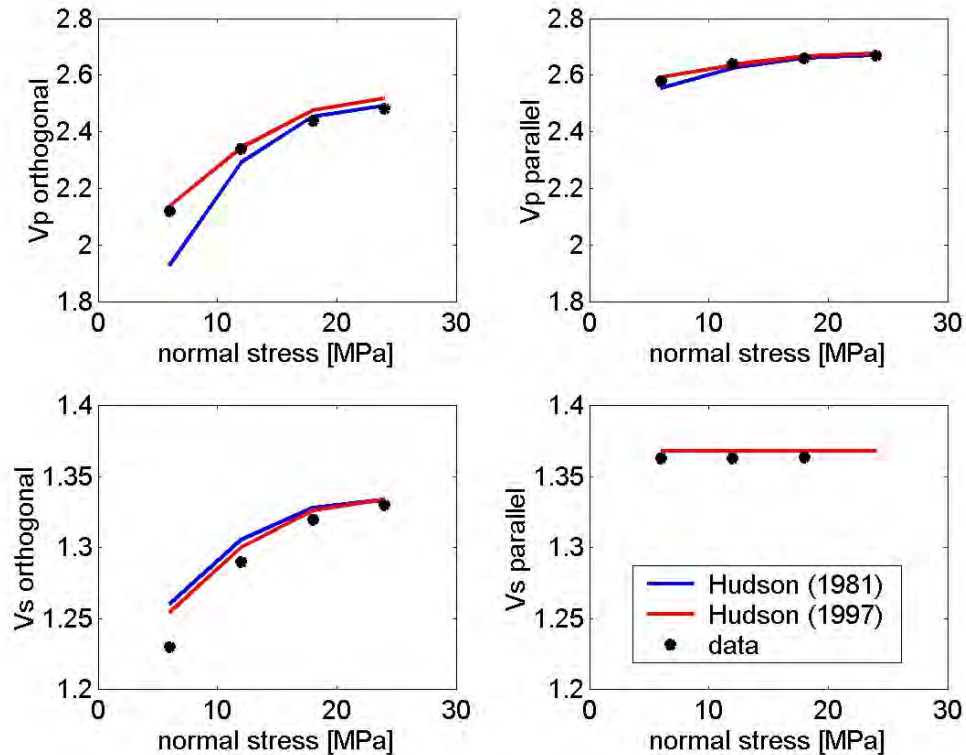
Figure 2.12: Comparison between ultrasonic velocity measurements on simulated fractured medium (Hsu and Schoenberg, 1993) – black dots, and the theoretical predictions of Hudson's models for volumetric distribution of cracks (Hudson, 1981) and planar distribution of cracks (Hudson, 1997). Aspect ratio of the cracks is considered 0.01.

However, if we allow for an additional degree of freedom through the aspect ratio of the cracks we can improve the agreement between the P-wave velocity orthogonal to the fracture planes predicted by Hudson's model and the data from Hsu and Schoenberg (Figure 2.13). For an aspect ratio of 0.0001, the theoretical prediction is only 3.8% smaller than the data measured at 6 MPa.
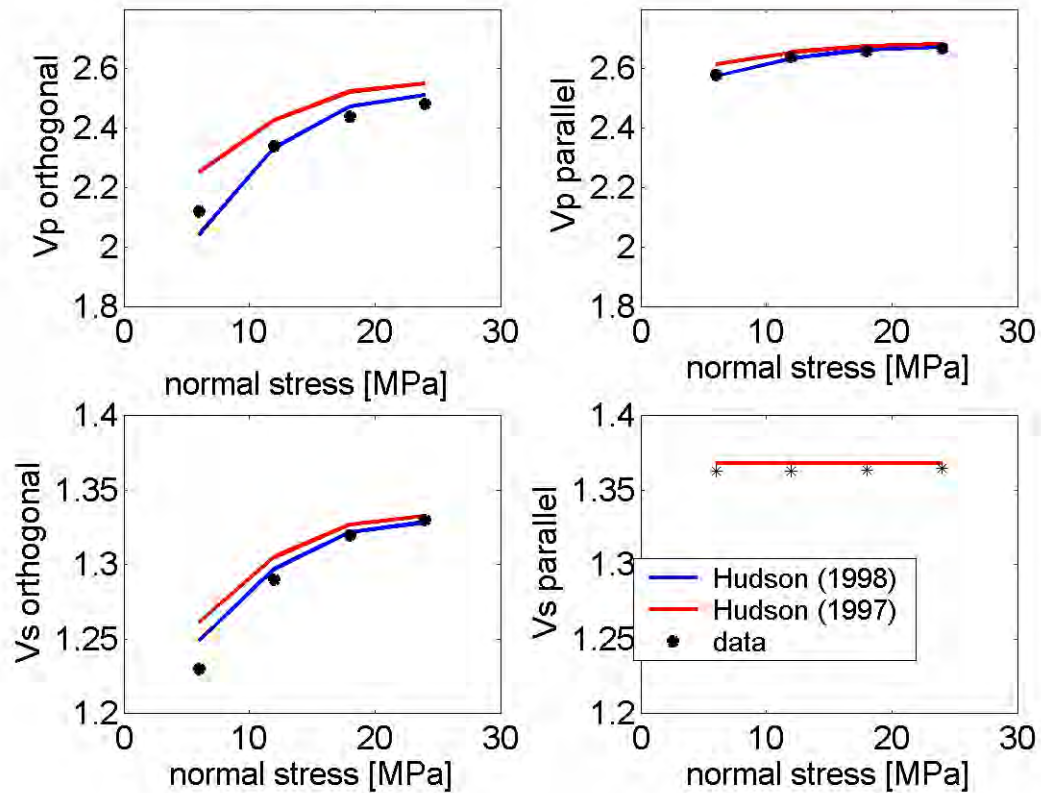
Figure 2.13: Comparison between ultrasonic velocity measurements on simulated fractured medium (Hsu and Schoenberg, 1993) – black dots, and the theoretical predictions of Hudson's models for volumetric distribution of cracks (Hudson, 1981) and planar distribution of cracks (Hudson, 1997). Aspect ratio of the cracks is 0.0001.

Another observation is the similarity of the results from Hudson's (1981, 1997) two different models with volumetric and planar distributions of cracks. This demonstrates that to the first order, it does not matter whether the cracks are distributed volumetrically or confined in planar surfaces.

To summarize, from the comparison of the theory with measurements, I observe that a value of 0.1 for crack density represents a large degree of fracturing. The highest estimation for crack density is 0.0869, obtained from the tangential excess compliance at 6 MPa. For most fractured reservoirs, the normal stress on the fracture planes is larger than 6 MPa. This suggests that, in most of the practical situations, we should expect values for crack density smaller than 0.1. In other words, the limit of validity for

Hudson's model (1981) may represent a large degree of fracturing. Also, from this analysis, I conclude that either Hudson's models (1981, 1997) or the Schoenberg's (1980, 1983, 1989) linear-slip model can be used to describe the effective elastic behavior of fractured media.

2.5   Field data: Practical bounds on crack density

In this section I present the collection of field data on shear-wave anisotropy reported by different authors and summarized by Crampin (1994). I use this data set to obtain insights into the distribution of shear-wave splitting, and implicitly crack density, as a function of depth. The results of the analysis presented in this section constitute valuable *a priori* information that can be used to constrain the crack density values for fracture modeling, depending on the depth of the reservoir.

The data were acquired in various environments, from sedimentary basins to igneous/volcanic and metamorphic rocks, and at different depths, from near surface, to more than 30 km depth. The shear-wave data were collected either from earthquakes or from controlled sources, such as reflection surveys, VSP, reversed VSP, and cross-hole surveys.

Table 2.7 presents this collection of the field data on azimuthal shear-wave anisotropy after Crampin (1994). The first column gives the types of rocks, or the environment, the second column gives the method used for acquiring the data, the third column presents the place where the data were collected, the fourth column gives the corresponding depth for the recorded anisotropy, the fifth column presents the percentage of shear-wave splitting anisotropy, while the last column indicates the reference.

Table 2.7: Observed percentage of azimuthal shear-wave velocity anisotropy from field data reported by different authors and collected by Crampin (1994).

type of rock	method	place	depth	anis%	reference
volcanic rocks	shear-wave splitting/ aftershocks	Campi Flegrei, Italy	<15km	1.4	1
gabbro	shear-wave splitting/earthquake	Anza, CA, USA	<17km	1.5	2
above subduction zone	shear-wave splitting/earthquake	Wellington, New Zealand	<60	2	3

mixed metam/sedim rocks	shear-wave splitting/earthquake	Los Angeles Basin, CA	<15	2,2.5	4
gabro	shear-wave splitting/earthquake	Anza, CA, USA	<3.5	2.3+ - 1.7	5
welded fractured tuff	shear-wave splitting/earthquake	Tazawako, Akita, Japan	<0.5	3	6
unspecified	Vs information omitted	Charlevoix Zone, Canada	unspec	3	7
crystalline rock	shear-vave splitting/earthquake	Mojave Desert, CA, USA	<0.45	3.5	8
metamorphic rocks	shear-wave splitting/earthquake	W. Deep Levels, S. Africa	<5	<4	9
granite	shear-wave splitting/earthquake	Manitoba, Canada	0.4-0.5	4	10
granite and mixed geology	shear-wave splitting/earthquake	Kinki, Honshu, Japan	<15	4	11
volcanic rocks	shear-wave splitting/earthquake	Rift zone, Japan	<10	4	12
mixed metam/sedim rocks	shear-wave splitting/earthquake	Los Angeles Basin, CA	<15	4.3	4
volcanic caldera	shear-wave splitting/earthquake	Long Valley, CA	<10	4.3	13
mixed metam/sedim rocks	shear-wave splitting/earthquake	TDP Izmit, Turkey	<12	4.5	14
mixed metam/sedim rocks	shear-wave splitting/earthquake	Shikoku, Japan	<10	4.5	15
volcanic rocks	shear-wave splitting/earthquake	E Rift Zone, Hawaii	<10	5	16
volcanic/ sedimentary rocks/ geothermal area	shear-wave splitting/earthquake	Takinoue, Honshu, Japan	<2	6	17
volcanic caldera	shear-wave splitting/earthquake	Long Valley, CA	<10	6.4	18
volcanic caldera	shear-wave splitting/earthquake	Phlegraean Fields, Italyl	<3.1	7	16
metamorphic rocks/aftershocks	shear-wave splitting/earthquake	Nahami, NWT, Canada	<20	7	19
granite/geothermal area	shear-wave splitting/earthquake	Cornwall, England	<2	8	20
volcanic caldera/resurgent dome	shear-wave splitting/earthquake	Long Valley, CA	<10	9.6	18
principally lower crust	shear-wave splitting/earthquake	TDP Izmit, Turkey	<30	10	21
above subduction zone	shear-wave splitting/earthquake	Wellington, New Zealand	<15	10	3
granulite facies	shear-wave splitting/earthquake	Arunta Block, Australia	<1	10	22
volcanic caldera/fault zone	shear-wave splitting/earthquake	Long Valley, CA	<10	15	23
volcanic/sedimentary rocks /geothermal area	shear-wave splitting/earthquake	Takinoue, Honshu, Japan	<2	18	17
mixed sediments	shear-wave splitting/VSP	Devine, TX, USA	<0.47	0.7-3.8	24
unspecified sediments	shear-wave splitting/RFL	Pennsylvania, USA	<6	1.4	25
mixed sediments	shear-wave splitting/RFL	Dimmit, Zavala, Frio Counties, TX	<2	1.5, 2, 2.5	26
clay, sandstones, limestones	shear-wave splitting/VSP	Caucasus Basin, Russia	<.9	1.4	27

shale, limestone	shear-wave splitting/VSP	Paris Basin, France	1.1-2	1.6	28
mixed sediments	shear-wave splitting/RFL	Silo Field, WY, USA	<2.4	1.0-4.0	29
unspecified sediments	shear-wave splitting/RFL	unspecified, USA	<3	2	30
mixed sediments	shear-wave splitting/RFL	Giddings Fld. TX, USA	<2.6	2	31
Palaeozoic sedim	shear-wave splitting/EQ	Enola, Arkansas, USA	<6	2	32
shale, limestone	shear-wave splitting/VSP	Paris Basin, France	0.6-1.1	3	33
shale, carbonates	shear-wave splitting/VSP	Romashkino, Russia	<1	3.3-4	34
mixed sediments	shear-wave splitting/VSP	Dilley, TX USA	<3	3.5+-0.5	35
unspecified sediments	shear-wave splitting/VSP	CBTF, OK, USA	<.6	4	36
unspecified sediments	shear-wave splitting/VSP	Lost Hills Field, CA	<.64	7	37
fractured chalk	shear-wave splitting/VSP	Silo Field, WY, USA	2.5	>7	38
fault zone	shear-wave splitting/VSP	Orroville, CA, USA	0.3	7.2-7.6	39
fault zone	shear-wave splitting/VSP	Parkfield, CA, USA	<1.4	8	40
unspecified sediments	shear-wave splitting/VSP	Railroad Gap Field, CA, USA	<0.4	9	41
fractured sandstone	shear-wave splitting/VSP	S. Casper Creek, WY, USA	0.8-0.85	10	42
clay, limestones	shear-wave splitting/RVSP	CBTF, OK, USA	<0.04	10.5	43
clay, limestones	shear-wave splitting/CHS	CBTF, OK, USA	<0.04	12	44
unspecified sediments	shear-wave splitting/VSP	Cymric Field, CA, USA	<0.47	14	41

(1) Iannaccone & Deschamps (1989); (2) Peacock et al. (1988), (3) Gledhill (1991); (4) Du (1990); (5) Aster &Shearer (1991); (6) Kuwahara, Ito & Kiguchi (1991); (7) Buchbinder (1985); (8) Li, Leary & Aki (1990); (9) Graham, Crampin & Fernandez (1991); (10) Holmes, Crampin & Young (1993); (11) Kaneshima, Ando & Crampin (1987); (12) Kaneshima, Ito & Sugihara (1989); (13) Savage, Peppin & Vetter (1990); (14) Booth et al. (1985), (15) Kaneshima & Ando (1989); (16) Savage, et al. (1989); (17) Kaneshima et al. (1988); (18) Shih & Meyer (1990); (19) Buchbinder (1990); (20) Roberts & Crampin (1986); (21) Graham & Crampin (1993); (22) Greenhalgh et al.. (1990); (23) Savage, Peppin & Vetter (1990); (24) Yardley & Crampin (1993); (25) Lynn & Thomsen (1990); (26) Li, Mueller & Crampin (1993); (27) Slater et al. (1993); (28) Bush & Crampin (1991); (29) Martin & Davies (1987), (30) Lynn & Thomsen (1986); (31) Mueller (1991); (32) Booth et al. (1990); (33) Lefeuvre, Cliet & Nicoletis (1989); (34) Cliet et al. (1991); (35) Alford (1986); (36) Queen & Rizer (1990); (37) Winterstein & Meadows (1991a); (38) Lewis, Davis & Vuillermoz (1991); (39) Leary, Li & Aki (1987); (40) Daley & McEvilly (1990); (41) Winterstein & Meadows (1991b); (42) Shuck (1991); (43) Liu et al. (1993a); (44) Liu, Crampin & Queen (1991);

As shown in Table 2.7, shear-wave splitting in crustal rocks has been widely observed in controlled-source reflection surveys, as well as associated with earthquakes. There are cases when the shear-wave splitting may be attributed to phenomena other than cracks, such as rock foliation or crystal alignment, but typically the anisotropy appears to be the result of aligned fractures or microcracks and preferentially oriented pore space.
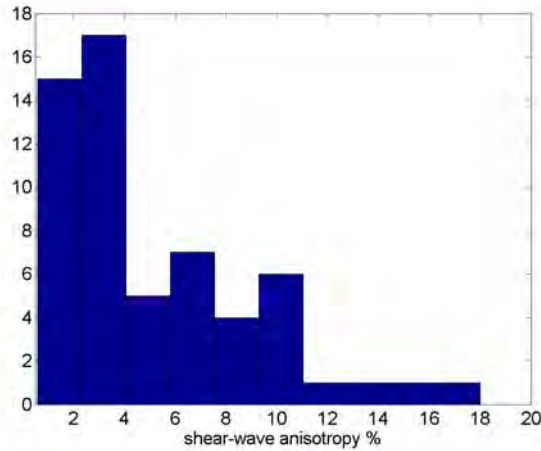
Figure 2.14: Histogram for the shear-wave splitting data from Table 2.7. Data collected by Crampin (1994).
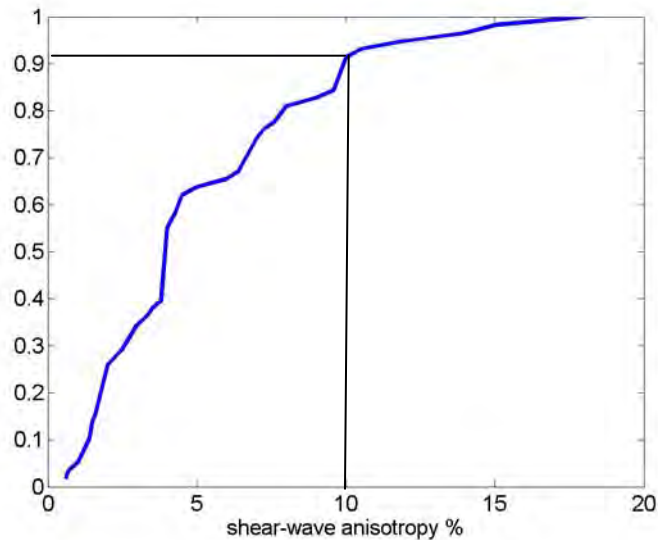
Figure 2.15: Cumulative distribution function for the shear-wave splitting data from Table 2.7. Data collected by Crampin (1994).

Figure 2.14 presents the histogram for the shear-wave splitting data from Table 2.7, while Figure 2.15 presents its corresponding cumulative distribution function. We can

observe from Figure 2.15 that more than 90% of the reported data corresponds to the shear-wave anisotropies of less than 10%.
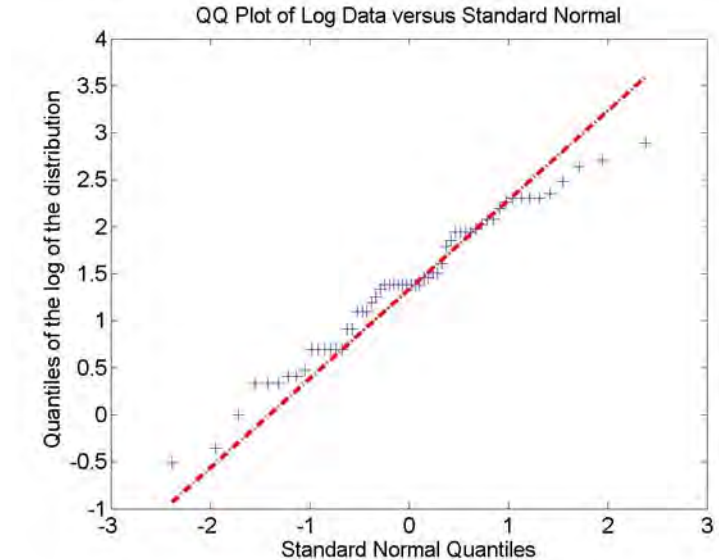
Figure 2.16: Q-Q plot for the logarithm of the shear-wave splitting data from Table 2.7. A linear trend close to the red line indicates a log-normal distribution for the data.

We can also observe from Figure 2.14 that the world-wide shear-wave anisotropy data does not follow a Gaussian distribution. From the shape of the histogram from Figure 2.14, it appears that the distribution of the shear-wave splitting data is more likely log-normal or exponential. In Figure 2.16, I show a quantile-quantile plot that compares the logarithm of the S-wave anisotropy distribution from Figure 2.14 with a normal distribution. The trend in Figure 2.16 is close to linear. This suggests that the world-wide *S*-anisotropy data follows more or less a log-normal distribution. Of course, there are departures from a log-normal distribution, as we can see in Figure 2.16. These departures are more significant especially for the large values of the shear-wave anisotropy.

We can obtain more insights about the world-wide shear-wave anisotropy data if we plot it against the depth, as in Figure 2.17. Figure 2.18 is similar to Figure 2.17, zooming on the first 6 km in depth.
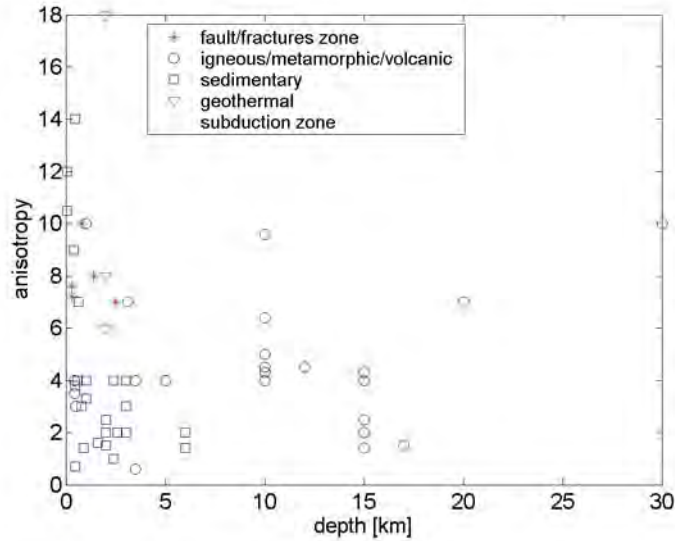
Figure 2.17: Shear-wave anisotropy data as a function of depth. Data collected by Crampin (1994).
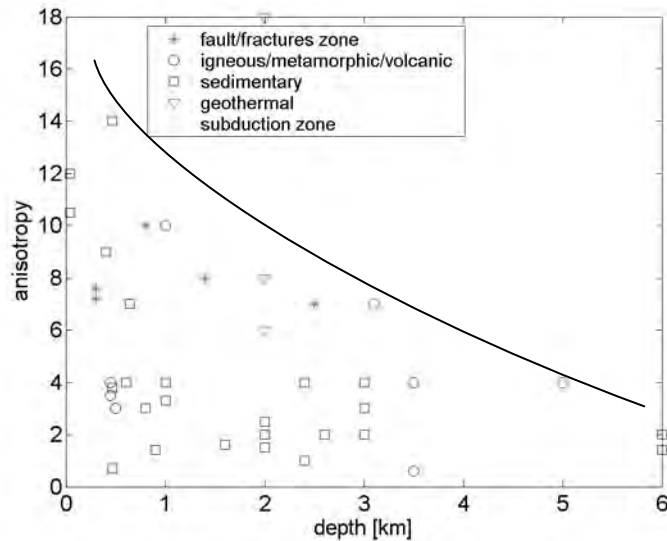
Figure 2.18: Shear-wave anisotropy data as a function of depth, for the first 6km. Data collected by Crampin (1994). The curve represents schematically the upper bound for the shear-wave data as a function of depth.

The data in Figure 2.18 acquired around the globe by different authors, suggests that there is an upper bound for shear-wave anisotropy that decreases with depth. For example, this data set suggests that at 0.5 km depth we may expect shear-wave anisotropy values between 0 and 14%, while at 6 km depth we should expect shear-wave anisotropy values

between 0 and 3%. The upper bound on the shear-wave anisotropy decreases from 14% at the surface to about 3% at 5 km depth.

Shear-wave splitting phenomena can sometimes be attributed to factors other than the presence of aligned cracks, such as rock foliation, crystal alignment, or structural effects. However, in most situations the azimuthal shear-wave anisotropy in the shallow crust appears to be the result of aligned fractures, or aligned microcracks.

The interpretation of the shear-wave splitting as crack-induced anisotropy requires elasticity theories that relate the observable seismic parameters to fracture parameters. For example, we can use Hudson's (1981, 1997) model to derive the corresponding crack densities that would generate the observed shear-wave anisotropy. In the weak anisotropy approximation, the relationship between the crack density of a fractured medium with aligned cracks, and the shear-wave splitting is given by (Bakulin, 2000):

$$e = \frac{3(3-2g)}{8}\gamma \ . \tag{2.41}$$

In the formula above, e is the crack density as defined in Hudson's model, g is the square of the S to P-wave velocity ratio $(V_S/V_P)^2$ of the unfractured background rock, and γ is the induced shear-wave anisotropy.
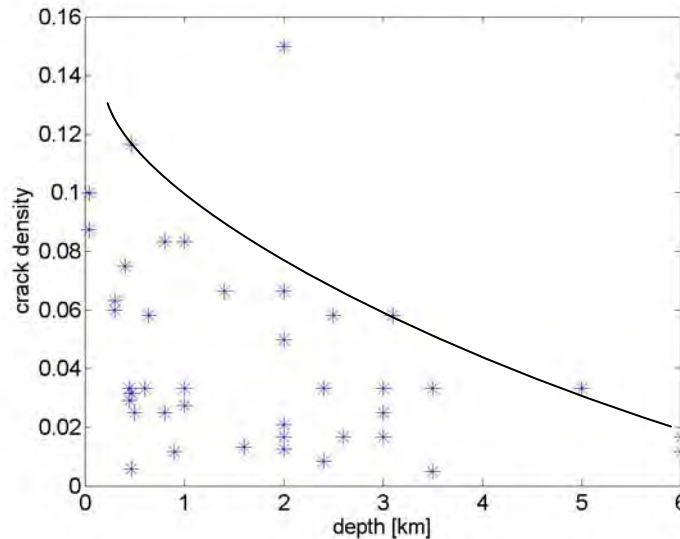
Figure 2.19: Computed crack density from the shear-wave anisotropy data using Hudson's penny-shaped crack model with volumetric distribution of cracks. I assume the V_P/V_S ratio of the host rock to be 1.7. The curve represents schematically the upper bound for the crack density as a function of depth.

The computed values of the crack density using Equation 2.41 are presented in Figure 2.19. The V_P/V_S ratio is assumed to be 1.7.

As expected, the computed crack densities also exhibit an upper bound, which decreases with depth, as is shown schematically in Figure 2.19. For example at 0.5 km depth the computed crack density varies approximately between 0 and 0.12, while at 6 km depth, the crack density varies in a narrower range, between 0 and 0.02. This may be explained by the effect of stress on cracks. Normally, increasing depth implies also increasing effective stress on the fracture planes. The stress is closing the cracks, therefore reducing the crack density. Another observation is that more than 95% of the computed crack density values are smaller than 0.1, which is the limit of validity for the Hudson's penny-shaped crack model. Therefore, this collection of field data also suggests that a crack density of 0.1 represents a relatively large degree of fracturing, which may be encountered especially at small depths, where the stresses are smaller. However, as the depth increases, the normal effective stress on the fracture planes increases as well, increasing the contact area on the fracture planes, and reducing the crack density. This collection of data suggests that in most practical situations we should expect crack density values smaller than 0.1.

As I discuss in the previous sections, Hudson also models fractures as linear, planar arrangements of cracks (Hudson, 1997). However, he shows that, to first order, it does not matter if the cracks are volumetrically distributed in the rock mass, or if they are confined in parallel planes. Therefore, in the assumption of planar distribution of cracks, we can obtain the average relative area of cracking on the fracture planes from the crack density from Figure 2.19. I assume that the ratio between the average radius of the cracks and the distance between fracture planes is constant and equal to 1. The relative area of cracking, *r*, is given by:

$$r = \pi \frac{H}{a} e \,. \tag{2.42}$$

Here, *H* is the distance between the fracture planes, *a* is the mean radius of the crack on the fracture plane, and *e* is the total crack density of the fractured rock mass computed from the shear-wave anisotropy data using Hudson's model (1981).

Figure 2.20 presents the relative area of cracking on the fracture planes as a function of depth, in the assumption that the ratio of the spacing between fracture planes to the radius of the cracks is 1. We can see, as expected, that the relative area of cracking on the fracture planes decreases with increasing depth. This is because the effective stress on the fracture planes is larger at higher depth, pressing the faces of the fractures closer together, and increasing the area of contact between them.
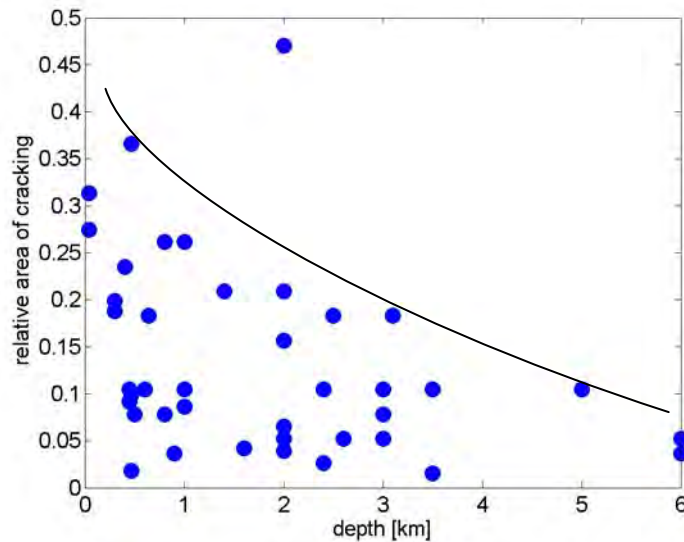
Figure 2.20: Computed relative area of cracking for planar distribution of cracks using Hudson's (1997) penny-shaped crack model. I assume the V_P/V_S ratio of the host rock to be 1.7. The curve represents schematically the upper bound for the relative area of cracking as a function of depth.

Figure 2.21 presents a summary for the analysis of the shear-wave anisotropy data. I converted the depth into the effective overburden stress, using a gradient of 15 MPa per km. The first panel shows the shear-wave anisotropy data as a function of effective overburden stress, the second panel shows the crack density as a function of effective overburden stress, and the third panel shows the relative area of cracking as a function of the effective overburden stress.
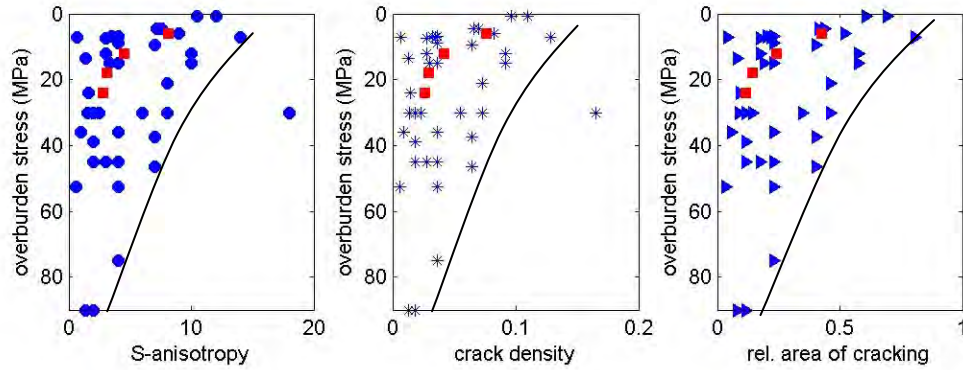
Figure 2.21: From left to right: Shear-wave anisotropy, crack density and the relative area of cracking as a function of the effective overburden stress computed using Crampin's collection (1994). Superimposed with red squares are the calculated values using Hsu and Schoenberg (1993) laboratory measurements. The effective overburden stress is estimated assuming a gradient of 15 MPa per km.

On the panels from Figure 2.21 are superimposed also the corresponding computed values from Hsu's and Schoenberg's measurements on simulated fractured media presented in the previous section.
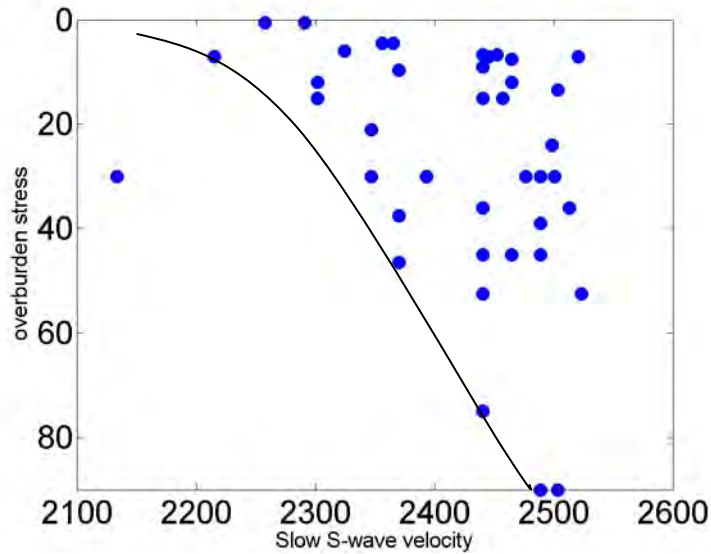
Figure 2.22: Computed S-wave velocity orthogonal to the fractures, using Hudson's model and the crack density, evaluated from the shear-wave anisotropy data from Crampin's collection.

Figure 2.22 presents the computed shear-wave velocity in the direction orthogonal to the fractures as a function of the overburden stress. The velocity is derived by using Hudson's model and the crack density evaluated from the shear-wave anisotropy data from Crampin's collection. I assume the same velocity for the unfractured background rock properties for all of the observed shear-wave anisotropy data. For the fractures, I assume an aspect ratio of 0.001. As expected, the computed shear-wave velocity increases with the estimated overburden effective stress. This happens because the cracks are closed gradually by the increasing stress as we go deeper in the Earth's crust, which has a stiffening effect on the elastic moduli. The increase in velocity with increasing pressure due to the closing of the cracks is one of the fundamental rock physics observations in the laboratory (Nur, 1971).

In conclusion, from the collection of the shear-wave anisotropy data acquired in various places around the globe, I observe a general trend of decreasing anisotropy with depth. More precisely, at each depth, the shear-wave anisotropy may vary from 0 to an upper bound. The upper bound values decrease with depth. Using elasticity theories that relate shear-wave anisotropy with fracture characteristics, I compute the crack density and the relative area of cracking on the fracture planes, and display them as a function of depth, as well as the corresponding effective overburden stress. The analysis puts valuable constraints on the values of fracture parameters we should use in the modeling, depending on the depth of the reservoirs.

Based on the collection of data by Crampin, I also observe that the shear-wave anisotropy values of all of the reported data taken together do not exhibit a Gaussian distribution, but rather a log-normal or exponential distribution. Therefore, the prior distribution for the crack density should also follow a log-normal or exponential distribution, as geological outcrop studies also suggest (Snow, 1968; Priest and Hudson, 1976; Sen and Kazi, 1984; La Pointe and Hudson, 1985; Rouleau and Gale, 1985; Bouroz, 1990; Villaescusa and Brown, 1990, Narr and Suppe, 1991). This is also an important result that can be used in assigning prior distributions to crack density as a measure of uncertainty due to natural variability.

2.6   Conclusions

Fracture models provide a quantitative link between the elastic properties of the cracked media and the physical parameters of fractures, such as fracture density. The literature abounds in papers on theoretical models of fractures. However, the validity of these various models has been rarely tested experimentally.

In this chapter I review some of the existing fracture models, such as Hudson's penny shaped crack model and the Schoenberg's linear-slip model, and the theoretical relations between them. I also compare their theoretical predictions with published laboratory measurements on simulated fractured media.

I show theoretically that if we push the validity limits for Hudson's model, we can obtain unphysical results. For example, for dry cracks the rock loses first its compressional strength and then the shear strength, due to increasing fracturing. The values of crack density for which the rocks lose their compressional strength are higher than 0.1. The maximum value of crack density is 0.18, which corresponds to a rock with an unfractured V_P/V_S ratio of 1.4.

The first-order equivalence between Hudson's model and the linear-slip model implies that for a certain crack density, the ratio between the normal and tangential weaknesses is fixed for dry cracks. In other words, the weaknesses (Δ_N and Δ_T) are not independent. I also derive upper limits for the normal and tangential weaknesses as defined in the Schoenberg's model, which correspond to a crack density limit of 0.1. These maximum values for normal and tangential weaknesses correspond to the upper limits for which we can get an equivalent crack density and obtain physically realistic description of elastic properties of a fractured medium using Hudson's model.

Hsu and Schoenberg (1993) perform ultrasonic velocity measurements on simulated fractured media. They use a block of lucite plates pressed together by a normal static stress to test the assumption of the linear-slip model. They find a good agreement between the linear-slip theory and the measurements. Their laboratory measurements show a decrease in the normal and tangential excess compliances with increasing normal

stress. This observation implies that the lucite plates get into closer contact, gradually increasing the contact area on the fracture surfaces.

I use their laboratory results to explore the validity of the relation between the linear-slip model and the penny-shaped crack models. I find very good agreement between the theoretical predictions of velocities parallel and perpendicular to fractures, and the actual measurements on the simulated fractured medium. From this analysis, I conclude that either Hudson's models (1981, 1997) or the Schoenberg's (1980, 1983) linear-slip model can be used to describe the effective elastic behavior of the fractured medium.

The theoretical predictions for fracture density, from penny-shaped crack models with both volumetric and planar distributions of cracks, decrease with increasing normal stress on the fracture planes, from 0.086 at 6 MPa to 0.022 at 24 MPa. The spacing between the fracture planes in the lucite block, however, does not change as we increase the normal stress on the fracture planes. This suggests that the fracture index taken alone (defined as the ratio between the fracture spacing and the bed thickness) is not a complete description for the seismic degree of fracturing, at least for analysis of seismic signatures of fractures. The relative area of cracking on the fracture planes is a very important parameter, which impacts significantly both the elastic and transport properties of the fractured medium.

The decrease in the crack density with normal stress indicates that the asperities on either side of the lucite plates get into closer contact, gradually decreasing the relative area of cracking on the fracture planes. From this point of view, Hudson's model with a planar distribution of cracks gives a better physical representation of the fractured medium.

However, the similarity between the velocity predictions from the two different penny-shaped crack models suggests that, to the first order, it does not matter whether the cracks are distributed volumetrically, or confined in planar surfaces. Seismic waves are not sensitive enough to distinguish between the two different types of crack distributions.

From the comparison of the theory with Hsu's and Schoenberg's (1993) laboratory measurements, I also observe that the value of 0.1 for crack density represents a relatively large degree of fracturing. In the absence of normal stress, the block of lucite plates would fall apart. However, as we increase the pressure on the fracture planes, we get

positive values for the elastic moduli of the corresponding TI medium. The highest estimation for crack density based on the lab measurements is 0.0869, obtained at 6 MPa. For most fractured reservoirs, the normal stress on the fracture planes is larger than 6 MPa. This suggests that, for reservoirs at depth, we should expect values for crack density smaller than 0.1.

I derive the same conclusion from the analysis of the shear-wave anisotropy data reported by different authors and summarized by Crampin (1994). The data were acquired in various environments, from sedimentary basins to igneous/volcanic and metamorphic rocks, and at different depths, from near the surface, to more than 30 km depth. The shear-wave data were collected either from earthquakes, or from controlled sources, such as reflection surveys, VSP, reversed VSP, and cross-hole surveys. More than 95% of the computed crack-density values based on these S-wave anisotropy data are smaller than 0.1. The larger values of crack density (around 0.1) correspond to data acquired at shallower depths, where the stress is smaller.

I also observe that the shear-wave anisotropy values of all reported data taken together exhibit not a Gaussian distribution, but rather a log-normal or exponential distribution. Therefore, the prior distribution for the crack density should also follow a log-normal or exponential distribution, as geological outcrop studies suggest (Snow, 1968; Priest and Hudson, 1976; Sen and Kazi, 1984; La Pointe and Hudson, 1985; Rouleau and Gale, 1985; Bouroz, 1990; Villaescusa and Brown, 1990, Narr and Suppee, 1991). This is also an important result that can be used in assigning prior distributions to crack density as a measure of uncertainty due to natural variability.

This collection of data suggests also that there is an upper bound on the shear-wave anisotropy, and implicitly on the crack density, that decreases with depth. For example, the upper bound on the shear-wave anisotropy decreases from 14% at the surface to about 3% at 5 km depth. This helps us put powerful constraints on the crack density values as a function of depth. For example, for a reservoir at 1 km depth the crack density values may vary between 0 and 0.09, while for a deeper reservoir around 5 km depth, the crack density values may vary within a narrower interval from 0 to 0.04.

The results of the analysis of the laboratory and field data are valuable *a priori* information that we can use to constrain the crack density in our fracture modeling. This can help us to estimate the feasibility of various seismic methods to detect fractures, depending on the depth of the reservoirs.

Chapter 3

Rock Physics Analysis and Stochastic Fracture modeling of the James Limestone Reservoir

3.1   Abstract

The first part of this chapter presents the rock physics analysis, based on well logs, of the fractured James Limestone reservoir. The objective is to understand if it is possible to seismically differentiate the gas-filled fractured zones from the other heterogeneities in the reservoir.

Using the information from the cross-dipole and FMI logs from one of the wells, I show that most of the fractures are associated with high velocity rocks, characterized by low porosity and a small amount of shale. This observation can be used to directly delineate fractured zones from seismic measurements. The association of fractures with high-velocity rocks also constrains the seismic properties of the background rocks that we use in our fracture modeling.

Based on the rock physics analysis, I consider that the reservoir may exhibit three main types of facies: 1) unfractured, clean limestones, 2) shaly limestones, and 3) fractured, clean limestones. The goal is to find the optimal combination of seismic attributes for distinguishing the gas-filled fractured zones from the shaly and unfractured limestones in the reservoir.

The second part of the chapter presents the results of the stochastic simulations of various seismic attributes for different models of fractures in the James Limestone reservoir. The modeling suggests that for the James Limestone reservoir, the interface attributes, such as amplitude variation with offset (AVO), as well as with azimuth (AVAZ), may be more useful than travel-time techniques. The advantage of using interface attributes, defined at the boundary between two layers, is that they provide localized information at the target of interest, unlike the travel-time methods. Besides, for thin reservoirs, travel-time techniques are not very useful for fracture detection.

Based on the modeling, I conclude that the fractures at this site do have a seismic signature, especially if they are saturated with gas. For example, the modeling predicts low PP reflectivity values for the gas-filled fractured zones. However, we also expect low amplitudes from the shaly rocks in the reservoir, which are less likely to get fractured. The *AVO gradient* can help resolve this ambiguity. Modeling shows that the shaliness moves the *AVO gradient* to smaller negative values as compared to the clean, unfractured limestones, while the gas-filled fractured zones move the *AVO gradient* to larger negative values as compared to the clean, unfractured limestones.

In summary, rock physics fracture modeling and stochastic simulations for seismic attributes of the James Limestone reservoir provide a framework for delineating gas-filled fractured zones from seismic data, and for estimating the uncertainty in fracture characterization due to natural variability.

3.2   Introduction

The James Limestone formation has been an exploration target on the onshore Gulf of Mexico since the discovery of the Fairway field in Texas basin in 1960 (Loucks et al,

1996). In the study area, the formation is a microcrystalline fractured limestone, with the unfractured matrix permeability between 0.001 and 0.1 mD (Marathon Oil Co., Internal Report). However, the presence of fractures can locally increase the permeability. Therefore, precise fracture localization can have a big impact on gas production.

The rock physics analysis of the cross-dipole and FMI logs from one of the wells suggests that most of the fractures are associated with rocks which have the least amount of shale, characterized by high velocity and small porosity values. The same preferential association of the fractures with a particular type of facies was also observed for the San Andres carbonate reservoir (Sava et. al, 2001). The association of the fractures with the high-velocity rocks constrains the seismic properties of the background rocks that I use in the fracture modeling.

The area of study is situated in a normal faulting regime. The maximum horizontal stress in the region is oriented E-W. In a normal faulting regime, the orientation of the faults is expected to be parallel to the maximum horizontal stress. A geological model based on the logs from horizontal wells suggests that the fractures are in part controlled by subseismic normal faults (Meeder, personal communication). These small faults can generate narrow damaged zones with high fracture density, due to increasing strain in the proximity of the faults (Nelson, 1985). Between these fracture swarms, the background fracture distribution may correspond to regularly spaced, vertical joints. This interpretation is supported by the FMI data from a nearby field. The fracture distribution interpreted from FMI log suggests the presence of a single set of vertical joints oriented approximately on the E-W direction. Therefore, for fracture modeling I consider the cases of both isotropic and anisotropic distributions of fractures. The isotropic distribution corresponds to the fracture swarms in the vicinity of faults, where the crack distribution is more chaotic, such as in brecciated zones. The anisotropic distribution corresponds to a single set of vertical joints that generates an azimuthally anisotropic elastic medium with HTI symmetry.

For the interface properties, I consider the boundary between the cap rock (Bexar shale), and the underlying James Limestone reservoir, modeled with different distributions of fractures.

I use *Monte Carlo* simulations for both fracture properties as well as for the background rocks to assess the feasibility of the seismic methods to delineate and characterize the fractured zones. The stochastic approach helps to incorporate the natural variability of the rock properties into deterministic models (Mavko and Mukerji, 1998; Mukerji et al., 2001). In this chapter, I show how I estimate the uncertainty due natural variability of both the background rock properties and the fracture parameters using Monte Carlo simulations.

3.3   Rock Physics Analysis

In this section, I use the well-log data available from two wells in the region to understand how the reservoir heterogeneities, and especially fractures, influence the seismic properties *(V_P* and *V_S)*.
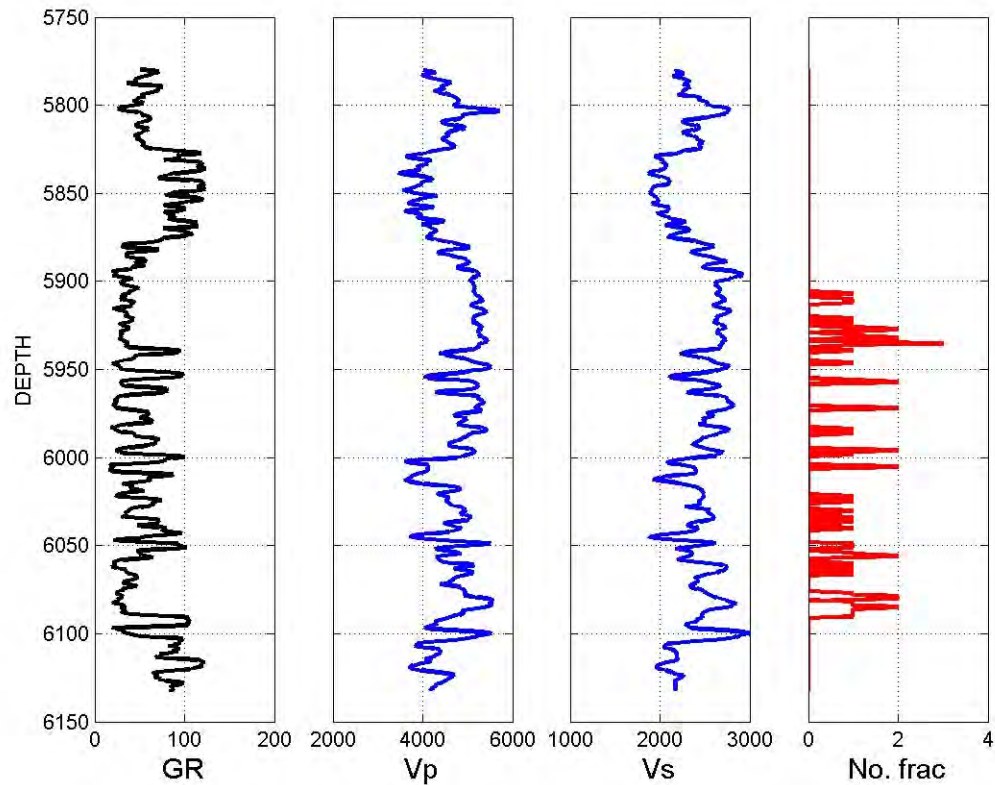
Figure 3.1: Well A: Well-log data over a depth interval corresponding to James Limestone reservoir. The depth is in feet. Gamma-Ray in first column is given in API, the V_P and V_S from the second and third columns respectively are in m/s, while the fourth column gives the number of fractures per foot interpreted from FMI data.

Figure 3.1 presents the well-log data from one of the key wells (Well A). The depth interval corresponds to the James Limestone reservoir. The first column gives the Gamma-Ray, the second and the third columns present the ultrasonic *P*- and *S*-wave velocities, while the fourth column shows the number of fractures per foot, interpreted from an FMI log. From Figure 3.1 we see a large variability in the gamma-ray, usually interpreted in terms of the volume of shale. This suggests that the reservoir is a heterogeneous limestone with intercalations of shaly rocks. As expected, the fractures occur primarily in the more brittle rocks, with lower content of shale, characterized by lower Gamma-Ray values.

Figure 3.2 presents the porosity as a function of the Gamma-Ray for the James Limestone reservoir. The data are color-coded by the number of fractures per foot, interpreted from the FMI. We see a trend of increasing porosity with Gamma-Ray. This implies that the rocks with higher shale content exhibit also higher porosities. The important observation is the association of the fractures with the reservoir rocks that have low Gamma-Ray and low porosity values. This implies that the fractures occur preferentially in the more brittle and tighter rocks inside the reservoir, as expected (Nelson, 1985).
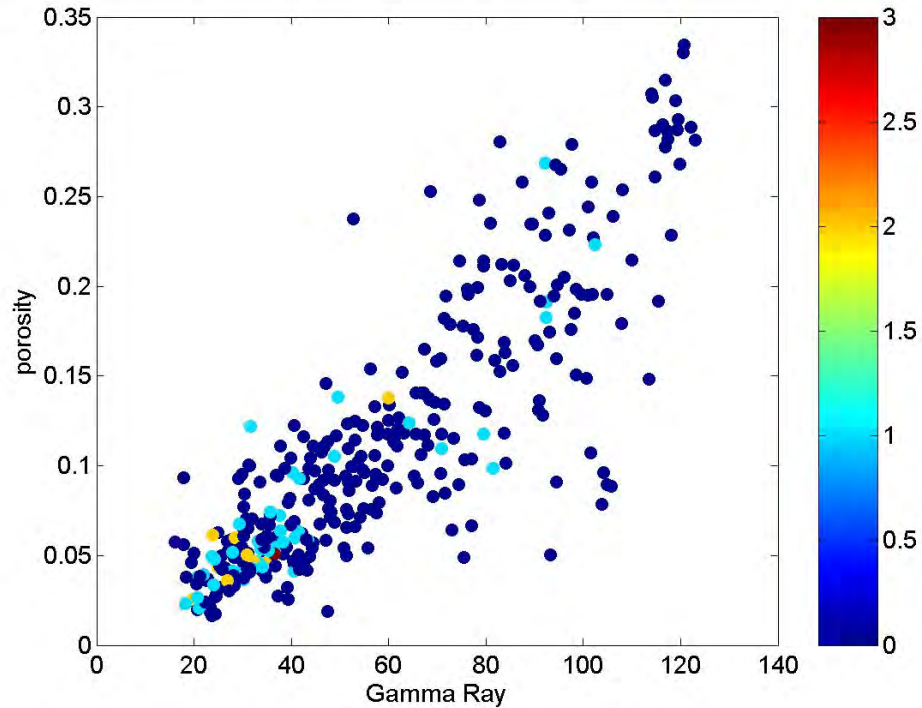
Figure 3.2: Porosity as function of the Gamma-Ray for the James Lime reservoir. The data are color-coded by the number of fractures per foot, interpreted from FMI. (Well A).

In the following sections I present the rock physics analysis, emphasizing the impact of shale content and fracture distribution on the seismic properties, such as the *P-* and *S-*wave velocities, using the well-log data from two wells.

3.3.1 V_P-porosity relation

A very common and useful plot in any rock physics analysis is the *P*-wave *velocity vs. porosity* scatter-plot, which gives information about the diagenetic processes that the rocks have experienced, as well as about the pore types (Anselmetti and Eberli, 1977).
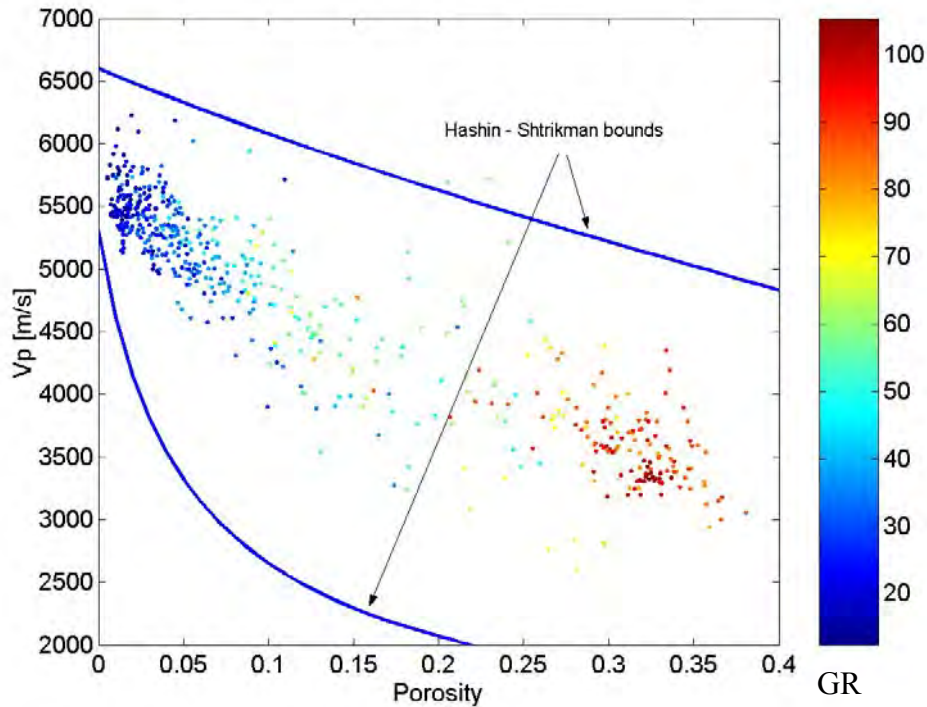
Figure 3.3: *V*$_P$-porosity scatter plot for James Lime reservoir. Data are color-coded by Gamma Ray (Well B).

Figure 3.3 presents the *V*$_P$ *vs. porosity* scatter-plot for the James Limestone interval from one well (Well B). The data are color-coded by Gamma-Ray intensity (API). We observe the expected trend of decreasing velocities with increasing porosity. We can also see that the higher velocities correspond to cleaner limestones (smaller values of Gamma-Ray), while the lower velocities correspond to rocks with higher shale content (larger values of Gamma-Ray). The porosity values for the shaly rocks are large, while those for the clean limestones are significantly smaller. This indicates that the cleaner limestones are tight, densely cemented rocks. Therefore, fracture permeability can have a big impact on the fluid flow in the areas of tight, clean limestones.

From Figure 3.3 we observe a larger scatter in the *V*$_P$-*porosity* domain for the shaly rocks than for the cleaner limestones. The scatter increases with porosity and shale content.
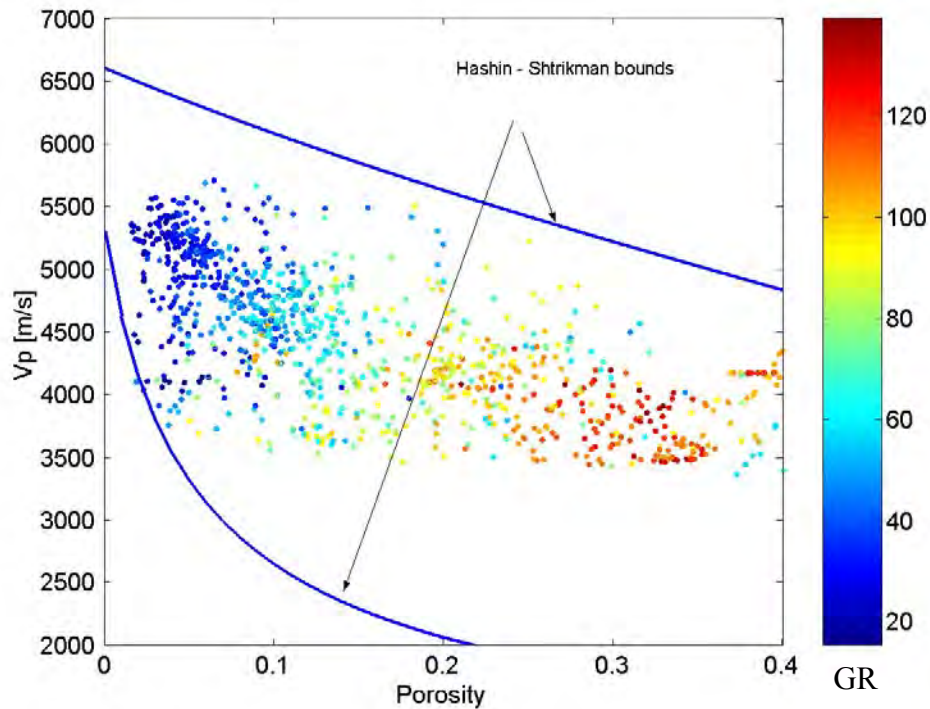
Figure 3.4: V_P-porosity scatter plot for the James Limestone reservoir. Data are color-coded by Gamma-Ray (Well A).

Figure 3.4 shows again a V_P *vs. porosity* scatter-plot, but for data from one of the key wells (Well A). We can observe the same expected trends of decreasing velocities with porosity, and decreasing velocities with Gamma-Ray, due to higher shale content. However, in this well there is more scatter in the velocities for the lowest porosities, in contrast with what we observed in the previous well (Figure 3.3). The *P*-wave velocities vary significantly, from approximately 5700 m/s to 4000 m/s, at about 5% porosity. We see from the color-coded Gamma-Ray that at these small porosities the shale content is relatively low. I also know from FMI data that fractures occur preferentially in the rocks with lower shale content. Therefore, I hypothesize that this large variation in the *P*-wave velocity at low porosities is the result of fractures. Fractures can greatly lower the velocities, without significantly increasing the porosities.

If we compare the V_P-*porosity* scatter plots for the two wells, we may interpret from the velocity variation, that Well A encountered more fractures than Well B. However, I can not verify this interpretation, since Well B does not have an FMI log.

3.3.1.1 Fracture distribution in the V_P-porosity domain

Figure 3.5 shows the same V_P *vs. porosity* scatter-plot for the James Limestone reservoir from Well A, but the data are color-coded by the number of fractures per foot. The fractures are interpreted from FMI log. I interpolated the number of fractures per foot to match the sonic log depth sampling. We can see that most of the fractures are in the brittle rocks, characterized by higher velocities, smaller porosities and lower shale content.
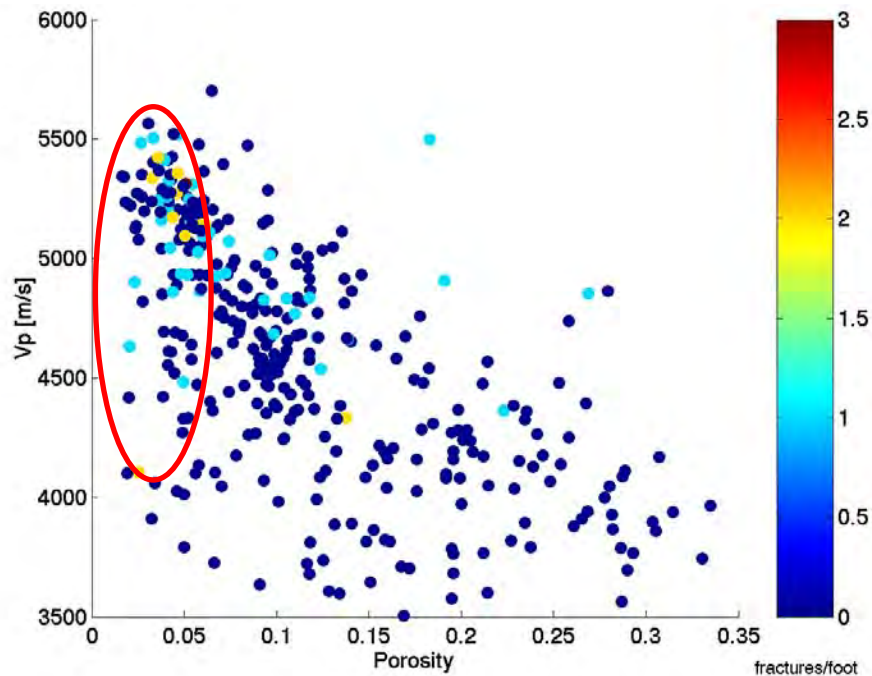
Figure 3.5: Fracture distribution in the James Limestone in the V_P-porosity domain. The data are color-coded by number of fractures per foot, determined through FMI in Well A.

In Figure 3.5, I highlight a zone of highly varying V_P at small porosity. This zone corresponds to intervals with a relatively larger number of fractures per foot, and it supports the hypothesis that the scatter in the velocities is due to fractures.

3.3.2 V_P-V_S relation

Another very important relation that we consider in any rock physics analysis is the one between the *P*-wave velocity and the *S*-wave velocity, since this is the key to

lithology, and also to fluid discrimination from seismic or sonic-log data. This relation is also very important for predicting V_S in cases when we have only *P*-wave information.
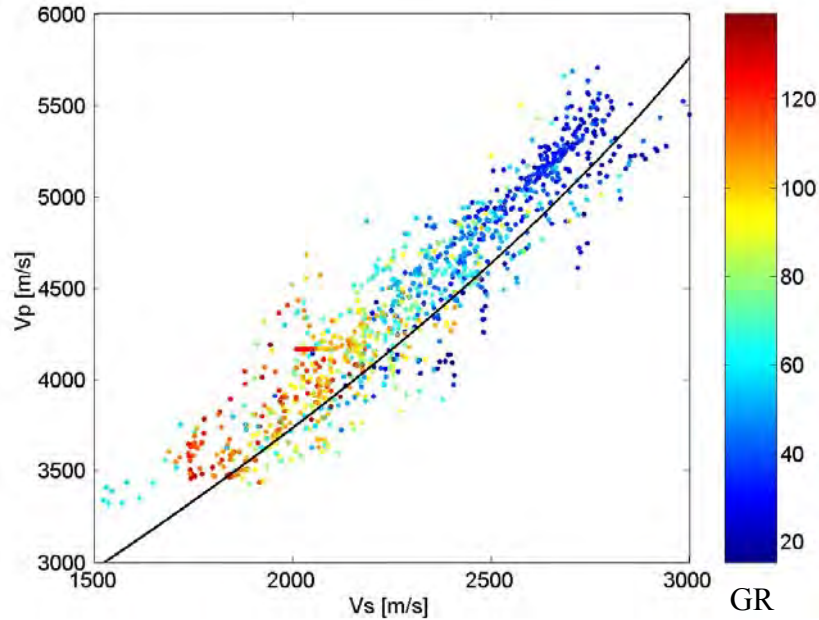
Figure 3.6: V_P-V_S scatter plot for James Lime reservoir. Superimposed is Castagna's line for Limestones. (Data from Well A).

For the area of study, I use the V_P-V_S relation from Well A, the only one which has shear-wave information. Figure 3.6 presents the V_P-V_S scatter plot for the James Limestone reservoir. Data are for brine-saturated rocks. I also superimposed the least-squares polynomial fit derived by Castagna et al. (1993) for limestones:

$$V_S = -0.05508\,V_P^2 + 1.0168\,V_P - 1.0305 \qquad (3.1)$$

We can see that for this data set, the *S*-wave velocity is slightly lower than the one predicted by the Castagna's empirical relation. In other words, the V_P/V_S ratio is a little higher for the James Limestone than is predicted by Castagna's relation. Nevertheless, there is a very distinct correlation between V_P and V_S, as expected.

3.3.2.1 Fracture distribution in the V_P-V_S domain

Figure 3.7 presents the same V_P-V_S scatter plot for an interval from the James Limestone reservoir. The data are color-coded by the number of fractures per foot.
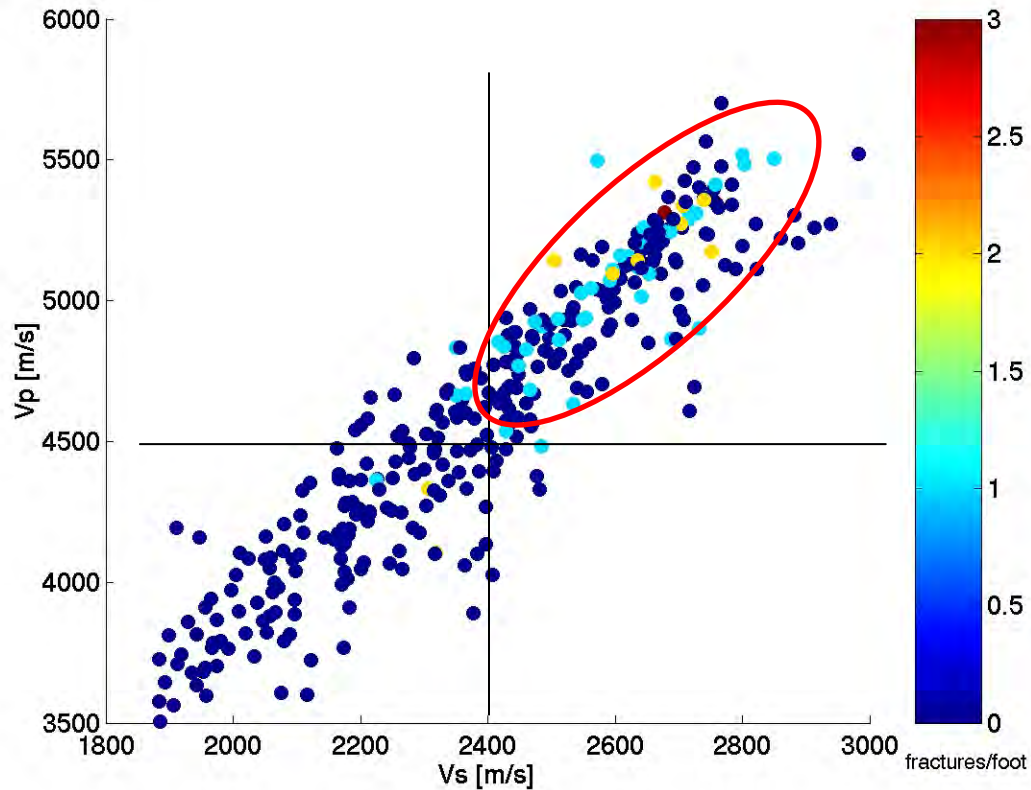
Figure 3.7: Fracture distribution in the James Limestone in the V_P-V_S domain. The data are color-coded by number of fractures per foot, determined through FMI. (Well A).

We observe that the fractures are mostly present in rocks with high *P*- and *S*-wave velocities. As a consequence, in the modeling I assume that the fractures are associated with high-velocity rocks, whose unfractured background properties exceed certain limits, such as 4500m/s for V_P and 2400m/s for V_S.

This association of the fractures with the high-velocity rocks was observed also for the San Andres reservoir, in the Yates Field (Sava et al, 2001). The association can play an important role in fracture delineation from seismic data. Even if the fractures will lower the velocity significantly in the most fractured zones, on average the velocities of

the fractured regions may be larger than the velocities of the unfractured rocks, characterized by higher shale content. Therefore, on average, higher impedance may correspond to the zones with higher probability of fractures, as the results from fracture modeling show in the next sections.

3.3.3   Gassmann fluid substitution

Another very important task in any rock physics analysis is to assess the fluid sensitivity in the seismic response. For this, I use Gassmann's (1951) low-frequency fluid substitution method (Mavko et al., 1998). Figure 3.8 shows the brine-saturated (blue) and the gas-saturated (red) properties of the James Limestone reservoir in the V_P-V_S domain. As expected, the fluid sensitivity is a little larger at smaller velocities. The superimposed lines are least-square linear fits to the data, for the brine and gas cases, respectively. We can observe that the variability in V_P and V_S from rock stiffness, clay content, and porosity is as large as the sensitivity to the fluid changes.

The average elastic fluid properties in the area of interest are presented in Table 3.1, and are evaluated using Batzle's and Wang's (1992) empirical relations:.

Table 3.1: Fluid properties for the James Limestone reservoir.

	Bulk modulus [GPa]	Density [g/cm3]
brine	2.51	1.018
gas	0.048	0.032

However, we expect the fluid sensitivity to be significantly enhanced by the presence of the fractures, as the modeling results show in the next sections.
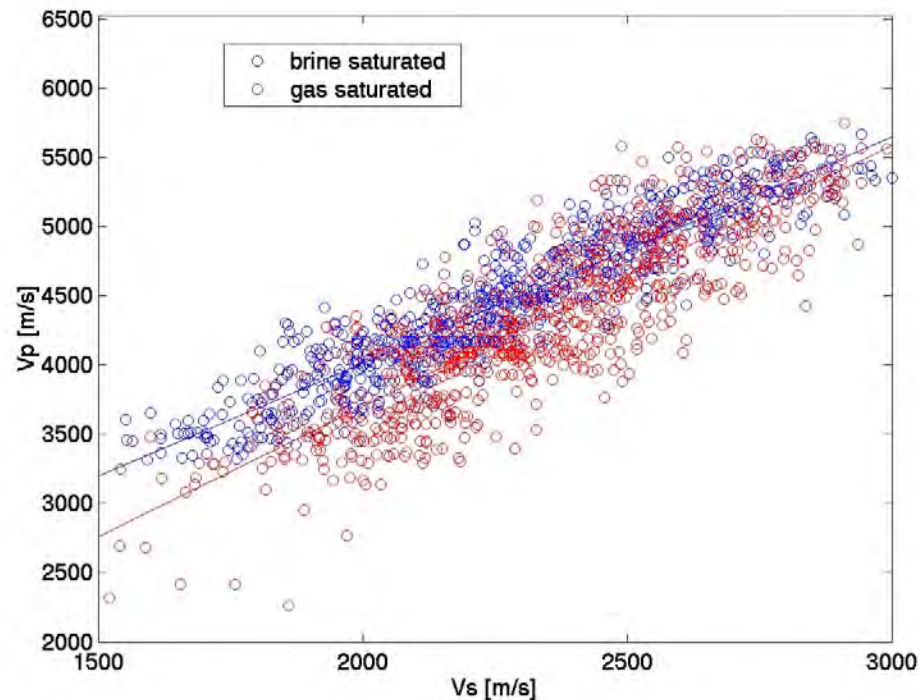
Figure 3.8: V_P-V_S scatter-plot for brine and gas-saturated cases for the James Limetone reservoir. Velocities are stochastically simulated.

3.3.4 Summary of the observations

In this section, I give a brief summary of the preceding rock physics analysis, based on the well-log data.

From the V_P-*porosity* scatter-plots color-coded by the Gamma-Ray, we see that the velocities decrease with porosity and shale content, as expected. The cleaner limestones have lower porosities and higher velocities than the more shaly rocks.

From the V_P-V_S scatter-plot color-coded by the number of fractures per foot, we can see that most of the fractures are associated with high V_P and V_S. This association can play an important role in fracture delineation from seismic data. As I show in the next section, high density of gas–filled fractures can significantly lower the velocities of the clean limestones. However, on average, the velocities of the fractured regions may still be larger than the velocities of the shaly rocks. Therefore, higher impedance values may correspond to the zones with higher probability of fractures.

This association of fractures with higher velocity rocks helps us in choosing the unfractured background properties that we need to input in the modeling. The elastic properties should correspond to rocks with velocities higher than certain limits, such as 4500 m/s for V_P and 2400m/s for V_S.

Based on these observations, I consider that the reservoir may exhibit three main types of facies: 1) unfractured, clean limestones, 2) shaly limestones, and 3) fractured, clean limestones that I model with various distributions of cracks.

3.4   Monte Carlo simulations and fracture modeling

In this section, I present the results of the fracture modeling and stochastic simulations of various seismic signatures, with the objective of determining the optimal seismic attributes for delineating the gas-filled fractured zones in the reservoir. The stochastic approach allows us to incorporate the natural geologic variability of rock properties into deterministic elastic models (Mavko and Mukerji, 1998; Mukerji et al., 2001, Avseth et al., 2005).

Fractures affect both the interval properties, such as velocities and travel-time, and the interface properties, such as reflectivity and AVO. If the fractures are aligned, they can also induce anisotropy for both interval and interface properties.

In most cases, seismic field studies for fracture detection are designed to find near-vertical and open joints (Teng, 1998; Grimm, 1999; Perez, 1999; Lynn, 1999). However, in the proximity of the faults, sometimes the host rock can be very fractured, giving rise to the so-called "breccia zone". In these cases the faults may have systematic alignment, but the smaller fractures can be distributed in all possible directions. Therefore, for this situation a more appropriate fracture model is one that assumes isotropic distribution of crack orientations.

For both isotropic and anisotropic distribution of fracture orientations, I use Hudson's (1981) penny-shaped crack model. More details about this model are given in the preceding chapter.

In this section, I consider the fractures to be 100% saturated with either brine or gas, but not necessarily with the same fluid as in the matrix porosity. I substitute the fluids in the fractures by changing the elastic moduli of the inclusion material in Hudson's (1981) equations. This procedure assumes that there is little communication between the fluids in the matrix pores and the fluids in the cracks during wave excitation. This assumption is most appropriate when the matrix porosity and permeability are small (Hudson, 1997, Teng, 1998). For the clean limestones that are most likely to get fractured, the porosity of the unfractured background rocks is smaller than 10%, while the permeability has also very low values, between 0.001 and 0.1mD (Marathon Oil Co., Internal Report).

To assess the uncertainty of fracture detection and characterization from seismic data, I run Monte Carlo simulations on the input parameters in the Hudson's model (1981). The input parameters are the crack density, aspect ratio of the ellipsoidal cracks, bulk modulus of the saturating fluid, and the V_P, V_S and *density* of the isotropic, unfractured background rocks.

For the crack density, I choose a uniform distribution between 0.01 and 0.1. The upper value of 0.1 corresponds to the limit of validity of Hudson model. As discussed in Chapter 2, this value represents a relatively large degree of fracturing, especially for a reservoir at approximately 2 km depth. By choosing a uniform distribution I assume maximum uncertainty over the interval considered for the crack density. For the aspect ratio of the penny-shaped cracks, defined as the ratio between the aperture and the radius of the crack, I also use a uniform distribution, on a logarithmic scale (from 0.001 to 0.1). More details about Hudson's model are given in Chapter 2.

For the unfractured matrix properties (V_P, V_S, *density*), I derive the distributions from the well-log data. . Figure 3.9 presents in the upper panels the histograms for the V_P, V_S and *density* of the clean limestones in the reservoir, obtained from the well logs. The lower panels in the same figure present the probability distribution functions (PDFs) of the V_P, V_S, and *density* derived from the histograms. Since the fractures occur preferentially in the high velocity rocks, as the rock physics analysis shows, I consider for the background properties of the host rocks only P-wave velocities greater than 4500m/s.
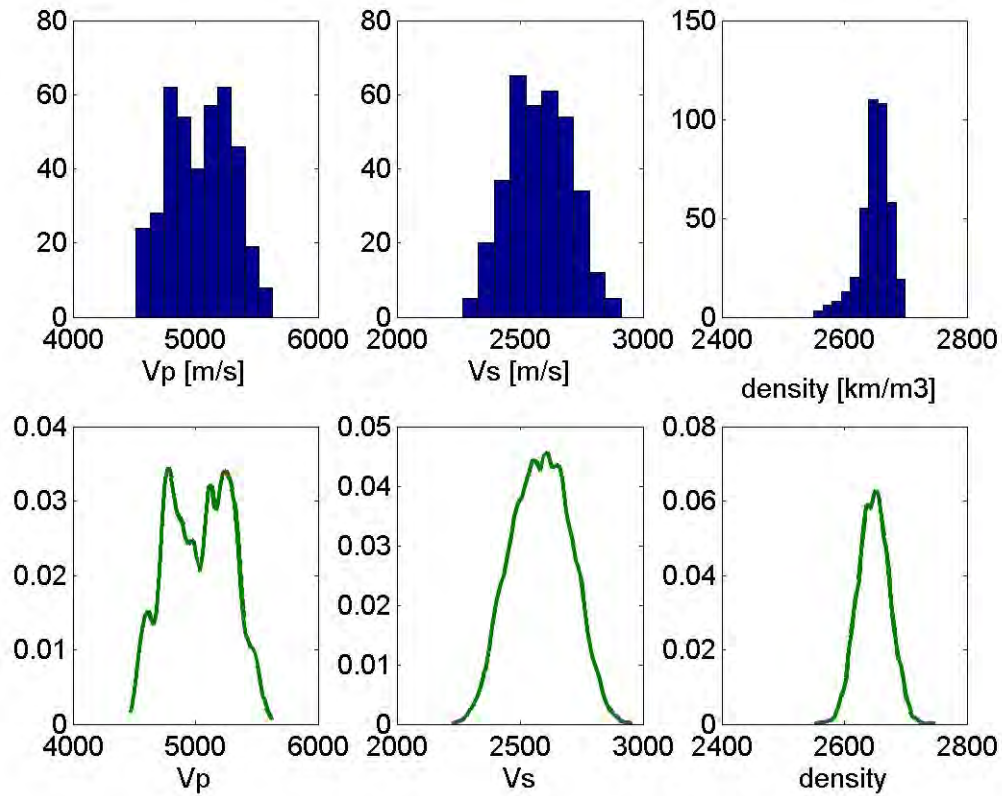
Figure 3.9: Upper panels: V_P V_S and density histograms derived from the well logs for the unfractured background rock properties. Lower panels: Corresponding probability density functions (PDFs).

The V_P, V_S, and *density* derived from the well logs are also upscaled to seismic wavelengths. The upscaling is performed on the well data using Backus (1962) averages for the bulk and shear modulus, and volumetric averages for density (Mukerji, 1995). The fluid that saturates the fractures is considered to be either gas or brine.

The *Monte Carlo* procedure consists in randomly drawing correlated sets of V_P, V_S, and *density* from the distributions derived from the well-logs for the unfractured background rock properties, and also from the assumed distributions for the crack density and the aspect ratio of the ellipsoidal cracks. For each realization of a set of V_P, V_S, and *density*, together with the crack density and the aspect ratio of the cracks, I compute the elastic properties for the fractured medium, using Hudson's model. If we repeat this procedure many times, we obtain a large number of realizations of elastic properties for the modeled fractured medium, to span the intrinsic natural variability.

I also simulate multiple realizations for the elastic properties for the other possible facies in the reservoir, such as the shaly rocks and the unfractured, clean limestones. In order to model the interface properties, I also simulate multiple realizations for the *Vp*, *Vs* and *density* of the cap rock, based on the distributions derived from the well logs.

Based on this large number of correlated realizations of elastic properties, I derive the joint probability density functions (PDFs) of various seismic attributes for each facies in the reservoir: 1) clean, unfractuered limestone, 2) shaly limestone, and 3) fractured, clean limestone. I compute both the interval and the interface seismic properties, to understand how we can separate the fractured zones filled with gas from the other facies in the reservoir, in different possible scenarios.

3.4.1   Interval properties

In this section, I present the results of our stochastic simulations for interval properties, such as *P*- and *S*-wave velocities, *P*-Impedance and Poisson's ratio and travel-times, in the hypotheses of a vertical set of fractures, and of randomly oriented cracks in the reservoir.

3.4.1.1 Interval velocities

Fractures can lower significantly the velocities of the initially unfractured host rock. I consider first the hypothesis of an isotropic distribution of fracture orientations, which corresponds to breacciated zones associated with faults.

I use *Monte Carlo* method and fracture modeling, as previously presented, and obtain the joint probability density function for the interval *P*- and *S*- wave velocities.

Figure 3.10 shows one of the results of the stochastic simulations for the three different possible facies in the reservoir. The contours represent the joint probability density functions (PDF) of V_P and V_S for the unfractured, clean limestone (blue), for the shaly rocks in the reservoir (red), and also for the fractured, clean limestone, modeled with randomly oriented cracks (green). The fractures are filled with gas.
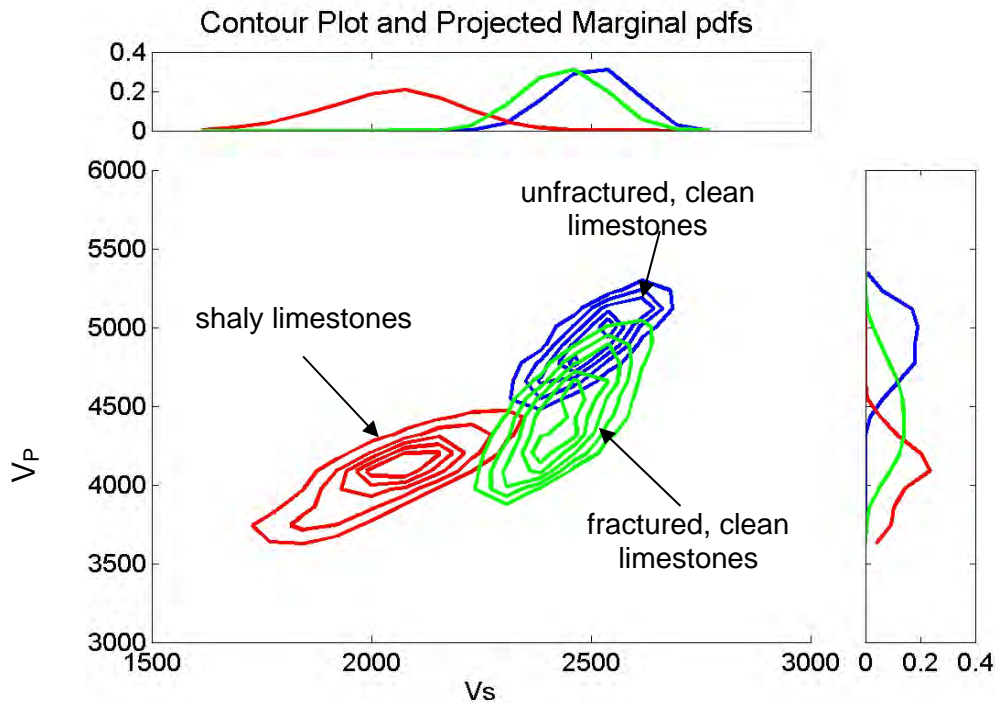
Figure 3.10: Joint probability distribution functions of V_P and V_S for the Monte Carlo simulations of the unfractured clean limestones (blue), fractured limestones with randomly oriented cracks (green), and shaly rocks (red). Fractures are filled with gas. The upper and right panels show the marginal distributions for V_S and V_P for each facies.

The uncertainty in the PDFs is due to the variability in the unfractured background properties. For the fractured facies, the scatter is also due to the variability in both the crack density and the aspect ratio of the cracks.

We can see that in the V_P-V_S *domain* there is some overlap of the joint probability distribution functions (PDF) between the modeled fractured rocks and the unfractured ones. The P-wave velocity of the fractured rocks filled with gas decreases more than the S-wave velocity. From the marginal distribution, presented in the right-side panel of Figure 3.10, we see that on average, the V_P of the fractured, clean limestone is larger than the V_P of the shaly rocks. However, as the fracture density increases, the P-wave velocity of the fractured, clean limestone becomes closer to the P-wave velocity of the shaly limestone. At the same time, the decrease in V_S due to fractures is smaller, such that the

S-wave velocities of the fractured, clean limestones remain significantly higher than the V_S of the shaly rocks. Therefore, the shear-wave information is valuable for discriminating between the gas-filled fractured zones and the shaly zones in the reservoir.
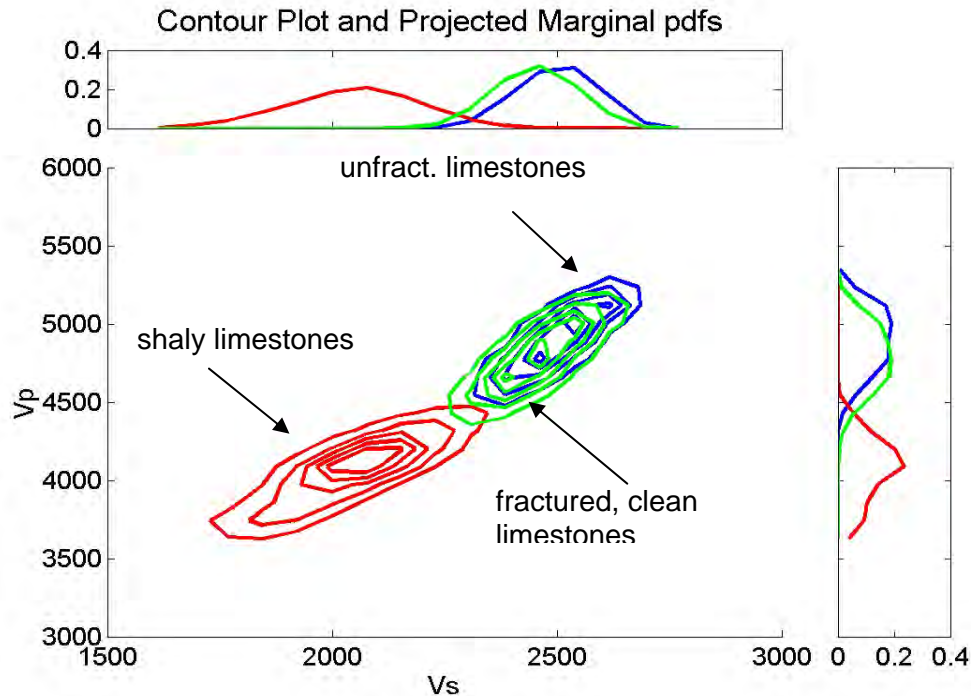
Figure 3.11: Joint probability distribution functions of V_P and V_S for the Monte Carlo simulations of the unfractured, clean limestones (blue), fractured limestones with randomly oriented cracks (green), and shaly rocks (red). Fractures are filled with brine. The upper and right panels show the marginal distributions for V_S and V_P respectively, for each facies.

Figure 3.11 presents the joint PDF of V_P and V_S for the three main facies in the reservoir. In this case, however, the fractures are saturated with brine. We observe very small decrease in both *P* and *S*-wave velocities as compared with the properties of the unfractured limestones. Modeling shows that in the V_P-V_S domain it is difficult to distinguish between unfractured, clean limestones and fractured zones, if the randomly oriented fractures are saturated with brine.

In the case of a vertical set of aligned fractures, the medium is anisotropic, and velocities vary with direction. Figures 3.12 and 3.13 show the joint PDF of V_P and V_S for the three possible facies in the reservoir.

The modeled V_P and V_S of the fractured limestones correspond to the waves polarized parallel to the fracture planes. In Figure 3.12, the cracks are gas-saturated, while in Figure 3.13, the cracks are brine-saturated. As Hudson's model predicts, the V_S of the fractured rocks polarized along the crack plane is not at all affected by the presence of the fractures. However, the *P*-wave velocity propagating parallel to fracture planes is slightly lowered, if the cracks are filled with gas. However, this decrease in V_P is not very large, such that the *P*-wave velocities propagating along the fracture planes remain higher than those of the shaly limestones in the reservoir.
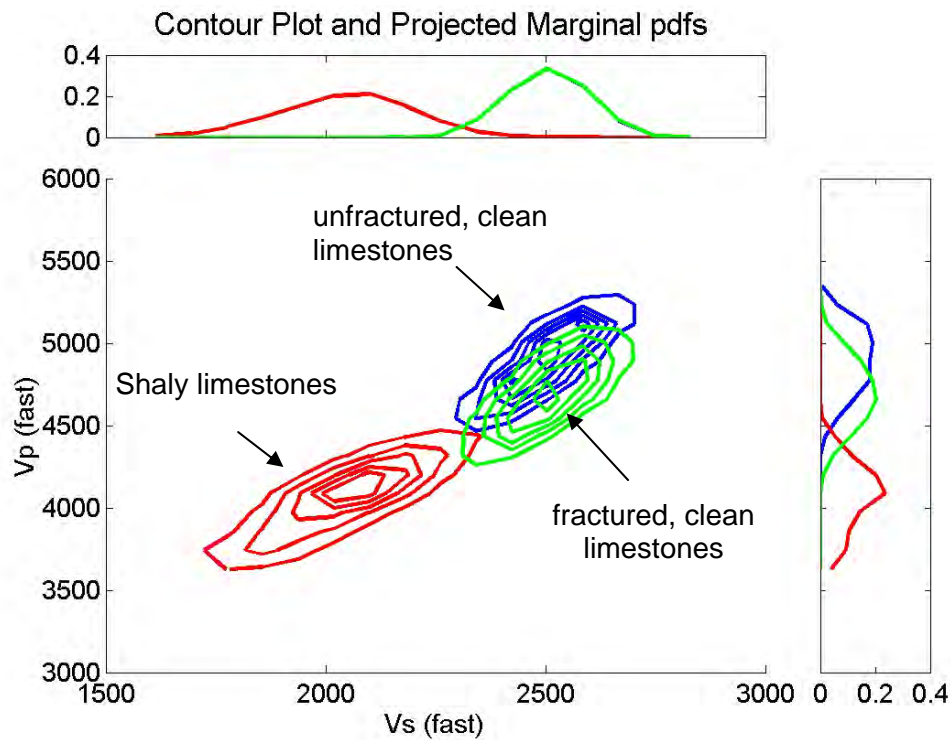
Figure 3.12: Joint PDFs of V_P and V_S for the Monte Carlo simulations of the unfractured clean limestones (blue), fractured limestones with a set of vertical cracks (green), and shaly rocks (red). Fractures are filled with **gas**. The V_P and V_S for fractured facies correspond to polarization **parallel to fractures**. The upper and right panels show the marginal distributions for V_S and V_P respectively, for each facies.

If the fractures are saturated with brine, then the fractured rock cannot be distinguished from the unfractured, clean limestones, as Figure 3.13 shows.
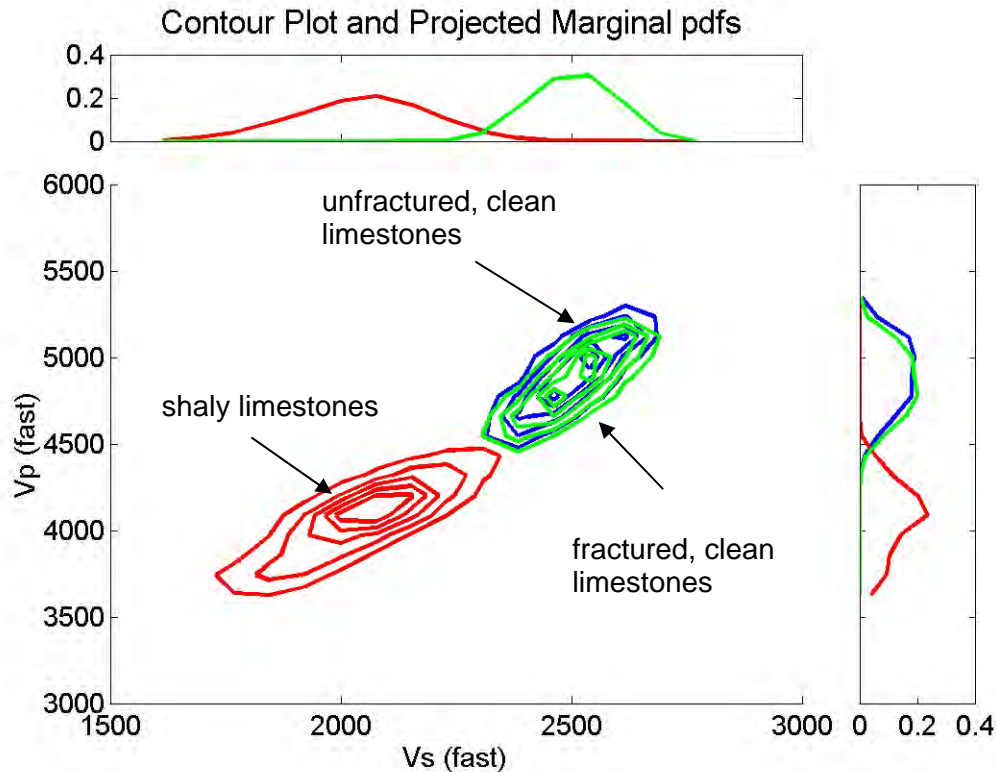
Figure 3.13: Joint PDFs of V_P and V_S for the Monte Carlo simulations of the unfractured clean limestones (blue), fractured limestones with a set of vertical cracks (green), and shaly rocks (red). Fractures are filled with **brine**. The V_P and V_S for fractured facies correspond to polarization **parallel to fractures**. The upper and right panels show the marginal distributions for V_S and V_P respectively, for each facies.

Figures 3.14 and 3.15 show again the joint PDFs for V_P and V_S. In these cases the properties of the fractured facies correspond to the wave polarization orthogonal to the fracture planes. The cracks are filled with gas (Figure 3.14), and brine (Figure 3.15), respectively. For the gas-saturated fractures, both V_P and V_S decrease significantly as compared with the properties of the unfractured, clean limestones. However, the modeling predicts a larger decrease in V_P, than in V_S. The *S*-wave velocities polarized orthogonal to the fracture planes remain significantly higher than the *S*-wave velocities of the shaly limestones, in contrast with the *P*-wave velocities. This result suggests that the shear information from waves polarized orthogonal to the fracture planes is important for discriminating between the gas-filled fractured zones and the shaly zones in the reservoir.
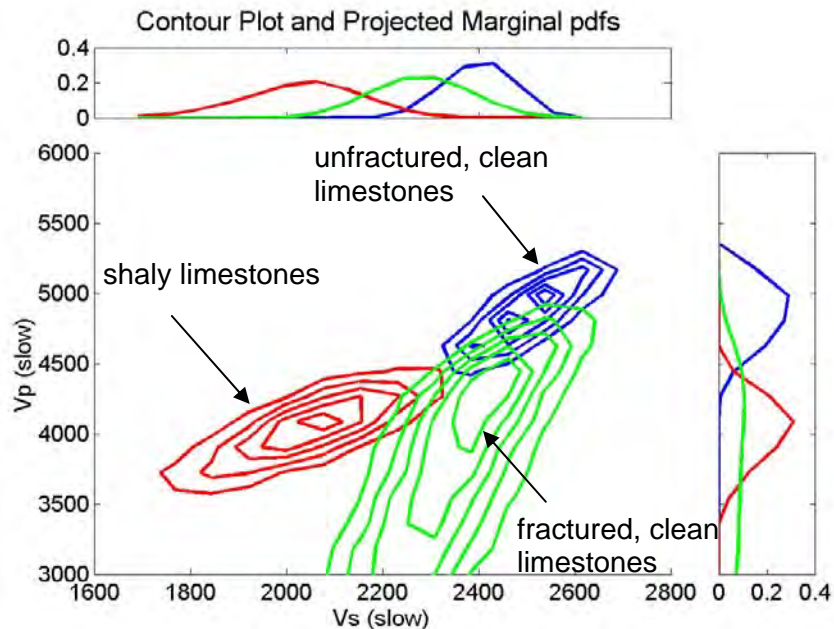
Figure 3.14: Joint PDFs of V_P and V_S for the Monte Carlo simulations of the unfractured clean limestones (blue), fractured limestones with a set of vertical cracks (green), and shaly rocks (red). Fractures are filled with **gas**. The V_P and V_S for fractured facies correspond to polarization **orthogonal to fractures**. The upper and right panels show the marginal distributions for V_S and V_P respectively, for each facies.

Figure 3.15 shows that, if the fractures are saturated with brine, the *P*-wave velocity polarized orthogonal to fractures decreases less than the corresponding *S*-wave velocity with the same polarization. Both V_P and V_S polarized orthogonal to brine-filled cracks are larger than the velocities of the shaly rocks in the reservoir.

From the modeling, we observe that in the V_P -V_S domain the gas-filled fractures are much more easily distinguishable from the unfractured rocks than the brine-filled fractures, for both isotropic and anisotropic distributions of fracture orientations.

If the fractures are saturated with gas, the modeling shows that the *P*-wave velocities are more sensitive than the *S*-wave velocities. As expected, the *P*-wave velocity decreases the most in the case of a vertical set of aligned fractures, if the waves are propagating orthogonal to the cracks. For large crack densities, the V_P of the fractured zones becomes comparable to the V_P of the shaly limestones in the reservoir, which are less susceptible to be fractured. The S-wave velocity decreases less than *P*-wave velocity, and its

expected values remain larger than the *S*-wave velocity of the shaly rocks. Therefore, V_S is a valuable piece of information to discriminate between the gas-filled fractured zones and the shaly limestones in the reservoir.
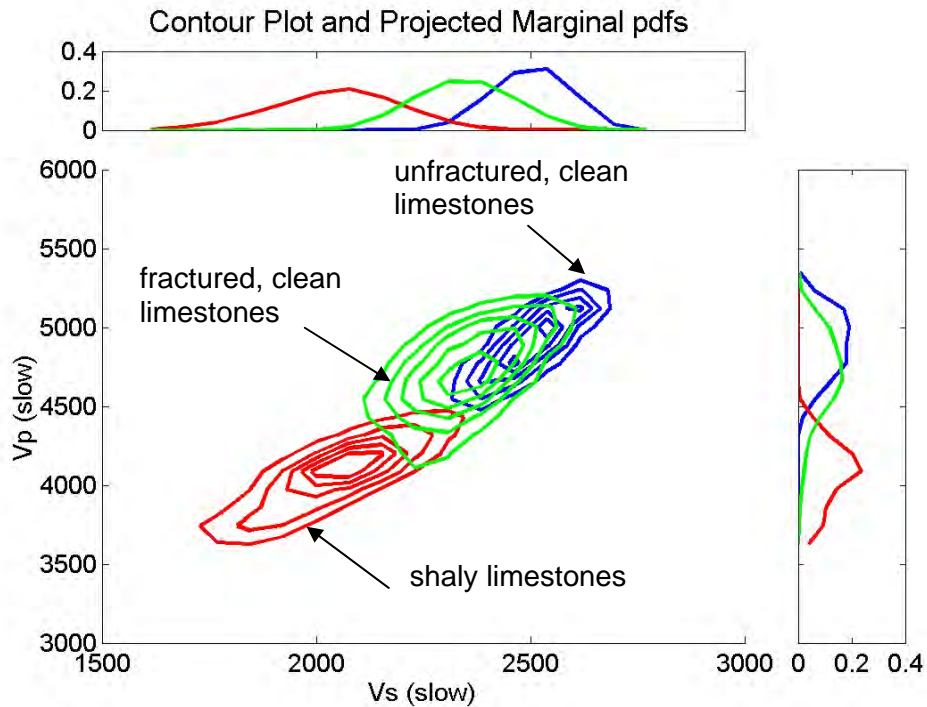
Figure 3.15: Joint PDFs of V_P and V_S for the Monte Carlo simulations of the unfractured clean limestones (blue), fractured limestones with a set of vertical cracks (green), and shaly rocks (red). Fractures are filled with **brine**. The V_P and V_S for fractured facies correspond to the polarization **orthogonal to fractures**. The upper and right panels show the marginal distributions for V_S and V_P respectively, for each facies.

If the fractures are brine-saturated, it is more difficult to distinguish the fractured zones from the unfractured ones. Both *P*- and *S*-wave velocities are little affected by the presence of the fractures, for both isotropic and anisotropic distribution of cracks. The fractured zones saturated with brine are the most visible in the V_P -V_S domain, when the waves are polarized orthogonal to the aligned fracture planes. This is the only case in which V_S is more sensitive to fractures than V_P (Figure 3.15). However, on average, *S*-wave velocity of the fractured zones remains larger than the *S*-wave velocity of the shaly limestones in the reservoir.

3.4.1.2 P-Impedance – Poisson's Ratio

Besides the V_P -V_S domain, I also consider the *P-Impedance - Poisson's Ratio* domain, in the case of an isotropic distribution of fractures.

Figures 3.16 and 3.17 present the joint PDF for the *P-Impedance* and *Poisson's Ratio*, again for the three possible facies in the reservoir: unfractured, clean limestones (blue), fractured limestones (green), and shaly rocks (red). Fractures are randomly distributed and filled with gas (Figure 3.16) and brine (Figure 3.17), respectively. The pores in the matrix rocks are brine-saturated.

From Figure 3.16 we can see very little overlap between the three different possible facies in the reservoir. The *P-Impedance* of the fractured rocks filled with gas may drop significantly, especially for high fracture density, as compared with the *P-Impedance* of the unfractured, clean limestones. However, as we observe from the marginal distributions of the *P-Impedance* for each facies (right panel of Figure 3.16), the expected value for the *P-Impedance* of the fractured zones is still larger than the one corresponding to the shaly limestones in the reservoir. Therefore, higher impedance may correspond to zones of higher fracture probability. *Poisson's ratio* is a good discriminator between the fractured, clean limestones and the shaly rocks. If the fractures are filled with gas, the *Poisson's Ratio* of the fractured limestones decreases drastically as compared to the *Poisson's Ratio* of both the shaly limestones and the unfractured, clean limestones.
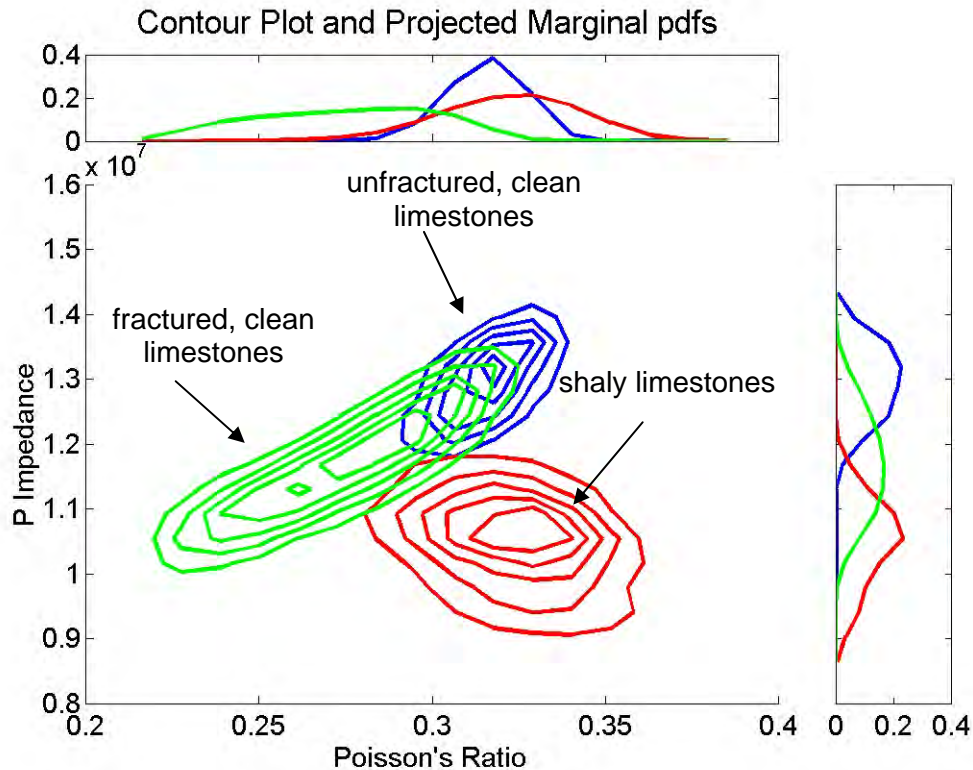
Figure 3.16: Joint probability distribution functions of the P-Impedance and Poisson's Ratio for the Monte Carlo simulations of the unfractured, clean limestones (blue), fractured limestones with **randomly oriented cracks** (green), and shaly rocks (red). Fractures are filled with **gas**. The upper and right panels show the marginal distributions for Poisson's Ratio and P-Impedance respectively, for each facies.

If the fractures are saturated with brine (Figure 3.17), then they are not distinguishable from the unfractured, clean limestones. We can observe very small decrease in the P-Impedance, and practically no change in the Poisson's Ratio, as compared to the unfractured properties.

These modeling results suggest that it is the gas in the fractures that makes the Poisson's ratio drop, not the fractures themselves, since the Poisson's ratio of the brine-filled fractured zones does not change significantly in comparison with the unfractured facies.
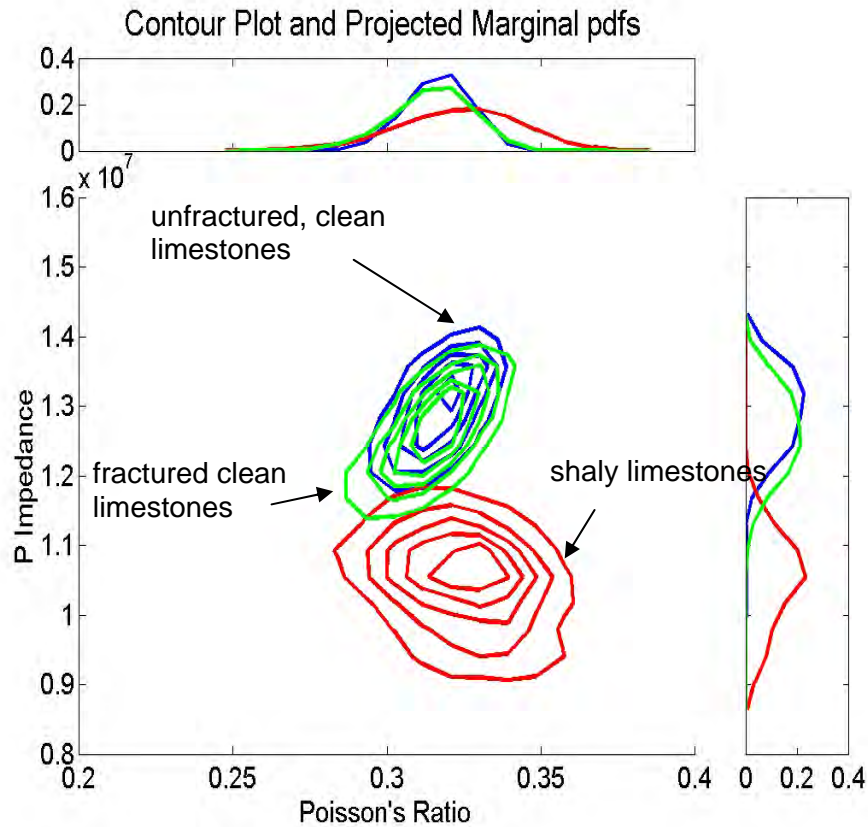
Figure 3.17: Joint probability distribution functions of the P-Impedance and Poisson's Ratio for the Monte Carlo simulations of the unfractured, clean limestones (blue), fractured limestones with randomly oriented cracks (green), and shaly rocks (red). Fractures are filled with **brine**. The upper and right panels show the marginal distributions for Poisson's Ratio and P-Impedance respectively, for each facies.

3.4.1.3 Thomsen's anisotropic parameters

A single set of aligned vertical fractures generates a transversely isotropic medium with horizontal axis of symmetry (HTI). Most of the seismic attributes for an HTI medium are given in the literature in terms of Thomsen's (1986) anisotropic parameters and modification of these developed by Tsvankin (1997).

I use again Hudson model (1980, 1981), together with stochastic simulations, to compute the anisotropic Thomsen's type parameters. The background properties are simulated through a correlated *Monte Carlo* approach, based on the V_P, V_S and *density* derived from well-log data.

Figures 3.18 and 3.19 present the stochastically simulated epsilon, gamma and delta anisotropic coefficients defined with respect to the vertical axis (Tsvankin, 1997). The scatter in the data is due to the variability in the unfractured background properties, and also in the crack density and aspect ratio of the fractures. I use the same distributions of the crack density and the aspect ratio for both gas-filled and brine-filled fractures.

In Figure 3.18 the data are color-coded by fracture density, which increases from 0.01 to 0.1. The anisotropy coefficients increase in absolute value with increasing fracture density, as expected.
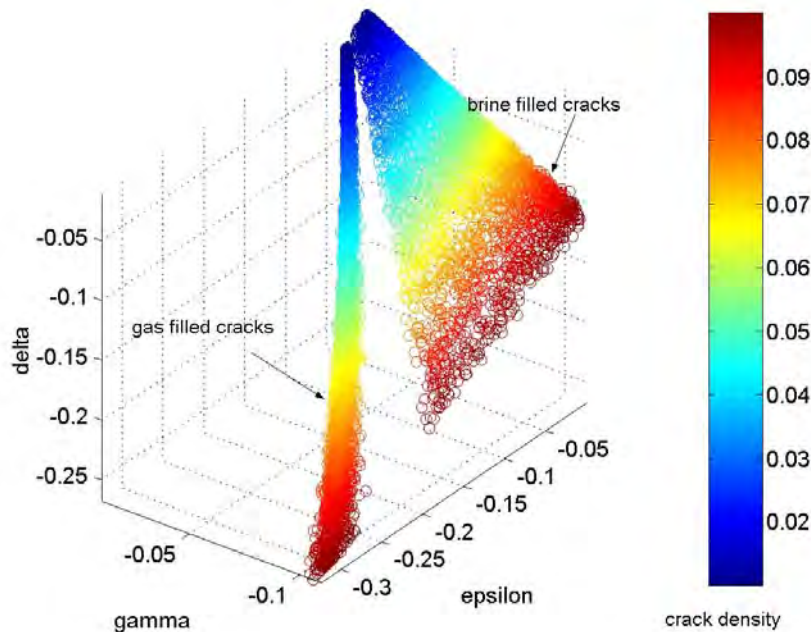
Figure 3.18: Stochastically simulated Thomsen type anisotropic parameters epsilon, gamma and delta defined with respect to vertical axis for HTI medium. Matrix porosity is brine saturated. Fractures are filled with gas and brine, respectively. Data are color-coded by the crack density.

We observe that the gas-filled and the brine-filled fractures have different signatures in the Thomsen's-parameter domain. More specifically, absolute values of the epsilon and delta parameters are larger for gas-filled fractures than for brine-filled fractures. However, as expected, the gamma parameter, which is a measure of the shear-wave anisotropy, does not change with the fluid.
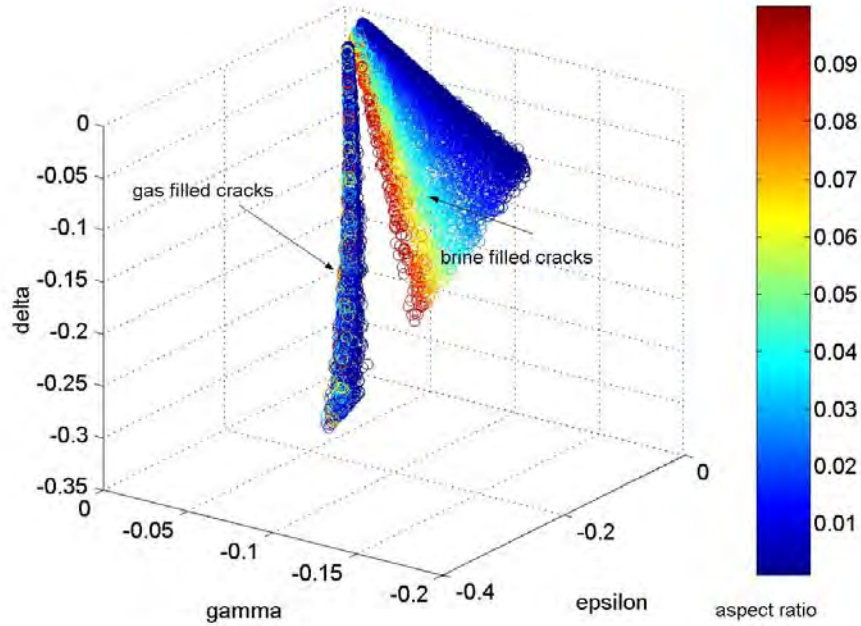
Figure 3.19: Stochastically simulated Thomsen type anisotropic parameters epsilon,
gamma and delta for HTI medium, defined with respect to vertical axis. Matrix
porosity is brine saturated. Fractures are filled with gas and brine, respectively. Data
are color-coded by aspect ratio of the cracks.

In Figure 3.19 the data are color-coded by the aspect ratio of the fractures. We see
that the brine-filled cracks are more sensitive to the aspect ratio than are the gas-filled
fractures. As a result, the scatter in the data for the brine-filled fractures is larger than for
the gas-filled fractures. At fixed crack density, the higher the aspect ratio of the brine-
filled cracks, the larger the absolute values of epsilon and delta. For smaller aspect ratios,
i.e., for very thin cracks, the presence of brine stiffens the cracks significantly, making
them almost invisible to the seismic waves.

For gas-filled fractures, I verify the weak anisotropy approximation for fracture
density, given by Bakulin (2000):

$$e = -3/8\varepsilon^{(V)}. \tag{3.2}$$

Here, e represents the fracture density, while $\varepsilon^{(V)}$ represents the epsilon parameter
defined with respect to the vertical axis (Tsvankin, 1997).

I vary the crack density in a deterministic way, and I use *Monte Carlo* method and Hudson's model to simulate the elastic stiffness matrix of the fractured medium, taking into account the variability in the unfractured background rock properties and in the aspect ratio of the cracks. Then, for each realization of elastic stiffness matrix, I derive the Thomsen's epsilon parameter with respect to vertical, and use Equation 3.2 to compute the crack density. These computed values of crack density are shown in Figure 3.20 (the open circles). To check the approximation from Equation 3.2, I superimposed the actual values of crack density used in the modeling (the horizontal lines).
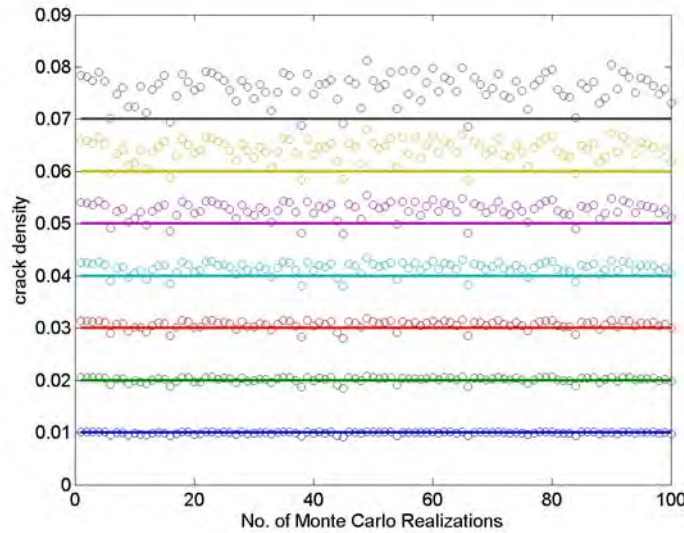
Figure 3.20: Verification of the weak-anisotropy approximation for crack density as a function of the Thomsen's epsilon parameter with respect to the vertical axis, for gas-filled fractures. The circles represent the computed crack density using the Equation 3.2 and Monte Carlo simulations for the elastic stiffness matrix of the fractured medium. The horizontal lines represent the actual values of crack density used in the modeling. The scatter in the data is due to variability in the background rock properties and aspect ratio of the cracks.

From Figure 3.20, we observe that, for small crack density up to 0.04, the Equation 3.2 gives good results for crack density. However, for larger crack density values, the weak anisotropy approximation overestimates the actual crack density. For example, in this case, for a crack density of 0.07 the overestimation is approximately 8%. Therefore, for gas-filled fractures, the crack density can be approximated by 3/8 of the absolute

value of Thomsen's epsilon parameter expressed with respect to vertical axis, especially for relatively small crack densities.

For the brine-filled fractures the absolute values of the epsilon parameter are smaller than those of the gas-filled fractures, as we can observe in Figures 3.18 and 3.19.

The delta parameter is also a function of the fluid type, and its absolute values are larger for the gas-filled fractures than for the brine-filled fractures, as we can observe in Figures 3.18 and 3.19.

The gamma parameter, also a linear function of the fracture density in the weak anisotropy approximation, does not change with fluid. This parameter represents the *S*-wave anisotropy. Bakulin (2000) gives an expression for the gamma parameter as a function of the ratio between V_P and V_S of the unfractured background rock:

$$\gamma^{(V)} = -\frac{8}{3(3-2g)}e,$$
(3.3)

$$\text{with } g = \left(\frac{Vs}{Vp}\right)^2.$$
(3.4)

Therefore, when the fluid is not known, gamma, the *shear-wave splitting parameter*, may be useful to predict fracture densities.

3.4.1.4 Travel time

In the hypothesis of a vertical set of aligned fractures in the reservoir the *P*-wave travel time varies with the direction of wave propagation.

Grechka and Tsvankin (1998) give the travel time variation for an HTI medium as a function of azimuth. Figure 3.21 is a contour plot of the difference between the P-wave travel time from the bottom of the James Limestone for the fractured and unfractured cases, as a function of azimuth and offset. The fractured James Limestone reservoir is modeled with vertical fractures filled with gas. In the modeling, I consider the crack density to be constant and equal to 0.07. The contour values in the plot are in seconds. We can see that the difference in travel time is larger in the direction perpendicular to fractures (azimuth 180) than in the direction parallel to fractures (azimuth 90), as

expected. Therefore, in principle, travel time may be used to determine the orientation of the main fracture system, and also to estimate fracture density. However, for the James Limestone reservoir, the difference in *P*-wave travel time between fractured and unfractured cases is very small. This is due because the reservoir is thin (approximately 200 ft).
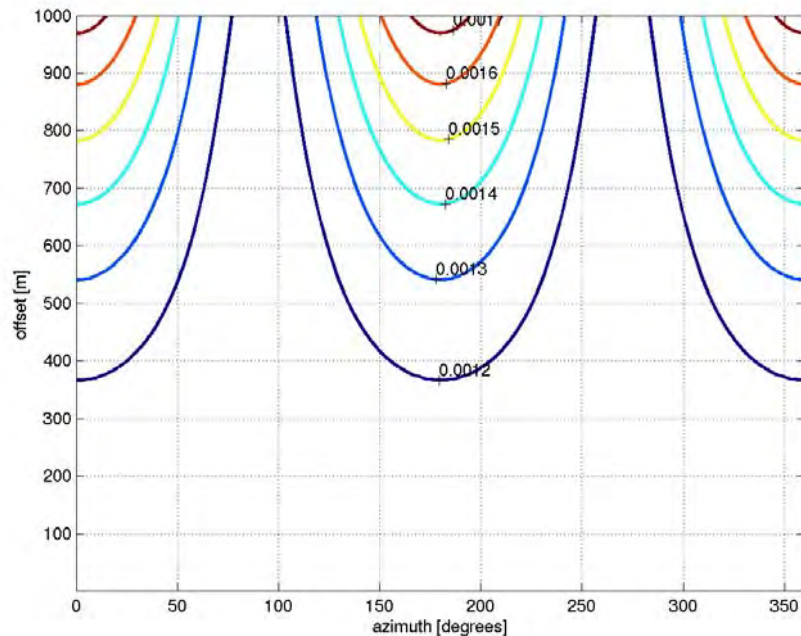
Figure 3.21: Contour plot for the travel time differences between the fractured and unfractured simulated James Limestone reservoir as a function of azimuth and offset. The values on the curves are in seconds.

For example, at the azimuth orthogonal to fractures and at an offset of 700m, the difference between the fractured and unfractured cases is approximately 1.4 milliseconds. Therefore, *P*-wave travel time difference between the fractured and unfractured zones through the James Limestone reservoir is not a practically useful attribute.

I also consider the hypothesis of a more chaotic distribution for fracture orientations, such as near the faults. Figure 3.22 shows the travel time from the bottom of the James Limestone for the unfractured (blue) and gas-filled fractured (red) cases, in the hypothesis of randomly distributed cracks. The travel time through the fractured region of the reservoir is larger than through the unfractured zones, as expected. The difference

between fractured and unfractured cases is approximately 5 milliseconds. This difference is higher than for the case of a nearly vertical set of fractures with the same fracture density of 0.07. However, the difference is relatively small to be useful for fracture characterization, since the dominant frequency of this seismic survey is relatively low.
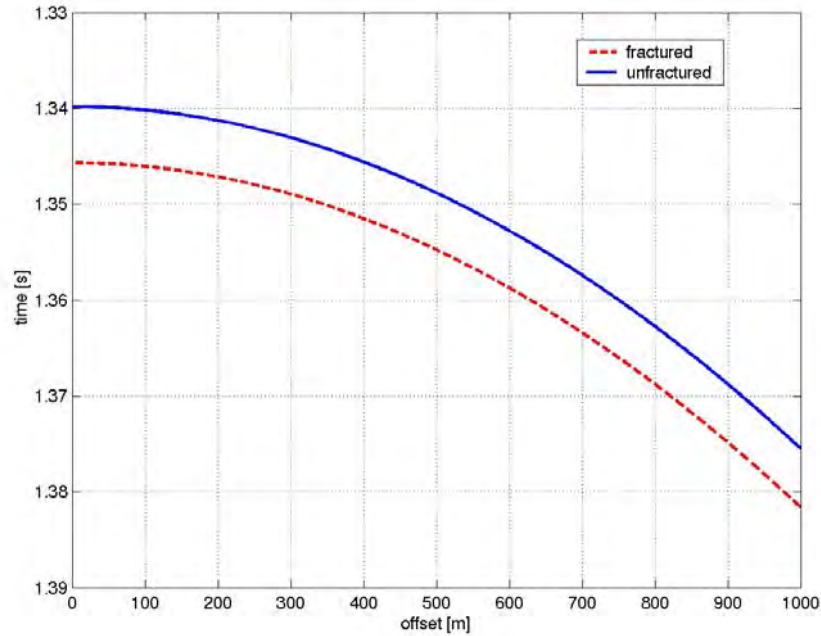
Figure 3.22: Expected travel time through the simulated James Limestone reservoir as a function of offset for the unfractured and fractured cases. Fractures are randomly distributed and filled with gas. Fracture density is 0.07.

I conclude that travel time methods are not very useful for fracture characterization in this case, since the James Limestone reservoir is too thin.

3.4.2   Interface properties

The advantage of using interface attributes, defined at the boundary between two layers, based on the contrast of their elastic properties, is that they provide localized information at the target of interest, unlike the travel time techniques. Besides, the interface properties are more appropriate than the travel time methods for thin reservoirs above the tuning thickness.

This section presents the results of the stochastic simulations for *PP reflectivity* Amplitude Variation with Offset (AVO) in the case of an isotropic distribution of cracks, and also for the PP reflectivity Amplitude Variation with Angle of Incidence and Azimuth (AVAZ) in the case of an HTI medium.

For the interface properties, I consider the boundary between the cap rock, represented by the Bexar shale, and the underlying reservoir, modeled with various distributions of fractures.

3.4.2.1 AVO gradient and Intercept

For the case of an isotropic distribution of cracks, I use Shuey's (1985) approximation for predicting the AVO gradient.

Figures 3.23 and 3.24 show the joint PDF of the *AVO Gradient* and *Intercept* of the reflected PP wave for the three different possible facies in the reservoir. The fractured facies (green) is modeled with randomly oriented fractures filled with gas and with brine. The corresponding results are presented in Figure 3.23 and Figure 3.24, respectively.

We observe a larger overlap between the different facies in the interface attributes domain than in the interval attributes domain. This is due to the larger variability in the seismic properties of the cap rock.

From Figure 3.23 we see that on average, the normal *PP reflectivity* from the fractured zones saturated with gas is smaller than that from the unfractured ones. The presence of the gas-filled fractures decreases the *PP reflectivity*. However, on average we should expect the smallest reflectivity from the shaliest rocks in the reservoir. As the fracture density increases, the *PP reflectivity* from the fractured zones decreases, and becomes closer to the *PP reflectivity* from the shaly limestones in the reservoir. The *AVO gradient* can help resolve this ambiguity. From the right-side panel of Figure 3.23, we see that on average, the *AVO gradient* for the shaly rocks is higher than that of the clean, unfractured limestones. At the same time, the *AVO Gradient* of the fractured limestones is smaller than that of the unfractured, clean limestones. Therefore, the shaliness moves the *AVO gradient* to smaller negative values as compared to the unfractured, clean

limestones, while the fractures filled with gas move the *AVO gradient* to larger negative values as compared to the clean, unfractured limestones. In conclusion, using reflectivity together with *AVO gradient* can help in better discriminating the gas-filled fractured zones from the shaly zones in the reservoir.
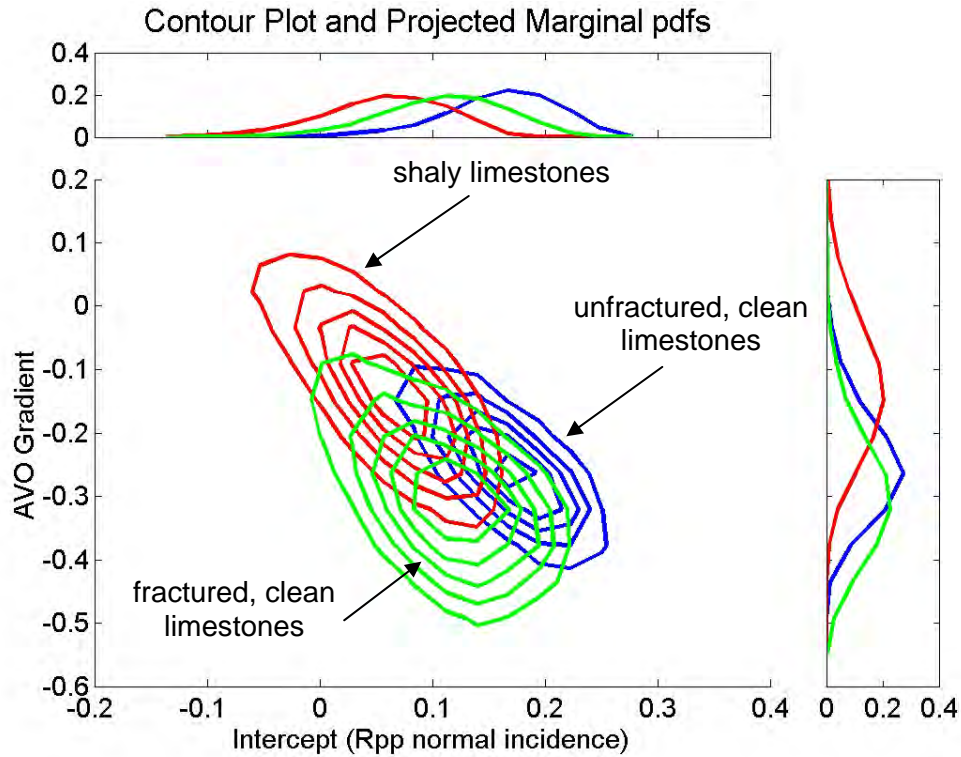
Figure 3.23: Joint probability distribution functions of the AVO Gradient and Intercept for the Monte Carlo simulations of the unfractured, clean limestones (blue), fractured limestones with **randomly oriented** cracks (green), and shaly rocks (red). Fractures are filled with **gas**.
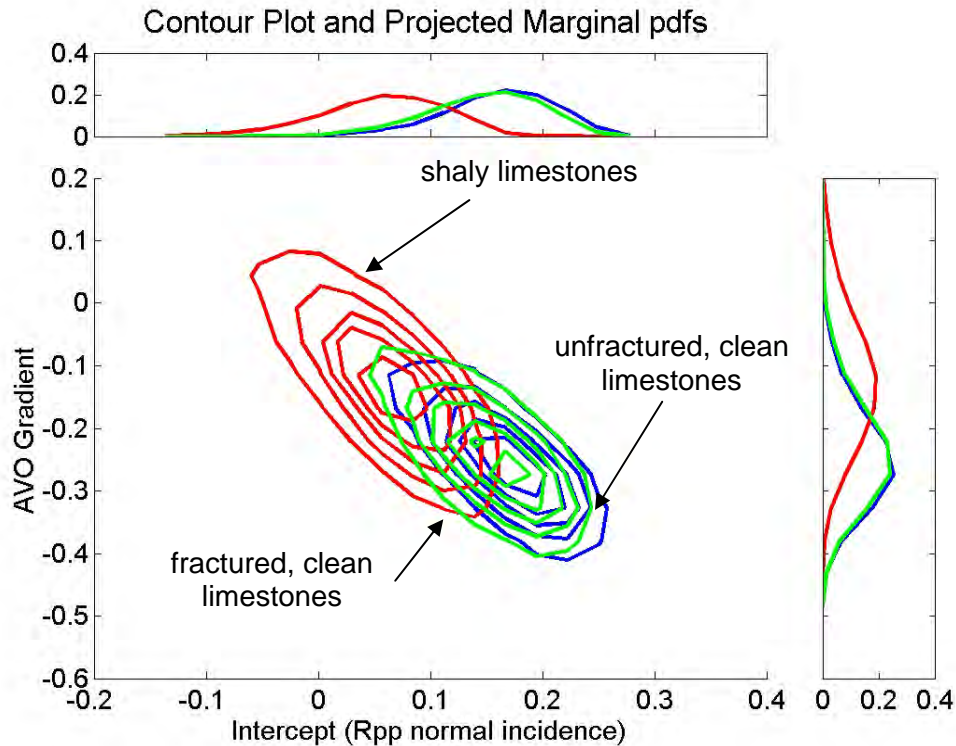
Figure 3.24: Joint probability distribution functions of the AVO Gradient and Intercept for the Monte Carlo simulations of the unfractured, clean limestones (blue), fractured limestones with **randomly oriented** cracks (green), and shaly rocks (red). Fractures are filled with **brine**.

From Figure 3.24 we see that the brine-filled fractured zones are not distinguishable from the unfractured clean limestones in the reservoir, if the fracture orientations are isotropically distributed. The assumption is that there is little fluid communication between the fluid in the fractures and the fluid in the matrix pores, during seismic excitation. This assumption is most appropriate when the matrix porosity and permeability are low, which is the case for the tight, clean limestones intervals in this reservoir.
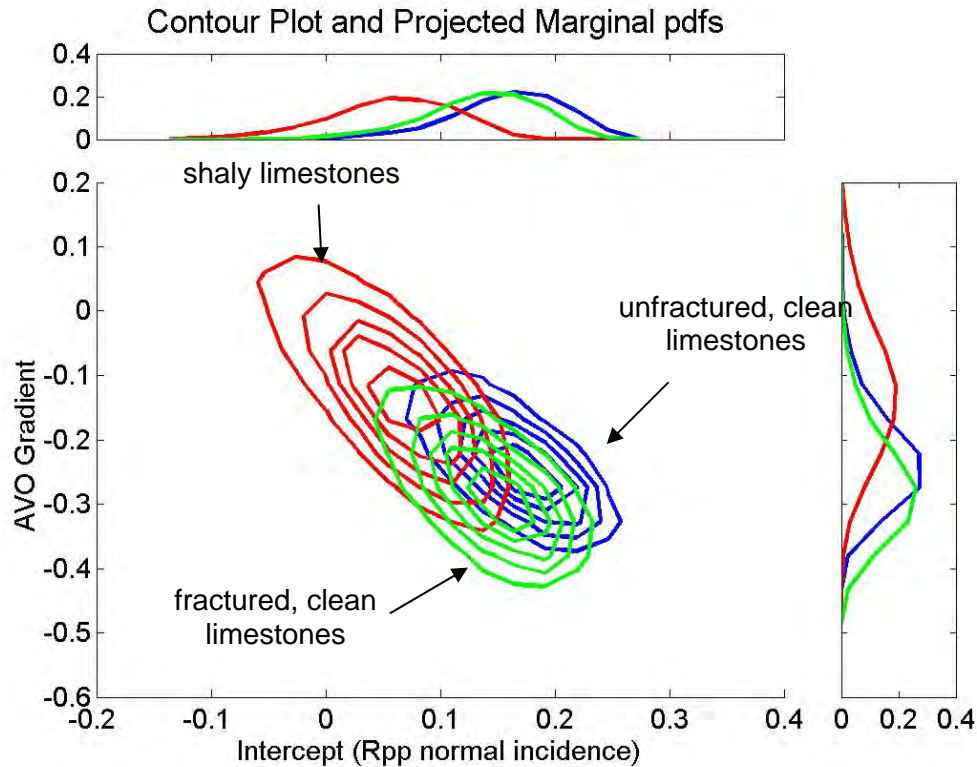
Figure 3.25: Joint probability distribution functions of the AVO Gradient and Intercept for the Monte Carlo simulations of the unfractured, clean limestones (blue), fractured limestones with **a vertical set of cracks** (green), and shaly rocks (red). Fractures are filled with **gas**. The azimuth is **parallel** to the crack's plane.

If we consider the case of vertical aligned fractures, the *AVO gradient* is a function of azimuth. I use Ruger's (1995, 1998) approximation to estimate the *AVO gradient* for the James Limestone reservoir modeled as an HTI medium. Figure 3.25 presents the *AVO gradient* parallel to fractures, while Figure 3.26 shows the *AVO gradient* orthogonal to fractures. The azimuthal variation of the *AVO gradient* for gas-filled fractures is insignificant.

In both cases we observe the same behavior as in the case of a random distribution of fractures filled with gas (Figure 3.23). The azimuthal variation of the *AVO gradient* for gas-filled fractures is small.
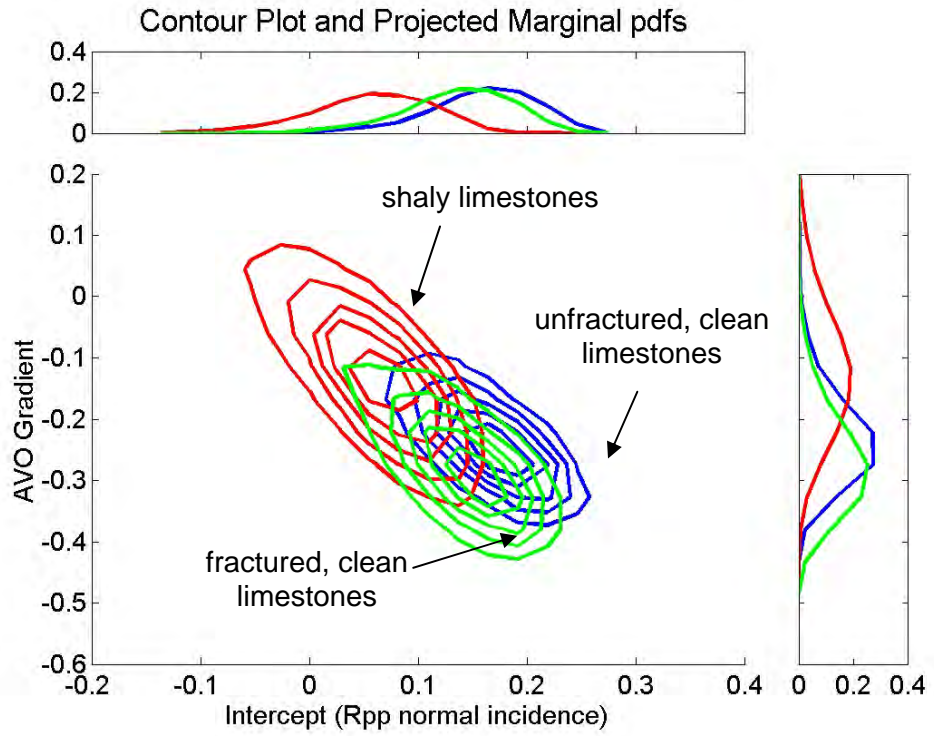
Figure 3.26: Joint probability distribution functions of the AVO Gradient and Intercept for the Monte Carlo simulations of the unfractured, clean limestones (blue), fractured limestones with **a vertical set of cracks** (green), and shaly rocks (red). Fractures are filled with **gas**. The azimuth is **orthogonal** to the crack's plane.
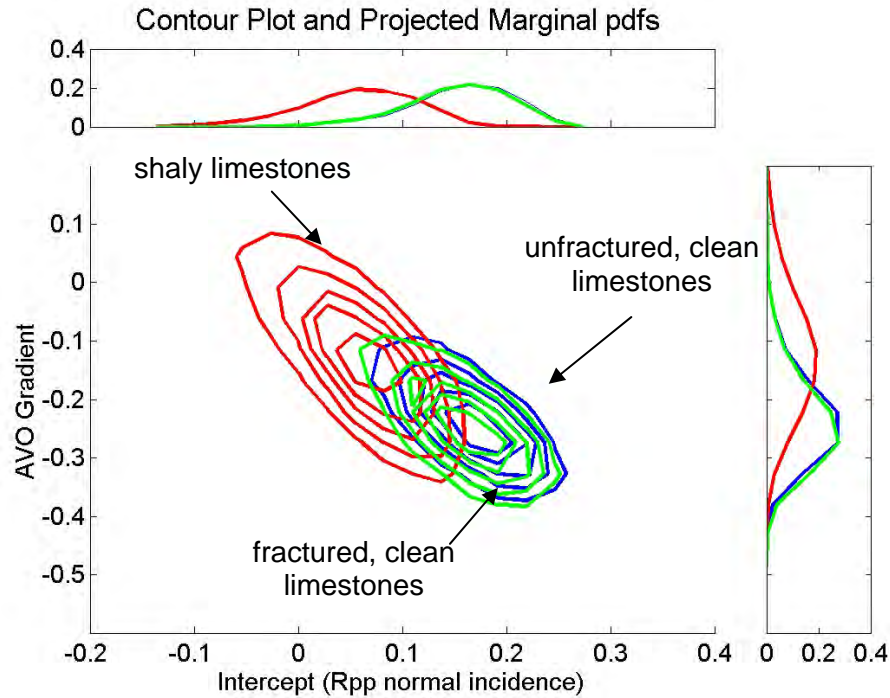
Figure 3.27: Joint probability distribution functions of the AVO Gradient and Intercept for the Monte Carlo simulations of the unfractured clean limestones (blue), fractured limestones with **a vertical set of cracks** (green), and shaly rocks (red). Fractures are filled with **brine**. The azimuth is **parallel** to the crack's plane.

Figures 3.27 and 3.28 show the joint PDF of the *AVO Gradient* and *Intercept* for brine-filled fractures in the directions parallel and orthogonal to fractures, respectively. We see that brine-saturated fractured zones are indistinguishable from the unfractured clean limestones.
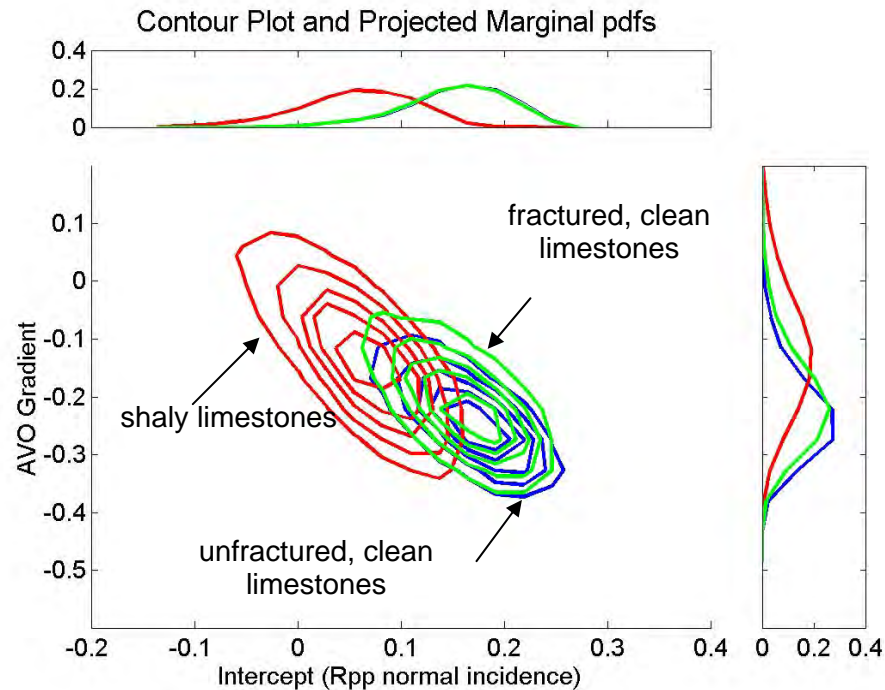
Figure 3.28: Joint probability distribution functions of the AVO Gradient and Intercept for the Monte Carlo simulations of the unfractured, clean limestones (blue), fractured limestones with **a vertical set of cracks** (green), and shaly rocks (red). Fractures are filled with **brine**. The azimuth is **orthogonal** to the crack's plane.

To summarize, brine-filled fractures are difficult to delineate in the *AVO Gradient – Intercept* domain, for both isotropic and anisotropic distributions of fractures. The gas-saturated fractured zones are easier to distinguish from the unfractured clean limestones. Independently of the fracture distribution, the *AVO gradient* of the gas-filled fractured zones has higher negative values than the unfractured clean limestones. The shaly limestones in the reservoir exhibit smaller negative values than the unfractured, clean limestones. Therefore, the *AVO gradient* is a useful attribute for delineating gas-saturated fractures from the shaly limestones in the reservoir. However, due to a larger variability in the seismic properties of the cap rock, there is a significant overlap between the different facies in the reservoir in the interface-attributes domain.

3.4.2.2 AVAZ modeling

For an HTI medium generated by a single set of vertical fractures, amplitude variation with incidence angle and azimuth (AVAZ) can be a useful technique for determining the main fracture orientation. AVAZ may also give us information about fracture density and type of fluid in the fractures. In the modeling I use Ruger's (1995, 1996, 1998) approximation for calculating *PP reflectivity* as a function of offset and azimuth.

Figures 3.29 and 3.30 show the statistical expected values of the *PP reflectivity (R$_{PP}$)* as a function of incidence angle and azimuth, for gas- and brine-saturated fractures, respectively. In both cases the matrix porosity is brine-saturated.
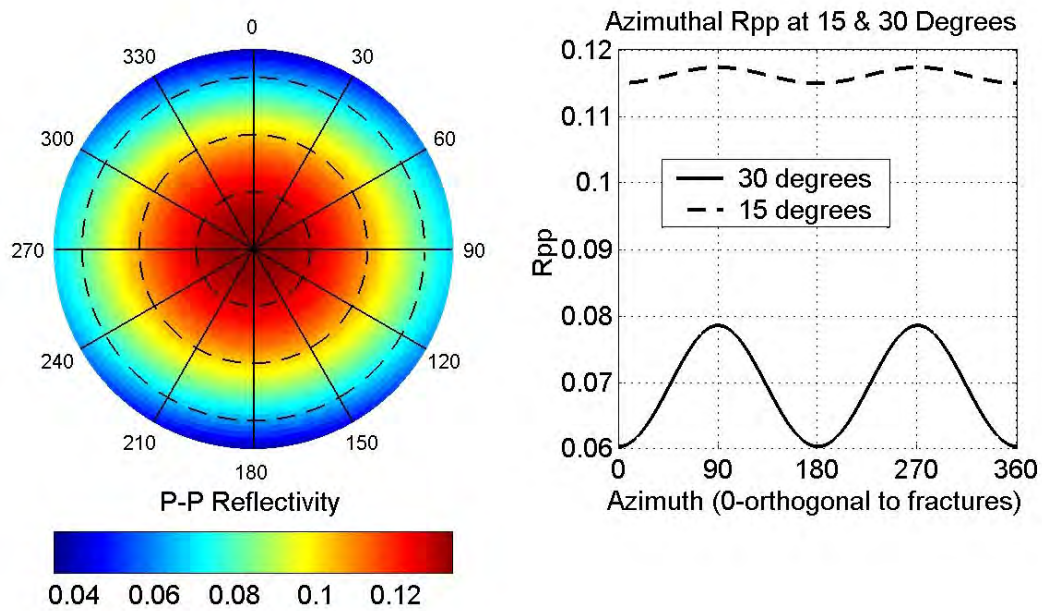
Figure 3.29: Expected values for the *PP reflectivity* as a function of angle of incidence and azimuth. The right side panel presents the *R$_{PP}$* amplitude variation with azimuth at 15 and 30 degree angles of incidence. Azimuth 0 is perpendicular to the fracture plane. Fractures are oriented E-W. Matrix porosity is brine-saturated, while the fractures are filled with **gas**.

The fractures are orientated E-W. The azimuth 0 corresponds to the symmetry axis of the HTI medium, orthogonal to fractures. On the right panels of Figures 3.29 and 3.30 is represented the R_{PP} as a function of azimuth for the 15 and 30 degree angles of incidence.
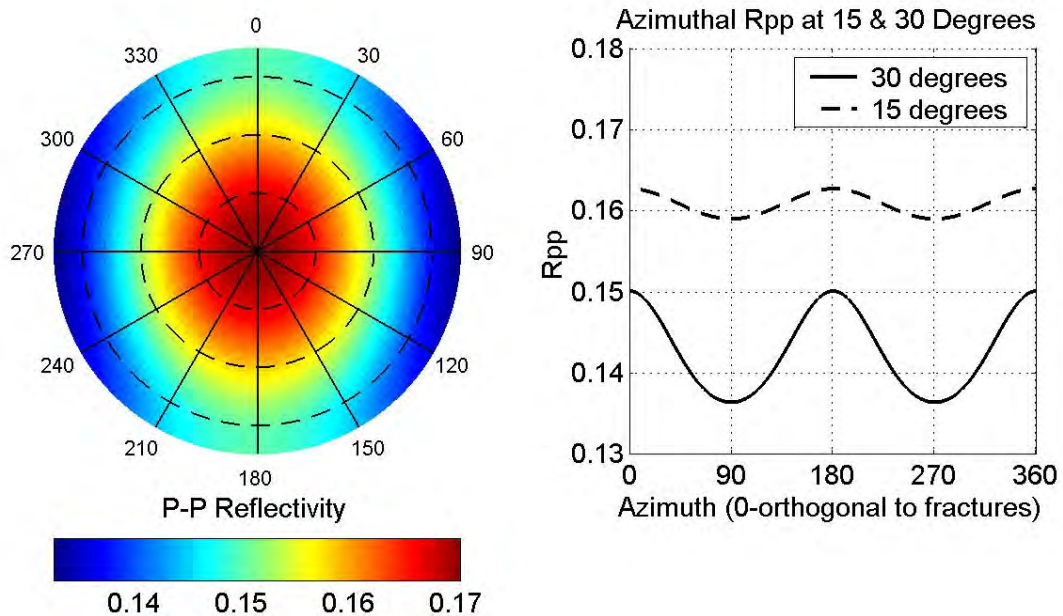
Figure 3.30: Expected values for the *PP reflectivity* as a function of angle of incidence and azimuth. The right side panel presents the R_{PP} amplitude variation with azimuth at 15 and 30 degree angles of incidence. Azimuth 0 is perpendicular to the fracture plane. Fractures are oriented E-W. Matrix porosity is brine saturated, while the fractures are filled with **brine**.

As expected, the azimuthal variation of *PP reflectivity* increases with angle of incidence, for both brine-filled and gas-filled fractures. The main difference between brine-saturated and gas-saturated fractures is that the polarity of the azimuthal variation is opposite. For the brine-filled fractures, the maximum R_{PP} value at a fixed angle of incidence is in the direction perpendicular to fractures, while for the gas-filled fractures the maximum R_{PP} value is in the direction parallel to fractures. This is an interesting result that can be used to differentiate between gas-filled and brine-filled fractures under the assumption that the azimuthal anisotropy is due only to the presence of a vertical set of joints.

3.5 Conclusions

The results of the rock physics analysis, together with the interpreted FMI information about fractures from one of the wells, show that fractures in the James Limestone reservoir are associated with the clean limestone intervals, which have higher velocities and smaller porosities. This association of fractures with the higher-velocity rocks may be used directly in fracture delineation from seismic data. Even if the velocity will be drastically lowered in the most highly fractured zones, on average the velocities of the fractured regions may be larger than the velocities of the unfractured rocks, but with higher shale content. Therefore, an impedance inversion may help in delineating the zones with higher fracture probability. Within each higher-impedance region, more detailed analysis can map the zones of higher fracture density.

As the rock physics analysis of the well log-data shows, the high-velocity rocks, with the least shale content are much more likely to be fractured. This is expected, since the fractures tend to be associated with the more brittle intervals. Therefore, I consider that the reservoir may exhibit three main types of facies: 1) unfractured, clean limestones, 2) shaly limestones, and 3) fractured, clean limestones, which I have modeled with different distributions of cracks. The goal is to find the optimal combination of seismic attributes for distinguishing the gas-filled fractured zones from the shaly and unfractured limestones in the reservoir.

A geologic model for the James Limestone reservoir suggests the presence of fracture swarms associated with small faults. Between these fracture swarms, the reservoir may exhibit regularly spaced vertical joints. Therefore, in the analysis of the fractured James Limestone reservoir I model the cases of both anisotropic and isotropic distribution of fractures. The anisotropic model that I use is a good representation for approximately vertical, parallel joints that create an HTI medium. The isotropic distribution of fractures can be a good approximation for the fractured zone in the vicinity of faults, where the cracks can be oriented randomly, like in a breccia zone.

For each of the hypotheses of isotropic and anisotropic fracture distribution I stochastically model seismic interval and interface properties such as velocities, travel

time, and *PP reflectivity* as a function of angle of incidence and azimuth. By using the stochastic approach we can incorporate natural variability in deterministic physical models.

The modeling shows that all of these seismic attributes may be influenced by the presence of the gas-filled fractures. However, the brine-filled fractures are difficult to distinguish, due to the smaller compressibility in comparison with that of the gas.

The interval velocities decrease with the fracture density. From the modeling we observe that in the V_P-V_S domain the gas-saturated fractures are much more easily distinguishable from the unfractured rocks than are the brine-saturated fractures, in both hypotheses of isotropic and anisotropic fracture distributions.

If the fractures are saturated with gas, modeling shows that the *P*-wave velocity is more sensitive to fractures than the *S*-wave velocity polarized orthogonal and parallel to fracture planes. As expected, the *P*-wave velocity decreases the most when the waves are propagating in the direction orthogonal to a set of aligned cracks. For large crack densities, the V_P of the gas-filled fractured zones becomes comparable to the V_P of the shaly limestones in the reservoir, which are less susceptible to fracture. The *S*-wave velocity decreases less than V_P, and its expected value remains larger than the *S*-wave velocity of the shaly rocks. Therefore, V_S is a valuable piece of information to discriminate between the gas-filled fractured zones and the shaly limestones in the reservoir.

If the fractures are brine-saturated, it is more difficult to distinguish the fractured zones from the unfractured ones. V_P and V_S are little or not at all affected by the presence of the fractures, in both the hypothesis of isotropic and anisotropic distribution of cracks.

In the case of an isotropic distribution for the fracture orientation, the *P*-wave *Impedance - Poisson's ratio* domain is an optimal combination of interval properties for delineating the gas-filled fractured zones in the reservoir. However, if the fractures are saturated with brine, it is difficult to distinguish them from the unfractured, clean limestones.

The travel time can be also influenced by the presence of fractures. However, for the James Limestone reservoir the travel time difference between the fractured and the unfractured cases is very small, due to the fact that the reservoir is too thin.

For the interface properties, the *AVO Gradient - Intercept* domain is a potentially useful combination for discriminating gas-filled fractures in the reservoir. However, due to a large variability in the seismic properties of the cap rock, the uncertainty in differentiating fractured zones from interface properties is a little higher than from interval properties, such as *P-Impedance* and *Poisson's Ratio*. As the fracture density increases, the *PP reflectivity* from the fractured zones decreases, and becomes closer to the *PP reflectivity* from the shaly limestones in the reservoir. The *AVO gradient* can help resolve this ambiguity. Modeling shows that the shaliness moves the *AVO gradient* to smaller negative values as compared to the clean, unfractured limestones, while the fractures filled with gas move the *AVO gradient* to larger negative values as compared to the clean, unfractured limestones. Therefore, the *AVO gradient* can help in better separating the gas-filled fractured zones from the shaly zones in the reservoir.

Brine-saturated fractures are difficult to distinguish also in the *AVO Gradient - Intercept* domain.

In the hypothesis of a nearly vertical set of joints, I also model the Amplitude Variation with Angle of Incidence and Azimuth (AVAZ). The azimuthal variation depends on the fluid type. In the assumption of little fluid communication between fractures and matrix porosity during a seismic period, the gas-filled fractures and brine-filled fractures have opposite azimuthal polarity. For the brine-saturated fractures, the maximum *PP reflectivity* value, at a fixed angle of incidence, is in the direction perpendicular to fracture strike, while for the gas-saturated fractures the maximum *PP reflectivity* value is in the direction parallel to fracture planes. This result can be used to differentiate between gas-filled and brine filled-fractures for a vertical set of joints. However, if we do not have additional geological information about the orientation of the main fracture system, the different responses in the azimuthal variation of the amplitudes due to fluids bring more ambiguity in determining the fractures' strike.

In summary, rock physics fracture modeling and stochastic simulations for seismic attributes of the James Limestone reservoir provide a framework for delineating fractured zones from seismic data, and for estimating the uncertainty in fracture characterization due to natural variability.

Chapter 4

3D Seismic data: Analysis of the Azimuthal Variation of Reflectivity

4.1   Abstract

Aligned vertical fractures can produce elastic anisotropy in the shallow crust that can be observed in seismic data, such as amplitude variation with angle of incidence and azimuth (AVAZ). AVAZ can be a useful technique that can give information about the fracture orientation, fracture density, and sometimes the type of fluid in the fractures.

In this chapter, I present the analysis of the *PP* reflectivity from a 3D seismic data set acquired over a fractured carbonate reservoir in East Texas, with the final goal of determining the orientations of the fractures and the relative intensity of fracturing.

I compare the results of the rock physics fracture modeling for AVAZ, based on the well-log data, with the seismic observations. Fracture modeling shows that the polarity of the azimuthal variation of the reflectivity changes with the fluid and fracture compressibility. Therefore, rock physics modeling is a key link between the observed seismic amplitude variation with azimuth (observable parameter) and the actual fracture parameters, such as fracture strike and density. Based on the results of the rock physics

modeling, I derive the mean fracture orientations from the seismic data using a bootstrap method. By using this technique, I quantify the uncertainty in fracture orientation due to the possible measurement errors.

I find a good agreement between the fracture orientation derived from the azimuthal variation of the seismic amplitudes at far offsets and the fracture orientation derived from the FMI logs from the nearby wells. There is also a good agreement between the mean fracture strikes from the azimuthal variation in the seismic amplitude and the present regional stress field. The mean fracture strike is approximately parallel to the maximum horizontal stress in the region.

From the seismic data, I also derive the map of the azimuthal anisotropy for the *PP* reflectivity at the top of the reservoir. The degree of anisotropy represents a measure of the relative degree of fracturing, if the cracks are gas-saturated.

In this chapter, I also emphasize the impact of the acquisition footprint on the seismic amplitudes. For this 3D seismic survey the fold is not uniform and it creates artificial stripes of low and high amplitudes that vary with both offset and azimuth. This footprint can mask the actual signatures of fractures. Therefore, to interpret the variations of the reflectivity with offset and azimuth in terms of fracture distribution, we first need to suppress this footprint. In this chapter, I show how increasing the bin size of the regular grid used for analyzing the seismic data gradually diminishes the acquisition footprint. However, this comes at the expense of the spatial resolution.

4.2   Introduction

Most of the seismic field studies for fracture detection have as targets, vertical and open joints (Grimm and Lynn, 1997, Teng, 1998; Grimm et al, 1999; Perez et al, 1999; Lynn et al., 1999). A single set of vertical, parallel fractures embedded in an isotropic background can be described using a transversely isotropic model with a horizontal axis of symmetry (HTI).

Earlier research on HTI media was focused on the propagation of shear-waves, due to their sensitivity to the direction and the amount of fracturing. More recently, *P*-wave

methods for fracture detection have attracted considerable interest. *P*-wave methods offer several advantages, such as decreased cost and increased data quality. Moreover, *P*-wave data are sensitive to fluids, unlike the *S*-wave data that contain information mainly about the rock frame.

One of the *P*-wave methods for fractures developed in the recent years is the Amplitude Variation with Offset (AVO). For aligned, vertical fractures the *P*-wave AVO response is azimuthally dependent. The azimuthal variations in the *P*-wave reflections have been observed in field data by different authors, such as Lynn, (1996), Mallick et al. (1998), Teng (1998), Perez et al. (1999), Shen et al. (2002). One important advantage of this method is that it can provide localized information at the interface of interest, unlike the travel time methods, which describe the cumulative effect over larger scales. Also, if the reservoir is thin, travel time techniques are not very useful for fracture characterization, as I showed in the preceding chapter.

The reservoir in our study area is approximately 7000 ft deep, and has an average thickness of 200 ft. The formation is a microcrystalline fractured limestone, with matrix permeability between 0.001 and 0.1 mD (Marathon Oil Co., Internal Report). However, the presence of fractures may significantly increase the permeability. Therefore, precise localization of fractured zones has a crucial impact on reservoir management.

The area of study is situated in a normal faulting regime. The maximum horizontal stress in the region is oriented E-W. In such regime, the strike of the faults is expected to be approximately parallel to the maximum horizontal stress. A geological model based on the logs from a horizontal well suggests that the fractures are controlled by subseismic normal faults (Meeder, personal communication). These small faults can generate narrow zones with high fracture density, where the cracks are more or less randomly oriented, as in brecciated zones. Between these fracture swarms, there may be vertical joints, more uniformly distributed. The rock physics fracture modeling predicts low *PP* reflectivity values associated with the fracture swarms (Sava et al., 2002), as I present in Chapter 3. These low reflectivity zones may be identified in the seismic data.

In this chapter, I present the analysis of the *PP* reflectivity from a 3D seismic data set acquired over this reservoir. The focus is on the Amplitude Variation with Azimuth

(AVAZ) in the hypothesis of a single set of vertical aligned fractures. AVAZ involves partial stacking the data on different ranges of azimuth. There is a tradeoff between the azimuthal resolution, which requires small ranges of azimuths, and the signal-to-noise ratio, which requires larger fold, and implicitly larger azimuth ranges. However, we can increase the fold either by considering larger azimuth bins (which diminishes the azimuthal resolution), or by considering larger spatial bins (which lowers the spatial resolution).

The acquisition footprint of the survey significantly impacts the reflectivity. The fold is not uniform and creates artificial stripes of low and high amplitudes that vary with both offset and azimuth. This footprint can mask the actual signatures of fractures. In this chapter, I investigate the influence of increasing the spatial bin size on reducing the survey footprint, such that the amplitude variations can be interpreted in terms of fracture distribution.

I also present the results of the rock physics fracture modeling for AVAZ, based on the well-log data, and I compare them with the seismic observations. The fracture modeling shows that the interpretation of the azimuthal variation of the *PP* reflectivity depends on both the compressibility of the fractures and of the fluids filling the fractures.

Based on the results of the rock physics fracture modeling, I derive the mean fracture orientations at the top of the reservoir from the azimuthal variation of the seismic amplitudes at far offsets. I use a bootstrap method that takes into account the possible measurement errors.

I also present the distribution of the azimuthal anisotropy of the *PP* reflectivity at the top of the reservoir derived from the seismic data. As the rock physics fracture modeling shows, the degree of reflectivity anisotropy may be a measure of the relative degree of fracturing, in the case of uniformly saturated fractures.

4.3 3D Seismic survey and the acquisition footprint

A 3D seismic data set was acquired over a fractured carbonate reservoir in East Texas. The source and receiver locations are presented in Figure 4.1. In Figure 4.1, as well as in all of the other figures showing the seismic data, the actual survey is rotated 34 degrees East with respect to North, for the purpose of display.
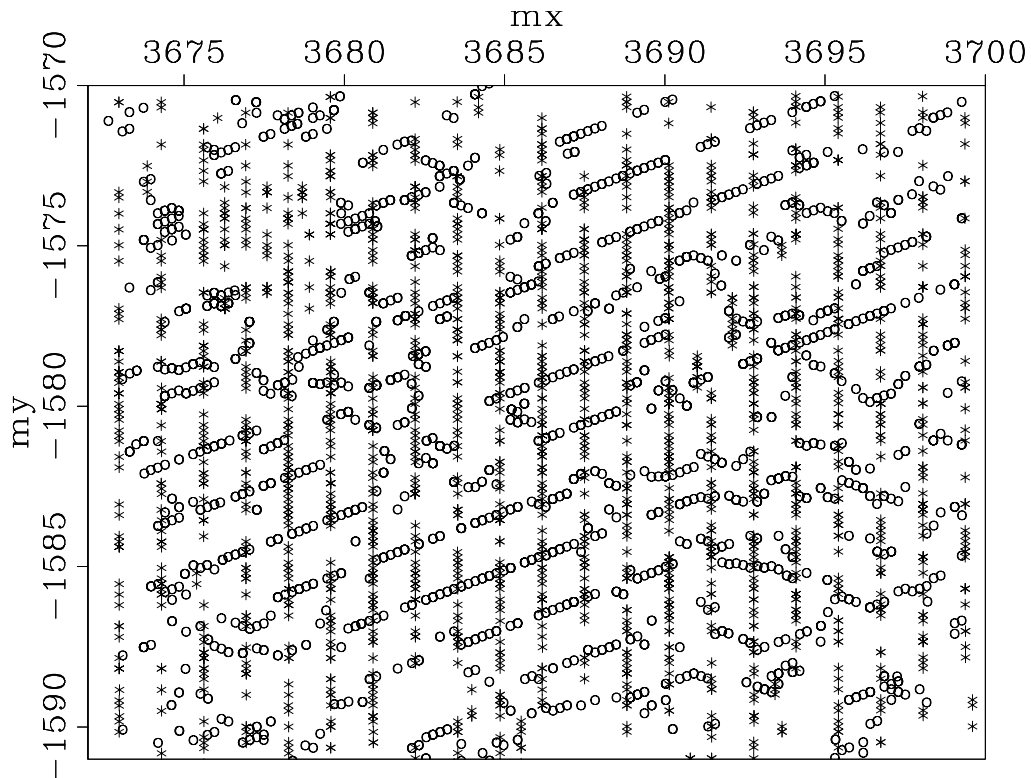
Figure 4.1: Map view with the source (open circles) and receiver (stars) locations. The survey is rotated 34 degrees East with respect to North.

From this acquisition geometry we can get a map of mid-point locations. Figure 4.2 presents a sub-sample of the mid-point positions.
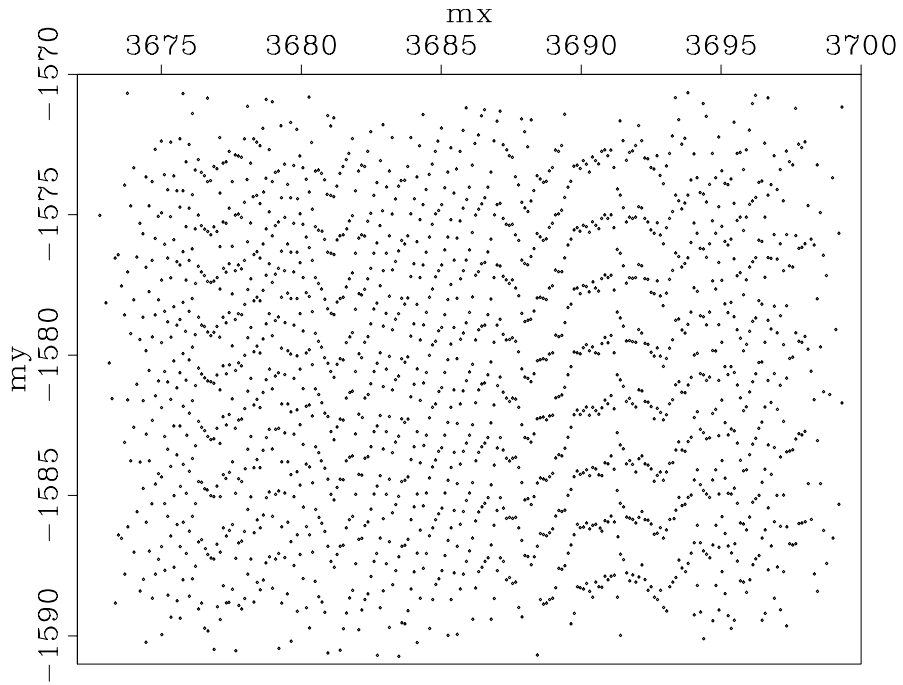
Figure 4.2: Map view with a sub-sample of the midpoint locations. The survey is rotated 34 degrees East with respect to North.
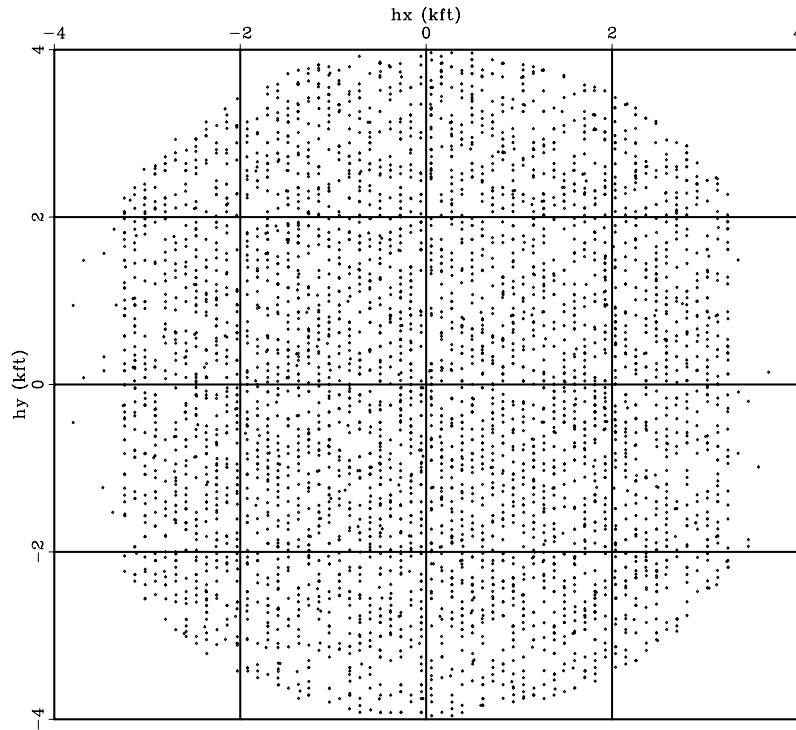
Figure 4.3: Scatter-plot with the x and y components of the offset vector for every 200th trace of the data set. The survey is rotated 34 degrees East with respect to North.

Figure 4.3 shows a scatter-plot with the x and y components of the offset vector, for every 200th trace of the dataset. The plot shows a wide azimuth acquisition, with a relatively uniform distribution, displaying no obvious preferential orientation of the acquisition with respect to azimuth.
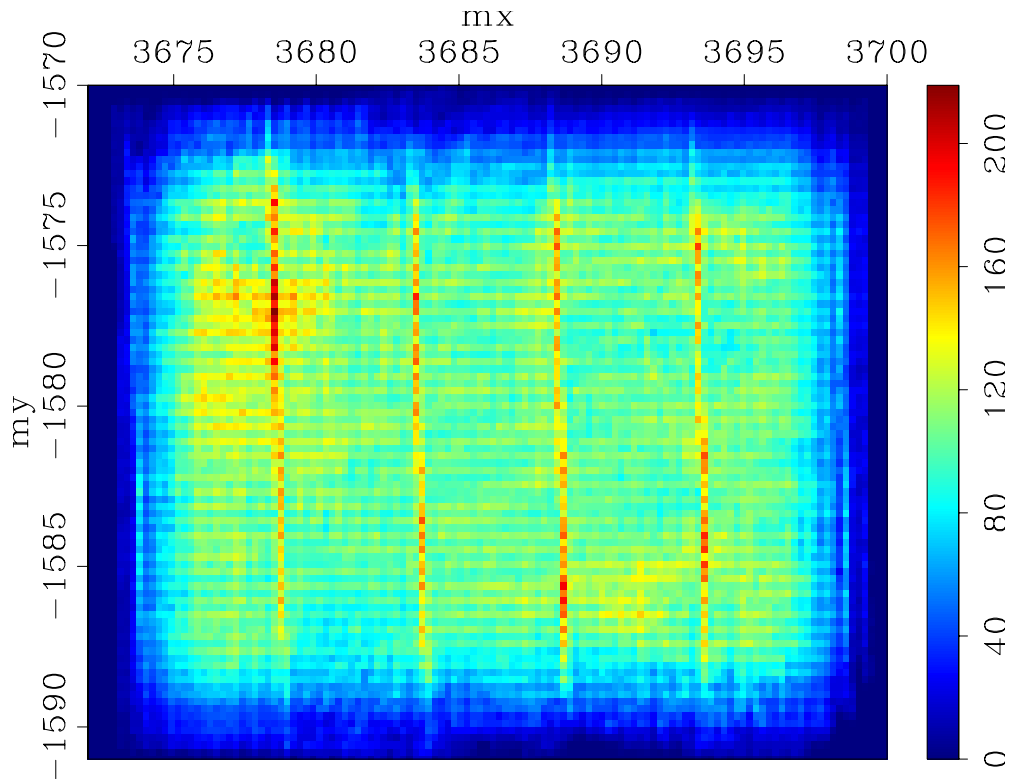
Figure 4.4: Map view with the fold for the stack data (**200ft bin size**).

Analysis of the reflectivity variations with offset and azimuth requires seismic data arranged on a regular grid. I first choose a small bin size equal to 200 ft. The corresponding fold map for the stack data of all azimuths and offsets is presented in Figure 4.4. We can see alternating parallel stripes of low and high fold along some of the receiver lines. This pattern can be misleading, especially when analyzing amplitude data.

Figures 4.5 and 4.6 show the impact of the acquisition footprint on the *PP* reflectivity maps for two different azimuth ranges of 60 degrees each, one centered about azimuth 0º, the other centered about azimuth 60º. The data are stacked for all offsets, between 0 and 8000 ft. The top panels of Figures 4.5 and 4.6 show the amplitude maps at 1.2 seconds, while on the bottom panels I present the amplitude maps at 1.3 seconds, corresponding to the top of the reservoir. The corresponding fold maps are presented on the top-right

panels in each figure, while the acquisition geometry for the survey is presented on the bottom-right panels. The left panels of both figures show the amplitude maps un-normalized by the fold, while the middle panels show the amplitude maps normalized by the fold.

By comparing Figures 4.5 and 4.6 we can see that the pattern of low and high seismic amplitude values varies with the azimuth, as the fold pattern changes. Normalizing the amplitude values by fold does not completely suppress the acquisition footprint.
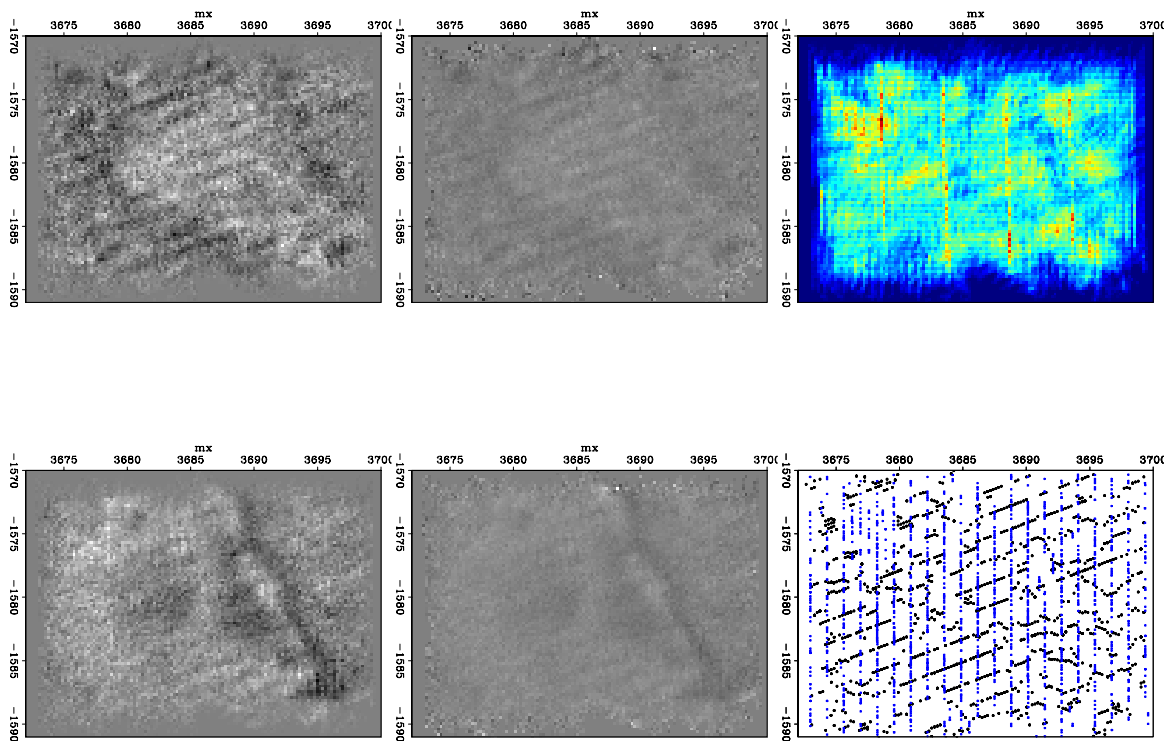
Figure 4.5: Amplitude maps for two time slices at 1.2 seconds (top) and 1.3 seconds (bottom) for an azimuth bin of 60 degrees, **centered about azimuth 0º**.Left panels show the un-normalized reflectivity maps. Centered panels show the corresponding reflectivity maps normalized by fold. Top right panel shows the fold map for the chosen azimuth range. Bottom right panel shows the acquisition geometry.
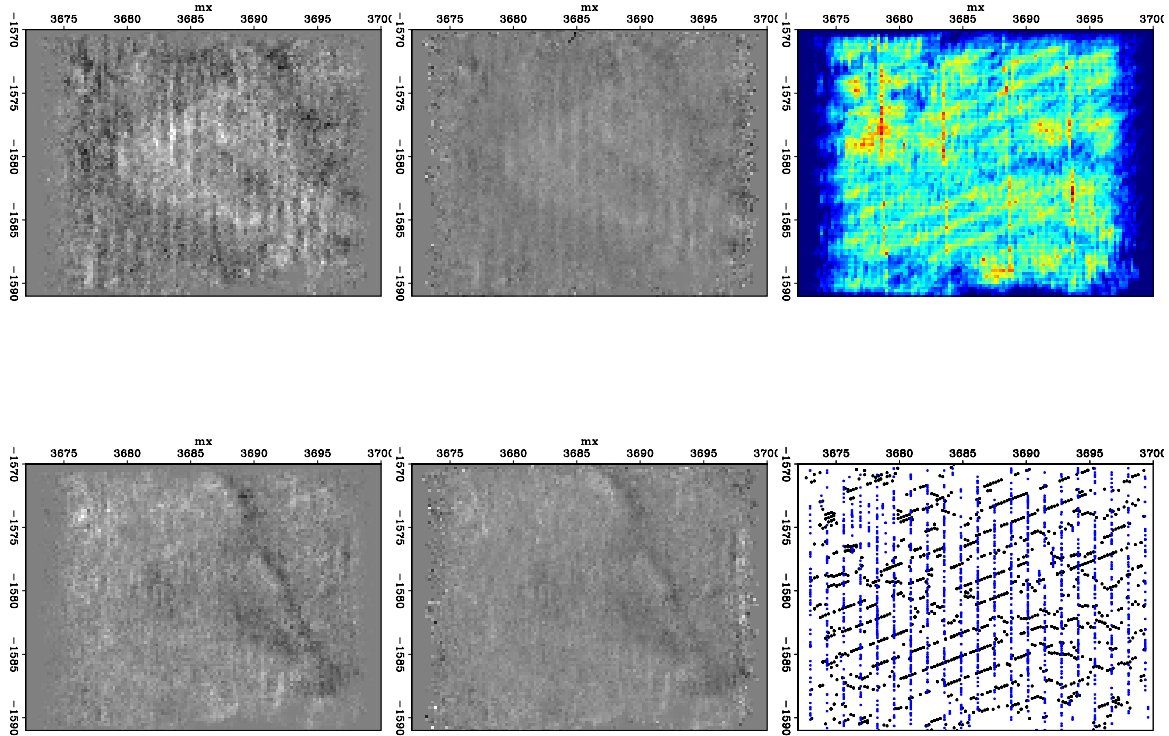
Figure 4.6: Amplitude maps for two time slices at 1.2 seconds (top) and 1.3 seconds (bottom) for an azimuth bin of 60 degrees, **centered about azimuth 60º**.Left panels show the un-normalized reflectivity maps. Centered panels show the corresponding reflectivity maps normalized by fold. Top right panel shows the fold map for the chosen azimuth range. Bottom right panel shows the acquisition geometry.

The structural geological model suggests the presence of fracture swarms in the proximity of the normal subseismic faults (Meeder, personal communication). Rock physics modeling shows decreased amplitudes associated with the gas-filled fractured zones in the reservoir (Sava et al, 2002). Therefore, we should expect to observe low *PP* reflectivity values on the 3D seismic data set, aligned with the possible subseismic faults. However, the acquisition footprint artificially creates alternating alignments of high and low amplitudes due to the alternating high and low folds along the sources and receiver lines (Figures 4.5 and 4.6). Therefore, to interpret the variations in reflectivity with offset and azimuth in terms of fracture distribution, we first need to eliminate this footprint.

To reduce the acquisition footprint, I choose to keep the azimuthal bins constant and change the spatial bin sizes. The next section shows how increasing the bin size reduces the acquisition footprint of the survey.

4.4   3D Seismic data processing for reflectivity analysis

In this section, I present the main processing steps of the 3D seismic data. The goal is to eliminate the survey footprint, such that the amplitude variations with offset and azimuth may be interpreted in terms of fracture orientation and relative degree of fracturing.

The data had refraction statics applied, and they were NMO corrected by Marathon Oil. Co. I initially binned the data into small bins of 200 ft size, as presented in the figures from the preceding section.

For a reliable azimuthal analysis of the *PP* reflectivity, I partially stack the data on relatively small azimuthal ranges of 20 degrees. In the ideal case of full coverage for all azimuth ranges, we get nine reflectivity values at each spatial bin location, corresponding to the 9 different azimuthal ranges. However, for small bin sizes, the azimuthal coverage is very low. We can increase the fold at each grid location by increasing the spatial bin size, while keeping the azimuthal ranges constant. There is a tradeoff between the spatial resolution, which requires small bin sizes, and the signal-to-noise ratio, which requires larger bin sizes. Ideally, we want to obtain the smallest grid size for which we get a more uniform distribution of the fold over the survey for each azimuthal range, and also a larger signal-to-noise ratio at each bin location.

Alternatively, for a fixed bin size we can increase the fold by increasing the azimuthal range. For 60º azimuthal bins, we expect a larger fold and consequently a larger signal to noise ratio than for smaller azimuthal bins of 20º. However, in this case we considerably diminish the resolution in the azimuthal variation of the *PP* reflectivity, and implicitly we reduce from our ability to determine accurately the fracture orientations.

Figure 4.7 shows a conceptual sketch of the competing effects between the spatial and azimuthal resolutions, and the fold. The curves represent schematic lines of constant fold, and emphasize the fact that we can obtain approximately the same fold by either increasing the spatial bin size and decreasing the azimuthal range (consequently decreasing the spatial resolution, while increasing the azimuthal resolution), or alternatively, by increasing the azimuthal range and decreasing the spatial bin size

(consequently decreasing the azimuthal resolution, while increasing the spatial resolution). The fold increases with both azimuthal range and spatial bin size.
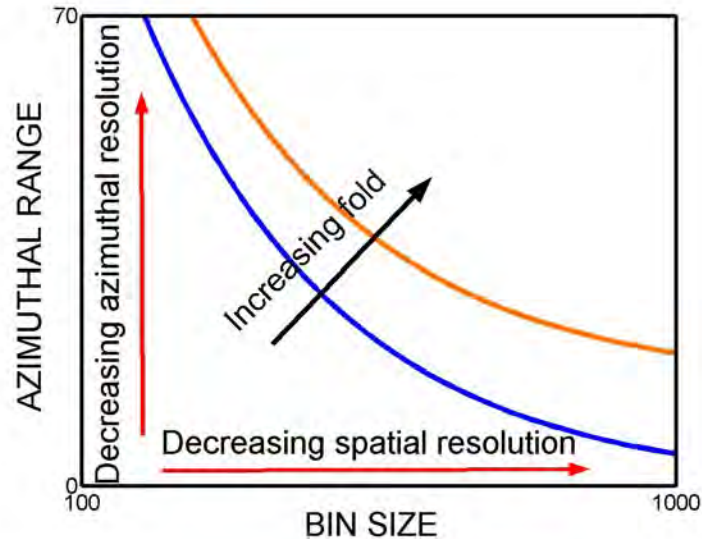
Figure 4.7: Conceptual variation of the fold with the azimuthal bin size and the spatial bin size. We can keep the fold approximately constant either by increasing the bin size and decreasing the azimuthal range (consequently decreasing the spatial resolution, while increasing the azimuthal resolution), or by decreasing the bin size and increasing the azimuth range (consequently increasing the spatial resolution, while decreasing the azimuthal resolution). The fold increases with both azimuthal and spatial bin sizes.

In this section, I present the analysis of the fold, and the corresponding amplitude maps, with increasing spatial bin sizes, at fixed azimuthal range. The goal is to determine the optimal grid dimension for which the acquisition pattern is significantly reduced.

At fixed spatial bin size, the fold varies with azimuth, as well as offset. For each of the spatial bin sizes considered, I partially stack the data for the near-offsets (0 –3000 ft) and for the far-offsets (4000-8000 ft). For each of the near- and far-offset stacks, I additionally sort the data and partially stack them on 9 different azimuth ranges of 20 degrees each.

Figure 4.8 shows the seismic amplitudes and the corresponding fold maps for the far-offset stack (top panels), and for the near-offset stack (bottom panels), at a time slice corresponding to the top of the reservoir. The size of the spatial bins is 200 ft. The azimuthal range is 20 degrees, centered about azimuth 20º. The left panels present the un-

normalized amplitude maps, while the middle panels present the amplitude maps normalized by the fold. We can observe a strong acquisition pattern on both near- and far-offset stacks for this azimuthal range.
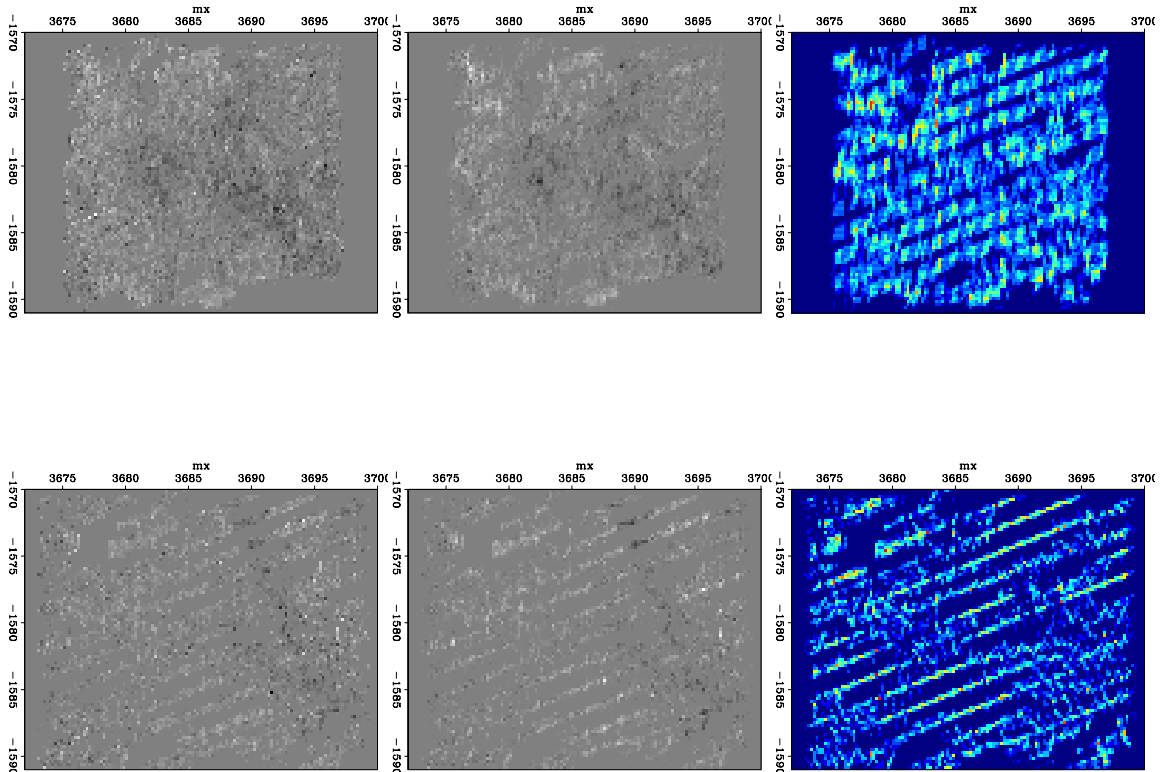
Figure 4.8: **200 ft bin size**. Amplitude maps for a time slice at 1.3 seconds for the far - offset stacks (top panels) and the near-offset stacks (bottom panels) with their corresponding fold maps (right panels). Left panels: amplitudes un-normalized by fold. Middle panels: amplitudes normalized by fold. Azimuth centered about 20º.

Figure 4.9 is similar with Figure 4.8, but corresponds to another azimuth range, centered at azimuth 80º. Comparing Figures 4.8 and 4.9, we can see that the fold maps change with the azimuth for both far and near offsets, as expected. The seismic amplitude maps also change with the azimuth.

For a small bin size of 200 ft, the azimuthal coverage is very low. For the specified ranges of azimuth and offsets, there are numerous bins that do not have any data. Furthermore, even for the bins that have data, the fold is very small, and therefore the

signal-to-noise ratio is not satisfactory to confidently interpret any seismic amplitude variations.
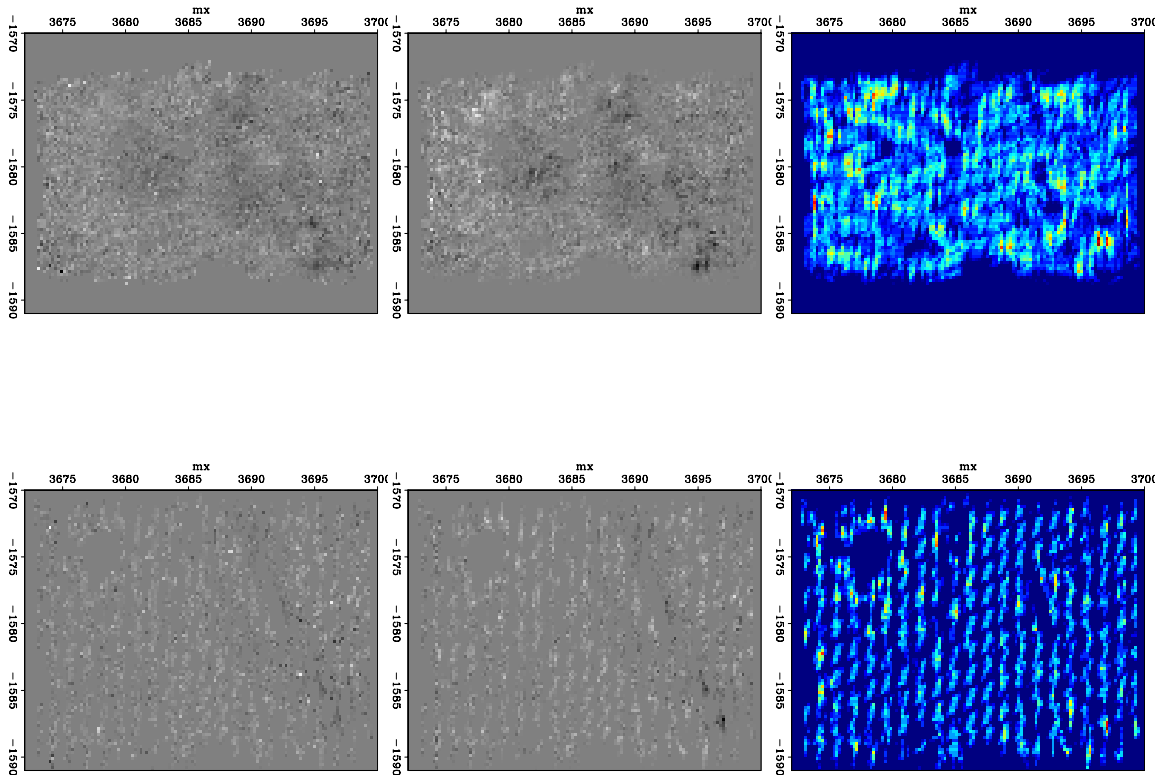
Figure 4.9: **200 ft bin size**. Amplitude maps for a time slice at 1.3 seconds for the far-offset stacks (top panels) and the near-offset stacks (bottom panels) with their corresponding fold maps (right panels). Left panels: amplitude un-normalized by fold. Middle panels: amplitude normalized by fold. Azimuth centered about 80º.

Next, I double the grid size, and repeat the analysis of the fold for the same ranges of azimuths and offsets. Figure 4.10 shows the fold map for all of the azimuths and offsets taken together, using bins of 400 ft. The acquisition footprint is not yet eliminated, although the fold increases, as compared to the case of 200 ft bin size (Figure 4.4).

However, from Figure 4.11 we can see that, for a grid size of 400 ft, the azimuthal coverage is still low. There are many bins that do not have any data for the specified ranges of azimuths and offsets. The acquisition footprint is still visible on the fold maps for the near- and far-offset stacks, corresponding to the range of azimuth centered about 80º.
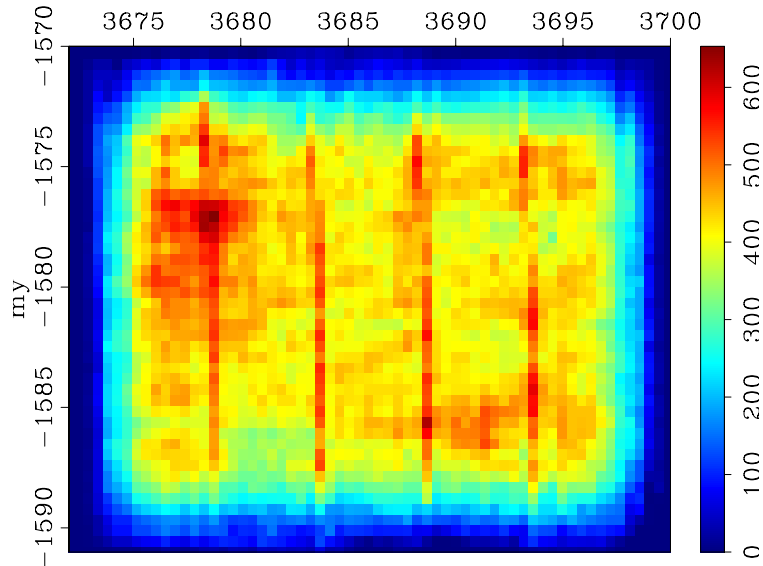
Figure 4.10: Map view with the fold for the stack data (**400 ft bin size**).
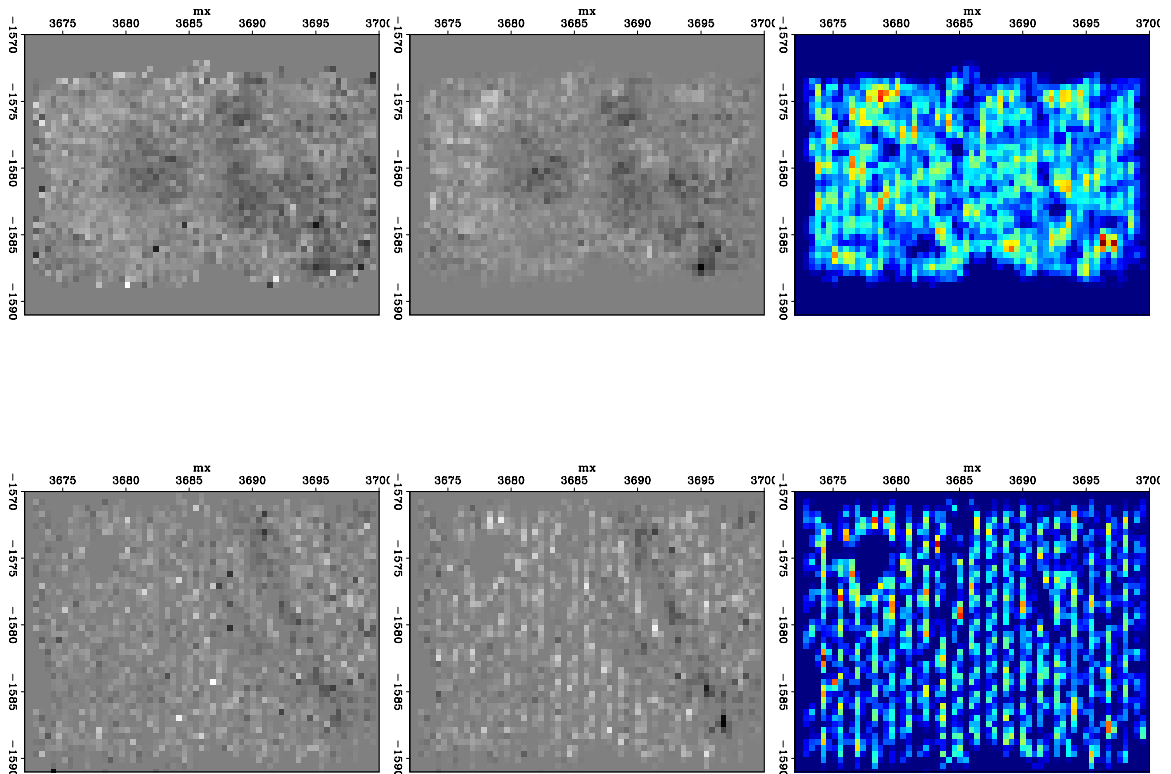
Figure 4.11: **400 ft bin size**. Amplitude maps for a time slice at 1.3 seconds for the far - offset stacks (top panels) and the near-offset stacks (bottom panels) with their corresponding fold maps (right panels). Left panels: amplitude un-normalized by fold. Middle panels: amplitude normalized by fold. Azimuth centered about 80º.

Figure 4.12 shows the fold map corresponding to superbins of 800 ft, for all offsets and azimuths. We can still observe the acquisition footprint at this large superbin size. However, as Figure 4.13 shows, the fold map for the far-offset stack corresponding to an azimuthal range of 20 degrees, centered about 80º, becomes more uniform than those corresponding to the smaller bin sizes. Therefore, I determine that, for a reliable azimuthal analysis of the reflectivity from this 3D seismic survey, the superbin size should be at least 800 ft, to get a satisfactory fold for the specified offset and azimuths ranges, for most of the grid points.
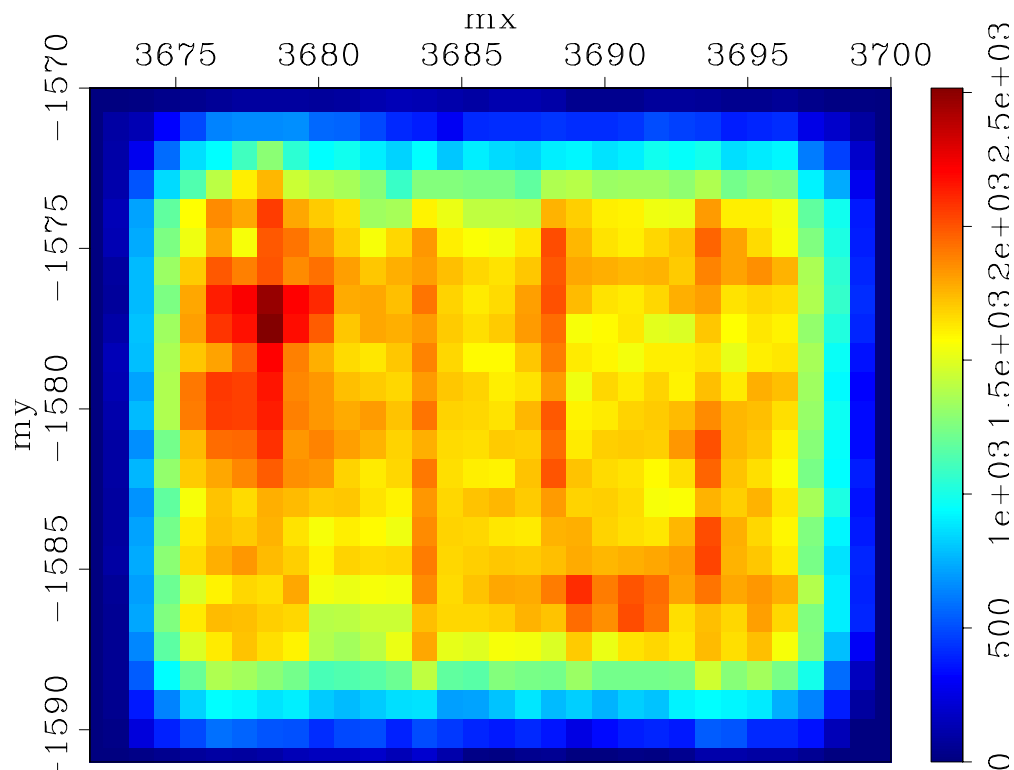
Figure 4.12: Map view with the fold for the stack data (**800 ft bin size**).

For completeness, I also consider superbins of 1600 ft. The corresponding fold map for all azimuths and offsets is presented in Figure 4.14. The fold map shows a much more uniform distribution over the survey. The acquisition footprint is eliminated at this superbin size. However, by using bins of 1600 ft size, we lose significantly on the spatial resolution.
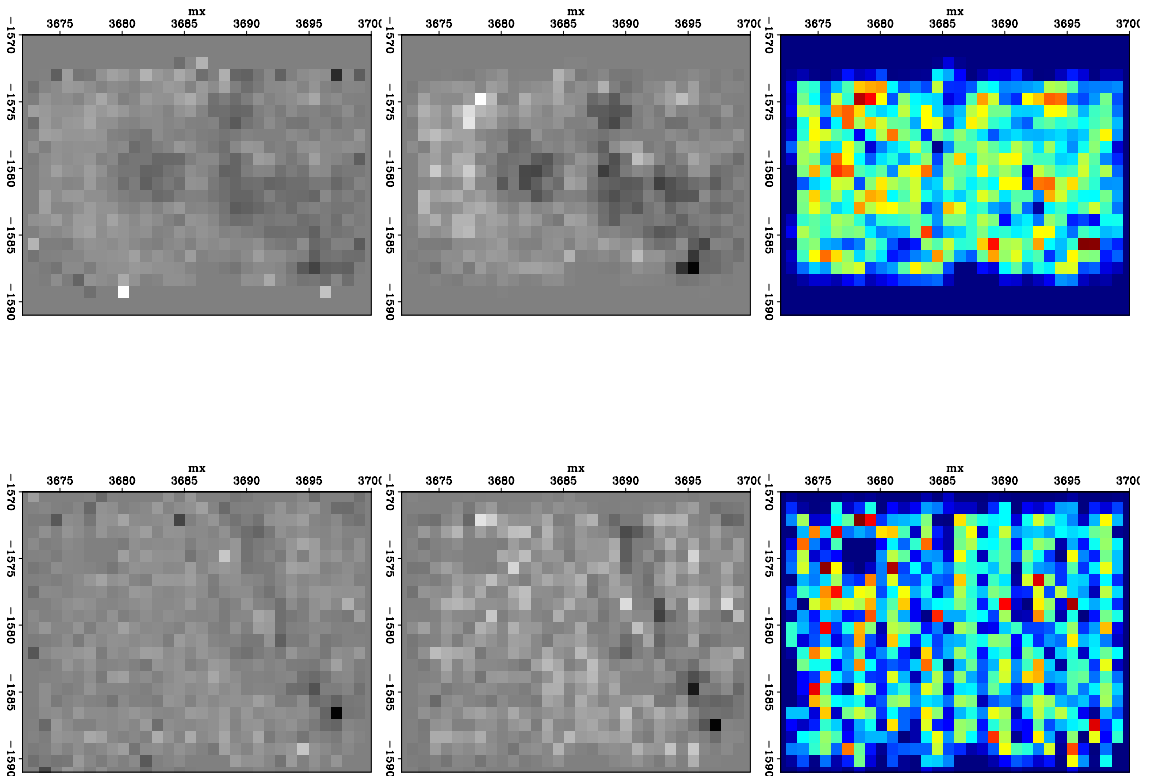
Figure 4.13: **800 ft bin size**. Amplitude maps for a time slice at 1.3 seconds for the far - offset stacks (top panels) and the near-offset stacks (bottom panels) with their corresponding fold maps (right panels). Left panels: amplitude un-normalized by fold. Middle panels: amplitude normalized by fold. Azimuth centered about 80º.
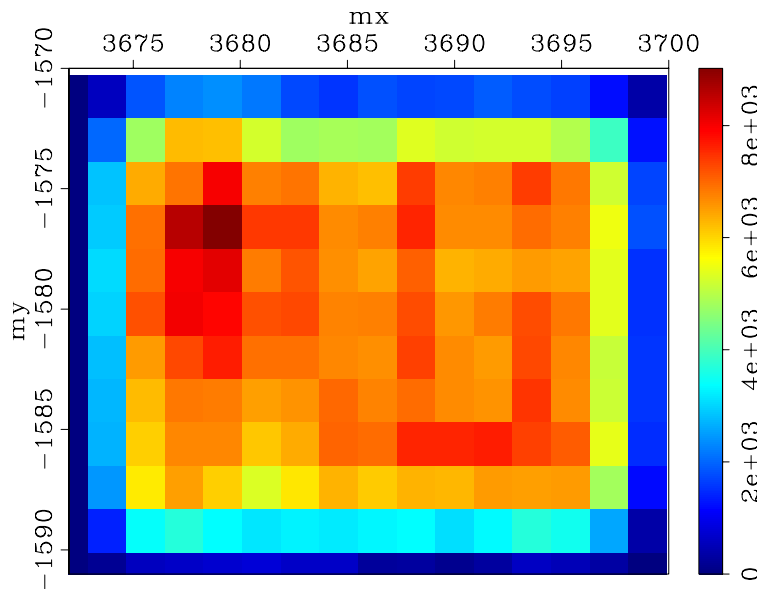
Figure 4.14: Map view with the fold for the stack data (**1600 ft bin sizes**).
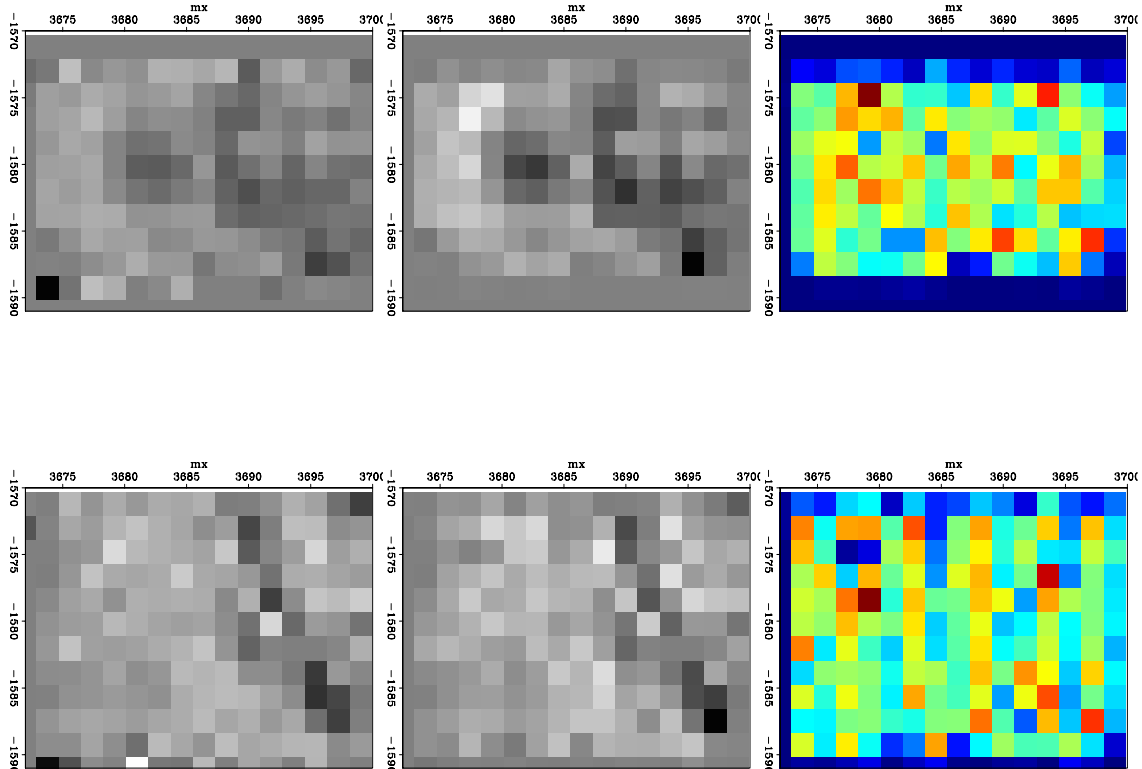
Figure 4.15: **1600 ft bin size**. Amplitude maps for a time slice at 1.3 seconds for the far -
offset stacks (top panels) and the near-offset stacks (bottom panels) with their
corresponding fold maps (right panels). Left panels: amplitude un-normalized by fold.
Middle panels: amplitude normalized by fold. Azimuth centered about 80º.

Figure 4.16 shows the amplitude maps at the top of the reservoir for the far-offset
stack, summed over all of the azimuths, for each of the bin sizes considered. We observe
the significant loss in spatial resolution due to increasing spatial bin size.

In conclusion, by increasing the spatial bin size, I reduce the influence of the
acquisition footprint, and I also increase the signal-to-noise ratio, by increasing the fold at
each superbin. However, the spatial resolution is diminished, as we can see in Figure
4.16, and therefore the ability to precisely localize possible fracture swarms is also
reduced.

From the analysis presented in this section, I consider that for this 3D seismic survey,
the superbin size should be at least 800 ft at 20º azimuthal ranges to make a reliable
interpretation of the *PP* reflectivity variation with offset and azimuth.
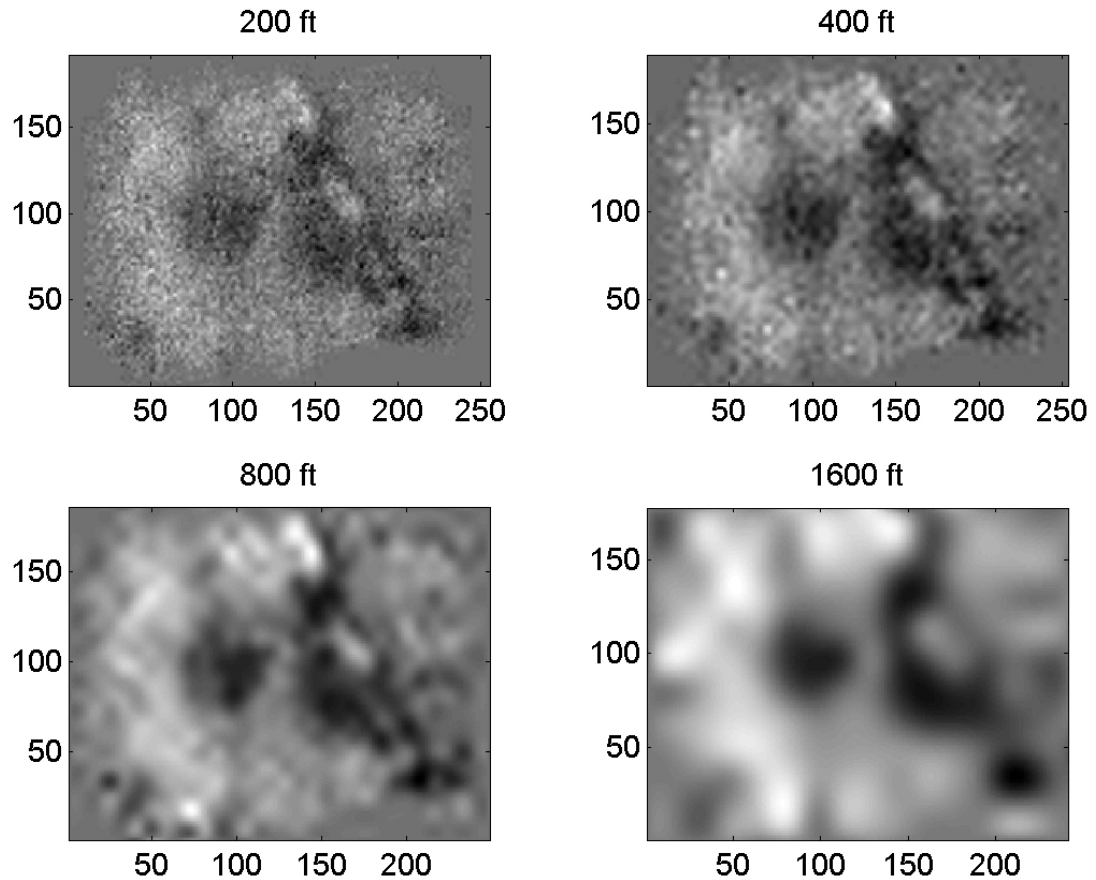
Figure 4.16: Interpolated amplitude maps for the far-offset stack and all azimuths corresponding to the four different spatial bin sizes considered. Top left panel: 200 ft. Top right panel: 400 ft. Bottom left panel: 800 ft. Bottom right panel: 1600 ft. We can see how the increasing bin size reduces the spatial resolution.

4.5 Bootstrap analysis of the PP reflectivity variation with azimuth

In this section, I present the method I use to analyze the *PP* reflectivity variation with azimuth for fracture characterization.

As previously discussed, the smallest superbin size we should use for the seismic amplitude analysis is 800 ft, when we consider azimuthal bins of 20 degrees.

Figure 4.17 presents the seismic amplitude values at the top of the reservoir as a function of azimuth, for both the far- and the near-offset stacks, corresponding to two randomly chosen superbin locations, each of 800 ft size. The top panel of Figure 4.17 shows very little azimuthal variation for both near- and far-offset stacks.

However, the azimuthal variation may be significant at other location, as we can observe on the bottom panel of Figure 4.17. As expected, the azimuthal variation of the seismic amplitudes is stronger for the far-offset stack than for the near-offset stack, as predicted by fracture modeling (Sava et al, 2002), as I also show in Chapter 3.
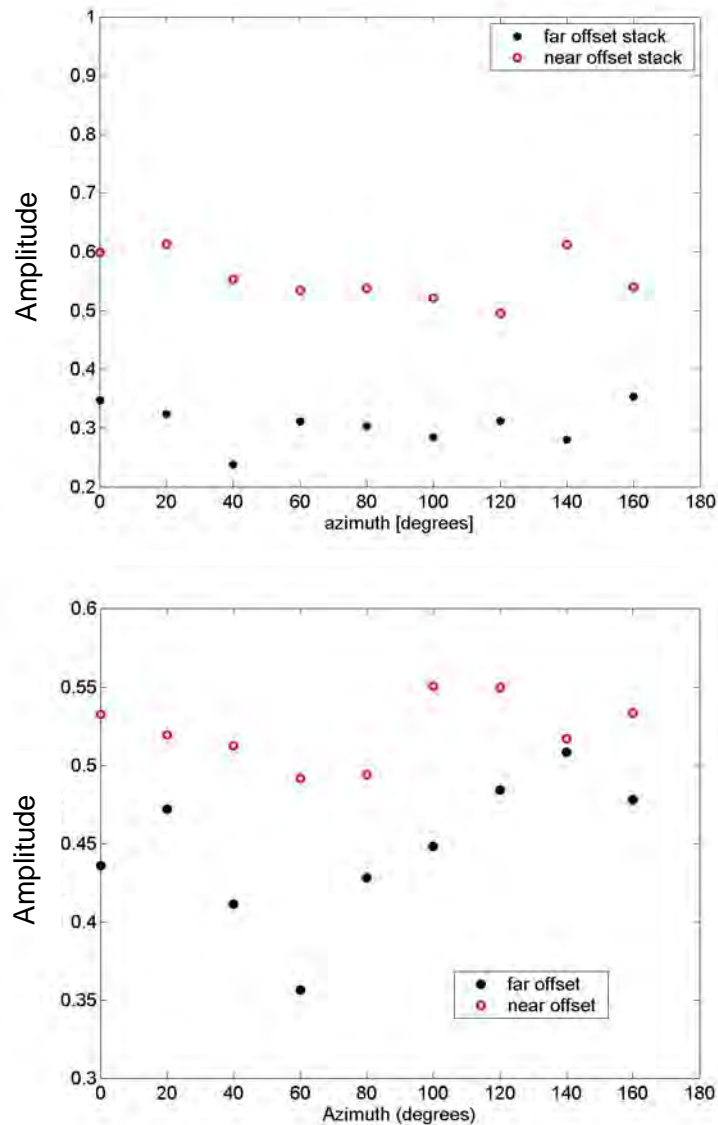
Figure 4.17: Amplitude for the far- and near-offset stacks as a function of azimuth at two different superbin locations.

For a fixed angle of incidence, the azimuthal variation of the reflectivity due to the presence of a single set of aligned fractures can be approximated by a cosine function

(Teng, 1998). The parameters of this cosine function are its mean value, the amplitude of the oscillation, and the phase. The mean value of the cosine function is influenced by the degree of fracturing, and the fluid type in the fractures. The amplitude of the cosine function is commonly interpreted as a measure of the fracture density, while the phase of the cosine function gives information about the fracture orientation.

To determine the parameters of the least-squares cosine fit to the observed azimuthal variation at each superbin, I use a bootstrap method (Efron and Tibshirani, 1998; Teng, 1998). The idea is that the measurements for the 9 different azimuthal ranges of 20 degrees can be treated as 9 random samples out of an infinite number of measurements we could have made. The errors in the reflectivity values are considered to be Gaussian. Therefore, each data value belongs to a normal distribution with the mean equal to the measured value, and the standard deviation evaluated as a percentage of the mean amplitude at the top of the reservoir, to represent the measurement uncertainty. Then, I draw a value independently from each of the 9 individual normal distributions. These 9 different values, corresponding to the 9 different azimuthal ranges of 20 degrees each, represent one realization. Next, I fit a cosine curve to these 9 values using the least-square method. This cosine curve represents one bootstrap realization for estimating the true model. I repeat the procedure many times and obtain hundreds of cosine functions that would fit the observations affected by errors. Therefore, from this large number of realizations we can derive the corresponding distributions for the cosine parameters, which represent a measure of uncertainty due to measurement errors. Figure 4.18 presents 100 realizations for the least-square cosine fits to the data corresponding to the far-offset stack presented at the bottom of the Figure 4.17.

However, the interpretation of the fracture parameters based on the cosine fitting alone is not enough. Rock physics modeling shows that the azimuthal variation of amplitudes depends strongly on the model we consider. Therefore, rock physics fracture modeling is the crucial link between the observed seismic data and the actual parameters of fractures.
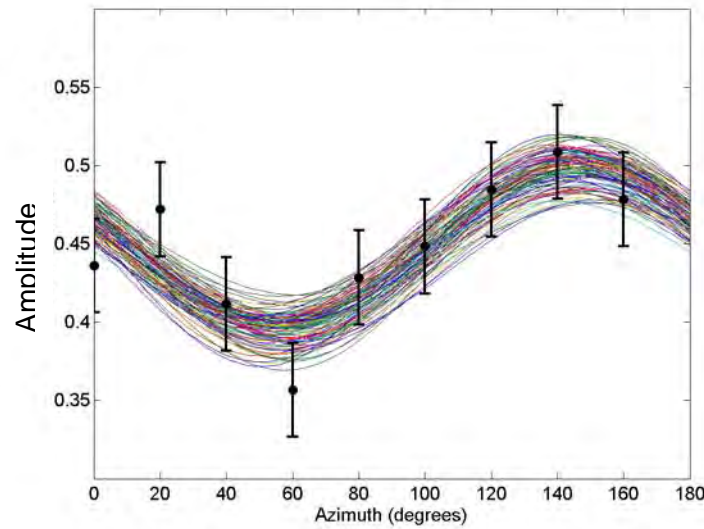
Figure 4.18: Amplitude variation with azimuth at a fixed superbin, and the 100 cosine
    fits obtained using a bootstrap method, taking into account the measurement errors
    represented by the error bars.

In the next section I present the results of the rock physics fracture modeling for the

PP reflectivity variation with azimuth for the James Limestone reservoir.

4.6   Rock physics fracture modeling of the PP reflectivity

In this section, I present the results of the *PP* reflectivity modeling, based on the well-

log data from a nearby field. More details and results are given in Chapter 3. The

carbonate reservoir is modeled with a single set of vertical fractures. The cap rock,

represented by a shaly formation, is considered unfractured. The seismic properties (V_P,

V_S, and *density*) for the cap rocks and the reservoir rocks are derived from the well-log

data, by upscaling, as I describe in more detail in the Chapter 3.

For an HTI medium generated by a single set of vertical fractures, the amplitude

variation with angle of incidence and azimuth (AVAZ) can help in determining the

fracture's strike. AVAZ can also give information about the degree of fracturing and the

type of fluid in the fractures.

In this analysis, I use Hudson's (1981) penny-shaped crack model to derive the elastic properties of the fractured reservoir. Then I use the approximation by Vavrycuk and Psencik (1998) to calculate the *PP* reflectivity variation with angle of incidence and azimuth at the interface between the reservoir, modeled with a vertical set of fractures, and the cap rock, represented by a shaly formation.

Figures 4.19 and 4.20 show the mean values of the *PP* reflectivity from the top of the reservoir, as a function of the incidence angle and azimuth, for the gas- and brine-filled fractures, respectively (Sava et al, 2002). In both cases the matrix porosity is brine saturated.

As expected, the azimuthal variation of the *PP* reflectivity (R_{PP}) increases with angle of incidence, for both brine-filled and gas-filled fractures. From the bottom panel of Figure 4.17, we observe that the *PP* reflectivity derived from the 3D seismic survey at this randomly chosen spatial bin shows qualitatively the same result as the one predicted by the rock physics fracture modeling. The modeling results are displayed on the whole 360º range for the azimuth (Figures 4.19 and 4.20, right panels), while the seismic derived amplitudes are displayed on a 180º range, due to symmetry considerations.

The modeling shows that there is a change in the polarity of the azimuthal variation of the *PP* reflectivity (R_{PP}) between 100% brine-filled fractures and 100% gas-filled fractures, as I also presented in Chapter 3. For the brine-filled fractures, the maximum R_{PP} value at a fixed angle of incidence is in the direction perpendicular to fractures, while for the fractures saturated with gas the maximum R_{PP} value is in the direction parallel to fractures. This result can be used to differentiate between gas-filled and brine-filled fractures, assuming that the azimuthal anisotropy is due only to the presence of a vertical set of joints. On the other hand, this fact introduces an additional ambiguity, when considering only the azimuthal variation of the amplitude. If we do not have information about the fluid type we cannot say, for example, if the fractures are oriented E-W or N-S, based on the azimuthal variation of the seismic amplitudes alone.
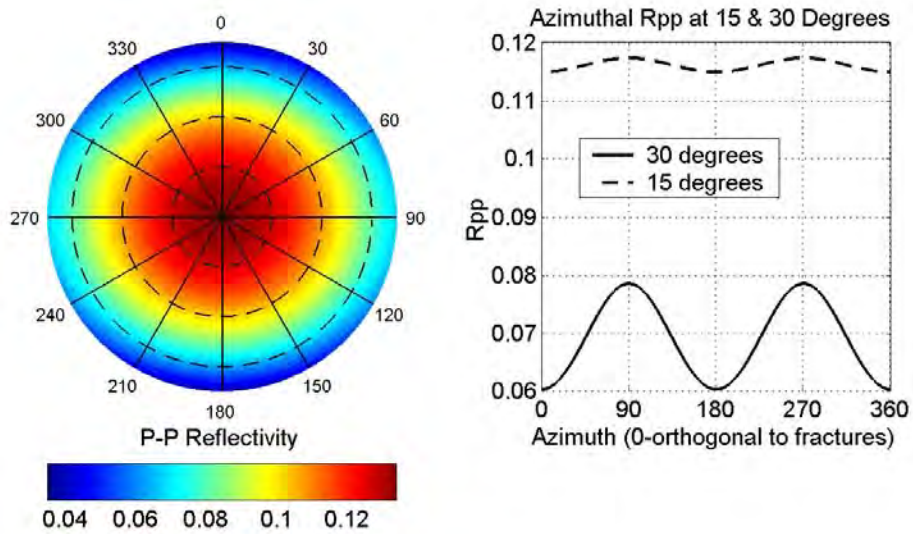
Figure 4.19: Expected values for the *PP* reflectivity as a function of angle of incidence and azimuth. The right side panel presents the R_{PP} amplitude variation with azimuth at 15º and 30º angles of incidence. Azimuth 0º is perpendicular to the fracture plane. Fractures are oriented E-W. Matrix porosity is brine saturated, while the fractures are 100% filled with **gas**. Aspect ratio of the fractures is 0.01.
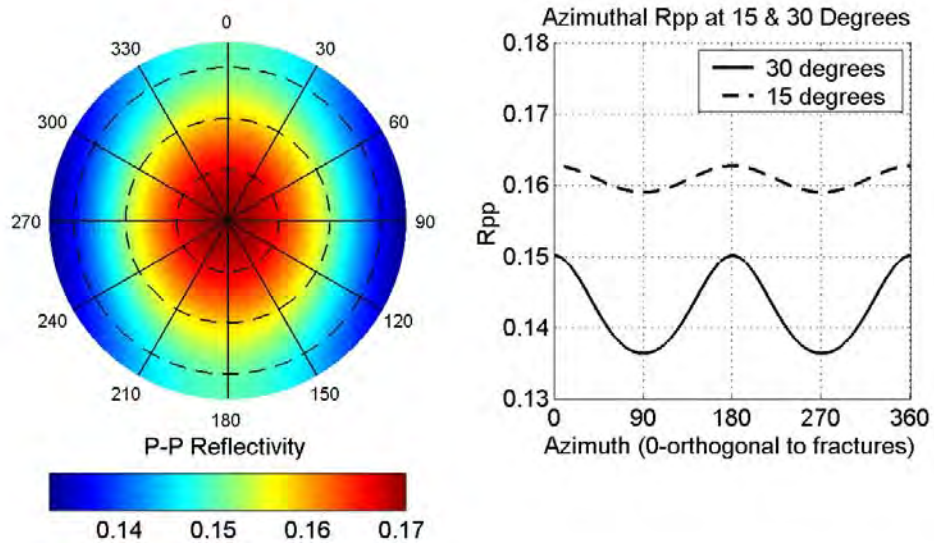
Figure 4.20: Expected values for the *PP* reflectivity as a function of angle of incidence and azimuth. The right side panel presents the R_{PP} amplitude variation with azimuth at 15º and 30º angle of incidence. Azimuth 0º is perpendicular to the fracture plane. Fractures are oriented E-W. Matrix porosity is brine saturated, while the fractures are filled with **brine**. Aspect ratio of the fractures is 0.01.

In practical situations the fractures may be partially saturated with gas. I investigate the azimuthal variation of the *PP* reflectivity with gas saturation. To determine the bulk modulus for the mixture of fluids, I consider both the fine-scale mixing of brine and gas, by using Reuss (1929) average, and also the patchy saturation, approximated by the Voigt average. I expect the patchy saturation to be more relevant for field studies, since the gas tends to segregate gravitationally from the brine.

Figure 4.21 presents the reflectivity variation with azimuth, at fixed angle of incidence, equal to 30º, for different gas saturations. The fracture density as defined in Hudson's model is 0.1, while the aspect ratio of the ellipsoidal cracks is 0.01. The different curves correspond to different gas-saturation levels (from 100% to 0%). The left panel corresponds to the fine-scale mixing of the gas and the brine, while the right panel corresponds to the large-scale mixing of the two fluids (patchy saturation). Azimuth 0º corresponds to the direction orthogonal to fractures. In the direction parallel to fractures (azimuth 90º), the *PP* reflectivity does not change significantly with the fluid type, as expected.

However, in the direction orthogonal to fractures, the *PP* reflectivity varies significantly. Also, the polarity of the azimuthal variation changes with gas saturation. The type of fluid-mixing law has also a significant influence on the amplitude variation. In the case of patchy saturation (right panel), the azimuthal polarity changes at a brine saturation of only 20%. Therefore, for fractures saturated 80% with gas and 20% with brine in a patchy manner, the polarity of the azimuthal variation becomes identical to that of the 100% brine saturated fractures. Also, we observe that in this example, for a gas saturation of 90%, the azimuthal variation is very small. Therefore, the modeling suggests that for some gas saturations, the azimuthal variation of the *PP* reflectivity may not be very useful to predict the main fracture orientation. In the case of the fine-scale mixing of gas and brine, the gas-saturation level at which the azimuthal polarity of the *PP* reflectivity becomes identical to that of the 100% brine filled fractures is around 30%.

The compressibility of the cracks also influences the azimuthal variation of the *PP* reflectivity. For a higher compressibility (aspect ratio of 0.001), the azimuthal variation of the *PP* reflectivity has the same polarity, independently of the gas concentration

(Figure 4.22). The *PP* reflectivity is has a maximum value in the direction orthogonal to the fracture plane. In this case, the azimuthal variation increases slightly with increasing brine saturation.

In conclusion, rock physics modeling enables us to understand the relations between the azimuthal variation of seismic amplitudes and physical parameters, such as fracture orientation, fluid content and compressibility of the fractures. Observing a certain azimuthal variation of the reflectivity in the seismic data does not determine fracture orientation and density. Rock physics of fractures shows that the variation of the *PP* reflectivity with azimuth depends significantly on the model considered. Therefore, careful analysis should be performed before interpreting the seismic observations.
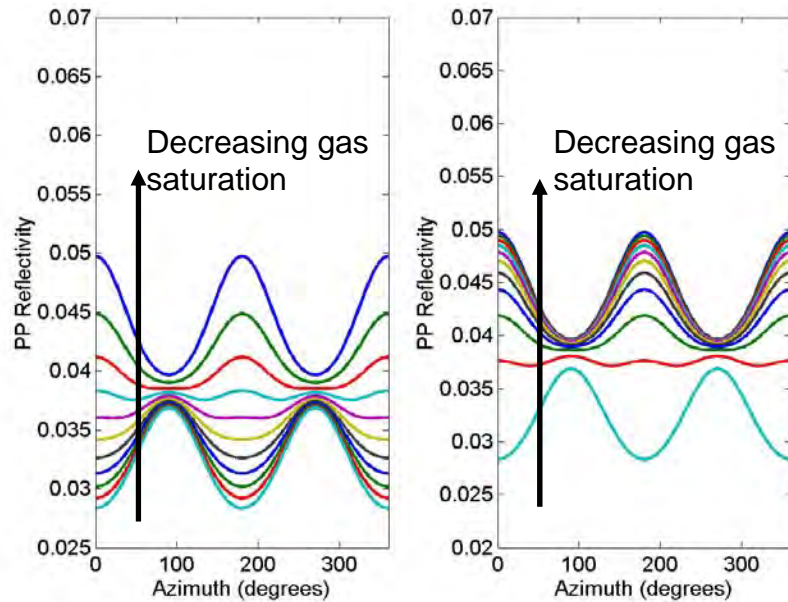
Figure 4.21: *PP* reflectivity as a function of azimuth at a 30º degrees angle of incidence. Different curves correspond to different gas-saturation levels (from 100% to 0%). Left panel corresponds to fine-scale mixing of gas and brine. Right panel correspond to patchy saturation. The arrow indicates decreasing gas saturation. **Aspect ratio** of the fractures is **0.01**. Azimuth 0º is orthogonal to fractures.
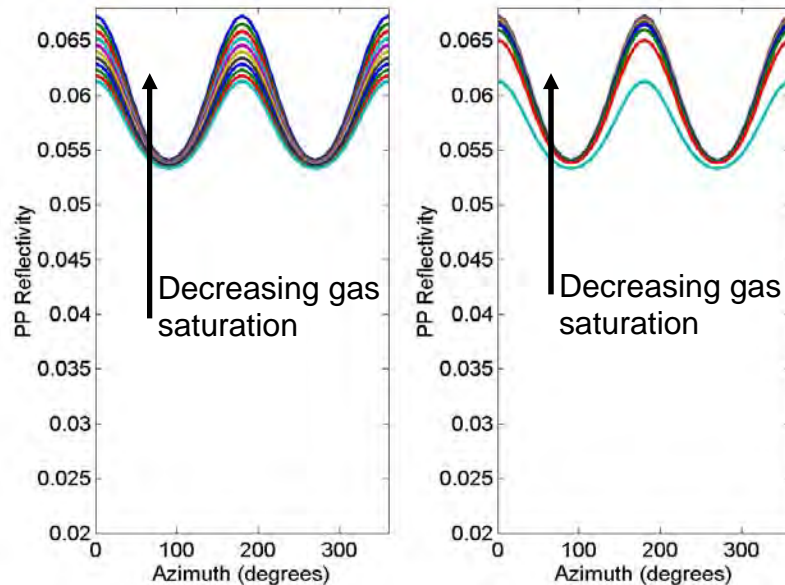
Figure 4.22: *PP* reflectivity as a function of azimuth at a 30º angle of incidence. Different curves correspond to different gas-saturation levels (from 100% to 0%). Left panel corresponds to fine-scale mixing of gas and brine. Right panel correspond to patchy saturation. The arrow indicates decreasing gas saturation. **Aspect ratio** of the fractures is **0.001**. Azimuth 0º is orthogonal to fractures.

4.7 Fracture distribution from the azimuthal variation of the PP reflectivity

In this section, I present the results of the azimuthal analysis of the *PP* reflectivity from the 3D seismic survey presented in previous sections. The goal is to determine the fracture orientations and the anisotropy of the azimuthal variation in the amplitudes at the top of the fractured carbonate reservoir. Since the geological structure is very flat, the top of the reservoir corresponds to a time slice at 1.3 seconds.

The fracture orientation at each bin location is derived from the azimuthal analysis of *PP* reflectivity at far-offset stacks (4000-8000 ft) using the bootstrap method presented in section 4.5. Therefore, I obtain not only a map with the mean fracture orientations, but also the associated standard deviations, due to measurement errors. These standard deviations correspond to a measurement error in the seismic amplitudes equal to 10% of the mean amplitude at the top of the reservoir.

As the rock physics modeling shows, the fracture strike may correspond to the azimuth for which we obtain either a minimum or a maximum of the amplitude, depending on the compressibility of the fluid and of the fractures.

Based on the modeling results for the carbonate reservoir, I determine the fracture strike such that it corresponds to the azimuth for which we get a minimum in the azimuthal variation of the reflectivity. This criterion corresponds primarily to two situations: either the fractures are highly compressible, independently of the type of fluids that saturate them (Figure 4.22), or the fractures are less compressible and partially saturated with 90% or less of gas, in a patchy manner (Figure 4.21, right panel).

Figure 4.23 presents the mean fracture orientations at each superbin locations. The bin size in this case is 1600 ft. The orientations of the red segments represent the mean fracture strikes, while those of the green and blue segments are the corresponding standard deviations from the mean orientation. The results for fracture orientation are superimposed on the map of the stack amplitudes on all offsets and azimuths, at a time slice of 1.3 seconds. The length of the red segments is proportional to the mean difference between the maximum and minimum values in the azimuthal variation of the reflectivity. The lengths of the blue and the green segments represent the standard deviations of this mean amplitude difference.

From Figure 4.23 we can observe that for some bin locations, the standard deviation of the mean orientation of the fractures is large, especially at the edges of the survey. However, for most of the superbins we obtain relatively small standard deviations, showing that the seismic data, with their associated measurement errors, constrain the fracture orientations reasonably well.
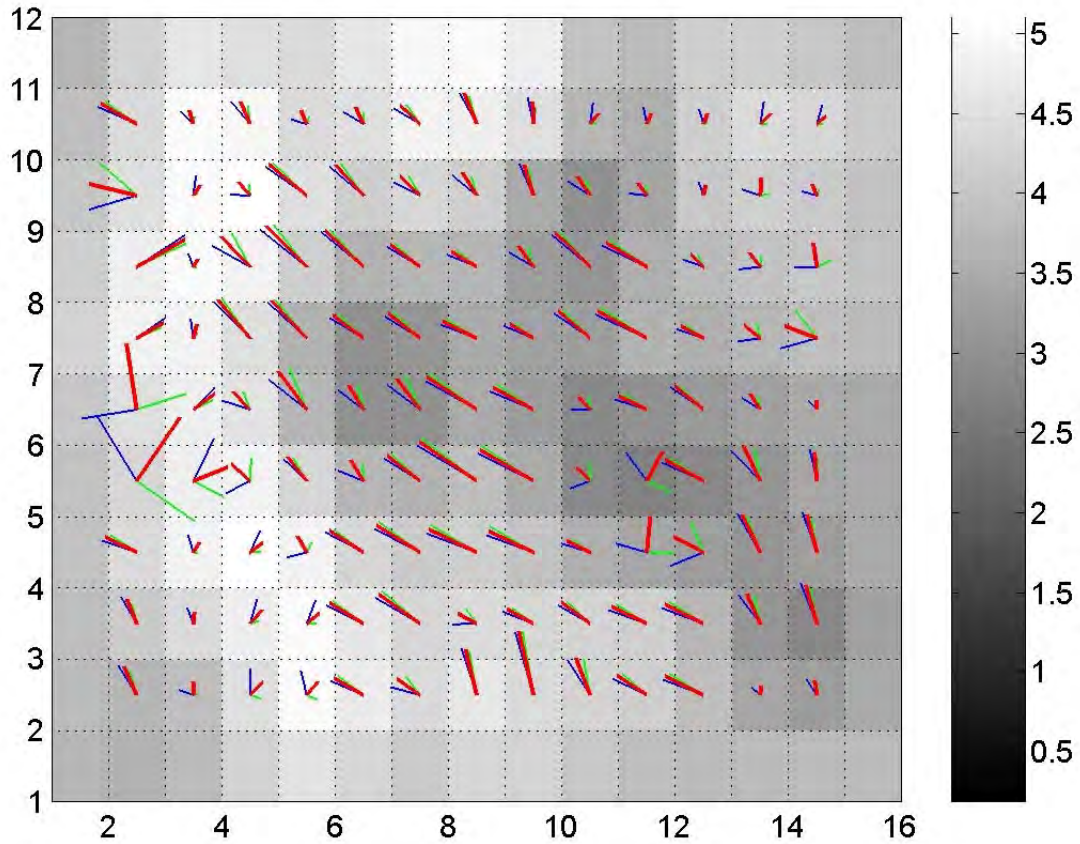
Figure 4.23: Fracture orientation at time slice of 1.3 seconds, corresponding to the top of James Limestone reservoir. The orientations of the red segments represent the mean fracture strikes, while the blue and green segments represent the standard deviations from the mean orientation. The length of the red segments is proportional to the mean of the difference between the maximum and minimum amplitudes at each bin location (reflectivity anisotropy). The lengths of the blue and green segments give the standard deviations from this mean difference in the amplitudes. The fracture strikes are superimposed on the stack amplitude map for the time slice. The superbin size is 1600 ft.

However, as we can see in Figure 4.23, the superbin size is very large, equal to 1600 ft. Thus, this map only gives average trends for fracture orientation. To obtain a more detailed interpretation we have to use smaller bin sizes. Therefore, I also consider the case of a superbin size of 800 ft. This dimension is the smallest we should use to avoid the artifacts introduced by the acquisition footprint, as I showed in the section 4.4.
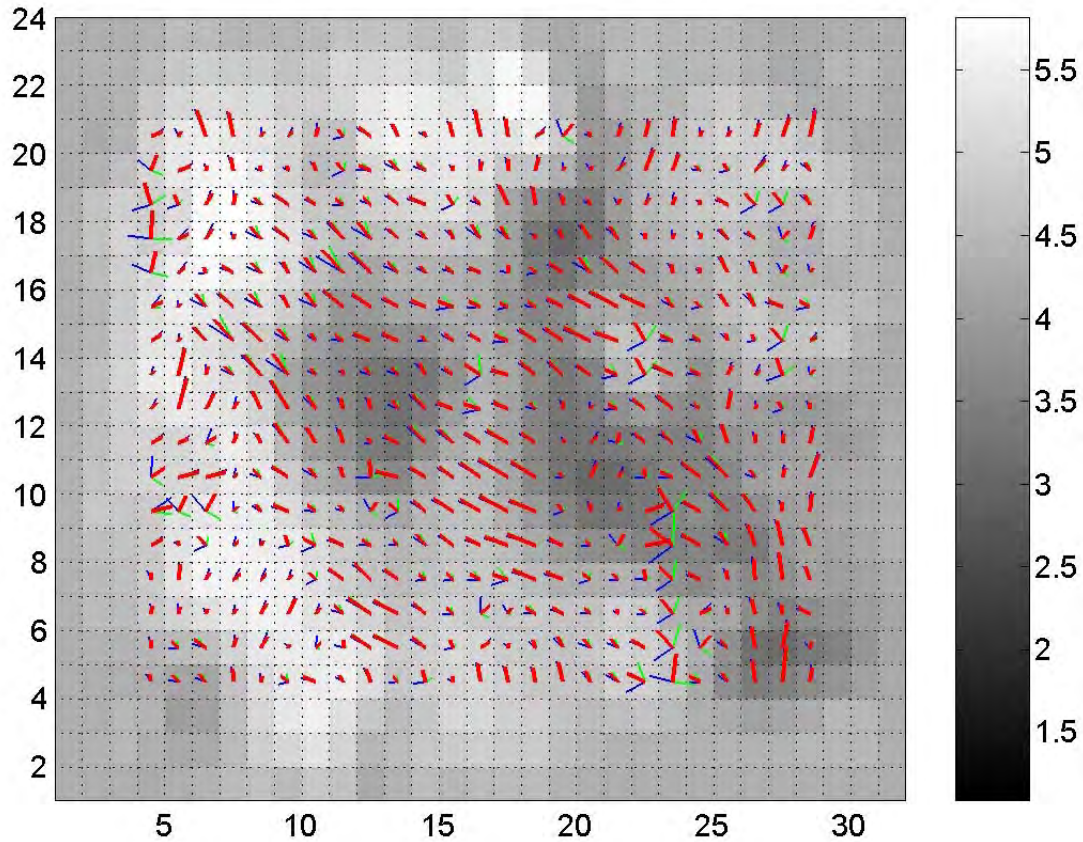
Figure 4.24: Fracture orientation at time slice of 1.3 seconds, corresponding to the top of James Limestone reservoir. The orientations of the red segments represent the mean fracture strikes, while the blue and green segments represent the standard deviations from the mean orientation. The length of the red segments is proportional to the mean of the difference between the maximum and minimum amplitudes at each bin location (reflectivity anisotropy). The lengths of the blue and green segments give the standard deviations from this mean difference in the amplitudes. The fracture strikes are superimposed on the stack amplitude map for the same time slice. The superbin size is 800 ft.

Figure 4.24 gives the same representation for the fracture orientation as Figure 4.23. However, in this case the superbin size is 800 ft, enabling us to obtain a more detailed interpretation of the fracture orientation at the top of the reservoir. We again observe some bins that show large standard deviations of the fracture strike determined from the azimuthal variation in the seismic amplitudes at far offsets. Most of the superbins display relatively small standard deviations, suggesting that the azimuthal variation in seismic amplitudes at far offset can be used to constrain the fracture orientation for this survey.

The distributions of the mean fracture orientations in the rotated coordinate system for both the 1600 ft and 800 ft bin size cases are presented in Figure 4.25. From the two rose diagrams, we observe that the mean fracture strikes derived from the amplitude variation with azimuth at far offsets does not change significantly with the bin size. The trends observed at smaller scale (800 ft bin size) are preserved also at larger scale (1600 ft).
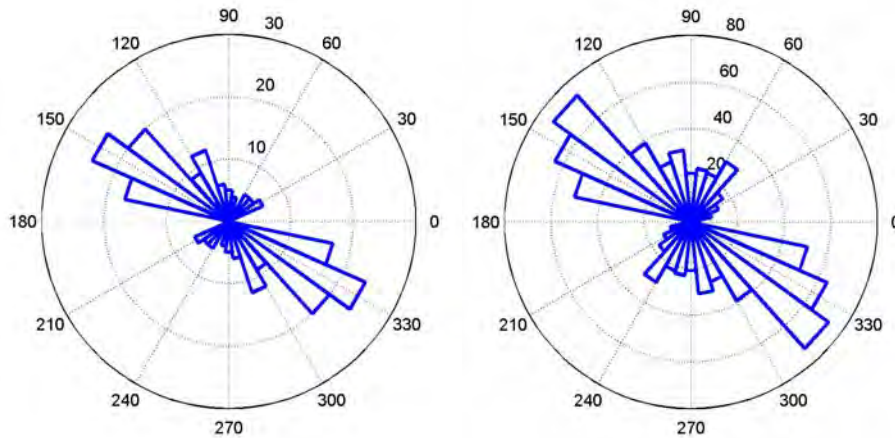
Figure 4.25: Rose diagrams for the fracture strike in the rotated coordinate system for 1600 ft bin size (left) and 800 ft bin size (right). This coordinate system is rotated 34º East with respect to the geographic North.

If we represent the fracture orientation in the original system of coordinates of the survey, we observe an E-W trend for the fracture strikes in this field.

The FMI log data show the existence of open, nearly vertical fractures with dips around 89 degrees, whose orientations are W10N-E10S. There is a relatively small spread of the mean fracture strike around this main orientation. I find a very good agreement between the fracture orientation derived from azimuthal analysis of the seismic amplitudes and the FMI measurements from the well, as we can see in Figure 4.27.
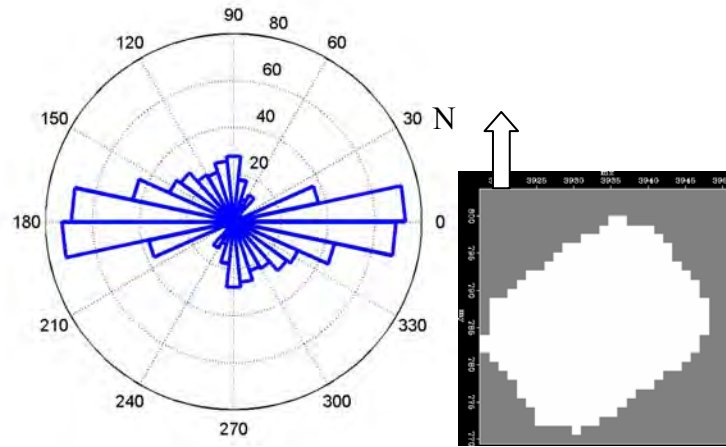
Figure 4.26: *Left:* Rose diagram for the fracture strike from azimuthal variation of PP reflectivity at far offsets in the original system of coordinates of the survey. In the rose diagram, 90 degrees azimuth corresponds to the geographical North. *Right*: Schematic representation of the seismic survey area.
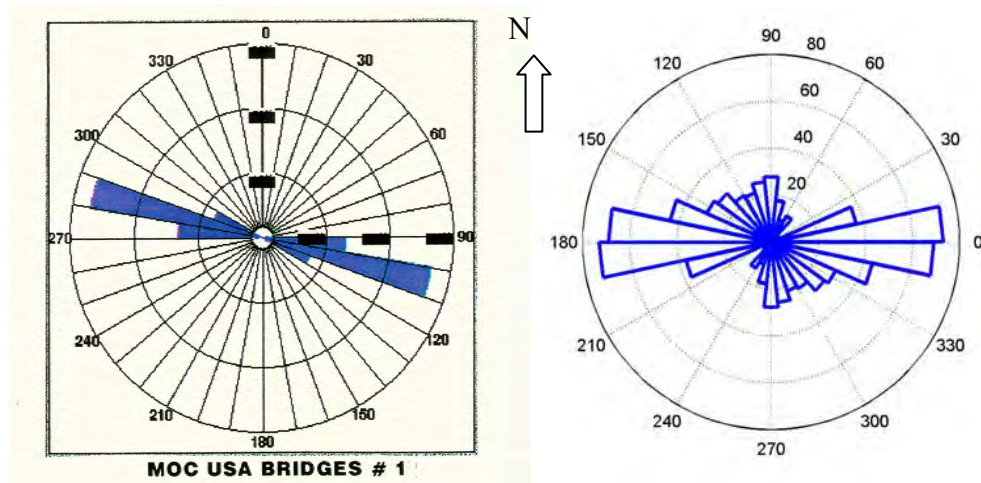
Figure 4.27: Comparison between the distributions of fracture strikes interpreted from a FMI log in James Limestone reservoir from a well in a nearby field (*left*) and the fracture strike interpreted from the azimuthal analysis of the seismic amplitudes at far offsets at the top of the James Limestone reservoir (*right*). Geographic North is the same for both rose diagrams. The observed fractures in the FMI log have dips of 89 degrees.

If we plot the mean fracture orientation from the distribution that we get from the azimuthal analysis of the *PP* reflectivity on the map with the regional stress field we observe again a good agreement. The mean fracture strike is almost parallel to the maximum horizontal stress (Figure 4.28).
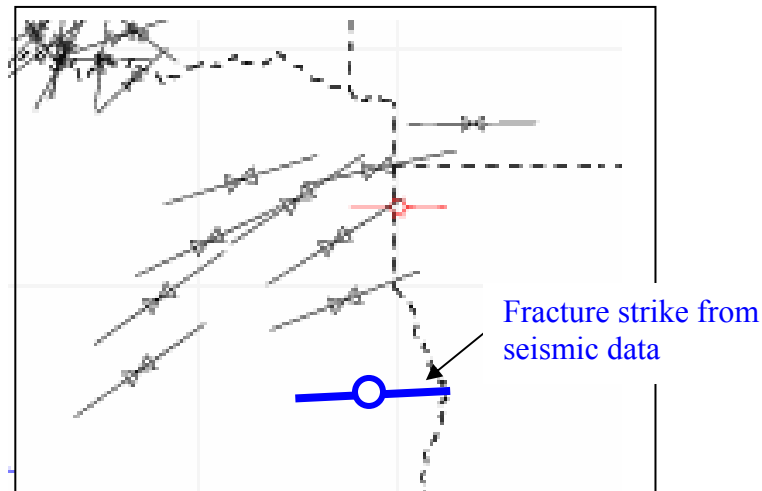
Figure 4.28: Map with the regional stress field (World Stress Map Project, data collected originally by Mary Lou Zoback). Superimposed is the fracture strike obtained from the azimuthal analysis of the PP reflectivity at far offsets (blue).

I also derive the relative anisotropy observed in the azimuthal variation of the seismic amplitudes at far offsets, and the associated standard deviation due to measurement errors, by using the bootstrap method. Figure 4.29 presents a map at the top of the reservoir with the mean values for the relative anisotropy of the azimuthal variation in the seismic amplitudes. The relative anisotropy is defined as:

$$R_{anis} = \frac{\left| R_{max} - R_{min} \right|}{\left| R_{min} \right|} \tag{4.1}$$

The modeling shows that the difference between the maximum and minimum values of the amplitude from the azimuthal variation at far offsets is a function not only of the crack density, but also of the compressibility of the fractures and of the fluids that saturate them. In the hypothesis of little variability in the fracture compressibility and of uniformly saturated fractures, the map presented in Figure 4.29 can be interpreted as a relative degree of fracturing at the top of the reservoir.

We can observe a relatively higher anisotropy in the proximity of an interpreted fault that penetrates the carbonate reservoir. This fault is schematically represented in Figure 4.28. This may be due to a relatively higher fracture density of nearly vertical fractures in the proximity of the fault. The anisotropy anomaly is slightly asymmetric with respect to

the fault. Larger values of the relative reflectivity anisotropy are encountered in the hanging wall, as some outcrop observations for analogs show (Florez, 2002). However, we can also observe a zone of higher azimuthal anisotropy in the seismic amplitudes away from the fault. This zone may also correspond to larger fracture densities associated with possible subseismic faults. This reflectivity anisotropy is used in Chapter 5 to constrain the fracture density distribution at the top of the reservoir.
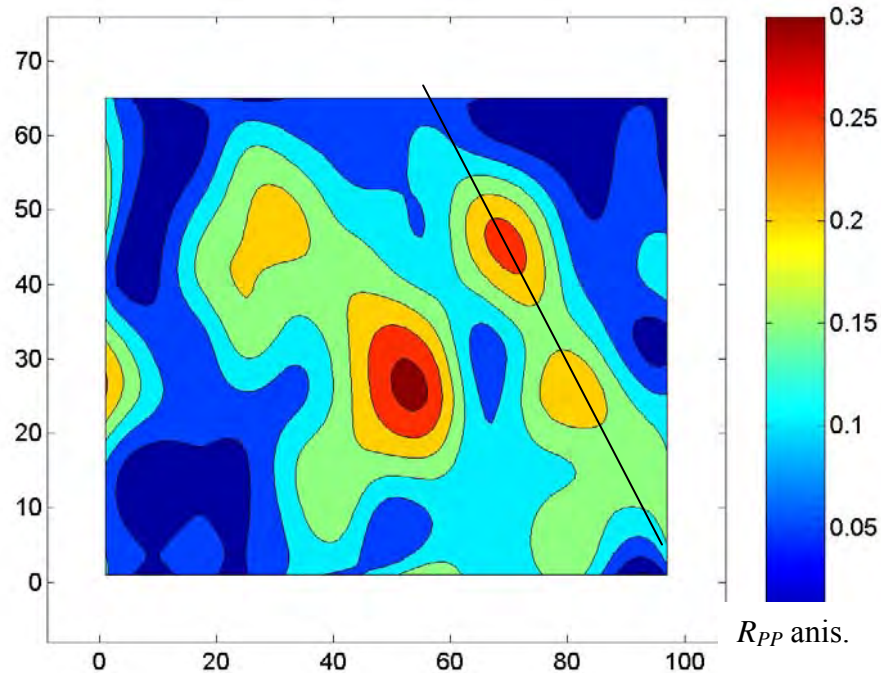
Figure 4.29: Map with the mean relative azimuthal anisotropy in reflectivity at the top of the reservoir.

In conclusion, I find an excellent agreement between the fracture orientation derived from the azimuthal variation of seismic amplitudes at far offsets and the fracture orientation derived from the FMI logs from the nearby wells. Furthermore, the mean fracture orientation derived from the seismic data is approximately parallel to the maximum horizontal stress in the region, as expected in a normal faulting environment.

The distribution of the azimuthal anisotropy in the *PP* reflectivity derived from the seismic data at the top of the reservoir may be interpreted as a relative degree of

fracturing, assuming little variability in the fracture compressibility for the zone of interest, and uniform saturation for the fractures.

4.8   Conclusions

In this chapter, I present the analysis of the *PP* reflectivity from a 3D seismic data set acquired over a fractured carbonate reservoir in eastern Texas, for determining the fracture orientations and the azimuthal anisotropy in reflectivity at the top of the reservoir.

In the first part of this chapter, I show the impact of the 3D seismic acquisition footprint on analyzing the variation of the reflectivity with both offset and azimuth. The acquisition footprint of this survey affects significantly the seismic amplitudes, as we observe on the reflectivity time slices. The fold is not uniform, and it creates artificial stripes of low and high reflectivity that can mask the actual signatures of fractures.

Azimuthal analysis of the *PP* reflectivity involves partial stacking of the data on different ranges of azimuth. There is a tradeoff between the azimuthal resolution, which requires small ranges of azimuth, and the signal-to-noise ratio that requires larger fold, and implicitly larger azimuthal bins. For a fixed azimuthal range we can increase the fold by increasing the bin size, at the expense of reducing the spatial resolution.

In this chapter, I show how increasing the spatial bin size can diminish the strong acquisition footprint, while increasing the fold and implicitly the signal-to-noise ratio at each superbin location. The azimuthal range for stacking the reflectivity is kept constant, equal to 20 degrees. Based on the analysis, I determine that for this 3D seismic survey, the superbin size should be at least 800 ft, at 20º azimuthal range, to make a reliable interpretation of the reflectivity variation with offset and azimuth.

Once we observe an azimuthal variation in the seismic amplitudes, the challenge is to interpret it in terms of fracture density, orientation, and fluid saturation. Rock physics fracture modeling enables us to link the observed seismic attributes to the actual parameters of fractures. Therefore, in the second part of this chapter I present more modeling results of the amplitude variation with incidence angle and azimuth (AVAZ)

for the fractured carbonate reservoir. The rock physics fracture modeling shows that the interpretation of the azimuthal variation of the *PP* reflectivity in terms of fracture orientation and relative degree of fracturing requires careful rock physics modeling and additional geological constraints. The polarity of the azimuthal variation of the reflectivity changes with both gas saturation and the compressibility of the cracks. Therefore, the fracture strike can be given by the azimuth corresponding to either a maximum or a minimum in the azimuthal variation of the reflectivity. This result that may be used to differentiate between gas-filled and brine-filled fractures, assuming that the azimuthal anisotropy is due only to the presence of a vertical set of joints whose orientation is determined from other sources of information. On the other hand, this fact introduces an additional ambiguity when we want to determine the fracture orientation from the AVAZ alone. If we do not have information about the fluid that saturates the fractures, in some situations we may not be able to determine the fracture strike.

Based on the rock physics analysis, I consider that the fracture strike at the top of the James Limestone reservoir is given by the minimum in the azimuthal variation of the reflectivity. This criterion corresponds to the cases for which either the fractures are highly compressible, independently of the type of fluids that saturate them, or the fractures are less compressible and partially saturated with 90% or less of gas, in a patchy manner. Under these hypotheses, I derive a map with the fracture orientation and the associated azimuthal anisotropy in the reflectivity at the top of the reservoir. Using a bootstrap method, I also estimate the uncertainty in the fracture orientation and the azimuthal anisotropy in the reflectivity due to measurement errors. I find an excellent agreement between the mean fracture orientations derived from the azimuthal variation of the seismic amplitudes at far offsets and the fracture orientations derived from the FMI logs from a nearby well. There is also a very good agreement between the mean fractures' strike from AVAZ and the present regional stress field. The mean fracture orientations are approximately parallel to the maximum horizontal stress in the region.

The distribution of the azimuthal anisotropy in the *PP* reflectivity at the top of the reservoir may be interpreted as a distribution of the relative degree of fracturing, assuming little variability in the fracture compressibility for the zone of interest, and

uniform saturation for the fractures. I observe a relatively higher anisotropy in the proximity of an interpreted fault that penetrates the James Limestone reservoir. This may be due to higher fracture densities in the proximity of the interpreted fault. The anisotropy anomaly is slightly asymmetric, with higher values of the anisotropy in the hanging wall of the fault. This interpretation is in agreement with field observations, and with the geological model for the reservoir. However, we can also observe a zone of higher azimuthal anisotropy in the seismic amplitudes away from the fault. This zone may also correspond to larger fracture densities, perhaps associated with subseismic faults.

Fracture characterization from AVAZ requires careful rock physics modeling and additional geological and geomechanical information on fracture compressibility and fluids distribution. However, in the absence of such information, using multiple seismic attributes can also help reduce the uncertainty in the interpretation of fracture orientation and density. For example, using the azimuthal variation in the reflectivity together with the seismic amplitude values either at the near- or far-offsets can better constrain the fracture distribution.

The next chapter presents the methodology for integrating quantitatively the geological information about fracture density with seismic data, to reduce the uncertainty in fracture characterization.

Chapter 5

Quantitative Integration for Fracture Characterization

5.1   Abstract

Subsurface property estimation in the geosciences is always subject to uncertainty. This is mainly due to measurement errors, to limited measurement resolution, to incomplete understanding of the physical and geological phenomena, to natural variability of the target rock properties, etc. Each geoscience discipline brings different information, often complementary, but sometimes contradictory, about the subsurface heterogeneities. Therefore, integrating different types of geological and geophysical information can better constrain the predictions on the subsurface properties.

In this chapter, I design a methodology for quantitative integration of geological and seismic data, using statistical rock physics. Rock physics theories provide a link between geology and seismics, while the statistical approach allows for quantitative integration of the various types of information.

Every geophysical measurement is designed to increase our knowledge of the subsurface properties we want to estimate. For example, in fracture characterization the

goal is to update the prior geological information about the crack density and orientation by acquiring seismic data. I formulate the integration methodology in the framework of an inverse problem. I use the language of probability theory and Bayesian statistics to combine quantitatively the different types of information from geology, well-log, seismic measurements, and rock physics theories, to better constrain the fracture distribution in the subsurface. The probabilistic approach also allows for estimating the associated uncertainty, and therefore, the method can have an impact on risk and decision analysis in reservoir development.

In this chapter, I illustrate the quantitative integration methodology with fracture characterization of a carbonate reservoir in eastern Texas. The main objective is to constrain the prior information about fracture density, from the geologic interpretation, with reflectivity attributes derived from the 3D seismic data set (Chapter 4), using rock physics theories on fractures (Chapter 2). I also present a method for estimating prior uncertainties on the fracture density, using geological constraints.

5.2   Introduction

Estimating the subsurface properties from geophysical measurements represents an inverse problem always subject to uncertainty. Among the contributing factors to this uncertainty are the measurement errors, the limited measurement resolution, the imperfect dependence between the measurements and the rock properties, etc. The information provided by seismic data about the subsurface fracture distribution is influenced by many factors, such as the type and number of seismic attributes, sensitivity of these attributes to the fracture properties, natural variability of the target rocks, and accuracy of the derived seismic attributes.

However, we often have prior, independent information about the spatial distribution for the variable of interest from the geological interpretation. In some cases, the prior information can play an important role in constraining the geophysical data, to reduce the uncertainty of our estimations.

This chapter presents a way to integrate quantitatively the geological and seismic observations using stochastic rock-physics modeling. The approach is based on the framework of an inverse problem, as formulated by Tarantola (1987), using the language of probability theory. The probabilistic approach allows us to integrate quantitatively the various types of information and also to estimate the uncertainty in our predictions (Tarantola, 1987; Houck, 1999; Takahashi et al., 1999). Therefore, this method can have a significant impact on risk and decision analysis for reservoir management.

The first part of this chapter presents the general methodology of integrating prior geological information with seismic data, using rock physics theories (Mavko et. al, 1998). This method can be applied not only to fracture characterization, but also to estimating other subsurface rock properties. However, the illustrative examples are related to fracture density estimation.

In any Bayesian (Bayes, 1783; Box and Tiao, 1992; Jaynes, 2003) analysis, we start by quantifying the *state of knowledge* about the variable of interest before acquiring new data, through the so-called *a priori* probability density function (PDF). In this chapter I also present a method to derive the *a priori* PDF for the fracture density, based on a set of constraints imposed by the geological interpretation and theoretical considerations.

Finally, I show an example of integrating prior geological information about fracture density and various reflectivity attributes from a 3D seismic dataset acquired over a fractured carbonate reservoir in eastern Texas.

5.3   Methodology

The methodology presented in this section is based on Tarantola's (1987) approach to solving inverse problems, by using Bayesian analysis. The inverse problem can be divided into the following steps:

1)   Decide on a minimal set of model parameters which represent the model space ($\mathcal{M}$),

2)   Define the physical laws that relate the model parameters to the observable, or data parameters,

3) Use measurements of the observable parameters, which constitute the data space ($\mathcal{D}$), to infer the actual values of the model parameters.

In fracture characterization, the model parameters are represented by the fracture density, fracture orientation, fracture compressibility, and type of fluids saturating the fractures. The physical laws that relate the model parameters to elastic properties that can be measured seismically are given by rock-physics fracture models, such as those of Hudson (1981) or Schoenberg (1980), presented in Chapter 2.

In this section, I present in more detail the three different components of the inverse problem for fracture characterization: the prior information on the model parameters, the theoretical relations between the model and the observable parameters, and the experimental data. Finally, I present the method of combining all these pieces of information to obtain the updated, or posterior state of information on the model parameters.

5.3.1 *A priori* PDF on the model parameters

As already mentioned, we often have some prior information on the model parameters, independent of the site-specific geophysical measurements. The general way of expressing mathematically the state of information over a parameter set is through a probability density function (Feynman et al., 1963; Tarantola, 1987). In estimation problems, the PDF provides us with a complete quantitative description of how likely is each of the parameter values.
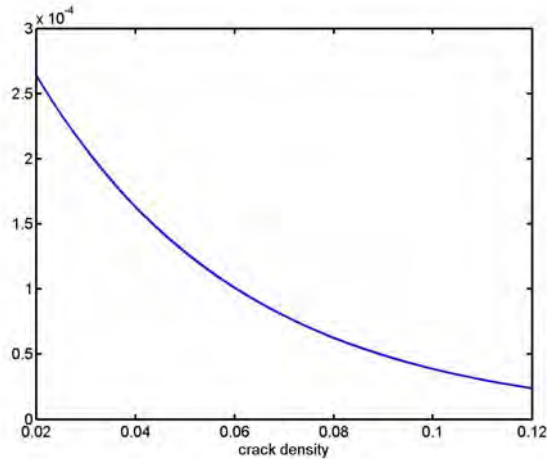
Figure 5.1: Probability density function for crack density. The PDF is assumed to be a truncated exponential on the interval 0.02 to 0.12, with mean 0.04. The small values are more probable than the large values.

For example, Figure 5.1 presents an *a priori* probability density function for the crack density (*e*) as defined in Hudson's (1981) model (see Chapter 2). The prior information often comes from geological observations in outcrops, from laboratory measurements, and also from previous field studies. In the example from Figure 5.1, the PDF is assumed to be exponential over the crack density interval from 0.02 to 0.12, with a mean equal to 0.04. This PDF suggests that the smaller values of the crack density are more probable than the higher values, as presented in Chapter 2.

In the case of a multi-dimensional parameter set, including for example, the fracture density, orientation, and compressibility of the fractures and of the saturating fluid, we can describe the prior information using the joint PDF over these variables. In the simple case of independence among the variables, the joint PDF is given by the product of the individual marginal PDFs for each of the variables. Following Tarantola's (1987) notation, $\rho_M(\mathbf{m})$ represents the probability density function for the prior information on the model parameters, where $\mathbf{m}$ is a vector representing the parameter set of the model space ($\mathcal{M}$).

In the example from Figure 5.1, the prior PDF of the crack density can be denoted as $\rho_M(e)$. In this case, the model parameter is the crack density, *e*.

The prior information about the model parameters is by definition statistically independent of the measurements, and represents an important component of any Bayesian analysis (Bayes, 1783). In this chapter, I also present a way of estimating the prior PDF based on constraints imposed by geological and theoretical information, in section 5.4.

5.3.2   Experimental data

The geophysical measurements, in our case the seismic data, are affected by errors. Thus, the most general way of expressing the uncertainty about the observed data is through probability density functions, often with a Gaussian distribution.
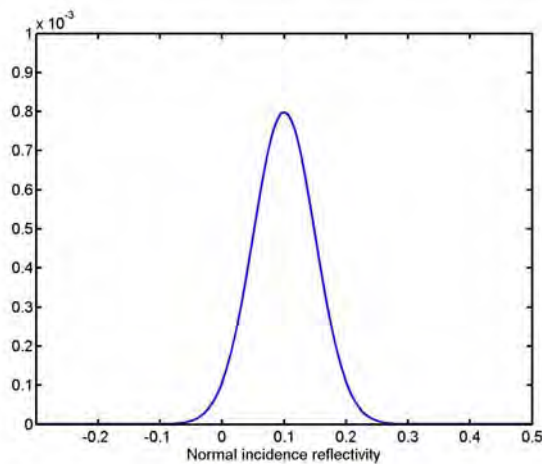
Figure 5.2: Probability density function for seismic reflectivity. The PDF is assumed Gaussian, with the mean centered about the observed value. The variance is a measure of the uncertainty about the observed value.

For example, Figure 5.2 presents a Gaussian PDF associated with a measurement of near-offset seismic reflectivity. The mean of the Gaussian represents the observed reflectivity, while the variance represents our degree of belief in that particular measured value.

The data space *(D)* usually includes different types of measurements, for example, the near- and the far-offset seismic reflectivity. I generically denote the joint PDF over

the data space as $\rho_D(\mathbf{d})$. Therefore, for multiple types of data, we can represent the measurement errors by a multivariate Gaussian, as follows:

$$\rho_D(\mathbf{d}) = Gaussian(\mathbf{d}, \mathbf{d}_{obs}, C_D), \tag{5.1}$$

In Equation 5.1, $\mathbf{d}$ is the vector with the data variables (such as the near- and the far-offset reflectivity), $\mathbf{d}_{obs}$ is the vector with the observed values, which contains the means of the multivariate Gaussian function, and C_D is the covariance matrix over the data space. If the data are assumed independent, the covariance matrix is diagonal with the variances of the individual data types.

In the example from Figure 5.2, the PDF expressing the uncertainty of the near-offset reflectivity value can be written as:

$$\rho_D(R_N) = Gaussian(R_N, R_{Nobs}, s^2) = \frac{1}{\sqrt{2\pi}s} \exp\left[-\frac{(R_N - R_{Nobs})^2}{2s^2}\right] \tag{5.2}$$

In this case, the data is represented by the near-offset reflectivity, R_N. The mean of the Gaussian function is the observed value of reflectivity R_{Nobs}, while the variance, s^2, is assumed to represent the uncertainty about the observed value.

5.3.3 Theoretical relation between model parameters and experimental data

Probability density functions can be used to express not only the *a priori* information on the model parameters and the measurement uncertainty in the data, but also the physical correlations between these model parameters and the measurable, or data parameters. The joint PDF between the model parameters and the measurable seismic attributes describes the uncertainty of the relation between them. This uncertainty can be caused by various factors, including the approximations in the physical theory, as Tarantola (1987) describes, which are difficult to estimate. However, the uncertainty due to the natural variability of the target rock properties may be a more significant source of uncertainty. In this case we can incorporate the natural variability of the rock properties into deterministic rock-physics theories, using stochastic simulations (Mavko and Mukerji, 1998; Mukerji et. al, 2001).

Figure 5.3 gives an example for the joint PDF between the model parameter (crack density), and the data parameter (azimuthal reflectivity anisotropy), in the assumption of aligned vertical fractures. The physical law from which I generate the joint PDF in Figure 5.3 is given by Hudson's (1981) theory, which relates the fracture density to the elastic properties of the fractured media. Using the elastic properties for the fractured rocks I estimate the seismic reflectivity anisotropy based on the Ruger's (1997) equations, in the hypothesis of a vertical set of fractures (more details in Chapter 4). The *Monte Carlo* simulations for deriving the theoretical joint PDF between the model parameters and the observable data will be presented in the following sections; more details are given in Chapter 3.
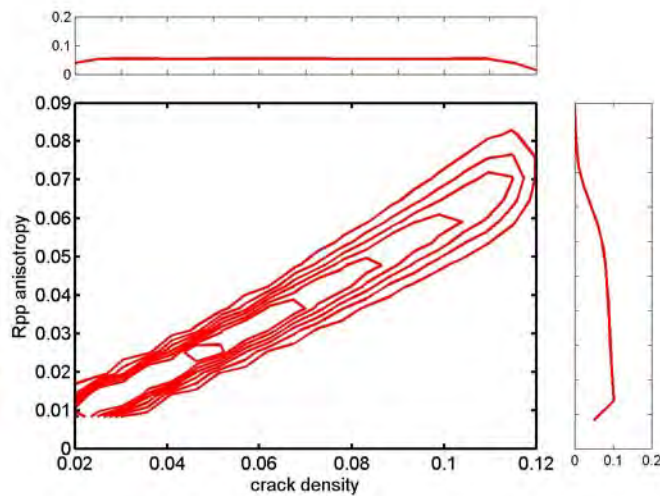
Figure 5.3: Joint PDF of crack density and azimuthal reflectivity anisotropy, showing uncertainty in the relation between model parameters and observable parameters due to natural variability of the rock properties.

The joint PDF that describes the theoretical relation between the model parameters and the data is symbolically represented as $\Theta(\mathbf{m},\mathbf{d})$.

In the example from Figure 5.3, the theoretical joint PDF can be written as $\Theta(e,A)$, where e is the crack density and A is the azimuthal reflectivity anisotropy.

5.3.4 Combining *a priori*, experimental and theoretical information

To summarize, any geophysical inverse problem has three different components: 1) the prior information on the model parameters, which often comes from geology, 2) the results of some experiments, often represented by the seismic data, and 3) the theoretical relation between the model parameters and the experimental data, which in fracture characterization is given by rock-physics theories. Therefore, the general question we should ask in solving an inverse problem is the following (Tarantola, 1987): Given a certain amount of prior information on the model parameters, and given an uncertain physical law relating the observable parameters to the model parameters, how should we modify the *a priori* information, given the uncertain results of some measurements?

In this framework, the inverse problem is solved by integrating quantitatively the prior, experimental, and theoretical information.

If we combine the prior PDF for the model parameters with the information on the data, we can define the prior joint PDF $\rho(\mathbf{m}, \mathbf{d})$ in the space $\mathcal{M} \times \mathcal{D}$. Since the *a priori* information on the model parameters is by definition statistically independent from the data, the joint PDF of the model parameters and the observable data is given by the product between the PDF for the model parameters $\rho_M(\mathbf{m})$ and the PDF for the data $\rho_D(\mathbf{d})$:

$$\rho(\mathbf{m}, \mathbf{d}) = \rho_M(\mathbf{m})\, \rho_D(\mathbf{d}) \tag{5.3}$$

The joint probability density $\rho(\mathbf{m}, \mathbf{d})$, defined on the $\mathcal{M} \times \mathcal{D}$ space, represents the prior geological information on the model parameters, $\mathbf{m}$, and the information from the geophysical data, $\mathbf{d}$.

On the other hand, we also have the theoretical PDF, $\Theta(\mathbf{m}, \mathbf{d})$, which represents the state of information on the physical correlations between the model parameters, $\mathbf{m}$, and the data, $\mathbf{d}$, which are given by the rock physics theories.

The solution to the inverse problem is obtained by combining these two states of information to produce the *a posteriori* state of information on the model parameters and the data, as follows (Tarantola, 1987):

$$\sigma(\mathbf{m}, \mathbf{d}) \sim \frac{1}{\mu} \rho(\mathbf{m}, \mathbf{d}) \, \Theta(\mathbf{m}, \mathbf{d}), \qquad (5.4)$$

where $\sigma(\mathbf{m}, \mathbf{d})$ represents the *a posteriori* state of information on the model parameters and the data, defined also in the $\mathcal{M} \times \mathcal{D}$ space. The *a posteriori* distribution is obtained by dividing the product of the two different states of information, $\rho(\mathbf{m}, \mathbf{d})$ and $\Theta(\mathbf{m}, \mathbf{d})$, as described above, by the non-informative PDF, also known as the homogeneous probability, μ (Tarantola, 1987). Although no coherent inverse theory can be set without the introduction of the homogeneous probability, it does not play an important role, and numerical inverse results do not critically depend on the particular form of μ (Tarantola, 1987).

The posterior PDF for the model parameters is obtained by integrating the *a posteriori* joint PDF for the model parameters and the observable parameters, $\sigma(\mathbf{m}, \mathbf{d})$, over the data dimension:

$$\sigma_{\mathrm{M}}(\mathbf{m}) = \int \sigma(\mathbf{m}, \mathbf{d}) \, d\mathbf{d}. \qquad (5.5)$$

The *a posteriori* distribution on the model parameters, $\sigma_{\mathrm{M}}(\mathbf{m})$, represents the updated state of information after integrating quantitatively the prior information, the measured data affected by errors, and the theoretical relations between the model parameters and data. From the posterior distribution on the model parameters, $\sigma_{\mathrm{M}}(\mathbf{m})$, we can obtain any type of information, such as the expected values and the median values. More importantly, we can obtain the probability that the model parameters will satisfy various criteria, such as the probability that fracture density is greater than certain thresholds.

In fracture characterization, the model parameters, represented by the vector $\mathbf{m}$, may include the fracture density, the fracture orientation, compressibility of the fractures and of the saturating fluid, etc., while the data may be represented by the near- and the far-offset reflectivity, the azimuthal reflectivity anisotropy, etc.
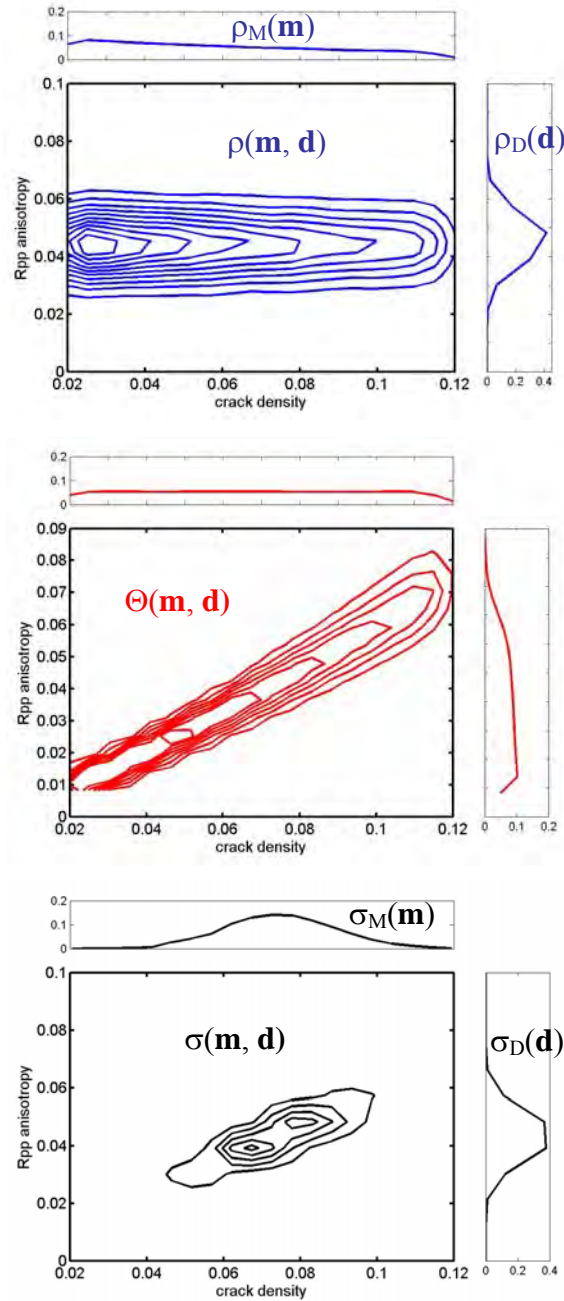
Figure 5.4: *Upper panel*: Joint PDF of the *a priori* information on the model parameter (crack density) and the information on the observable parameters (reflectivity anisotropy). *Middle panel*: Theoretical Joint PDF between crack density and reflectivity anisotropy derived using Hudson's model for randomly oriented fractures. *Lower panel*: *A posteriori* PDF for the model and data, computed by combining the information in the joint prior PDF and theoretical PDF presented in the upper and middle panels.

Figure 5.4 illustrates graphically how we can determine the *a posteriori* PDF, $\sigma(\mathbf{m}, \mathbf{d})$, and its marginal distribution on the model parameters, $\sigma_M(\mathbf{m})$, from $\rho(\mathbf{m}, \mathbf{d})$ and $\Theta(\mathbf{m}, \mathbf{d})$. In this example, the model parameter is the crack density (e), as defined in Hudson's (1981) model, while the data is the azimuthal reflectivity anisotropy (A). The geological hypothesis is that there is a single set of aligned vertical fractures.

The upper panel presents $\rho(e, A)$, the prior joint PDF for the crack density and the azimuthal reflectivity anisotropy, with the corresponding marginal PDFs for the model parameter, $\rho_M(e)$, and for the data, $\rho_D(A)$.

The theoretical joint PDF, $\Theta(e, A)$, presented in the middle panel of Figure 5.4, represents the physical correlation between the crack density and the azimuthal reflectivity anisotropy. In this example the theoretical joint PDF is derived using stochastic simulations and deterministic rock-physics fracture modeling, assuming a single set of aligned fractures. The uncertainty in the relation between the crack density and the reflectivity anisotropy is due to the natural variability of the unfractured rock properties (V_P, V_S, and *density*) of the reservoir and cap rocks, derived from the well-log data. However, the uncertainty due to imperfections and approximations in the physical model is not considered.

The lower panel of Figure 5.4 presents the *a posteriori* joint PDF, $\sigma(e, A)$, for the crack density (e) and the azimuthal reflectivity anisotropy (A). This *a posteriori* PDF is obtained by multiplying the prior joint PDF and the theoretical PDF, using Equation 5.4. The homogenous probability is considered constant. To obtained the updated distribution of crack density $\sigma_M(e)$, shown in black on the top of the lower panel in Figure 5.5, I integrate the *a posteriori* joint PDF $\sigma(e, A)$ over the reflectivity anisotropy (A), as in Equation 5.5. The *a posteriori* distribution, $\sigma_M(e)$, represents the updated measure of uncertainty about the fracture density after conditioning the prior independent information from geological interpretation with the observed azimuthal reflectivity anisotropy. Based on this posterior PDF, presented at the top of the lower panel, we can obtain any central estimators, such as expected values or median values, as well as the probability that the model parameters satisfy certain criteria.

5.3.5   Independent data information

Bayesian analysis (Bayes, 1783) provides mathematical rules for changing our existing knowledge in the light of new evidence. In other words, it allows scientists to combine new data with their existing knowledge or expertise, for better constrained inferences.

Bayes' rule is based on the concept of conditional probability and it allows us to update our information about the model parameters **m**, given the data, **d**. Specifically, our posterior knowledge, expressed in terms of a conditional probability, $P(\mathbf{m} \mid \mathbf{d})$, is proportional to the prior information, $\rho(\mathbf{m})$, multiplied by the likelihood function, $P(\mathbf{d} \mid \mathbf{m})$, (Box and Tiao, 1992). The *a posteriori* distribution presented in the preceding section, $\sigma_M(\mathbf{m})$, may be interpreted as a conditional probability, $P(\mathbf{m} \mid \mathbf{d})$,.about the model parameters, **m**, given the observed data, **d**.

If we have different types of data, $\mathbf{d_1}$, $\mathbf{d_2}$,…, $\mathbf{d_n}$, statistically independent of one-another, we can derive many posterior distributions on the model parameters, $P(\mathbf{m} \mid \mathbf{d_1})$, $P(\mathbf{m} \mid \mathbf{d_2})$,…, $P(\mathbf{m} \mid \mathbf{d_n})$, by separately conditioning the prior information on the different datasets. The question is how to combine quantitatively the different posterior distributions into one result, which contains the information from all datasets. This problem reduces to combining the different conditional probability density functions, $P(\mathbf{m} \mid \mathbf{d_1})$, $P(\mathbf{m} \mid \mathbf{d_2})$,…, $P(\mathbf{m} \mid \mathbf{d_n})$, into a single conditional probability model, $P(\mathbf{m} \mid \mathbf{d_1}, \mathbf{d_2},…, \mathbf{d_n})$.

From the definition of the conditional probability we obtain the following expression:

$$P(\mathbf{m} \mid \mathbf{d_1}, \mathbf{d_2},…, \mathbf{d_n}) = \frac{P(\mathbf{m}, \mathbf{d_1}, \mathbf{d_2},…, \mathbf{d_n})}{P(\mathbf{d_1}, \mathbf{d_2},…, \mathbf{d_n})} . \tag{5.6}$$

The numerator from the Equation 5.6 can be written, using the general multiplication law (Ross, 2001), as follows:

$$P(\mathbf{m}, \mathbf{d_1}, \mathbf{d_2},…, \mathbf{d_n}) = P(\mathbf{m})P(\mathbf{d_1} \mid \mathbf{m})P(\mathbf{d_2} \mid \mathbf{m}, \mathbf{d_1})…P(\mathbf{d_n} \mid \mathbf{m}, \mathbf{d_1},…, \mathbf{d_{n-1}}). \tag{5.7}$$

In Equation 5.7, $P(\mathbf{m})$ is the *a priori* information on the model parameters, $\rho(\mathbf{m})$, from the preceding sections. Using again the general multiplication law, the denominator from Equation 5.6 can be written as follows:

$$P(\mathbf{d_1},\mathbf{d_2},...,\mathbf{d_n}) = P(\mathbf{d_1})P(\mathbf{d_2}|\mathbf{d_1})...P(\mathbf{d_n}|\mathbf{d_1},...,\mathbf{d_{n-1}}). \tag{5.8}$$

Since the data $\mathbf{d_1}$, $\mathbf{d_2}$,…, $\mathbf{d_n}$ are independent, we can write the following relations:

$$P(\mathbf{d_i} \mid \mathbf{m}, \mathbf{d_1}, \mathbf{d_2},..., \mathbf{d_{i-1}}) = P(\mathbf{d_i} \mid \mathbf{m}), \quad (\forall)\, i = 1, 2,...,n, \tag{5.9}$$

and also:

$$P(\mathbf{d_i} \mid \mathbf{d_1}, \mathbf{d_2},..., \mathbf{d_{i-1}}) = P(\mathbf{d_i}), \quad (\forall)\, i = 1, 2,...,n. \tag{5.10}$$

Therefore, Equation 5.6 can be rewritten as follows:

$$P(\mathbf{m} \mid \mathbf{d_1}, \mathbf{d_2},..., \mathbf{d_n}) \; \frac{P(\mathbf{m})P(\mathbf{d_1} \mid \mathbf{m})P(\mathbf{d_2} \mid \mathbf{m})...P(\mathbf{d_n} \mid \mathbf{m})}{P(\mathbf{d_1})P(\mathbf{d_2})...P(\mathbf{d_n})} = P(\mathbf{m})\prod_{i=1}^{n} \frac{P(\mathbf{d_i} \mid \mathbf{m})}{P(\mathbf{d_i})}. \tag{5.11}$$

At the same time, Bayes' rule gives the following expressions:

$$P(\mathbf{d_i} \mid \mathbf{m}) = \frac{P(\mathbf{m} \mid \mathbf{d_i})P(\mathbf{d_i})}{P(\mathbf{m})} \quad (\forall)\, i = 1, 2,...,n. \tag{5.12}$$

If we use Bayes' rule from Equation 5.12 in Equation 5.11, we obtain the following result:

$$P(\mathbf{m} \mid \mathbf{d_1}, \mathbf{d_2},..., \mathbf{d_n}) = \frac{P(\mathbf{m} \mid \mathbf{d_1})P(\mathbf{m} \mid \mathbf{d_2})...P(\mathbf{m} \mid \mathbf{d_n})}{[P(\mathbf{m})]^{n-1}} = P(\mathbf{m})\prod_{i=1}^{n} \frac{P(\mathbf{m} \mid \mathbf{d_i})}{P(\mathbf{m})}. \tag{5.13}$$

Equation 5.13 allows us to integrate quantitatively the different conditional probability density functions, $P(\mathbf{m} \mid \mathbf{d_1})$, $P(\mathbf{m} \mid \mathbf{d_2})$,…,$P(\mathbf{m} \mid \mathbf{d_n})$, derived by independently using each of the statistically independent data, $\mathbf{d_1}$, $\mathbf{d_2}$,…, $\mathbf{d_n}$, into one single conditional probability model, $P(\mathbf{m} \mid \mathbf{d_1}, \mathbf{d_2},..., \mathbf{d_n})$. In other words, if we derive different posterior distributions for the model parameters, based on different types of independent data by using the methodology presented in the preceding sections, we can combine all of these

posterior probabilities into a single posterior probability model, conditioned on all of the data, $\mathbf{d_1}$, $\mathbf{d_2}$,…, $\mathbf{d_n}$, by simply multiplying the individual posterior distributions.

Next section presents a summary with the practical steps for the quantitative data integration applied to fracture characterization.

5.3.6   Summary for the methodology of integration

I present the following practical steps for integrating the prior information about fracture distribution, obtained from the geological interpretation, with the well-log and seismic measurements, using stochastic rock physics modeling within a Bayesian framework:

1) Model parameters

We first decide which model parameters are needed to answer the question under consideration. The model parameters may include the fracture density, orientation and compressibility, the type of fluid in the fractures, the connectivity of the fractures, etc. In some practical problems, we may be interested only in some of these parameters.

2) Geological hypotheses

Next we evaluate the possible geological hypotheses for the fracture model parameters, based on the site-specific outcrop observations, if available, or outcrop analogs, as well as on the well-log information. Another valuable source of information for fracture distribution is the geological structure of the reservoir, which can be obtained from the interpretation of seismic data.

3) Rock-physics modeling and stochastic simulations: Theoretical PDF

We perform rock-physics forward modeling and stochastic simulations based on the well-log data available, under the chosen geological hypotheses. The goals of this step are, first, to choose the most informative seismic attributes with respect to the model parameters (Takahashi, 2000), and second, to derive the physical relations between the model parameters and the chosen seismic attributes. We use rock-physics fracture modeling and stochastic simulations to incorporate the natural variability of the background rock properties. Thus, we run *Monte Carlo* simulations on the input parameters of the deterministic fracture models. One physical theory often used is

Hudson's (1981) model. The input parameters in Hudson's penny-shaped crack model are the crack density, the aspect ratio of the ellipsoidal cracks, the elastic properties of the fluid saturating the cracks, and the V_P, V_S and *density* of the unfractured background rocks, derived from the well-logs. For the crack density, we use a uniform distribution, assuming maximum uncertainty over the interval of variation for the crack density. For the aspect ratio of the penny-shaped cracks, defined as the ratio between the aperture and the radius of the crack, we use a uniform distribution, on a logarithmic scale. For the elastic properties of the fluid, we can use deterministic values, when the fluid saturating the fractures is known, or we can use a uniform distribution spanning the possible values for the bulk modulus and density at reservoir conditions. For the unfractured matrix properties (V_P, V_S, *density*), we use the correlated PDF for V_P, V_S, and *density* derived from the well-log data. If no addition information indicates otherwise, these properties are considered representative and stationary over the area of study. By using *Monte Carlo* simulations, we obtain many realizations of sets of fracture parameters and seismic attributes that span the intrinsic natural variability. Based on these realizations, we can estimate the theoretical joint PDF $\Theta(\mathbf{m}, \mathbf{d})$, which describes the physical relations between the fracture parameters and the seismic attributes. This PDF represents a measure of uncertainty about the relation between the model parameters and the observable data, with its inherent non-uniqueness and non-linearity, due to natural variability of the target rock properties. If the correlated distributions of V_P, V_S and *density* for the reservoir and cap rocks are assumed representative and stationary over the area of study, the theoretical PDF, which describes the relations between the fracture parameters and seismic attributes, may also be assumed stationary and representative for the area of study. However, this theoretical joint PDF is site specific.

4) Prior PDF for fracture parameters

Based on the structural-geology model of the reservoir we estimate the *a priori* PDF $\rho_M(\mathbf{m})$, for fracture parameters at each grid point of the target. More details are given in section 5.3.1, and also in the example from section 5.5.1.2.

5) Seismic data

Seismic measurements are affected by errors. Thus, we need to estimate the uncertainty associated with the observed seismic attributes and describe it using a PDF, $\rho_D(\mathbf{d})$.

6) Combining the prior information on fracture parameters with seismic data

Next we derive the joint PDF, $\rho(\mathbf{m}, \mathbf{d})$, for the fracture parameters and the data at each grid point, assuming that the prior information about the fracture parameters and the actual seismic data are statistically independent.

7) Posterior PDF for fracture parameters: integration of geology and seismic data

Finally, we compute the *a posteriori* PDF, $\sigma(\mathbf{m}, \mathbf{d})$, over the fracture parameters and data by combining the theoretical PDF, $\Theta(\mathbf{m}, \mathbf{d})$, which is considered stationary, with the prior PDF for the model parameters and observable data, $\rho(\mathbf{m}, \mathbf{d})$, which varies with location. Then we integrate the *a posteriori* PDF, $\sigma(\mathbf{m}, \mathbf{d})$, over the seismic attributes space to obtain the updated distribution of fracture parameters $\sigma_M(\mathbf{m})$. This *a posteriori* PDF for the fracture parameters represents the solution to the inverse problem, and it gives a measure of uncertainty about the fracture parameters after integrating prior geological information with seismic data.

From this *a posteriori* PDF for the fracture parameters, we can derive any statistical information, such as any central estimators, like expected or median values. More importantly, we can compute the probability that a certain model will satisfy any criteria, for example, the probability that the fracture density exceeds certain thresholds.

Figure 5.5 presents a flow-chart for integration.
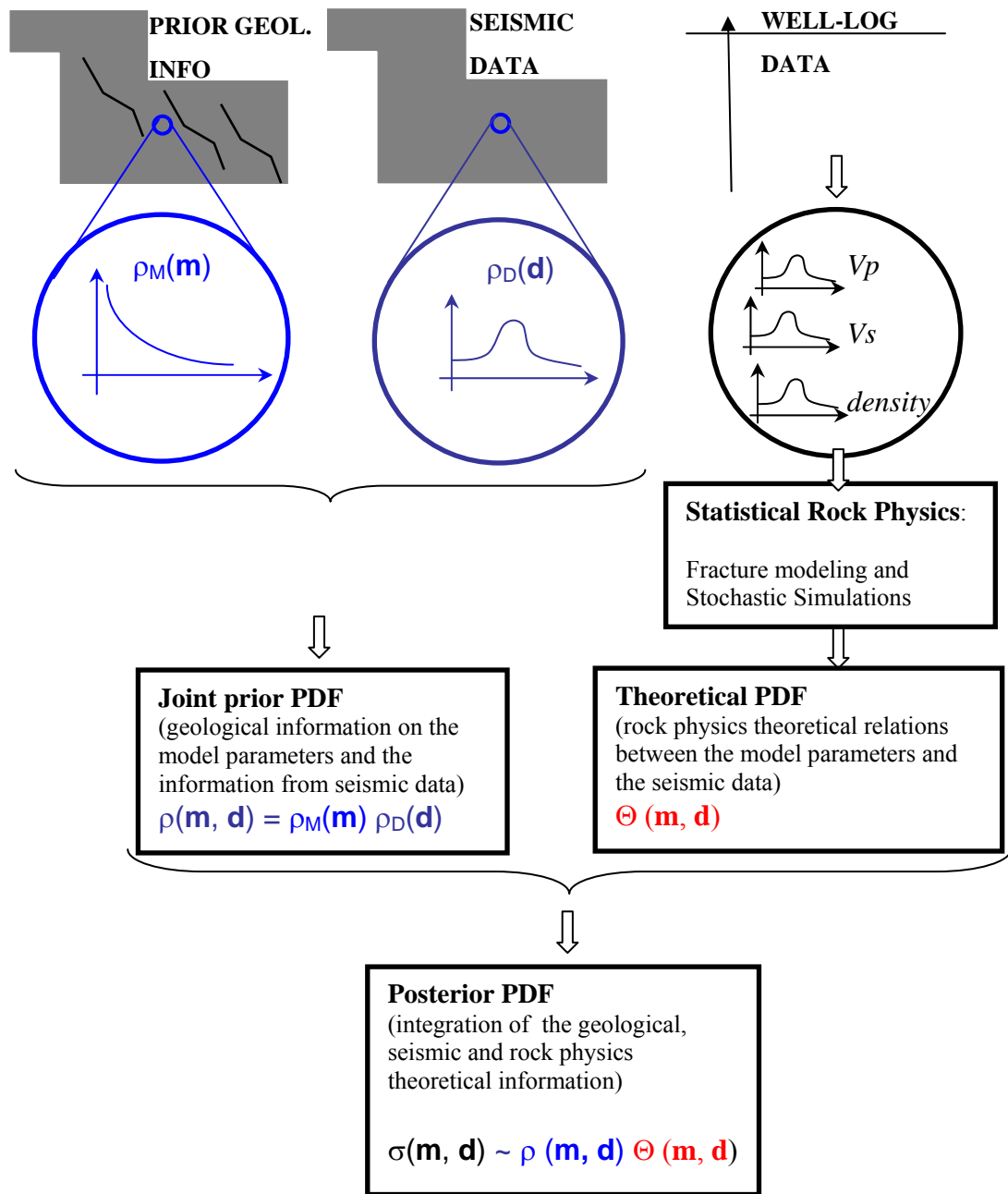
Figure 5.5: Flow-chart with the methodology of integration.

In the next section, I present a method of estimating the prior PDF for the fracture parameters by using geological and theoretical constraints.

5.4   The *a priori* PDF for fracture density

The prior distribution of the variable of interest is an important ingredient in any Bayesian analysis (Bayes, 1783), and it may sometimes play an important role in determining the final results. Even if the prior information is vague, using it helps in formulating well-posed inverse problems.

Traditionally, all probabilities were treated as frequencies. Here, the word "frequency" is used in the sense of the number of times an event occurs. However, Bayesian theory does not define a probability as a frequency of occurrence of an event, but as a reasonable degree of belief (Laplace, 1814). In other words, the probability is viewed as a measure of the uncertainty about a particular parameter, and it represents the *state of knowledge* about that parameter. Therefore, probability is related to the state of uncertainty, and not (only) to the outcome of repeated experiments. This view of the probability is much more useful in most of the practical applications in science and engineering.

However, assigning the prior probability is one of the most controversial areas in Bayesian probability. Yet, to a Bayesian, it is the most natural of things. No one would think of trying to solve any problem without using all of his prior experiences. There are different ways of assigning prior probabilities (Jaynes, 1983), but one of the most used is based on the Maximum Entropy Principle, as defined by Jaynes (1983), which has its foundation on Shannon's (1948) information theory.

In information theory, uncertainty is quantified by a parameter called "information entropy", *H(X)*. *H(X)* is a statistical parameter that quantifies the state of knowledge for parameter *X*, and it can be calculated from the PDF of *X*, *P(X)*, using the following formula:

$$H(X) = -\sum_i P(x_i)\log[P(x_i)].$$ (5.14)

This quantity is a measure of the amount of ignorance in the probability distribution of the variable *X* (Shannon, 1948; Takahashi, 2000).

Jaynes' Maximum Entropy Principle states that from all of the probability distribution functions consistent with a given set of constraints, we should choose the one that maximizes the uncertainty, as defined by Shannon (1948).

In the discreet case, it can be shown that if nothing is known, except that the probability distribution should be normalized, the maximum entropy principle reduces to the uniform prior. This is Laplace's *principle of insufficient reason* (Laplace, 1814). However, the maximum entropy is more general, because it allows one to assign probabilities that are maximally uninformative, while still incorporating the known information. The term "uninformative" may sound negative, but its meaning is related to defining PDFs that do not convey unintentional biases. Therefore, the principle of maximum entropy represents a useful tool for assigning probabilities based only on the information that one actually possesses.

Therefore, to estimate prior probabilities for fracture density, we should first quantify the geological constraints at each spatial location. Then, we can determine the maximum entropy PDF at that location by maximizing Shannon's entropy, consistent with the local constraints. This is a classical problem of optimization under constraints, for which we can use the method of Lagrange multipliers.

One of the constraints we can put on fracture density from both practical and theoretical considerations is related to its range of variability. Fracture density should not be smaller than 0, because negative fracture density has no physical meaning. At the same time, fracture density has also an upper bound, beyond which the rock loses its strength, as I discuss in Chapter 2 (Figure 2.3). If no other constraints are specified from geology, then the maximum entropy PDF is given by a uniform distribution over the interval between 0 and the theoretical upper bound of fracture density (e^{up}), as follows:

$$P(e) = \begin{cases} \dfrac{1}{e^{up}}, & e \in \begin{bmatrix} 0 & e^{up} \end{bmatrix} \\ 0, & else \end{cases} \qquad (5.15)$$

If from the geological interpretation we additionally obtain the local mean value of fracture density (*m*), then the maximum entropy PDF is given by a truncated exponential as follows:

$$P(e) = \begin{cases} ce^{-ke}, & e \in \begin{bmatrix} 0 & e^{up} \end{bmatrix} \\ 0, & else \end{cases}. \tag{5.16}$$

The constants c and k in the above formula are determined from the conditions that the $p(e)$ is a PDF and therefore integrates to 1, and that the expected value of this PDF is equal to the known mean value m. These conditions are expressed as follows:

$$c \int_0^{e^{up}} \exp(-ke) = 1, \quad and \quad c \int_0^{e^{up}} e \, \exp(-ke) = m. \tag{5.17}$$

The probability density function for fracture density, defined as an exponential distribution, is in good agreement with the outcrop observations, which suggest exponential or log-normal distributions for fracture density (Snow, 1968; Priest and Hudson, 1976; Sen and Kazi, 1984; La Pointe and Hudson, 1985; Rouleau and Gale, 1985; Bouroz, 1990; Villaescusa and Brown, 1990; Narr and Suppee, 1991; Rives et. al, 1992). I derive the same conclusion also from the field data on shear-wave anisotropy, collected by different authors and summarized by Crampin (1994). Assuming that the shear-wave anisotropy is caused by the alignment of fractures, the computed crack density exhibits an approximately exponential, or log-normal distribution, as I discuss in Chapter 2 (Figures 2.14 and 2.16).

The Maximum Entropy Principle is a very useful tool to define prior probabilities for Bayesian analysis that are consistent with a given set of constraints imposed by the geological interpretation.

5.5   Real data example

In this section, I illustrate the integration of prior geological information on fractures with reflectivity attributes from a 3D seismic data set acquired over a fractured carbonate reservoir in eastern Texas. More information on the reservoir and the seismic data are presented in Chapters 3 and 4.

The goal is to update the information on the fracture density, as described in Hudson's (1981, 1997) model, by integrating the prior information with seismic data.

Thus, the model parameter is the crack density, while the observable, or data parameters are the reflectivity attributes. I assume that the fractures are gas-saturated, and the objective is to delineate the zones of higher fracture density at the top of the reservoir.

Based on the geological information about the reservoir, I consider two geological hypotheses. The first hypothesis is that the fractures are vertical, aligned, and fairly regularly spaced, such that they generate an anisotropic medium. The fracture orientation in this hypothesis was already determined from the Amplitude Variation with Azimuth at far offsets, using a bootstrap method presented in the previous chapter. Therefore, the fracture orientation is not a model parameter, since it was already determined from the seismic data.

The second hypothesis is that the fractures occur in swarms associated with possible subseismic faults, and are more-or-less randomly oriented, such as in brecciated zones. In this hypothesis, the fracture orientation is not a model parameter either, since the assumption is that the fractures are randomly oriented.

5.5.1   Available information

In this section I present the seismic attributes extracted from the 3D seismic data set presented in the previous chapter, which I use for constraining the prior information on fracture density. I also show an example of estimating the prior information about the fracture density, based on a geological interpretation.

5.5.1.1 Seismic data

The seismic data used is represented by the amplitude of the seismic waves at the top of the fractured gas reservoir. The distribution of the near-offset (0 –3000 ft) reflectivity is shown in Figure 5.6, while the distribution for the far-offset (4000 ft – 8000 ft) reflectivity is shown in Figure 5.7. I use large superbins of 1600 ft to eliminate the strong impact of the acquisition footprint on the seismic amplitudes, as I present in Chapter 4, sections 4.3 and 4.4.
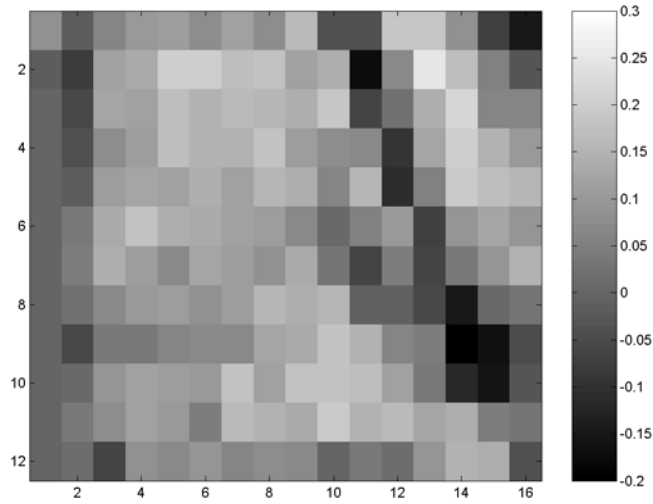
Figure 5.6: Map with the near-offset stack of *PP* reflectivity at the top of the reservoir for large superbins (1600 ft).
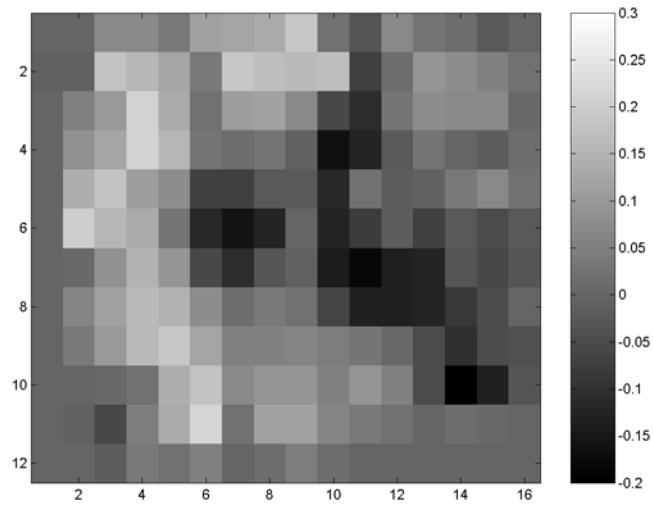
Figure 5.7: Map with the far-offset stack of *PP* reflectivity at the top of the reservoir for large superbins (1600 ft).

Figure 5.8 shows the difference between the near- and far-offset reflectivity, stacked over all azimuths, at a time slice corresponding to the top of the reservoir.
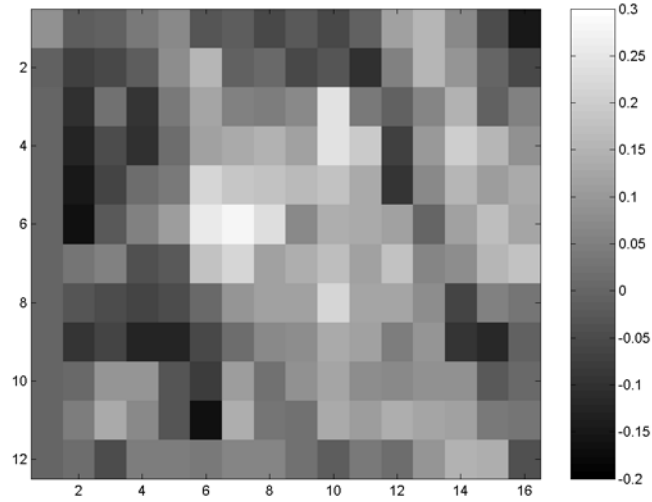
Figure 5.8: Map with the difference between the near- and the far-offset *PP* reflectivity
stacks over all azimuths at the top of the reservoir for large superbins (1600 ft).

In the hypothesis of a nearly vertical set of fractures, as the FMI data from a nearby well suggests, the reflectivity at far offsets varies with azimuth. At a fixed angle of incidence, the variation of the reflectivity with azimuth can be approximated by a cosine function (Teng, 1998). I use a least-square cosine fitting procedure to describe the observed azimuthal variation of the reflectivity at far offsets, as presented in the previous chapter, section 4.5. I take into account the measurement errors associated with the reflectivity, by using a bootstrap method to derive the uncertainty in the parameters describing the sinusoidal variation with azimuth: the mean value of the reflectivity, the amplitude of the oscillation, and the phase. More details on the procedure are given in Chapter 4.

I define the azimuthal anisotropy of reflectivity to be the amplitude of the oscillation. This amplitude is given by the absolute difference between the maximum and the minimum values in the azimuthal variation of the reflectivity at far offsets, as follows:

$$A= |R_{max} - R_{min}|. \tag{5.18}$$

Rock-physics modeling shows that, at a fixed angle of incidence, this amplitude increases with increasing crack density, as I show later in this chapter.

Figure 5.9 shows the distribution for the mean values of the azimuthal reflectivity anisotropy at the top of the reservoir, determined in Chapter 4.
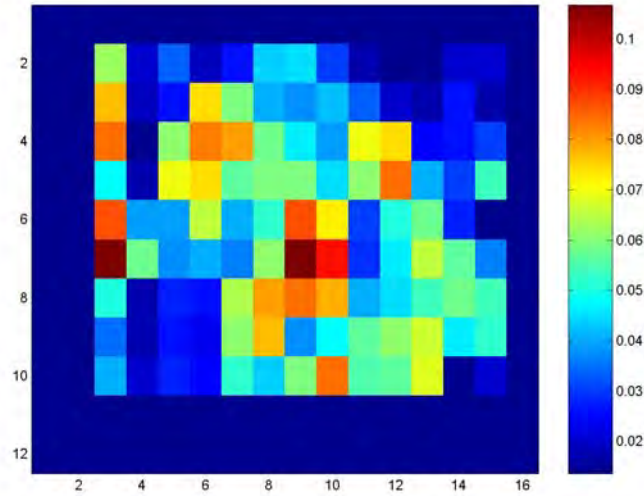
Figure 5.9: Map with the mean values of the azimuthal reflectivity anisotropy (*A*) at far offsets at the top of the reservoir. Superbin size is 1600 ft.

Figure 5.10 shows the distribution of the standard deviation associated with the mean values of the azimuthal reflectivity anisotropy from Figure 5.9, determined by using a bootstrap method (Chapter 4, section 4.5).
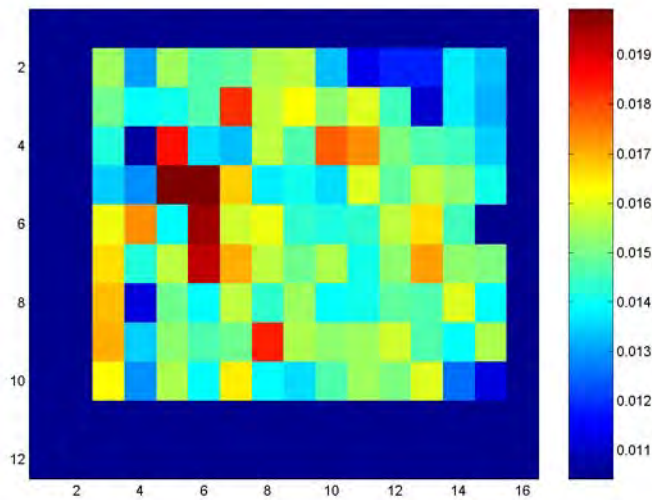
Figure 5.10: Map with the standard deviation for the azimuthal reflectivity anisotropy (*A*) at far offsets at the top of the reservoir. Superbin size is 1600 ft.

As the geological model for this carbonate reservoir suggests, I consider two hypotheses: a vertical set of fractures, and a random distribution for fracture orientations.

In the hypothesis of randomly oriented fractures, the data space consists of the near- and the far-offset reflectivity, presented in Figures 5.6 and 5.7, respectively.

Using Tarantola's (1987) formulation, we can express the uncertainty about the data using a probability density function over the data space. In this example, I assume the PDF to be a correlated bivariate normal distribution, as follows:

$$\rho_D(R_N, R_F) = \text{Gaussian} \ (R_N, R_F, R_{Nobs}, s^2, R_{Fobs}, s^2, r), \quad\quad (5.19)$$

where R_N represents the near-offset reflectivity and R_F is the far-offset reflectivity. R_{Nobs} and R_{Fobs} are the observed data values, which represent the means of the Gaussian bivariate function. The standard deviation, s, of the near- and the far-offset reflectivity is assumed the same over the entire survey, equal to a percentage of the mean value of reflectivity at the top of the reservoir. In Equation 5.19, r represents the correlation coefficient between the near- and the far-offset reflectivity. This correlation coefficient is estimated from the data to be 0.6.

For the case of a vertical set of fractures, the data space is represented by the azimuthal anisotropy of reflectivity at far offsets, presented in Figure 5.9, together with the difference between the near- and the far-offset reflectivity, stacked over all azimuths, presented in Figure 5.8. In this case, the probability density function over the data space is assumed as follows:

$$\rho_D(A, G) = \text{Gaussian} \ (A, A_{obs} , s_A^2) \ \text{Gaussian} \ (G, G_{obs}, s_G^2), \quad\quad (5.20)$$

where A is the azimuthal anisotropy of reflectivity at far offsets. A_{obs} are the observed values from Figure 5.9, which are considered to be the means of the Gaussian function, with the standard deviation s_A presented in Figure 5.10. G represents the difference between the near- and far offset reflectivity. G_{obs} are the observed values, presented in Figure 5.8, which are considered to be the mean of the Gaussian function, while s_G is the standard deviation of the difference between the near- and far-offset reflectivity. Equation 5.20 implies that the variables A and G are independent. This assumption may be justified, since the data shows a very small correlation coefficient between these variables. In this case the joint PDF over the data space is given by the product between

the two marginal distributions. The standard deviation squared, s_G^2, of the variable G, corresponds to the variance of the difference between the near- and far-offset reflectivity, and it is given as follows:

$$s_G^2 = Var\ (G) = Var(R_N\text{-}R_F) = Var(R_N) + Var(R_F)\ \text{-}\ 2Cov(R_N,\ R_F) = 2s^2\ \text{-}\ 2r/s^2,\quad (5.21)$$

where s represents the standard deviation of the near- and far-offset reflectivity, and r represents the correlation coefficient between the near- and far-offset reflectivity, estimated from the data.

5.5.1.2 Prior geological information

Rocks undergoing fracturing exhibit increased fracture density with increased strain (Nelson, 1985). Therefore, large fracture densities are usually associated with the presence of faults. Fracture density increases in the proximity of faults, and it decreases away from them. Outcrop studies show that the decrease of the fracture density with increasing distance from a fault may follow an exponential law (Davatzes, 2003).

Figure 5.11 presents a map with the distribution of the mean values of fracture density at the top of the fractured reservoir. This spatial distribution is based on the geological interpretation of a fault from seismic data (Figure 5.12). In the proximity of the fault, the expected crack density is larger than away from the fault. Outcrop observations can help in calibrating the initial distribution of the mean values for fracture density in relation to the fault observed from seismic data. However, the fracture density values from outcrops should be transformed to the corresponding reservoir stresses.

In this example, I assume a smooth exponential decay for the mean fracture density with increasing distance from the fault, as we can observe in Figure 5.11. The expected fracture density in the proximity of the fault is assumed to be 0.07. This value corresponds to an upper value for the crack density of a reservoir at 2 km depth, based on the shear-wave data collected by Crampin (1994), as I discuss in Chapter 2 (Figure 2.19).
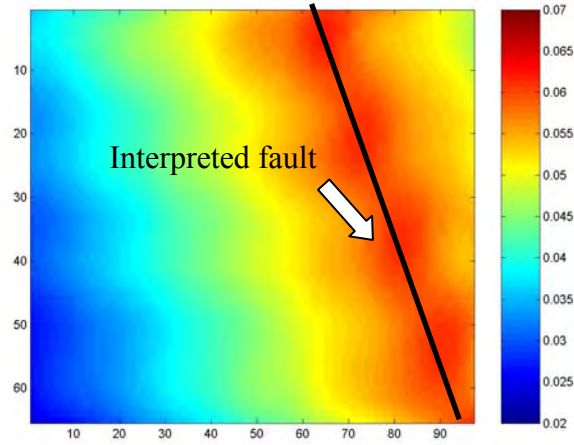
Figure 5.11: Map with the interpolated *a priori* spatial distribution of the mean value of fracture density at the top of the reservoir, based on the geological interpretation of a fault.
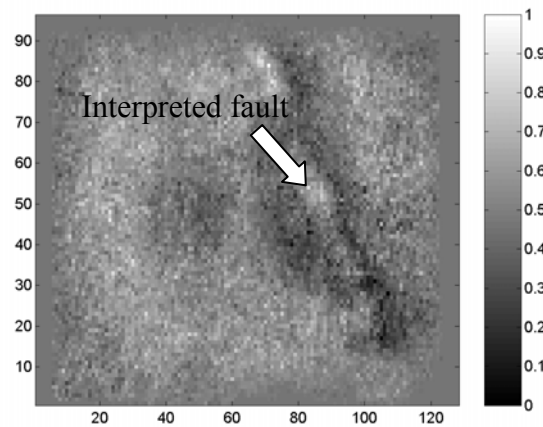
Figure 5.12: Amplitude map at the top of a fractured carbonate reservoir, with the interpreted fault. Bin size is 200 ft.

Of course, there is a large uncertainty about these mean values of fracture density presented in Figure 5.11, which is quantified through the local *a priori* probability density functions. I estimate the local prior PDF for fracture density at each grid point, using the Maximum Entropy Principle, presented in the preceding section. At each spatial location, the *a priori* PDF for fracture density is given by a truncated exponential over the interval 0.02 to 0.12, with the expectation given by the local mean values from Figure 5.11.

Therefore, the prior PDF on the model parameter, represented by the crack density e, is expressed as follows:

$$\rho_M(e) = \begin{cases} ce^{-ke}, & e \in [0.02 \ \ 0.12] \\ 0, & else \end{cases}. \tag{5.22}$$

In Equation 5.22, e represents the crack density as described in Hudson's (1981) penny-shaped crack model. The lower value of the interval for which the PDF is defined corresponds to a small degree of fracturing, while the upper value of 0.12 is slightly larger than the limit of validity for the Hudson's model, and it corresponds to a high degree of fracturing for the reservoir conditions.

The constants c and k from Equation 5.22 are to be determined at each special location, such that the function in Equation 5.22 satisfies the condition of a PDF (its integral is 1), and such that its expectation is equal to the local mean, derived from the geological interpretation, presented in Figure 5.11.

5.5.2 Theoretical PDF: Rock-physics stochastic modeling

Rock-physics theories (Mavko et al., 1998) provide the link between the fracture parameters and the seismic data.

This section presents the rock-physics fracture modeling and stochastic simulations to describe the theoretical relations between the fracture parameters and the *PP* reflectivity attributes, taking into account the natural variability of the target rock properties.

I use Hudson's (1981, 1997) penny-shaped crack model to predict the elastic properties of the fractured media. I also use Vavrycuk's and Psencik's (1998) approximation for weak contrast and weak anisotropy to compute the reflectivity variation with incidence angle and azimuth from the top of the reservoir, in the case of a vertical set of fractures. I use the Zoeppritz (1919) equations in the case of randomly oriented fractures.

For example, in the hypothesis of a vertical set of aligned fractures, we can write generically the relation between the fracture parameters and the elastic properties of the fractured media:

$$[C^{bot}, den^{bot}] = g(V_p^{bot}, V_S^{bot}, density^{bot}, e, \alpha, K_{fl}), \tag{5.23}$$

where C^{bot} and den^{bot} represent the elastic stiffness matrix and the density of the fractured reservoir rocks, modeled with a single set of aligned cracks. The input parameters in Hudson's model are the *P*-wave velocity, the *S*-wave velocity, and the density (V_P^{bot}, V_S^{bot}, $density^{bot}$) of the unfractured isotropic rocks, the crack density (e), the aspect ratio of the cracks (α), and the bulk modulus (K_{fl}) of the fluids saturating the fractures.

After I derive the elastic properties of the fractured media, I use the approximation from Vavrycuk and Psencik (1998) to compute the reflectivity at the interface between the reservoir, modeled with a set of vertical fractures, and the cap rocks. The relation between the fracture parameters and the reflectivity attributes can be written as follows:

$$\begin{aligned} [R_N, R_F, A,] &= f(C^{top}, den^{top}, C^{bot}, den^{bot}) = \\ &= f(\ g(V_p^{bot}, V_S^{bot}, density^{bot}, e, \alpha, K_{fl}), \ V_P^{top}, V_S^{top}, den^{top}) \end{aligned} \tag{5.24}$$

In Equation 5.24, the function *f* represents symbolically the approximation for the reflectivity variation with incidence angle and azimuth, at the interface between the reservoir and the cap rocks. C^{top} and den^{top} are the elastic stiffness matrix and the density of the cap rocks. If the cap rocks are isotropic, the elastic properties can be fully described by the *P*- and *S*-wave velocities (V_P^{top}, V_S^{top}). The function *g* represents Hudson's theory, symbolically shown in Equation 5.23. R_N, R_F and A represent the reflectivity attributes: the near- and far-offset reflectivity, as well as the azimuthal anisotropy of reflectivity at far offsets (Equation 5.18).

Theoretically, given a set of elastic parameters corresponding to the cap and the reservoir rocks, we can predict uniquely the near- and far-offset reflectivity, as well as the amplitude of the sinusoidal variation of the reflectivity at far offset as a function of azimuth. However, the relations between the fracture parameters and the reflectivity attributes are uncertain, because of approximations in the theory, and, more importantly, because the subsurface rock properties are naturally variable. When deriving the relations between the fracture parameters and the reflectivity attributes, I ignore the uncertainties due to theoretical approximations, and I account for the uncertainty due to natural variability of the target rocks. Therefore, I run *Monte Carlo* simulations on the input

parameters in Hudson's model (1981). As already mentioned, the input parameters are the crack density (e), aspect ratio (α) of the ellipsoidal cracks, defined as the ratio between the small and the long semiaxes, the bulk modulus of the saturating fluid (K_{fl}), and the V_P^{bot}, V_S^{bot} and *density^{bot}* of the unfractured background rocks.

To estimate the theoretical PDF, which describes the uncertain relations between the fracture parameters and the observable parameters due to natural variability, I use a uniform distribution for fracture density, between 0.02 and 0.12. This represents a relevant interval for the fracture density. The lowest value of the interval corresponds to practically intact rocks, while the upper value corresponds to a relatively large degree of fracturing, especially for a reservoir at approximately 2 km depth, as I discuss in Chapter 2 (Figure 2.19). For the aspect ratio of the penny-shaped cracks I also use a uniform distribution, on a logarithmic scale (from 0.001 to 0.1). More details about Hudson's model are given in Chapter 2.

For the unfractured matrix properties (V_P, V_S, *density*), I derive the distributions from the well-log data. Figure 5.13 presents in the upper panels the histograms for the V_P^{bot} V_S^{bot}, and *density^{bot}* of the clean limestones in the reservoir, obtained from the well-log data from a nearby well. The lower panels in the same figure present the probability distribution functions (PDF) of the *P*-wave velocity, *S*-wave velocity and density derived from the histograms.

The V_P, V_S, and *density* properties derived from the well logs for both reservoir and cap rocks are upscaled to seismic wavelengths. The upscaling is performed on the well data using Backus (1962) averages for the bulk and shear moduli, and volumetric averages for density (Mukerji, 1995).

The distributions for the seismic properties (V_P, V_S, and *density*) for both reservoir and cap rocks are assumed representative and stationary over the area of study.
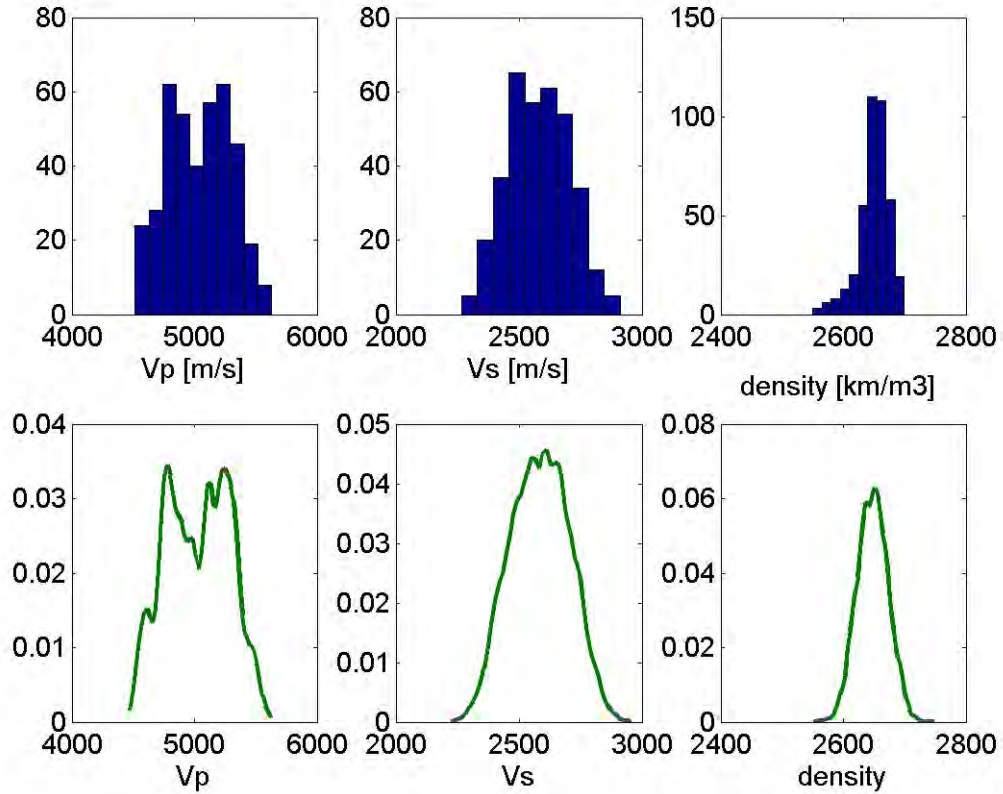
Figure 5.13: Upper panels: V_P V_S and density histograms derived from the well logs for the unfractured background rock properties. Lower panels: Corresponding probability density functions (PDFs).

The *Monte Carlo* procedure consists of randomly drawing correlated sets of V_P^{bot}, V_S^{bot}, and *density*^{bot} from the distributions derived from the well logs for the unfractured background rock properties, and also from the assumed distributions for the crack density (*e*) and the aspect ratio (α) of the ellipsoidal cracks. I assume fractures to be saturated with gas. For each realization of a set of V_P^{bot}, V_S^{bot}, and *density*^{bot}, together with the crack density and the aspect ratio of the cracks, I compute the elastic properties for the fractured medium, using Hudson's model. If we repeat this procedure many times, we obtain a large number of realizations of elastic properties for the modeled fractured medium, which spans the intrinsic natural variability of the target rock properties.

For each realization, I again randomly draw a correlated set of V_P^{top}, V_S^{top}, and *density*^{top} from the distribution corresponding to the cap rocks. Then, I compute the reflectivity at 0 and 40 degrees, stacked over all azimuths, corresponding to the near-

offset reflectivity (R_N) and the far-offset reflectivity (R_F). I also compute the difference between the near- and far-offset reflectivity (R_N-R_F), as well as azimuthal anisotropy of reflectivity at 40 degrees (*A*), using equations from Vavrycuk and Psencik (1998).
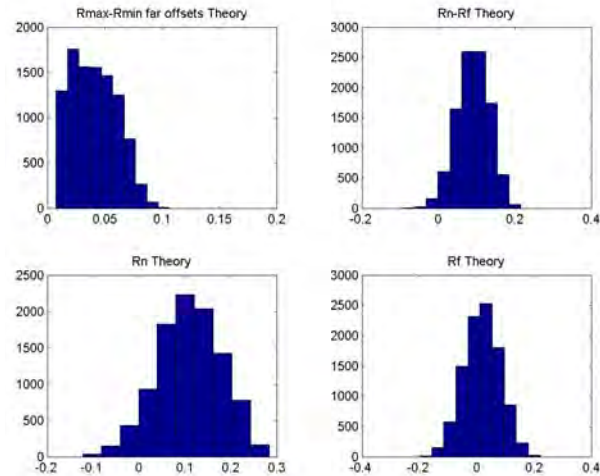
Figure 5.14:   Histograms for the modeled reflectivity attributes. Top-left panel: Azimuthal anisotropy of reflectivity (*A*), evaluated at a 40 degree angle of incidence. Top-right panel: difference between the near- and far-offset reflectivity (R_N –R_F). Bottom-left panel: Near-offset reflectivity (R_N) Bottom-right panel: Far-offset reflectivity (R_F).

Figure 5.14 presents the histograms for the four different reflectivity attributes (R_N, R_F, R_N-R_F, and *A*) theoretically modeled, using the procedure described above. For comparison, Figure 5.15 presents the histograms for the same reflectivity attributes obtained from the seismic data. In both figures, the top-left panel presents the histogram for the azimuthal anisotropy in reflectivity at far offsets. We can observe that the theoretical and data-derived distributions are very similar. This suggests that the range of the crack density used in the modeling is relevant for this reservoir. The distributions for the near- and far-offset reflectivity presented on the bottom panels of both Figure 5.14 and 5.15 also agree reasonably well.
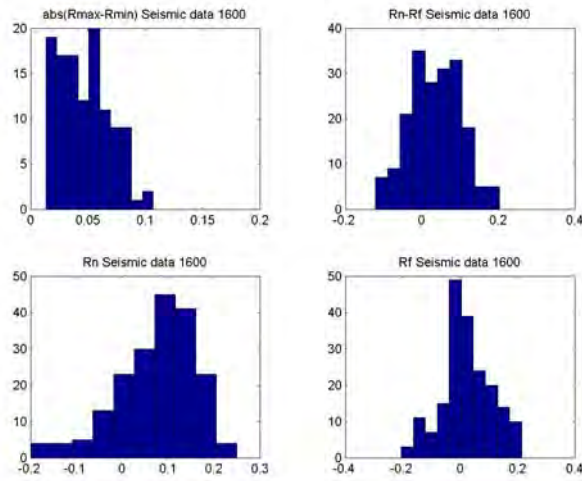
Figure 5.15: Histograms for the seismic reflectivity attributes derived from the real data. Top-left panel: Azimuthal anisotropy in reflectivity (A), evaluated at a 40 degrees angle of incidence Top-right panel: difference between the near- and far-offset reflectivity ($R_N - R_F$). Bottom-left panel: Near-offset reflectivity (R_N) Bottom-right panel: Far-offset reflectivity (R_F).

Figure 5.16 presents a 3D scatter-plot for the *Monte Carlo* realizations for sets of crack density, corresponding azimuthal anisotropy of reflectivity (A) at far offsets, and the difference between the near- and far-offset reflectivity ($R_N - R_F$).
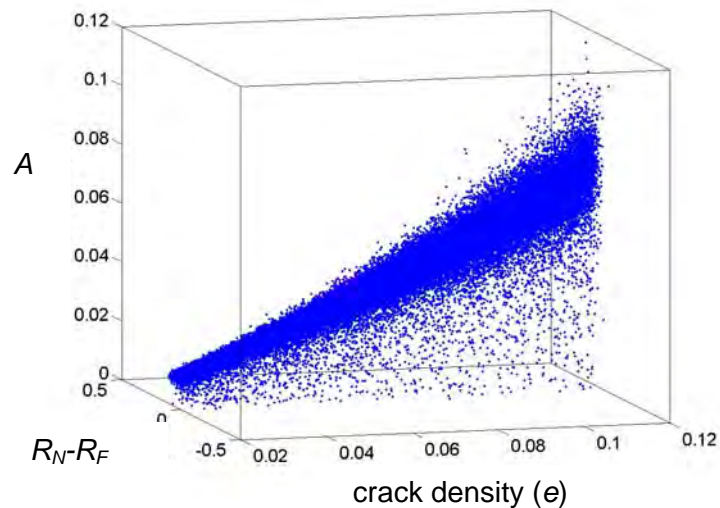
Figure 5.16: 3D scatter-plot for the 50,000 Monte Carlo realizations of sets of crack density (e), corresponding azimuthal anisotropy of reflectivity (A) at far offsets, and difference between the near- and the far-offset reflectivity ($R_N - R_F$).

From Figure 5.16, we can observe, as expected, that the azimuthal anisotropy in reflectivity at a fixed angle of incidence increases with crack density. Figure 5.17 presents the same scatter-plot for the *Monte Carlo* realizations as Figure 5.16, but projected in the plane of crack density and the difference between the near and the far reflectivity (R_N-R_F). We can observe that the rock-physics fracture modeling predicts that the difference between the near- and far-offset reflectivity increases with crack density. This observation is in accordance with the modeling results presented in Chapter 3, where I show that the gas-filled fractured zones move the *AVO* gradient to larger negative values as compared to the *AVO* gradient of the unfractured rocks.
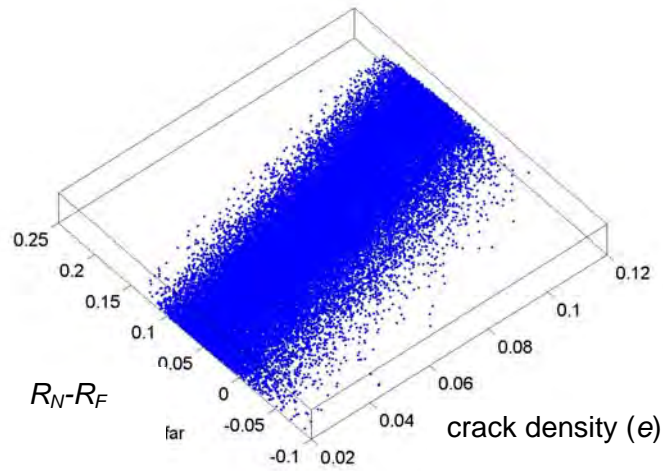
Figure 5.17: Scatter-plot for the 50,000 Monte Carlo realizations of sets of crack density (*e*) and the corresponding difference between the near- and the far-offset reflectivity (R_N –R_F).

Based on these 50,000 realizations of sets of crack density and reflectivity attributes, I derive the theoretical joint PDF, presented in Figure 5.18 as slices at constant *A* values. This theoretical PDF describes the relations between the fracture density and the observable data, represented by the reflectivity attributes, assuming a single set of vertical fractures. I denote this theoretical PDF as $\Theta(e, A, G)$, where *G* is given by the difference between the near- and far-offset reflectivity *(R_N-R_F)*.
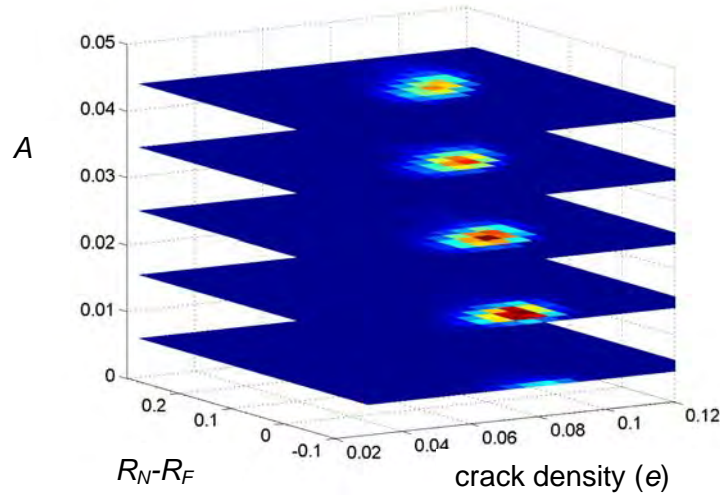
Figure 5.18: Theoretical Joint PDF based on the 50,000 Monte Carlo realizations of sets of crack density (e), corresponding azimuthal reflectivity anisotropy (A), and difference between the near- and the far-offset reflectivity ($R_N - R_F$). The PDF is presented as slices at constant A values.

I also consider the case of isotropic distribution of fracture orientations, corresponding to the highly fractured, brecciated zones. In this case, I use Hudson's (1981) model for isotropic distribution of the crack normals, and also Zoeppritz (1919) equations to derive the observable parameters, represented by the near- and far-offset reflectivity.

For both the isotropic and anisotropic fracture distributions, I assume the fractures to be saturated with gas.

In the next section, I present the results of integrating the prior information about fracture density with the reflectivity attributes from the 3D seismic data set, for hypotheses of both isotropic and anisotropic distribution of fractures.

5.5.3 *A posteriori* **fracture density distribution**

To obtain the updated distribution of fracture density at each spatial location, we need to combine the prior information, the reflectivity attributes affected by errors, and the theoretical information about the relations between the crack density and the seismic attributes, as presented in the previous sections.

I first obtain the updated fracture density distribution in the geological hypothesis of a vertical set of aligned fractures.

Figure 5.19 presents a map with *a posteriori* spatial distribution of the posterior expected values for fracture density at the top of the reservoir, conditioned only on the azimuthal anisotropy of reflectivity at far offsets (*A*).

Figure 5.19: Map of the expected values for crack density derived from the *a posteriori* distribution, obtained by constraining the *a priori* information with the azimuthal anisotropy of reflectivity at far offsets (*A*), in the hypothesis of a vertical set of aligned fractures.

We observe a relatively higher fracture density in the proximity of the fault that penetrates the carbonate reservoir, sketched in Figure 5.19. We can also observe the asymmetric distribution of the expected crack density with respect to the fault, with higher values of fracture density in the hanging wall. This result is in agreement with outcrop observations that suggest higher fracture density in the proximity of the fault, especially in the hanging wall (Florez, 2003). We can also observe zones of higher fracture density away from the fault. These zones may also correspond to possible

subseismic faults. Also, the expected posterior values for the crack density are significantly larger than the prior values, presented in Figure 5.11, which were calibrated using Crampin's (1994) collection of field data (Chapter 2) The stochastic rock physics modeling predicts a large correlation coefficient between the crack density and the azimuthal anisotropy in reflectivity, equal to 0.96. Therefore, the theory predicts that the azimuthal anisotropy in reflectivity is very constraining, such that the prior distribution for fracture density does not play a crucial role in the final results, in this case.

However, if I consider larger uncertainty in the data, the impact of the prior information is more significant. For example, Figure 5.20 presents a map with *a posteriori* distribution of the expected values for fracture density at the top of the reservoir, conditioned on the azimuthal anisotropy of reflectivity at far offsets (*A*), whose standard deviations of the measurement uncertainty are one order of magnitude larger than the ones derived from the bootstrap procedure (Chapter 4).

Figure 5.20: Map of the expected values for crack density derived from the *a posteriori* distribution, obtained by constraining the *a priori* information with the azimuthal anisotropy of reflectivity at far offsets (*A*), in the hypothesis of a vertical set of aligned fractures. Standard deviations of the measurement uncertainty are one order of magnitude larger than those in Figure 5.10.

We can observe that, when the measurement uncertainty is significantly larger, the prior information has a bigger impact on the posterior distribution of the crack density. The expected posterior values of crack density from Figure 5.20 are significantly closer to the prior values, than the ones from Figure 5.19.

Next I obtain the distribution for the posterior expected values of fracture density at the top of the reservoir, conditioned on the difference between the near- and far-offset reflectivity ($G= R_N-R_F$), presented in Figure 5.21.
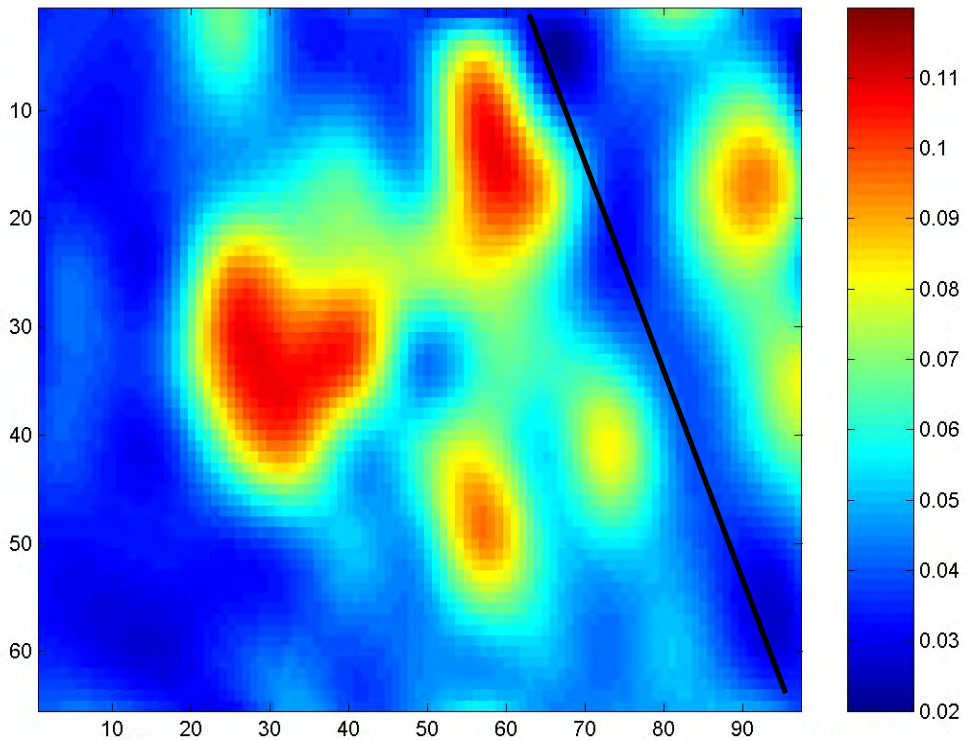
Figure 5.21: Map of the expected values for crack density derived from the *a posteriori* distribution, obtained by constraining the *a priori* information with the difference between the near- and far-offset reflectivity (G), in the hypothesis of a vertical set of aligned fractures.

From Figure 5.21 we observe that, by conditioning on the difference between the near- and the far-offset reflectivity, the expected values for fracture density along the fault are small. This is because along the fault the difference between the near- and far-offset reflectivity is small (Figure 5.8), and the rock-physics modeling predicts lower fracture density for smaller differences between the near- and far-offset reflectivity, as we can see in Figure 5.17. This result apparently contradicts the geological hypothesis of

larger fracture densities along the fault. One explanation may be that the fault acts as a scattering feature for the seismic waves, generating small amplitudes for the near-offsets, such that the difference between the near- and the far-offset reflectivity is itself small. On the other hand, the theoretical relations between the fracture properties and the seismic amplitudes derived through rock-physics fracture modeling and stochastic simulations correspond to effective medium theory, and they do not account for phenomena such as scattering.

However, we can still observe relatively higher fracture density in the proximity of the fault, especially in the hanging wall, as well as away from the fault (Figure 5.21). On average, the expected crack-density values obtained by combining the prior information with the difference between the near- and far-offset reflectivity (*G*) are smaller than the expected values for crack density obtained by combining the prior information with the azimuthal anisotropy of reflectivity at far offsets (*A*). This is because the stochastic rock physics modeling predicts a smaller correlation coefficient between the crack density and *G* (0.63), than between the crack density and *A* (0.96). Therefore, the impact of the prior crack density distribution on the posterior distribution obtained by conditioning on *G* is more significant than on the posterior distribution obtained by conditioning on *A*.

I also obtain the updated distribution of the expected values for fracture density at the top of the reservoir using jointly both reflectivity attributes: the azimuthal anisotropy of reflectivity at far offsets (*A*), and the difference between the near- and far-offset reflectivity (*G*).

Figure 5.22 presents the posterior expected values of fracture density jointly conditioned on both attributes. We can see that the distribution of the expected values for the crack density at the top of the reservoir conditioned on both attributes *A* and *G* is dominated by the reflectivity anisotropy (*A*) at far offsets. This is because the rock-physics fracture modeling and stochastic simulations predict higher correlation between the crack density and *A* than between the crack density and *G*.
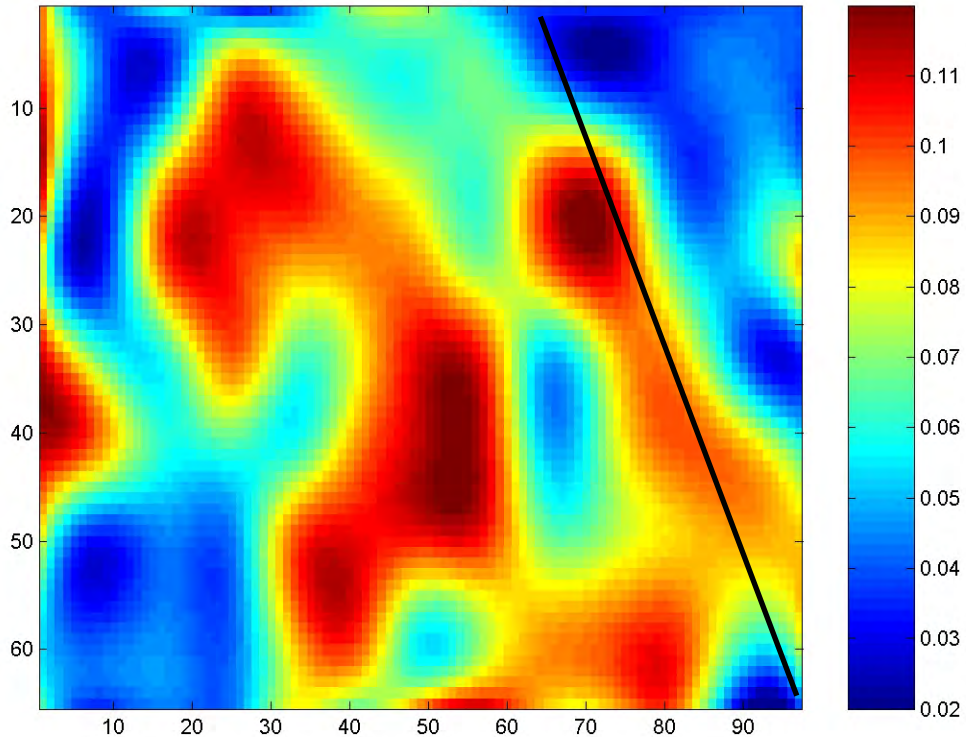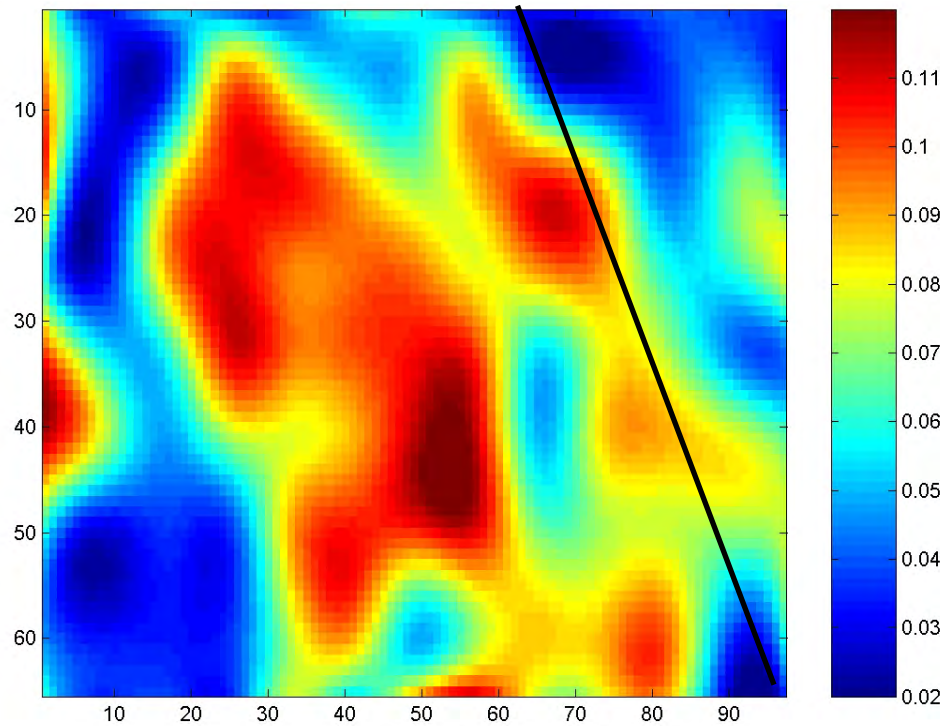
Figure 5.22: Map of the expected values for crack density derived from the *a posteriori* distribution, obtained by jointly constraining the *a priori* information with both the azimuthal anisotropy of reflectivity at far offsets (*A*) and the difference between the near- and far-offset reflectivity (*G=R$_N$-R$_F$*), in the hypothesis of a vertical set of aligned fractures.

However, if I consider the measurement uncertainty in the reflectivity anisotropy (*A*) to be one order of magnitude larger, then the posterior distribution for the expected values of crack density, conditioned both on *A* and *G* in Figure 5.23, is significantly different from the distribution in Figure 5.22. In this case, the impact of the prior information is more important. The values of fracture density are smaller, closer to the prior values of crack density.
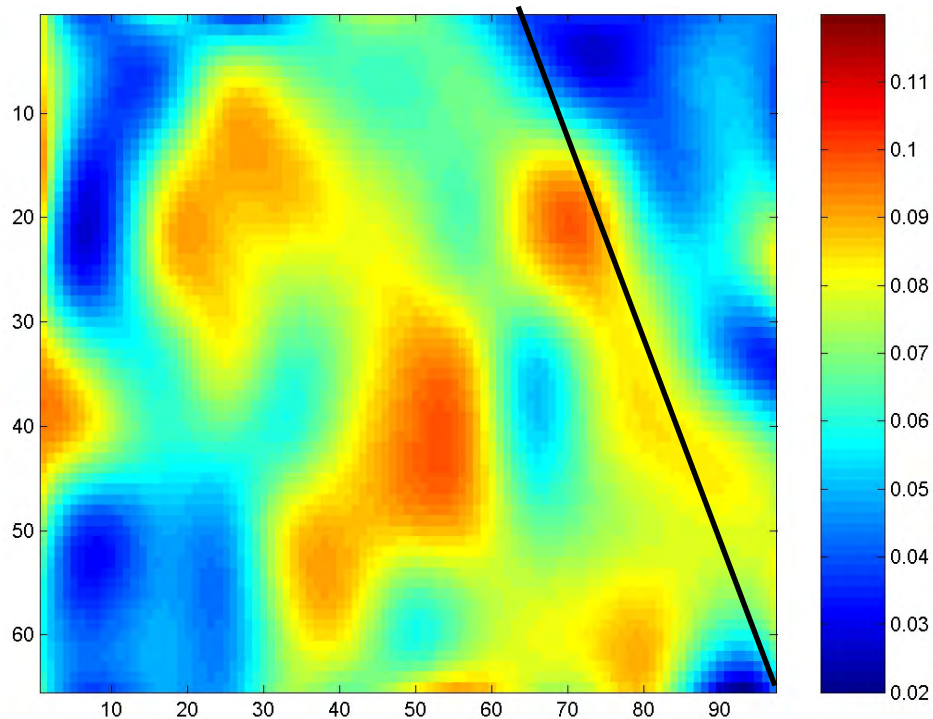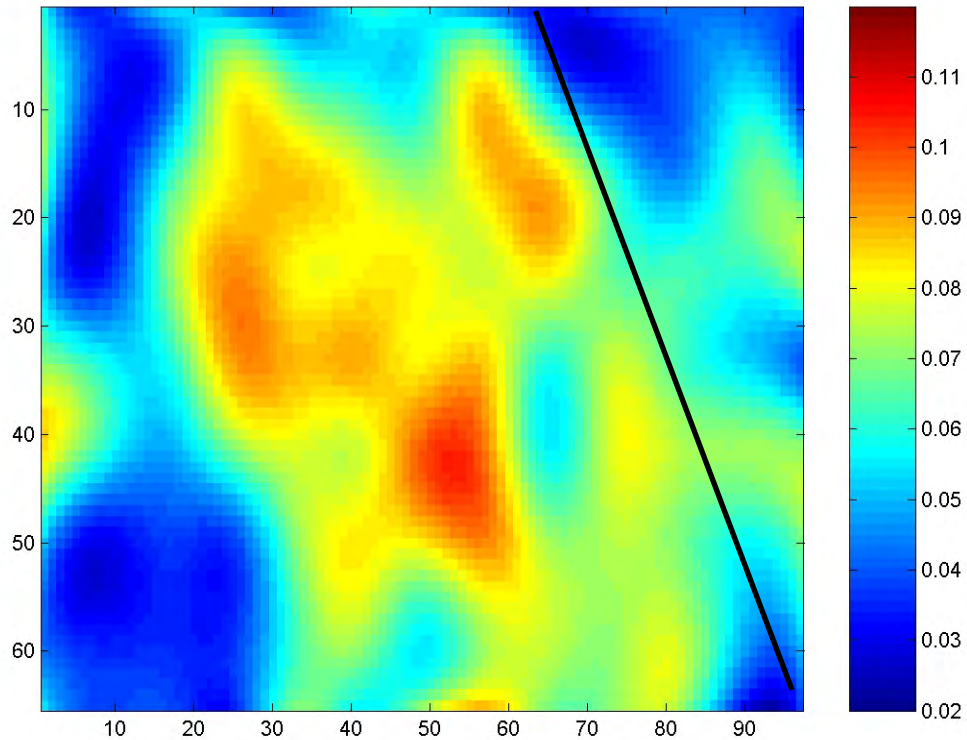
Figure 5.23: Map of the expected values for crack density derived from the *a posteriori* distribution, obtained by jointly constraining the *a priori* information with both the azimuthal anisotropy of reflectivity at far offsets (*A*) and the difference between the near- and far-offset reflectivity (*G=R_N-R_F*), in the hypothesis of a vertical set of aligned fractures. Standard deviations of the measurement uncertainty are one order of magnitude larger than those in Figure 5.10.

At each spatial location, I obtain not only the expected value of crack density, but the posterior probability density function (PDF). Figure 5.24 shows the prior PDF (red) for the crack density at a randomly chosen location, and also the *a posteriori* PDF after conditioning separately on *A* (black) and *G* (green), as well as the *a posteriori* PDF after jointly conditioning on *A* and *G* (blue).
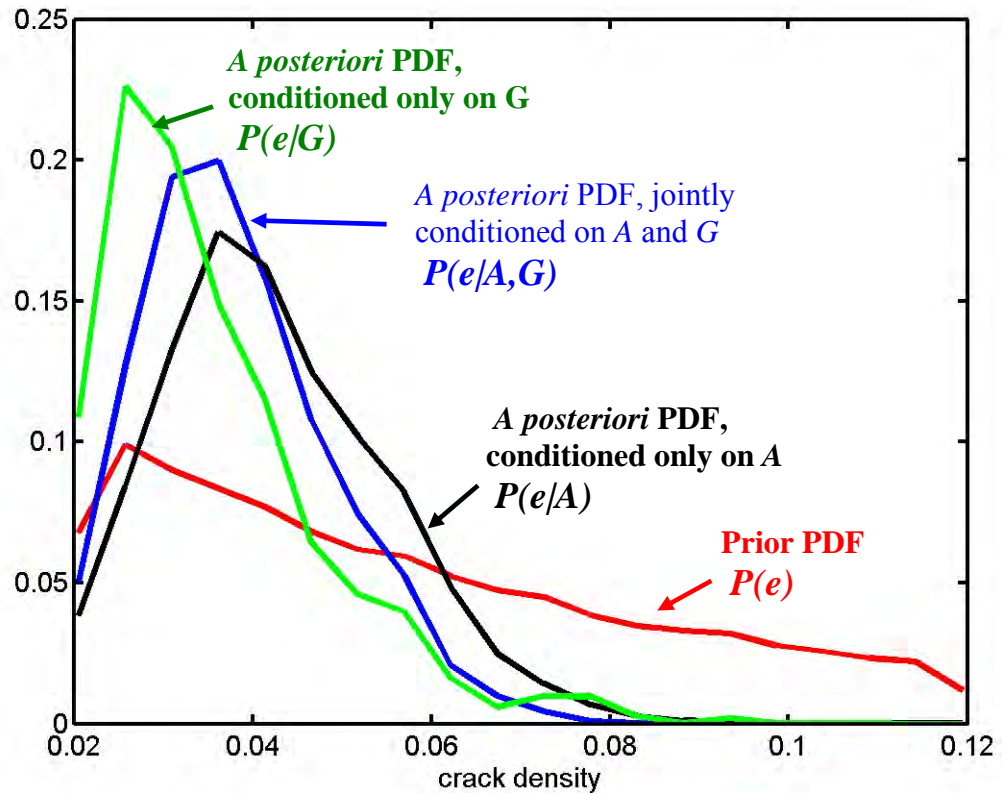
Figure 5.24: Probability density function for crack density at a randomly chosen location at the top of the reservoir. Red: *A priori* PDF for fracture density. Black: *A posteriori* distribution, conditioned only on the azimuthal anisotropy of reflectivity (*A*) at far offsets Green: *A posteriori* distribution for crack density conditioned only on the difference between the near- and the far-offset reflectivity (*G*). Blue: *A posteriori* distribution for crack density jointly conditioned on *A* and *G*.

The *a posteriori* distribution of crack density represents the updated measure of uncertainty after I combine the prior, the experimental and the theoretical information available. The standard deviation of the *a posteriori* distribution is a good measure for uncertainty when the posterior distribution is Gaussian. For example, Figure 5.25 presents the standard deviation about the expected values for fracture density from Figure 5.22, evaluated from the posterior PDF at each spatial location.
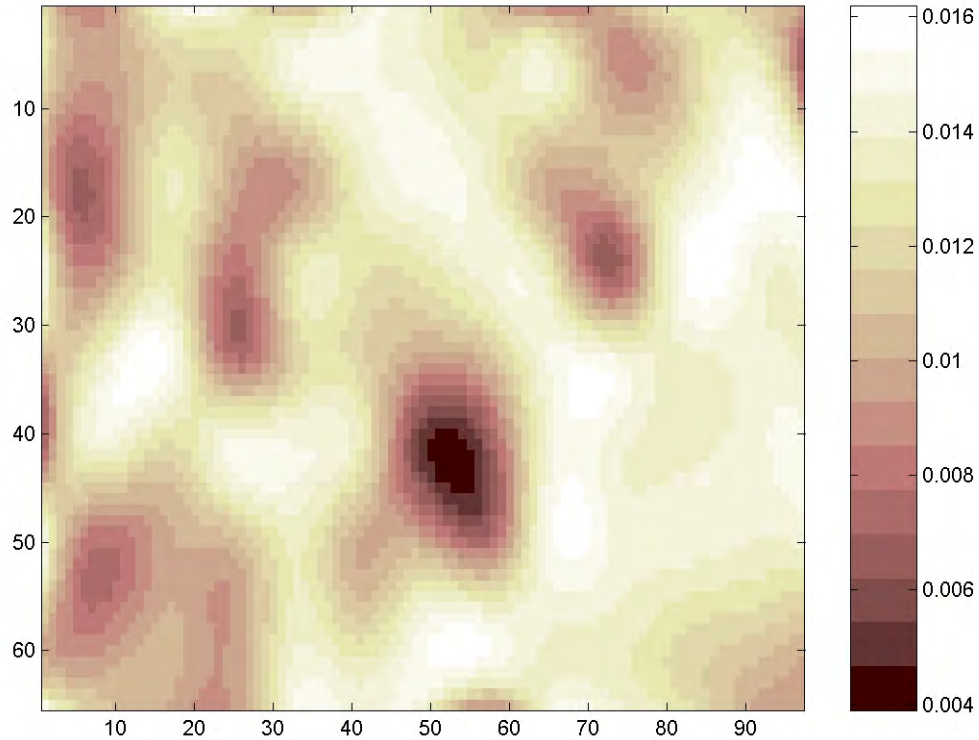
Figure 5.25: Map of the standard deviation about the expected values for crack density from Figure 5.21, derived from the *a posteriori* distribution obtained by jointly constraining the *a priori* information with both the azimuthal anisotropy of reflectivity at far offsets (*A*) and the difference between the near- and far-offset reflectivity (*G=R$_N$-R$_F$*), in the hypothesis of a vertical set of aligned fractures.

However, a more general way of expressing the uncertainty about the fracture density is through probability maps. At each grid point we can determine the probability that the fracture density exceeds a certain threshold. The probability that the fracture density exceeds a value of 0.09 is calculated at each grid point from the posterior PDF, as follows:

$$P(e > 0.09) = 1 - \int_{-\infty}^{0.09} \sigma_M(e)\, de \ . \tag{5.25}$$

For example, Figures 5.26 shows the probability map for crack density exceeding a value of 0.09, based on jointly conditioning the prior PDF on the azimuthal reflectivity anisotropy (*A*) and the difference between the near- and the far-offset reflectivity (*G*).
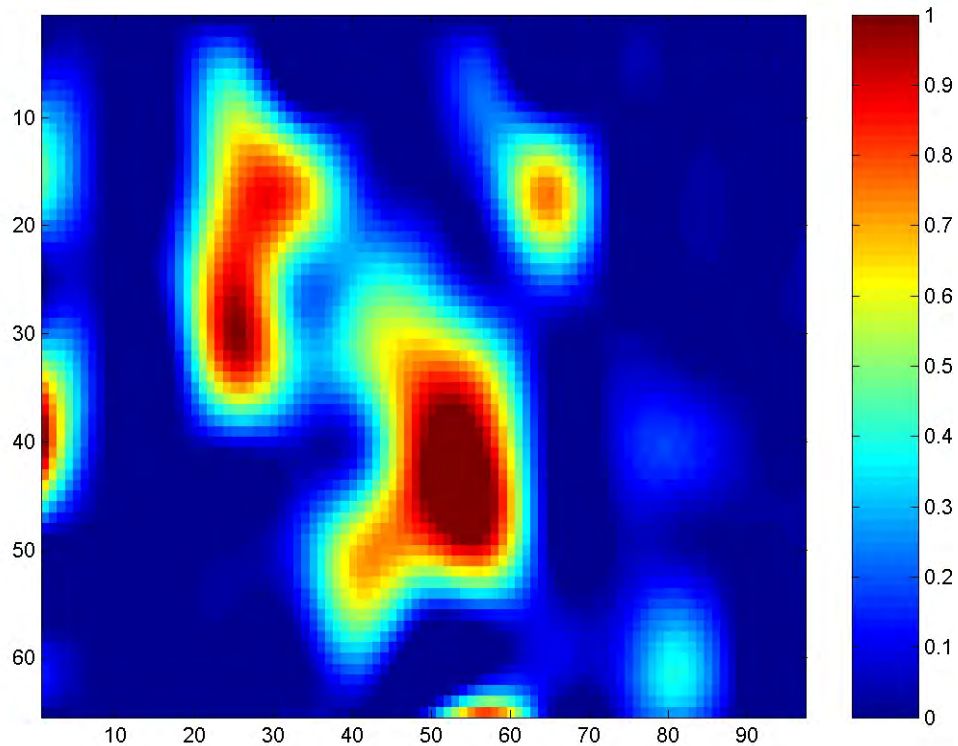
Figure 5.26: Probability map for fracture density exceeding a value of 0.09, obtained by jointly conditioning on the azimuthal reflectivity anisotropy (*A*) at far offsets and the difference between the near- and far-offset reflectivity (*G*). Geological hypothesis: a vertical set of aligned fractures.

From Figure 5.26 we can see that the probability of the fracture density exceeding a value of 0.09 is relatively small, except in two zones. Therefore, in the hypothesis of a vertical set of aligned fractures, the areas of higher probability of fractures are the ones highlighted in red on the probability map from Figure 5.26.

Figure 5.27 presents the same probability map as in Figure 5.26, but in this case the measurement uncertainty in the reflectivity anisotropy (*A*) is one order of magnitude larger. We can see that in this case, the probability that the fracture density exceeds the value of 0.09 is much lower, since the impact of the prior information, which indicates smaller fracture density values, is more significant.
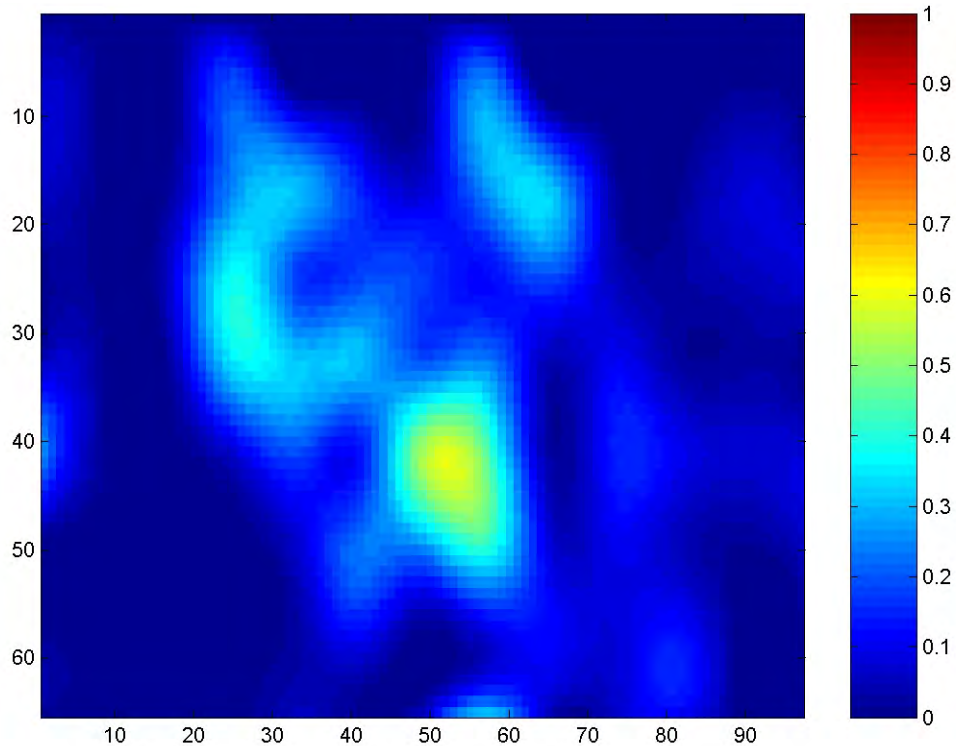
Figure 5.27: Probability map for fracture density exceeding a value of 0.09, obtained by jointly conditioning on the azimuthal reflectivity anisotropy (*A*) at far offsets and the difference between the near- and far-offset reflectivity (*G*). Geological hypothesis: a vertical set of aligned fractures. Standard deviations of the measurement uncertainty are one order of magnitude larger than those in Figure 5.10.

We can also obtain at each spatial location, the probability that the fracture density is smaller than a certain threshold. For example, Crampin (1994) suggests that a fracture density of 0.04 corresponds to a relatively small degree of fracturing. Therefore, it is important to evaluate at each location the probability that the fracture density is smaller than this value. In this way we can estimate the risk of drilling a new well in a zone of small fracture density.

Figure 5.28 shows a probability map for fracture density being smaller than 0.04, after combining the prior information with the azimuthal anisotropy in the reflectivity at far offsets, and the difference between the near- and far-offset reflectivity. The highlighted zones in red from Figure 5.28, correspond to the areas where the probability that the fracture density is smaller than 0.04 is high. If the permeability of the reservoir is

dominated by the open fractures, then these areas should be avoided for drilling production wells.
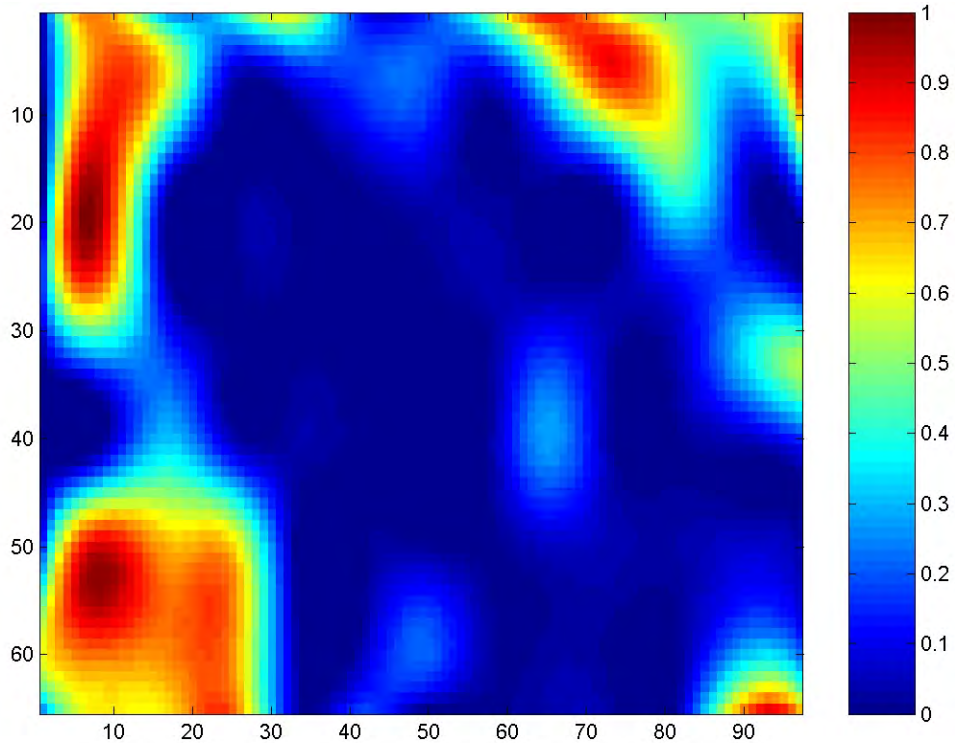
Figure 5.28: Probability map for fracture density being smaller than a value of 0.04, obtained by jointly conditioning on the azimuthal reflectivity anisotropy (*A*) at far offsets and the difference between the near- and far-offset reflectivity (*G*). Geological hypothesis: a vertical set of aligned fractures.

I also consider the geological hypothesis of randomly oriented fractures, which may correspond to brecciated zones in the proximity of possible subseismic faults. In this case, I combine the prior information about fracture density from geological interpretation with the near- and the far-offset reflectivity attributes.

Figure 5.29 presents a map with the expected values of crack density after conditioning the prior information on the far-offset reflectivity (R_F).

Figure 5.29: Map of the expected values for crack density derived from the *a posteriori* distribution obtained by constraining the *a priori* information with the far-offset reflectivity (R_F), in the hypothesis of randomly oriented fractures.

We can observe relatively larger crack density values in the hanging wall of the fault, schematically represented in Figure 5.29, as well as away from the fault.

Figure 5.30 presents a map with the expected values of crack density after conditioning the prior information on the near-offset reflectivity (R_N). In the vicinity of the fault, we observe a very good agreement between the geological hypothesis of higher fracture densities associated with the interpreted fault, and the actual near-offset reflectivity data. The seismic amplitudes are significantly smaller along the fault, implying that the assumed randomly oriented cracks have higher density in this area. However, there may be other phenomena associated with the interpreted fault, such as scattering, which are not accounted for by the theory used in this case.

Figure 5.30: Map of the expected values for crack density derived from the *a posteriori* distribution, obtained by constraining the *a priori* information with the near-offset reflectivity (R_N), in the hypothesis of randomly oriented fractures.

If I assume independence between the near- and far-offset reflectivity, I can derive the updated distribution of the crack density conditioned on both the near- and far-offset reflectivity, by simply multiplying each of the individual posterior probability density functions (PDF), as presented in section 5.3.5. Equation 5.26 is derived from Equation 5.13, showing that the *a posteriori* PDF conditioned on R_N and R_F, $\sigma_M(e/R_N,R_F)$, is proportional to the *a posteriori* PDF conditioned on R_N, $\sigma_M(e/R_N)$ multiplied by the *a posteriori* PDF conditioned on R_F, $\sigma_M(e/R_F)$. In Equation 5.26, $\rho_M(e)$ represents the prior PDF for fracture density.

$$\sigma_M(e/R_N,R_F) = \frac{1}{\rho_M(e)} \sigma_M(e/R_N)\sigma_M(e/R_F) \tag{5.26}$$

Figure 5.31 presents a map with the expected values of the crack density computed from the *a posteriori* PDF, $\sigma_M(e/R_N,R_F)$, assuming independence between the variables R_N and R_F (Equation 5.26).

Figure 5.31: Map of the expected values for crack density derived from the *a posteriori* distribution, assuming independence between the near- and far-offset reflectivity (Equation 5.26). Geological hypothesis: randomly oriented fractures.

If I jointly condition the prior information about fracture density on both the near- and the far-offset reflectivity, without assuming independence, I obtain a different distribution for the expected values of crack density at the top of the reservoir, presented in Figure 5.32. In this case, the correlations between the near- and the far-offset reflectivity are taken into account, by using the general framework of the methodology presented in section 5.3.4.

By comparing Figures 5.31 and 5.32, we can observe that, assuming independence in this case leads to a different distribution for the expected crack density than is derived by jointly conditioning on the near- and far-offset reflectivity. The correlation coefficient between the near- and far-offset reflectivity calculated by rock-physics stochastic simulations is 0.86. This value shows a significant correlation between the variables, and that is why the assumption of independence does not hold in this case. Therefore, if the

variables that we condition on are not independent, deriving the *a posteriori* PDF for the model parameters using Equation 5.26 may be misleading.
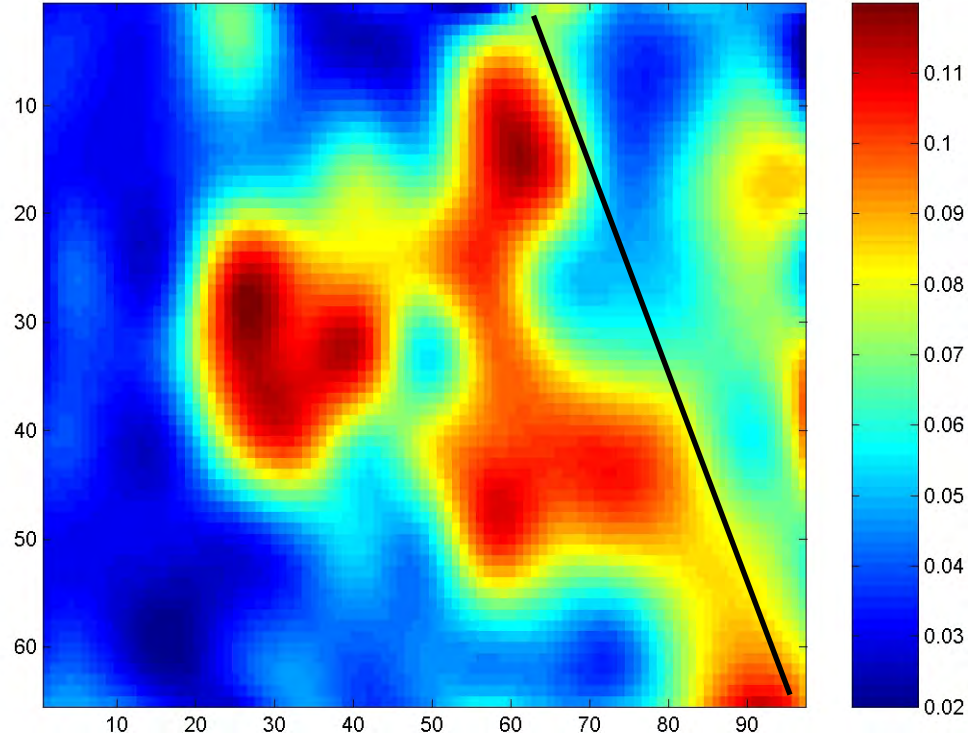
Figure 5.32: Map of the expected values for crack density derived from the *a posteriori* distribution obtained by jointly constraining the *a priori* information with both the near- and far-offset reflectivity, in the hypothesis of randomly oriented fractures.

I also use the difference between the near- and far-offset reflectivity, $(G=R_N-R_F)$, to obtain the updated crack density distribution. Figure 5.33 presents the map with the expected values of crack density after conditioning the prior information on the difference between the near- and far-offset reflectivity (G).

For the geological hypotheses of a single set of vertical fractures and of randomly oriented cracks, the distributions of the expected fracture density at the top of the reservoir, obtained by combining the prior information with the difference between the near- and far-offset reflectivity stacked over all azimuths, are very similar, as we can see from Figures 5.21 and 5.33.
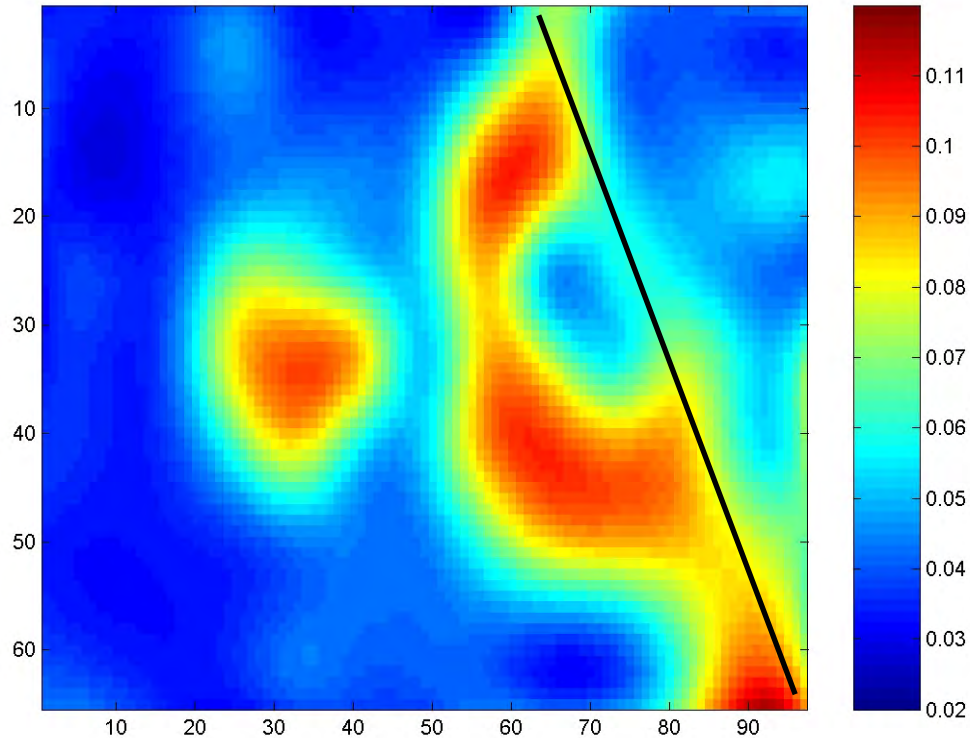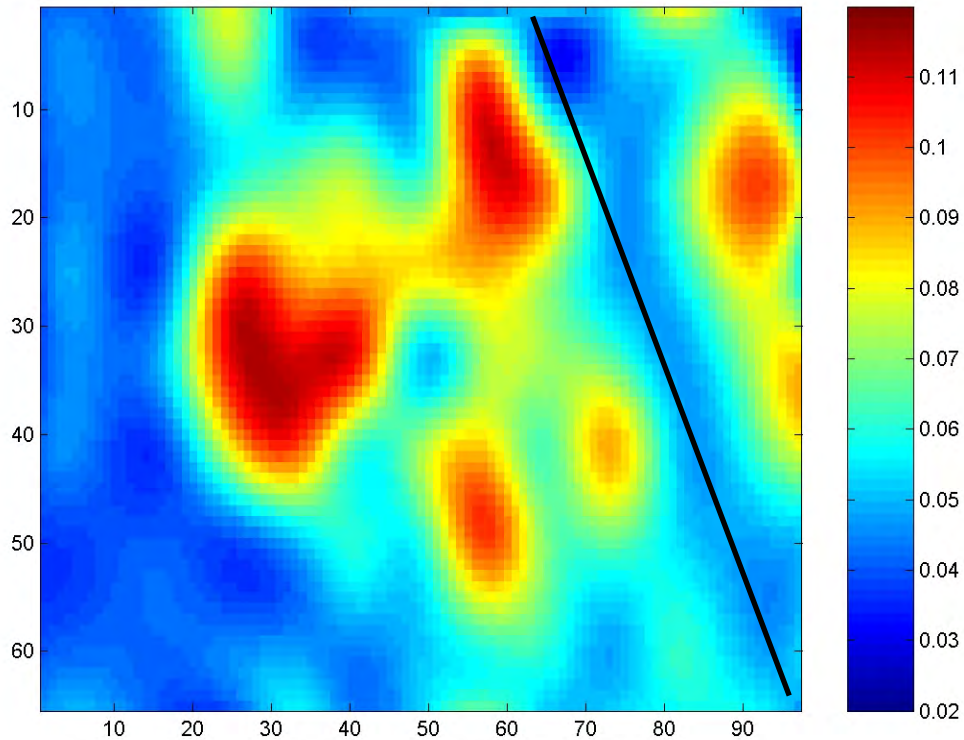
Figure 5.33: Map of the expected values for crack density derived from the *a posteriori* distribution obtained by constraining the *a priori* information with the difference between the near- and far-offset reflectivity (*G*), in the hypothesis of randomly oriented fractures.

Next, I obtain the updated distribution of fracture density at the top of the reservoir by jointly conditioning the prior PDF on both the far-offset reflectivity (R_F) and the difference between the near- and far-offset reflectivity (*G*). Figure 5.34 presents the map with the expected values of fracture density jointly conditioned on both reflectivity attributes (R_F and *G)*.
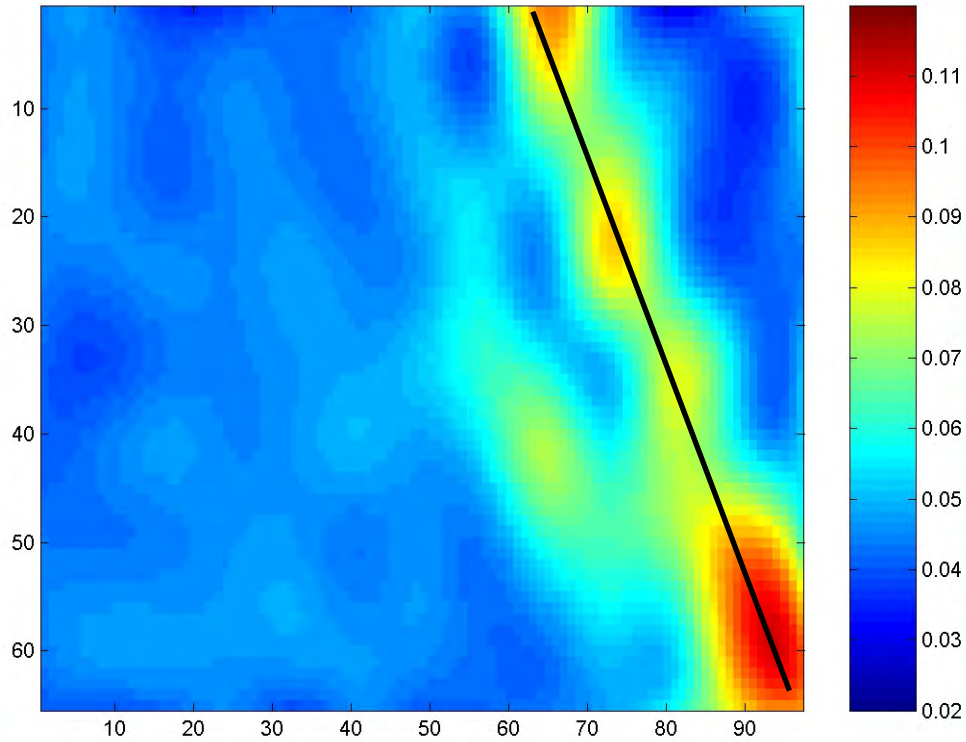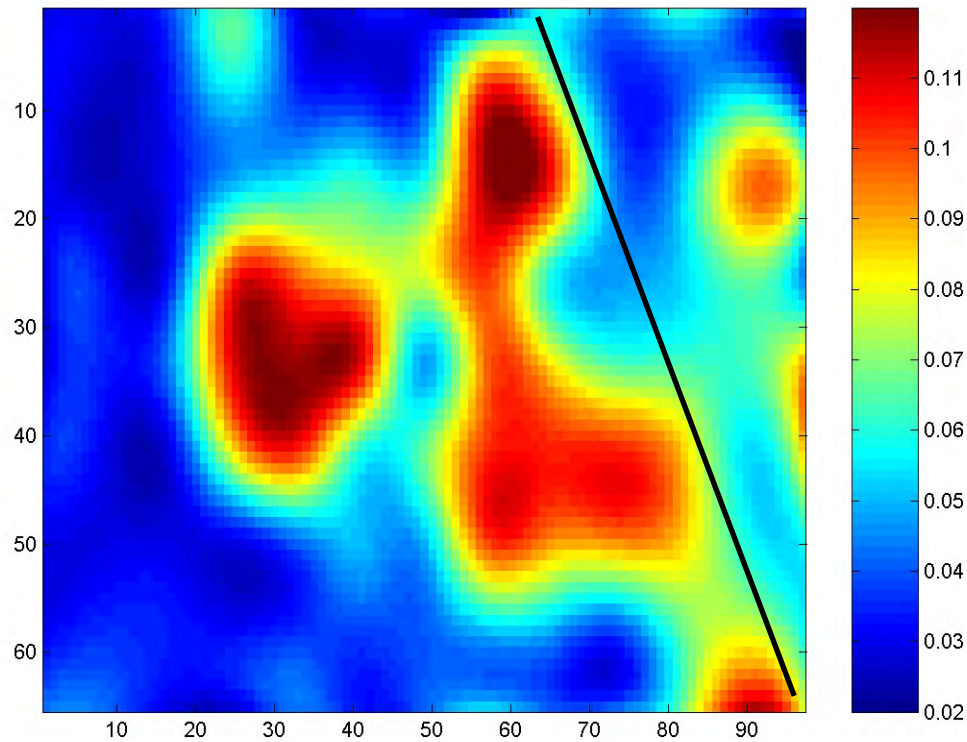
Figure 5.34: Map of the expected values for crack density derived from the *a posteriori*
distribution obtained by jointly constraining the *a priori* information with both the
far-offset reflectivity (R_F) and the difference between the near- and far-offset
reflectivity (*G*), in the hypothesis of randomly oriented fractures.

By comparing Figures 5.32 and 5.34, we can observe that the distributions for the
posterior expected fracture densities obtained by jointly conditioning on R_N and R_F
(Figure 5.32) are practically identical to those obtained by jointly conditioning on R_F and
the difference R_N-R_F (Figure 5.34). This result is expected, suggesting that data
manipulation does not bring new information. The two different pieces of information
used in both cases are the near- and far-offset reflectivity.

However, data manipulation may play a role in obtaining independent variables, such
that we can use the independence assumption to derive the *a posteriori* PDF on the
fracture parameters. For example, Figure 5.35 presents the updated distribution for the
expected values of fracture density derived by assuming independence between *G* and R_F,
by using the Equation 5.13, from section 5.3.5, as follows:

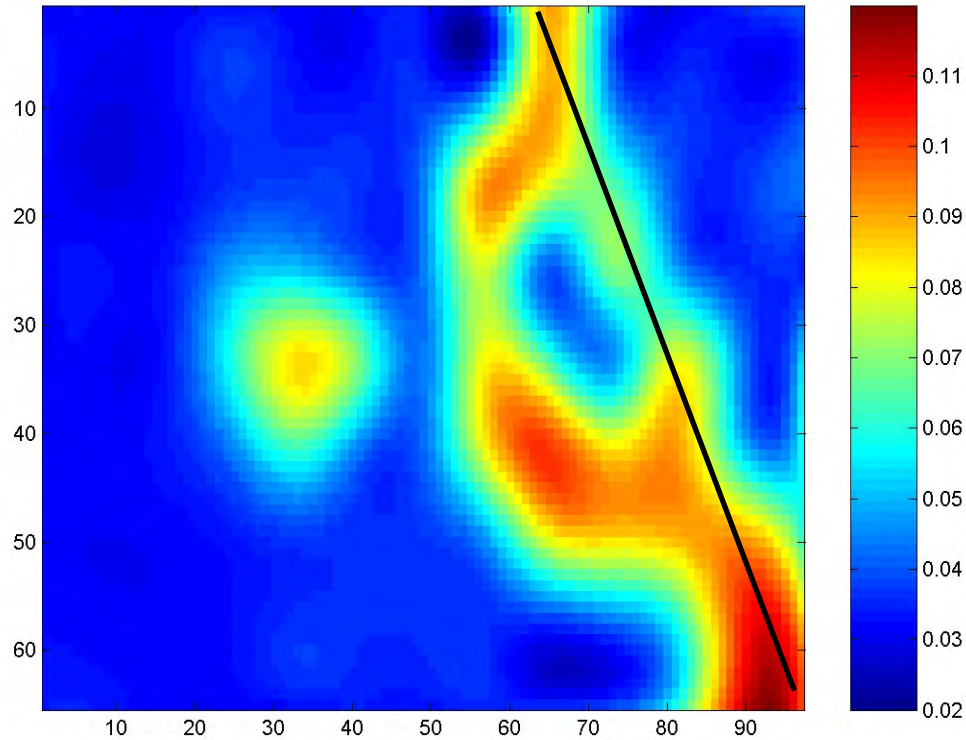$$\sigma_M(e/G,R_F) = \frac{1}{\rho_M(e)} \sigma_M(e/G)\sigma_M(e/R_F). \tag{5.27}$$
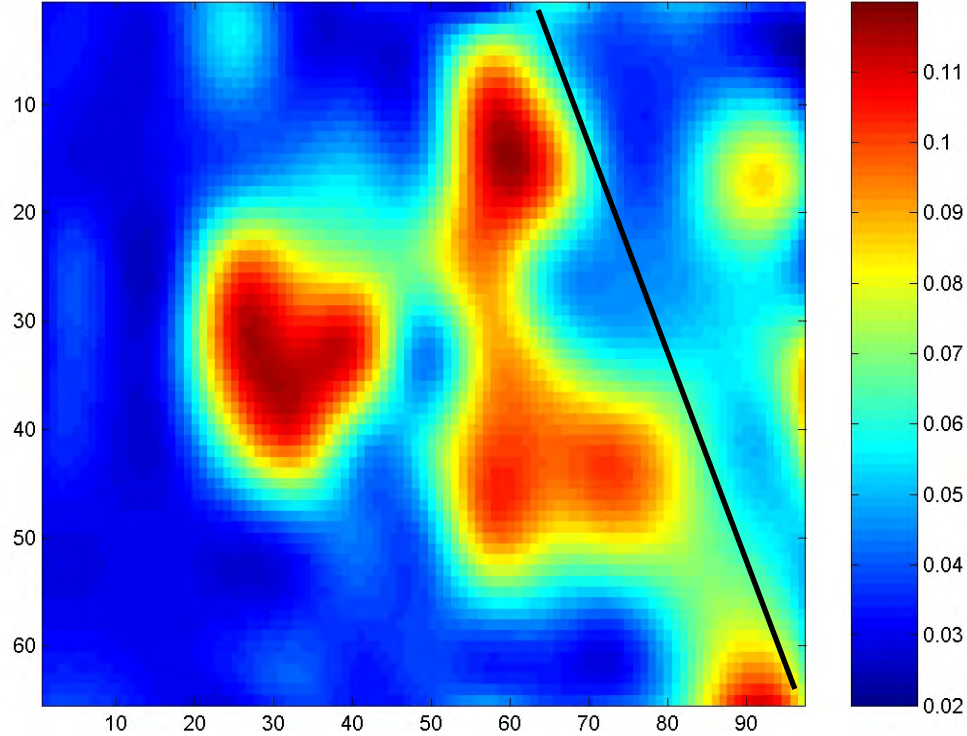
Figure 5.35: Map of the expected values for crack density derived from the *a posteriori* distribution by assuming independence between the far-offset reflectivity (R_F) and the difference between the near- and far-offset reflectivity (G), using Equation 5.27. Geological hypothesis: randomly oriented fractures.

In this case, the map of the expected values for fracture density at the top of the reservoir, derived by assuming independence between R_F and G (Figure 5.35), is very similar to the map obtained by jointly conditioning the prior PDF of fracture density on R_F and G (Figure 5.34). This suggests that the variables R_F and G (R_N-R_F) can be considered independent. Their correlation coefficient calculated based on the rock physics modeling and stochastic simulations has a small negative value of -0.18. This is why the distribution for the expected values of the crack density derived based on R_F and G by assuming independence is almost the same as the distribution for the expected crack-density values jointly conditioned on the G and R_F.

For both geological hypotheses of isotropic and anisotropic distribution of cracks, the prior information about the fracture distribution for this reservoir does not play a crucial role in the final results of the integration. This is because the rock-physics fracture modeling predicts that the seismic data is very constraining compared to the prior uncertainty about the fracture density. However, the prior information can sometimes have a significant impact on the posterior distribution of the model parameters. This happens when the uncertainty in the data and/or in the theoretical PDF, due to natural variability of the rock properties, are comparable with the prior uncertainty on the model parameters.

To conclude, in this section I show examples of integrating the prior information about fracture density with seismic-reflectivity attributes from a 3D seismic data for a fractured carbonate reservoir, under two geological hypotheses. The first hypothesis is that the fractures are vertical, aligned and more-or-less regularly spaced, such that they generate an azimuthally anisotropic medium. The second hypothesis is that the fractures occur in swarms associated with possible subseismic faults, and they are more randomly oriented, such as in brecciated areas.

Under both geological hypotheses I highlight the zones of higher fracture density at the top of the reservoir by conditioning the prior PDF of fracture density on different reflectivity attributes. The final result is represented by the *a posteriori* PDF of the fracture density at each spatial location. The posterior PDF of fracture density provides us with a complete measure of uncertainty after integrating the available geological, theoretical, and seismic information.

5.6   Conclusions

This chapter presents a way of integrating prior geological information with seismic data for improved subsurface property estimation, using statistical rock-physics within the framework of an inverse problem, as defined by Tarantola (1987). I illustrate the method with fracture characterization. The rock-physics theories provide the link between the fracture parameters and the seismic data, while the statistical approach

allows us to integrate quantitatively all the various types of information derived from geology, theory, well-log and seismic measurements.

The most general way to express mathematically the state of knowledge about the fracture parameters is through probability density functions. The language of Probability Theory allows us to account for the measurement errors and for the uncertainty in the relation between the fracture parameters and the seismic data due to natural variability of the target rock properties. This approach enables us to also estimate the uncertainty about our predictions, and to quantify the value of each type of information in reducing this uncertainty. Therefore, this method can have a significant impact on risk and decision analysis.

The methodology for quantitative data integration provides a new framework for estimating the subsurface rock properties and the uncertainty of our estimations, emphasizing the key importance of the rock physics theories in linking geological observations and seismic measurements. In this approach I use stochastic simulations together with deterministic rock-physics theories to estimate the uncertainty between the fracture parameters and seismic data due to natural variability of the rock properties. The well-log data represents an essential piece of information for calibrating the seismic properties of the target rocks. The natural variability of the rock properties is derived from the well-logs. Therefore more logged wells can help in better estimating the variability of the target rock properties.

To summarize, there are three different types of information that we need to integrate quantitatively: 1) the prior information on the fracture parameters, which often comes from geology, 2) the results of some experiments, often represented by the seismic data, and 3) the theoretical relation between the fracture parameters and the experimental data, which is given by the rock-physics theories, and calibrated using well-log data. The solution to the integration methodology is obtained by combining the prior, the experimental, and the theoretical information, to derive the *a posteriori* state of knowledge (Tarantola, 1987) of the fracture parameters. The *a posteriori* probability density function represents the updated measure of uncertainty about the fracture parameters after conditioning the prior information with the observed seismic data.

An important component of the integration methodology is the prior information on the fracture parameters. This chapter also presents a method to estimate the prior uncertainty about the fracture parameters, using a probability density function derived from the maximum entropy principle (Jaynes, 1983). This principle allows us to assign probabilities that are maximally uninformative, while still incorporating the information that one actually possesses. Therefore, we can estimate the *a priori* PDF based on a set of constraints imposed by geological interpretation.

In this chapter I emphasize not only the theoretical approach of combining prior geological information with seismic data, but I also present the practical steps of the methodology for quantitative data integration, giving an example from a fractured carbonate reservoir of gas in eastern Texas.

Based on the geological information about the reservoir, I consider two geological hypotheses. The first hypothesis is that the fractures are vertical and aligned, such that they generate an anisotropic medium. The second hypothesis is that the fractures occur in swarms associated with possible subseismic faults, and they are more or less randomly oriented, such as in brecciated zones.

In the example presented in this chapter, the model parameter is the fracture density. The prior distribution for the expected values of fracture density at the top of the reservoir is derived based on the interpretation of a major fault, resolved by the seismic data. The uncertainty about the prior values of fracture density is estimated using the Maximum Entropy Principle.

The observable data parameters used in this example are represented by various reflectivity attributes, such as the near- and the far-offset reflectivity, and also the azimuthal anisotropy of reflectivity at far offsets. The uncertainty in the reflectivity data is assumed to be Gaussian.

The theoretical relations between the fracture parameters and the observable data are derived using rock physics modeling and stochastic simulations, in both geological hypotheses of isotropic and anisotropic fracture distributions. The theoretical PDFs represent the uncertainty in the relation between the fracture density and seismic

attributes due to natural variability, and it is assumed representative for the entire study area.

Finally, I combine the prior information, the reflectivity attributes and the theoretical information to obtain the *a posteriori* distribution of fracture density at each spatial location. From the *a posteriori* PDF on the fracture density we can compute the posterior expected values. The integration methodology predicts in both hypothesis of isotropic and anisotropic distribution of fractures relatively higher fracture density values in the proximity of the fault. However, I also highlight zones of higher fracture density away from the fault, possibly associated with smaller, subseismic faults, which may have not been predicted otherwise.

The *a posteriori* PDF derived at each spatial location represents a complete measure of uncertainty, from which we can derive, for example, the probability that the fracture density is smaller than certain thresholds. In this way we can assess the risk of drilling a new well in an area with small fracture density. These probability maps can serve as a decision-making guideline for reservoir management.

Chapter 6

Conclusions

In this thesis I design a methodology for quantitative integration of prior geological information with seismic data, using rock physics theories (Mavko et al., 1998), within the framework of an inverse problem, as defined by Tarantola (1987). This method is general and can be applied for estimating various subsurface rock properties, using rock physics theories. In this dissertation, I illustrate the method with fracture characterization of a gas reservoir in eastern Texas.

The fracture parameters analyzed in the thesis are the fracture density, fracture orientation, and the type of fluid saturating the fractures, with an emphasis on the fracture density. The data parameters are the reflectivity attributes from a 3D seismic data set acquired over a fractured carbonate reservoir.

Rock physics theories provide the quantitative link between the fracture characteristics (model parameters) and the seismic measurements (data parameters). Although there are many published papers on elastic fracture models, little work has been done on testing the reliability of these models for seismic fracture characterization. Therefore, I explore the validity of the theoretical models by comparing their predictions with lab ultrasonic velocity measurements on simulated fractured media, whose geometric characteristics are known. Based on the comparison of the various fracture

models with lab measurements presented in Chapter 2, I conclude that either Hudson's (1981, 1997) models or Schoenberg's (1980, 1983) model can be used interchangeably to characterize the effective elastic properties of fractured media. Also, from the comparison of the theoretical predictions with the laboratory results, I conclude that the limit of validity for fracture density of Hudson's model of 0.1 represents a relatively large degree of fracturing at realistic reservoir pressures. I also analyze the collection of field data on shear-wave anisotropy as a function of depth, collected by Crampin (1994) from different authors. I use Hudson's fracture models to obtain the distribution of different fracture parameters from the field data, assuming that the observed shear-wave anisotropy is due to the alignment of fractures. From the analysis of this data, I observe a practical upper bound for the shear-wave anisotropy, and implicitly for the fracture density, that decreases with depth. This result puts valuable prior constraints on the fracture density as a function of depth, and helps calibrate the input parameters of the rock physics models.

In seismic fracture characterization, the relationship between the fracture parameters and the seismic attributes, given by rock physics theories (Chapter 2), is non-unique, due to the natural variability of the unfractured reservoir rocks, as well as of the cap rocks. Therefore, in order to assess the uncertainty in seismic interpretation of fracture density, fracture orientation, and fluid type, caused by the geologic variability of the target rocks, I use Monte Carlo simulations on the input parameters of the deterministic fracture models. Chapter 3 presents the results for the fracture modeling and stochastic simulations, based on the well logs for a fractured carbonate reservoir in eastern Texas. I derive the natural variability of the unfractured reservoir and cap rocks from the well-log data, which is an essential piece of information for calibrating the seismic properties of the target rocks. From the well-log data, I observe that the fractures are preferentially associated with the clean limestones, with small a amount of shale and low porosities, but high velocities. The reservoir is heterogeneous, and based on the rock physics analysis from well data, I consider that it exhibits three main types of facies: 1) the unfractured clean limestones, 2) the shaly limestones, less likely to get fractured, and 3) the clean, fractured limestones. I show that both interval and interface seismic attributes may be

useful to differentiate the gas-filled fractures from the other heterogeneities in the reservoir. However, the brine-filled fractures are more difficult to distinguish, due to the smaller compressibility in comparison with that of the gas. Also, the interface properties, such as the reflectivity from the top of the reservoir, are more useful seismic attributes than the interval properties, because the reservoir thickness is relatively small.

Therefore, the data parameters I consider are various reflectivity attributes from a 3D seismic data set acquired over the carbonate reservoir in eastern Texas (Chapter 4). In the geological hypothesis of a single set of aligned fractures, I use the amplitude variation with azimuth (AVAZ) at far offsets to determine the fractures' strike. I use a bootstrap method (Efron and Tibshirani, 1998; Teng, 1998) to estimate not only the mean fracture orientations, but also the uncertainty in fractures' strike due to the measurement errors in the reflectivity data. I find good agreement between the fracture orientation derived from seismic AVAZ and the fracture orientation derived from the well logs. In addition, the mean fracture strikes determined from AVAZ are approximately parallel to the maximum horizontal stress in the region.

Finally, the main contribution of the thesis is the methodology for integrating prior geological information with seismic data, using rock physics theories (Chapter 5). I give an example of combining quantitatively the prior information on fracture density, obtained from the geological interpretation of a fault at the top of the reservoir, with reflectivity attributes derived from the 3D seismic data set presented in Chapter 4. I also show a method to estimate the prior uncertainty in the fracture density values using the Maximum Entropy Principle (Jaynes, 1983). I consider the geological hypotheses of isotropic distribution of fractures, which may correspond to brecciated areas associated with subseismic faults, as well as a single set of vertical aligned fractures, which generates an anisotropic medium, as suggested by well-log data. The final result of this approach is the posterior distribution of fracture density, after integrating the geological, the seismic and the rock physics information, for both geological hypotheses considered.

The integration methodology predicts relatively higher fracture density values in the proximity of the interpreted fault at the top of the reservoir, which is consistent with the prior geologic information. In addition, I also highlight zones of higher fracture density

away from the fault, possibly associated with smaller, subseismic faults. Those zones are not known *a priori*.

Finally, I emphasize the impact of the prior geological information in comparison with that of the seismic data on the final results for fracture density distribution. The method allows us to derive the posterior expected values for fracture density, as well as the associated uncertainty, after integrating the prior geological information, the seismic data, and the rock physics theoretical information. The posterior uncertainty is illustrated using probability maps, as presented in Chapter 5. For example, these probability maps help us delineate the areas in the reservoir where the fracture density exceeds different thresholds with certain probabilities. Therefore, the probability maps can serve as a decision-making guideline for reservoir development.

References

Alford, R.M., 1986, Shear data in the presence of azimuthal anisotropy: Dilley, Texas, 56th Ann. Int. SEG Meeting, Houston, Expanded Abstracts, 476-479.

Anselmetti, F.S. and Eberly, G.Pl., Sonic velocity in carbonate sediments and rocks, Cabonate Seismology, ed. Palaz, I. and Marfurt, K.J., SEG.

Aster, A. C., Shearer, P. M., 1991, High frequency borehole sismograms recorded in the San Jacinto fault zone, Southern California, Bull. Seism. Soc. Am., 81, 1057-1080.

Avseth, P., Mukerji, T., and Mavko, G., 2005, Quantitative seismic interpretation, Cambridge University Press, in press.

Backus, G., 1962, Long-wave elastic anisotropy produced by horizontal layering, J. Geophys, Res., 76, 4427-4440.

Bakulin, A., Grechka, V. Tsvankin, I., 2000, Estimation of fracture parameters from reflection seismic data – Part I: HTI model due to a single fracture set, Geophysics, 65, 1788-1802.

Bai, T., and D.D. Pollard, 2000, Fracture spacing in layered rocks: a new explanation base on the stress transition, Journal of Structural Geology, 29, p.43-57.

Batzle, M., Wang, Z., 1992, Seismic properties of pore fluids, Geophysics, Vol. 57, No. 11, 1396-1408.

Bayes, T., 1783, An essay towards solving a problem in the doctrine of chances, Phil. Trans. Roy. Soc., 53, 370-418.

Booth, D.C, Crampin, S., Evans, R., Roberts, G., 1985, Shear -wave polarizations near the North Anatolian Fault-I Evidence for anisotropy induced shear-wave splitting, Geophys. J. R. astr. Soc., 83, 61-73

Booth, D. C.,Crampin, S., Lovell, J.H., Chiu, J.-M., 1990, Temporal changes in shear wave splitting during an earthquake swarm in Arkansas, J. Geophys. Res., 95, 11151- 11164.

Box, G. E. P., Tiao, G. C., 1992, Bayesian Inference in Statistical Analysis, (edited by Wiley- Interscience).

Buchbinder, G. G, 1985, Shear wave splitting and anisotropy in the Charlevoix seismic zone, Quebec, Geophys. Res. Lett., 12, 425-428.

Buchbinder, G. G., 1990, Shear wave splitting and anisotropy from the aftershocks of the Nahanni, Northwest Territories, earthquakes, J. Geophys. Res., 95, 4777-4785.

Bush, I., Crampin, S., 1991, Paris Basin VSPs: case history establishing combinations of matrix-and crack-anisotropy modeling shear wave-fields near point singularities, Geophys. J. Int., 107, 433-447

Castagna, J.P., Batzle, M.L.,and Kan,T.K., 1993, Rock-Physics- the link between the rock properties and AVO response, Offset-Dependent Reflectivity-Theory and Practice of AVO Analysis, eds. Castagna J.P. and Backus, M.M., SEG, Tulsa.

Cliet, C., Brodov, L, Tikhonov, A., Marin, D. Michon, D., 1991, Anisotropy survey for reservoir definition, Geophys. J. Int, 107, 417-427.

Crampin, S., 1994, The fracture criticality of crustal rocks, Geophys. J. Internat., 118, 428-438.

Daley, T. M., McEvilly, T. V., 1990, Shear-wave anisotropy in the Parkfield Varian Well VSP, Bull. Seism. Soc. Am., 80, 857-869.

Davatzes N., 2003, Ph.D. Dissertation, Stanford University

Du, X., 1990, On shear-wave splitting in the Los Angeles Basin, Pure and Applied Geophys., 134,175-194.

Efron B., Tibshirani, R., 1998, An introduction to the bootstrap: Chapman and Hall/CRC.

Feynman, R., Leighton, R., and Sands, M.,1963, The Feynman lectures on physics: Wesley, Reading, MA.

Florez, J. M., Mavko, G., 2002, Evolution of conjugate normal faults in sedimentary sequences with high brittleness/ductility contrast, Stanford Rock Physics and Borehole Geophysics Project (SRB) report, Stanford University Vol. 84, paper F2.

Gassmann, F., 1951, On the elasticity of porous media: Vier. Der Natur. Gesllschft in Zurich, 96, 1-23.

GledhillK.R., 1991, Evidence for shallow and pervasive seismic anisotropy in the Wellington Region, New Zealand, J. Geophys. Res., 96, 21505-21516.

Graham, G., Crampin, S. Fernandez, L. M., 1991, Observations of the shear-wave polarizations from rockbursts in a South African gold field and analysis of acceleration and velocity recordings, Geophys. J. Int., 107, 661-672.

Graham, G., Crampin, S. 1993 Shear-wave splitting from regional earthquakes in Turkey, Can. J. expl. Geophys., 29, 371-379.

Greenhalgh, S. A., Wright, C., Goleby, B., Soleman, S., 1990, Seismic anisotropy in granulite facies rocks of the Arunta Block, Central Australia, Geophys. Res. Lett. ,17, 1513-1516

Grechka , V. and Tsavankin, I., 1998, 3-D description of normal moveout in anisotropic inhomogeneous media, Geophysics, 63, 1079-1092.

Grimm R.E. and Lynn, H.B., 1997, Effects of acquisition geometry, large scale structure and regional anisotropy on AVOA: an example from the Wind River Basin, 67th Ann. Internat. Mtg. Soc. Expl. Geophys., Exp. Abstracts, 1997-2000.

Grimm, E.R., Lynn, H. B., Bates, C. R., Phillips, D. R., Simon K. M., Beckham, W. E., 1999, Detection and analysis of naturally fractured gas reservoirs: Multiazimuth seismic surveys in the Wind River basin, Wyoming, Geophysics, 64, 1277-1292.

Holmes, G.M., Crampin, S., Young R.P., 1993, Preliminary analysis of sher-wave splitting in granite at the Underground Research Laboratory, Manitoba, Can. J. Expl. Geophys, 29, 140-152.

Houck, R., 1999, Estimating uncertainty in interpreting seismic indicators: The Leading Edge, 18, 3, 320-325.

Hsu, C-J.,Schoenberg M., 1993, Elastic waves through a simulated fractured medium, Geophysics, 58, 964-977.

Hudson, J. A., 1980, Overall properties of a cracked solid, Math. Proc. Camb. Phil. Soc., 88, p. 371-384.

Hudson, J. A., 1981, Wave speeds and attenuation of elastic waves in material containing cracks: Geophys. J. Roy. Astr. Soc., 64, p. 133-150.

Hudson, J. A., 1990, Overall elastic properties of isotropic materials with arbitrary distribution of circular cracks, Geophys. J. Int., 102, p. 465-469.

Hudson, J. A., 1994, Overall properties of anisotropic materials containing cracks, Geophys. J. Int., 116, p. 279-282.

Hudson, J.A., Liu, E., and Crampin, S., 1996, The mechanical properties of materials with interconnected cracks and pores, Geophys. J. International, 124, 105-112.

Hudson, J.A., 1997, The mean transmission properties of a fault with imperfect facial contact, Geophys. J. Int, 129, 720 –726.

Hudson, J.A., Liu, E., 1999, Effective elastic properties of heavily faulted structures, Geophysics, 64, 479-485.

Innanaccone G., Deschamps, A. 1989 Evidence of shear-wave anisotropy in the upper crust of central Italy, Bulletin of seism Soc Am., 79 1905-1912.

Jaynes, E. T., 2003, Theory of Probability: The logic of science, Cambridge Univ. Press.

Jaynes, E. T., 1983, Papers on Probability, Statistics and Statistical Physics, Rosenkrantz, R. D. ed.

Kaneshima, S., Ando, M. Crampin, S., 1987, Shear wave splitting above small earthquakes in the Kinki District of Japan, Phys. Earth. Planet Inter., 45, 45-58.

Kaneshima, S., Ito, H. Sugihara, M. 1988, Shear wave polarization anisotropy observed in a rift zone in Japan, Tectonophysics, 157, 281-300.

Kaneshima, S., Ando, M., 1989, An analysis of split shear-waves observed above crustal and uppermost mantle earthquakes beneath Shikoku, Japan, implications in effective depth extent of seismic anisotropy, J. Geophys. Res., 94, 14077-14092.

Kuwakhara, Y. Ito, H., Kiguchi, T., 1991, Comparison between natural fractures and fracture parameters derived from VSP, Geophys. J. Int., 107, 475-483.

Laplace, P., S., 1814, A philosophical Essay on Probabilities, reprint, Dover Publications, Inc., New York, 1951.

La Pointe, P. R., Huston, J. A., 1985, Characterization and interpretation of rock mass joint patterns, Spec. Pap. Geol. Soc. Am., 199, 1-37.

Leary, P.C., Li Y.-G, Aki, K., 1987, Observation and modeling of fault-zone fracture seismic anisotropy -I P, SV and SH travel times, Geophys. J. R. Astr. Soc., 91, 461-484.

Lefeuvre, F., Cliet, C. Nicoletis, L., 1989, Shear-wave birefringence measurement and detection in the Paris basin, 59th Ann. Int. SEG Meeting, Dallas, Expanded Abstracts, 2, 786-790.

Lewis, C., Davis., T. L., Vuillermoz, C., 1991, Three-dimensional multicomponent imaging of reservoir heterogeneity, Silo Field, Wyoming, Geophysics, 56, 2048-2056.

Li, Y.-G, Leary, P.C., Aki, K., 1990, Ray series modeling seismic wave travel times and amplitudes in three-dimensional heterogeneous anisotropic crystalline rock: borehole vertical seismic profiling seismograms from the Mojave Desert, California, J. geophys. Res., 95, 11225-11239.

Li, X.-Y, Mueller, M.C., Crampin, S., 1993, Case studies of shear-wave splitting in reflection surveys in South Texas, Can. J. expl. Geophys., 29, 189-215.

Liu, E., Crampin, S., Queen, J. H., Reizr, W. D., 1993a Velocity and attentuation anisotropy caused by microcracks and macrofractures in azimuthal reverse VSPs, Can. J. expl. Geophys., 29 177-188.

Liu, E., Crampin, S., Queen, J. H., 1991, Fracture detection using crosshole surveys and reverse vertical seismic profiles at the Conoco Borehole Test Facility, Oklahoma, Geophys. J. Int., 107, 449-463.

Loucks, R. A., Cole, M. Ver Hoeve, 1996, Paleotopography association, litho-facies architecture and reservoir quality of the upper James Lime reservoir (Pearsall Fm, Lower Cretacesous) in the Poplarville Field, Pearl River County, Mississippi, AAPG Gulf Coast Association of Geolog. Soc., San Antonio, TX., XLVI 235-248.

Lynn, H.B., Thomsen, L.A., 1986, Reflection shear-wave data along the principal axes of azimuthal anisotropy, 56th, Ann Int. SEG Meeting, Houston, Expanded Abstracts, 473-477.

Lynn H. B., Simon, K. M. and Bates, C.R. 1996, Correlation between P-wave AVOA and S-wave traveltime anisotropy in a naturally fractured gas reservoir, The Leading Edge, 15, 931-935.

Lynn, H.B., Thomsen, L.A., 1990, Reflection shear-wave data collected near the principal axes of azimuthal anisotropy, Geophysics, 55, 1147-156.

Lynn, H. B., Campagna, D., Simon, K. M., Beckham, W. E., 1999, Relationshiop of P-wave seismic attributes, azimuthal anisotropy and commercial gas pay in #D P-wave multiazimuth data, Rulison Field, Piceance Basin, Colorado, Geophysics, 64, 1293-1311.

Mallick, S., Craft, K. L., Meister, L. J., Chambers, R.E, 1998, Determination of the principle directions of azimuthal anisotropy from P-wave seismic data: Geophysics 63, 692-706.

Martin, M.A., Davies, T.L., 1987, A new tool for evaluating fractured reservoirs, The Leading Edge, 6, 6, 22-28.

Mavko G., and Mukerji, T., 1998, A rock physics strategy for quantifying uncertainty in common hydrocarbon indicators, Geophysics, 63, 1997-2008.

Mavko G., Mukerji, T., Dvorkin, J., 1998, The rock physics handbook, Cambridge University Press.

Molotkov, L. A., Backulin, A. V., 1997, An effective model of a fractured medium with fractures modeled by the surfaces of discontinuity of displacements, Journal of Math. Sci., 86, 2735-2746.

Mueller, M.C., 1991, Prediction of lateral variability in fracture intensity using multicomponent shear-wave surface seismic as a precursor to horizontal drilling in Austin Chalk, Geophys. J. Int., 107, 409-415.

Mukerji, T., Avseth, P., Mavko, G., Takahashi, I., Gonzales, E., 2001, Statistical rock physics: combining rock physics, information theory, and geostatistics to reduce uncertainty in seismic reservoir characterization, The Leading Edge, 20, No 3, 313-319.

Mukerji, T., 1995, Ph. D. dissertation, Stanford University.

Narr, W., Suppe, J., 1991, Joint spacing in sedimentary rocks, J. Struct. Geol., 13, 1037-1048.

Nelson, R.A., 1985, Geologic analysis of Naturally Fractured Reservoirs, Houston: Gulf Pub CO., Book Division, c1985.

Nur, A., 1971, Effects of stress on velocity anisotropy in rocks with cracks, J. Geophys. Res., 76, 2022-2034.

Peakock, S., Crampin, S., Booth, D. C., Fletcher, J. B., 1988 Shear-wave splitting in the Anza seismic gap, Southern California: temporal variations as possible precursors, Journal Geoph Rws., 93, 3339-3356.

Perez, M.A, Grechka V., Michelena, R. J., 1999, Fracture detection in a carbonate reservoir using a variety of seismic methods, Geophysics, 64, 1266-1276.

Queen, J.H., Rizer, W.D., 1990, An integrated study of seismic anisotropy and the natural fracture system at the Conoco Borehole Test Facility, Kay County, Oklahoma, J. geophys. Res., 95, 11255-11273.

Reuss, A., 1929, Berechunung der fliessgrense von mischkristallen auf grund der plastizitatsbedinggung fur einkristalle, Zeitschrift fur Angewandte Mathematik and Mechanik, 9, 49-58.

Priest, S. D., Houston, J. A., 1976, Discontinuity spacing in rocks, Int. J. Rock Mech. Mining Sci Geomech. Abs., 13, 135-148.

Rives, T., Razack, M., Petit, J.-P., Rawnsley, K. D., 1992, Joint spacing: analogue and numerical simulations, Journal of Structural Geology, Vol 14, No 8/9, 925-937.

Roberts, G., Crampin, S., 1986, Shear-wave polarizations in a hot-dry-rock geothermal reservoir: anisotropic effects of fractures, Int. J., Rock Mech. Min. Sci., 23, 291-302.

Ross, S., 2001, A first course in probability theory, 6th edition, Prentice Hall.

Rouleau, A, Gale, J. E., 1985, Statistical characterization of the fracture system in the Stripa granite, Sweden, Int. J. Rock Mech. Mining Sci Geomech. Abs., 22, 353-367.

Rüger, A., 1995, P-wave reflection coefficients for transversely isotropic media with vertical and horizontal axis of symmetry, Expanded Abstracts, Society of Exploration Geophysicists, 65th Annual Meeting, 278-281.

Rüger, A., 1996, Variation of P-wave reflectivity with offset and azimuth in anisotropic media, Expanded Abstracts, Society of Exploration Geophysicists, 66th Annual Meeting, 1810-1813.

Ruger, A., 1998, Variation of P-wave reflectivity with offset and azimuth in anisotropic media, Geophysics, **63**, 935-947.

Sava, D. C., Mukerji, T., Florez, J. M., Mavko, G., 2001, Rock physics analysis and fracture modeling of the San Andres reservoir, Yates field, 71th Ann. Int. SEG Meeting, San Antonio, TX, Expanded Abstracts, 1748-1751.

Sava, D. C., Florez, J. M., Mukerji, T., Mavko, G., 2002, Seismic fracture characterization using statistical rock physics: James Lime reservoir, Neuville field, 72nd Ann. Int. SEG Meeting, Salt Lake City, UT, Expanded Abstracts,1889-1892.

Savage, M.K., Shih, X.R., Meyer, R.P., Aster, R.C., 1989, Shear-wave anisotropy of active tectonic regions via automated S-wave polarization analysis, Tectonophysics, 165, 279-292.

Savage, M.K., Peppin, W. A., Vetter, U.R., 1990, Shear-wave anisotropy and stress direction in and near Long Valley Caldera, California, 1979-1988, J. Geohys. Res. 95, 11165-11177.

Schoenberg, M., 1980, Elastic behavior across linear-slip interfaces, 1980, J. Acoustic Society Am., 68, 1516-1521.

Schoenberg, M., 1983, Reflection of elastic waves from periodically stratified media with interfacial slip, Geophys. Prosp. 31, p. 265-292.

Schoenberg, M and Muir, F, 1989, A calculus for finely layered anisotropic media, Geophysics, 54, 581-589.

Schoenberg, M and Douma, J., 1988, Elastic wave propagation in media with parallel fractures and aligned cracks, Geophys. Prosp., 36, p. 571-590

Schoenberg, M and Sayers, C. 1995, Seismic anisotropy of fractured rock, *Geophysics*, 60, 204-211.

Sen, Z., Kazi, A., 1984, Discontinuity spacing and RQD estimates from finite length scanlines, Int. J. Rock Mech. Mining Sci. Geomech. Abs., 21, 203-212.

Shannon, C., 1948, A mathematical theory of communication: Bell System Technical Journal, 27, 379-423, 623-656.

Shen, F., Sierra, J., Burns, D. R., Toksoz, M. N., 2002, Azimuthal offset-dependent attributes applied to fracture detection in a carbonate reservoir, Geophysics, 67, 355-364.

Shih, X.R., Meyer R. P., 1990 Observations of shear-wave splitting from natural events:

Shuey, R. T., 1985, A simplification of the Zoeppritz equations, Geophys., 50, 609-614.

South Moat of Long Valley Caldera, California, June 29 to August 12, 1982, J. geophys. Res., 95, 11179-11195.

Shuck, E. L., 1991, Azimuthal anisotropy analysis from shear VSPs, Geophys. J. Int., 107, 639-647.

Slater, C., Crampin, S., Brodov, L..Y., Kuznetsove, V.M., 1993, Observations of anisotropic cusps in transversely isotropic clay, Can. J. Expl. Geophys, 29, 216-226.

Snow, D. T., 1968, Anisotropic permeability of fractured rocks. In: Hydrology and Flow through Porous Media (edited by De Wiest, R. J. M.)

Takahashi, I., Mavko, G., Mukerji, T., 1999, A strategy to select the optimal seismic attributes for reservoir property estimation: Application to information theory, Soc. Expl. Geophys., Expended Abstracts.

Takahashi, I., 2000, Ph.D. dissertation, Stanford University.

Tarantola, A., Vallete, B., 1982, Inverse problems = Quest for information: J. Geophys., 50, 150-170.

Tarantola, A., 1987, Inverse Problem Theory, Elsevier Science B. V.

Teng, L., 1998, Ph.D. dissertation, Stanford University.

Thomsen, L., 1986, Weak elastic anisotropy: Geophysics, 51, No. 10, 1954-1966.

Tsvankin, I., 1997, Reflection moveout and parameter estimation for horizontal transverse isotropy, Geophysics, 62, 614-629.

Vavrycuk, V. and Psencik, I., 1998, PP-wave reflection coefficients in weakly anisotropic elastic media, Geophysics, 63, 2129-2141.

Villaescusa , E, Brown, E. T., 1990, Characterizing joint spatial correlation using geostatistical methods. In: Rock Joints (edited by Barton, N. and Stephansson, O.), Balkema, Rotterdam, 115-122.

Winterstein, D. F., Meadows, M.A., 1991a, Shear-wave polarization and subsurface stress directions at Lost Hills field, Geophysics, 56, 1331-1348.

Winterstein, D. F., Meadows, M.A., 1991b, Changes in shear-wave polarization azimuth with depth in Cymric and Railroad Gap oil fields, Geophysics, 56, 1349-1364.

Yardley, G.S., Crampin, S., 1993 Shear-wave anisotropy in the Austin Chalk, Texas, From multi-offset VSP data: case studies, Can. J. Expl. Geophys., 29, 163-176.

Zoeppritz, K., 1919, Erdbebenwellen VIIIB, On the reflection and propagation of seismic waves. Gottinger Nachrichten, I, 66-84.